DEVELOPING DIFFERENT ARCHITECTURES OF CAPACITIVE DEIONIZATION FOR ENHANCED REMOVAL OF HEAVY METALS FROM WASTEWATER

BY

NGUYEN TAN THONG

A DISSERTATION SUBMITTED IN PARTIAL FULFILLMENT OF THE REQUIREMENTS FOR THE DEGREE OF DOCTOR OF PHILOSOPHY (ENGINEERING AND TECHNOLOGY)
SIRINDHORN INTERNATIONAL INSTITUTE OF TECHNOLOGY
THAMMASAT UNIVERSITY
ACADEMIC YEAR 2024

THAMMASAT UNIVERSITY
SIRINDHORN INTERNATIONAL INSTITUTE OF TECHNOLOGY

DISSERTATION

BY

NGUYEN TAN THONG

ENTITLED

DEVELOPING DIFFERENT ARCHITECTURES OF CAPACITIVE DEIONIZATION FOR ENHANCED REMOVAL OF HEAVY METALS FROM WASTEWATER

was approved as partial fulfillment of the requirements for
the degree of Doctor of Philosophy (Engineering and Technology)

on November 19, 2024

Chairperson _____
(Associate Professor Tanujjal Bora, Ph.D.)

Member and Advisor _____
(Professor Sandhya Babel, D.Tech.Sc.)

Member _____
(Associate Professor Paiboon Sreearunothai, Ph.D.)

Member _____
(Associate Professor Chanatip Samart, Ph.D.)

Member _____
(Kritapas Laohhasurayotin, Ph.D.)

Director _____
(Professor Pruettha Nanakorn, D.Eng.)

Dissertation Title	DEVELOPING DIFFERENT ARCHITECTURES OF CAPACITIVE DEIONIZATION FOR ENHANCED REMOVAL OF HEAVY METALS FROM WASTEWATER
Author	Nguyen Tan Thong
Degree	Doctor of Philosophy (Engineering and Technology)
Faculty/University	Sirindhorn International Institute of Technology/ Thammasat University
Dissertation Advisor	Professor Sandhya Babel, D.Tech.Sc.
Academic Years	2024

ABSTRACT

Capacitive deionization (CDI) is an emerging technique in water treatment due to its simplicity, energy saving, and environmental sustainability. It has been widely studied for desalination; however, its potential for heavy metals (HMs) removal is an area of ongoing research. In this study, several actions were implemented to assess the feasibility of employing CDI for remediating wastewater with HMs. To achieve the specified goals, lab-scale CDI cells were constructed and operated continuously. The study analyzed synthetic wastewater for the removal of Cr^{6+}, Cr^{3+}, Cu^{2+}, and Ni^{2+}, (with concentrations from 50 to 1000 mg/L) and then assessed real electroplating wastewater. Two approaches were utilized, including a modified electrode nanostructure and a fabricated cation exchange membrane. The effects of operational conditions in the CDI system were also analyzed. The following is a summary of the results and findings of this study: (1) Grafting MnO_2 nanostructures onto activated carbon cloth (ACC/MnO_2) significantly increased the capacitance of the material, enhancing removal of chromium. The adsorption amount of ACC/MnO_2 was 7.86 mg/g, which was greater than the adsorption amount of pristine ACC (6.65 mg/g) for Cr^{6+} removal. (2) The

modification of the activated carbon fiber surface with ZnO nanorods (ACC/ZnO-nRs) resulted in enhanced the electric field, leading to higher adsorption capacity of Cu^{2+} removal. The ACC material presented a specific capacitance of 38.43 F/g, while ACC/ZnO-nRs demonstrated a higher value of 45.08 F/g. (3) Using fabricated heterogeneous cation exchange membranes in a membrane capacitive deionization (MCDI) cell exhibited more significant adsorption of Ni^{2+} than the CDI cell, reaching 3.42 mg/g, while the CDI cell achieved 2.15 mg/g. (4) Increasing potential improved adsorption capacity and recovery rates for Cr^{6+}, Cr^{3+}, Cu^{2+}, and Ni^{2+}, while initial concentrations, pH, and flow rates notably influenced adsorption capacity. (5) The utilization of ACC/ZnO-nRs electrodes and commercial ion exchange membranes in the MCDI cell showed significant promise in treating real electroplating wastewater, meeting Thailand's industrial wastewater discharge regulation. This study found successful performance in eliminating HMs through appropriately configured and operated capacitive deionization systems. The findings of this study highlight the potential of CDI technique to effectively mitigate HMs contamination in wastewater, including synthesis and electroplating wastewater.

Keywords: Capacitive deionization, Wastewater, Heavy metals, Nanostructures, Activated carbon, Membrane

ACKNOWLEDGEMENTS

I heard that “Out of hundreds of millions of raindrops, not a single drop falls in the wrong place. None of the people we meet are by chance. Everything is predestined by fate”.

First and foremost, I extend my most profound appreciation to my advisor, Prof. Dr. Sandhya Babel, for granting me the opportunity to pursue my studies at Thammasat University. Her patient guidance, encouragement, and unwavering support have been invaluable in helping me develop the skills and knowledge necessary to complete my research.

I am incredibly thankful to Assoc. Prof. Dr. Tanujjal Bora for his valuable guidance during the initial stages of my dissertation and for his insightful feedback throughout my research. I am particularly grateful to Assoc. Prof. Dr. Paiboon Sreearunothai for his invaluable advice and support with his device, without which I could not have completed my experiments. Additionally, I am profoundly grateful to Dr. Kritapas Laohhasurayotin and Assoc. Prof. Dr. Chanatip Samart, my committee members, for their insightful feedback, which significantly shaped my research.

I appreciate my former advisor, Prof. Dr. Nguyen Phuoc Dan, and my manager, Assoc. Prof. Dr. Thai Phuong Vu, for their guidance and support over a long time. I am also thankful to my friends and labmates, especially Dr. Ta Tuan Anh and Dr. Nguyen Hoang Dung, for their support during my research in Thailand.

I would like to acknowledge the staff at Thammasat University for their academic support and services. This research would not have been possible without the financial aid provided by the Excellent Foreign Students (EFS) scholarship from Sirindhorn International Institute of Technology, Thammasat University, and the Doctoral Scholarship for Research from Thammasat University.

I would like to express my heartfelt thanks to my father, Ông Nguyễn Đức Thịnh, my mother, Bà Trần Thị Kim Oanh, and my sister's family for their unwavering love and support throughout my studies abroad. Their sacrifices and understanding have always been a source of strength for me.

Thank you all for your inspiration and encouragement during my time in Thailand.

Nguyen Tan Thong

TABLE OF CONTENTS

LIST OF TABLES

LIST OF FIGURES

LIST OF SYMBOLS/ABBREVIATIONS

Symbols/Abbreviations	Terms
CDI	Capacitive deionization
MCDI	Membrane capacitive deionization
IEMs	Ion exchange membranes
CEM	Cation exchange membrane
AEM	Anion exchange membrane
HMs	Heavy metals
PFO	Pseudo-first order
PSO	Pseudo-second order
DI water	Deionized water
AC	Activated carbon
ZnO	Zinc oxide
MnO_2	Manganese dioxide

CHAPTER 1

INTRODUCTION

1.1 Background

In the past few decades, global water scarcity has become increasingly severe as the demand for clean water keeps increasing while conventional water sources have been reducing alarmingly (UN, 2023). The increasing need for water, driven by several factors, including population growth, urbanization, and industrialization, is exerting tremendous pressure on freshwater supplies. Considering these challenges, innovative techniques for treating water optimally using energy and saving costs are essential to solving the water problem. These innovative techniques should not only be able to provide a sustainable solution but also have less of a negative ecological impact on the environment than conventional water treatment methods currently in use. Besides, heavy metals (HMs) in industrial wastewater from activities like electroplating, mining, textile manufacturing, pesticide production, and chemical manufacturing require severe control measures before releasing them into the environment (Fu & Wang, 2011; Qasem et al., 2021). The existence of HMs in industrial wastewater has a significant negative influence on water resources. Even at low concentrations, specific HMs harm human health (Fairbrother et al., 2007a). Moreover, HMs possess properties distinct from organic molecules, rendering them resistant to degradation by chemical or biological means (Fairbrother et al., 2007a; Goyer et al., 2004). Consequently, source control of wastewater is crucial for environmental protection, as it safeguards not only the present ecosystem but also the well-being of future generations.

Numerous strategies involving diverse physical and chemical approaches, including chemical precipitation, ion exchange, adsorption, and membrane separation, have been studied to treat wastewater containing HMs (Qasem et al., 2021). While these methods exhibit specific efficacy in removing metals, they also face challenges (Crini & Lichtfouse, 2019; Fu & Wang, 2011). For example, chemical precipitation is commonly employed due to its simplicity and ability to handle high wastewater concentrations. However, it generates secondary sludge that is challenging and costly to treat (Fu & Wang, 2011). Ion exchange, similarly, leads to secondary pollution as

chemical agents are required to regenerate the resin and treat the metals absorbed during the regeneration phase (Zhao et al., 2018). Additionally, adsorption and membrane filtration encounter difficulties when dealing with wastewater containing high concentrations of HMs and incurring long-term operational costs (Abdullah et al., 2019; Singh et al., 2017). Therefore, it is imperative to find cost-effective techniques that minimize generated waste while efficiently reducing HMs levels.

1.2 Problem statement

To date, capacitive deionization (CDI) is an emerging technique in water treatment due to its simplicity, energy saving, and environmental sustainability (Luo et al., 2020; Xing et al., 2020). It has been widely studied for desalination; however, its potential for HMs removal is an area of ongoing research (Ahmed & Tewari, 2018; L. Liu et al., 2017). The CDI technique operates on the principle of electrostatic attraction, whereby ions existing in water are captured and subsequently stored within porous electrodes. The stored ions are later released when the electric field is reversed, allowing for the electrodes' regeneration and freshwater production. Several efforts are aimed at expanding the performance and usefulness of the CDI technique, which includes enhancing the properties of electrode materials, designing CDI architectures, and establishing the optimal operation parameters (Cheng et al., 2019; Tang et al., 2019a; Xing et al., 2020). It is essential to note that electrode material properties and the CDI configuration positively impact the CDI system's effectiveness (Cheng et al., 2019; Shi et al., 2019; Tang et al., 2019a).

Electrode material is crucial to achieving efficiency in CDI systems (Cheng et al., 2019; Zhang et al., 2020). Activated carbon is frequently employed as electrode material in CDI systems. This preference is due to activated carbon's extraordinary physical properties, such as its low cost, lightweight, high surface area, porosity, and stability, making it supremely well-suited for the CDI application (Kyaw et al., 2020; Wu et al., 2021). Furthermore, deliberate surface modification of activated carbon can be carried out to optimize its performance in CDI operations. Introducing functional groups, which include carboxyl, hydroxyl, and amino groups, onto the surface of activated carbon allows for the customization of its surface charge and the enhancement

of its adsorption properties (Kyaw et al., 2020). Besides, the introduction of metal oxide nanostructures onto carbonaceous materials, including zinc oxide (ZnO) and manganese dioxide (MnO_2), demonstrated significant upgrades in the capacitance of electrode materials for use in electrochemical applications (Bharath et al., 2019; J. Feng et al., 2022; Huang et al., 2014).

Researchers investigated a promising approach to enhance desalination processes by incorporating ZnO into activated carbon, which results in a localized electric field enhancement at the electrode-nanoparticle interface (Kyaw et al., 2020; Laxman et al., 2018). This property effectively concentrates electric field lines within the area covered by the nanorods, thereby locally amplifying the electric field. Laxman et al. found that coating ACC with ZnO nanorods resulted in a 40% increase in the efficiency of desalination compared to pristine ACC electrodes (Laxman et al., 2015). Yasin et al. reported that ZnO nanoparticles that co-incorporated activated carbon had superior specific capacitance, enhanced salt removal efficacy, and electrosorption capacity (Yasin et al., 2021). Moreover, it was discovered that the morphology of ZnO structures like nanoparticles and nanorods on ACC surfaces impacts the salt removal capacity (Myint et al., 2014). Recently, some studies have demonstrated that the ZnO integrated carbon material may improve the adequate adsorption capacity of HMs (Kyaw et al., 2020; Li et al., 2022). Significant studies have been on the ability of different materials for adsorption, such as graphene oxide and metal-organic frameworks, but the role of ZnO structures is still entirely unexplored in the CDI technique (Yang et al., 2020; Zhang & Kong, 2020). The intensified electric field produced by ZnO nanostructures augments the electrostatic attraction between the electrode surface and ions, significantly improving the performance of metal ions removal from the solution. In addition, it is widely believed that the ZnO material becomes naturally hydrophilic because of the existence of hydroxyl groups on the surface, which improves ion attachment on the material's surface (Kyaw et al., 2020). A thorough understanding of ZnO nanostructures can offer a straightforward and efficient approach to improving HMs removal capabilities.

On the other hand, MnO_2 is widely regarded as the most promising candidate for grafting onto carbonaceous materials (Cheng et al., 2019; Liu et al., 2016). To

synthesize MnO_2 nanostructures, various techniques, including sol-gel, hydrothermal, co-precipitation, and electrodeposition, were performed, with the hydrothermal method particularly notable for its ability to regulate material shape and its suitability for large-scale applications (Adorna Jr et al., 2020; Han et al., 2020; Liu et al., 2016). However, understanding the role of MnO_2 nanostructures on activated carbon material in HMs removal remains largely unknown. Furthermore, relatively little research has been conducted on removing HMs using electrode materials modified by ZnO or MnO_2 nanostructures.

Despite ongoing efforts to improve electrode materials for CDI, some limitations remain. The performance of the CDI system may be negatively affected due to the co-ion phenomenon, which appears to be a significant factor influencing the electrode (P. M. Biesheuvel & A. van der Wal, 2010; Tang et al., 2017). When counter-ions in solution are drawn towards the electrode surface as they are charged, co-ions are simultaneously repulsed by their respective electrodes, leading to energy loss in the CDI cell (Cheng et al., 2019). Additionally, some improvements in electrode materials heavily rely on Faradaic reactions, which have the potential to induce irreversible redox reactions at the electrode surface and result in a decline of the applied voltage due to redox processes (Leong et al., 2021; Zhang et al., 2018). These factors limit CDI performance, leading to an increase in the required energy and, thus, operational expenses. Membrane capacitive deionization (MCDI) is a modified configuration of the CDI system to enhance its performance. In MCDI, ion exchange membranes (IEMs) are strategically located in front of the cathode and anode, facilitating the practical separation of ions and providing several positive implications. Firstly, IEMs improve the speed of ions' movement in the electrosorption process by minimizing co-ion expulsion (P. M. Biesheuvel & A. van der Wal, 2010; Tan & Babel, 2023). Secondly, IEMs prevent the occurrence of adsorptive reversal during the discharge phase, facilitating the complete desorption of adsorbed counter-ions (Li & Zou, 2011). Thirdly, installing the IEMs as a barrier limits oxygen diffusion towards the electrode, thereby restricting the appearance of Faradaic reactions that are effective to the electrode and reducing CDI performance (Tang et al., 2017). By this approach, the MCDI cell performs superior to the CDI cell without membrane regarding ion removal

efficiency and potential regeneration. However, evaluating the balance between price, efficiency, and lifetime is essential, as IEMs constitute a significant portion of the overall costs associated with MCDI, accounting for approximately 50% of the total price of MCDI water production (Hand et al., 2019). Moreover, only a limited quantity of research has been carried out regarding the impact of IEMs on removing HMs in terms of MCDI's work (Zhao et al., 2019).

IEMs can be categorized into two primary groups: homogeneous and heterogeneous (Volodina et al., 2005). A homogeneous IEMs is characterized by the presence of the ion exchange material, whereas a heterogeneous IEMs incorporates the ion exchange material within an inert binder (Millet, 2011). While homogeneous membranes possess various advantageous properties, the lower cost of heterogeneous membranes predominantly contributes to their widespread application, particularly in electrodialysis and other fields (Shi et al., 2019). Similarly, the limited availability of flexible and cost-effective commercial membranes impedes the widespread adoption of CDI systems. To date, heterogeneous cation exchange membranes have been employed in some studies for desalination (Li & Zou, 2011; Mudau et al., 2022; Tong et al., 2016); however, using heterogeneous cation exchange membranes for HMs removal remains unexplored mainly (Mudau et al., 2022). Therefore, further research is needed to ascertain the feasibility of employing commercially available membranes and heterogeneous cation exchange membranes in the MCDI cell for HMs removal under different operational conditions.

1.3 Objectives of the study

The research question is to see if the capacitive deionization technique can be employed for remediating wastewater with high concentrations of HMs, such as electroplating wastewater. The specific goals are as follows:

(1) Investigating the utilization of activated carbon-based materials, specifically by incorporating ZnO and MnO_2 nanostructures onto activated carbon fibers, aiming to enhance the efficiency of HMs removal.

(2) Determining the efficiency of utilizing ion exchange membranes in MCDI cell, encompassing fabricated heterogeneous cation exchange membrane compared to commercially available membrane, to enhance performance in overall CDI systems.

(3) Investigating the success rate of removal/recovery of HMs from wastewater generated by an electroplating plant.

1.4 Scope of the study

To achieve the specified goals, laboratory-scale CDI cells were constructed and operated continuously in both CDI and MCDI configurations. The study initially employed synthesis wastewater to target the removal of Cr^{6+}, Cr^{3+} (200 - 1000 mg/L), Cu^{2+} (50 - 1000 mg/L), and Ni^{2+} (50 - 500 mg/L). Afterwards, experiments were conducted with electroplating wastewater, collected from a local plant, to evaluate compliance with Thailand's HMs regulations following treatment by the CDI system. Two approaches were utilized, including the modification of electrode materials, specifically activated carbon fiber felt modified with ZnO and MnO_2 nanostructures via the hydrothermal method, and the fabrication of a heterogeneous cation exchange membrane via the nonsolvent-induced phase inversion method for the CDI system. Effect of flowrates, pH and metal concentrations were also evaluated. The properties of the electrode materials were thoroughly analyzed for surface characteristics, including specific surface area, N_2 adsorption/desorption isotherms, pore-size distribution, and morphological features using SEM, EDS, and XRD. Their electrochemical properties were also assessed through electrochemical impedance spectroscopy and cyclic voltammetry. The fabricated membranes were evaluated for functional groups, morphology including surface roughness, SEM, wettability property such as water contact angle, water content, and ion exchange capacity. Parameters observed from adsorption processes were assessed using kinetic models, adsorption capacity and recovery rate to determine performance in CDI system. In addition, performance of activated carbon fiber felt materials modified with ZnO and MnO_2 nanostructures for removal of selected HMs, is compared.

CHAPTER 2

LITERATURE REVIEW

2.1 Heavy metals in wastewater

2.1.1 Classification of heavy metals

Srivastava & Majumder classifies HMs as elements with a specific gravity of more than 5g/cm^3 and atomic weights ranging from 63.5 g/g/mol to 200.6 g/g/mol (Srivastava & Majumder, 2008). While some metals are widely recognized as nutritionally essential for people or living organisms, other metals appear to have potential benefits, no known nutritional or no beneficial effects on human health which may be seen in nature (Fairbrother et al., 2007a; Goyer et al., 2004). The risk for exposure and toxicity from these metals is not readily preventable, so action must be required to reduce human exposure to the lowest. Moreover, unlike organic compounds, metals are neither produced nor degraded by biological or chemical processes; nonetheless, these processes can change their valence levels or between inorganic and organic forms (Fairbrother et al., 2007a). As a result, HMs removal has become a concern in terms of human health and ecological for a strategy of sustainable development goals.

There are a variety of point sources that produce large amounts of HMs pollutants, including wastewater from industries such as electroplating, chemicals, tanneries, pesticides, pharmaceuticals, rubber and plastics, sometimes municipal wastewater, and wastewater from other activities such as mining and landfills (Srivastava & Majumder, 2008). The HMs present in wastewater may be carried by runoff water from the industrial site to downstream of water sources. HMs can adhere to the surface of microorganisms and even invade their cells (Fairbrother et al., 2007a). Moreover, HMs can be chemically changed when the microorganism employs chemical reactions to break down food (Fairbrother et al., 2007a). To correctly manage and control HMs in water sources, it is essential to satisfy government regulations to minimize the influence of wastewater on the environment.

2.1.2 Heavy metals in electroplating wastewater

Electroplating is the technique of depositing improved layers on material surfaces to alter their appearance, protection, covering properties, engineering or mechanical features, or a mixture of these that is by electrolysis methods. Cd, Cr, Cu, Ni, Pb, Zn, and other metals are commonly used in electroplating (Martín-Lara et al., 2014; Singh & Ram, 2016). Since the presence of one or more HMs is determined by the manufacturing process as well as the function of the galvanic coating, the composition and characteristics of electroplating wastewater are complicated.

Tartaric acid, ethylene diamine tetra-acetic acid, pyrophosphate, citric acid, and other additives that can form moderately strong complexes with HMs increase the quality of the plating pieces (Qin et al., 2018). As a result, electroplating wastewater will contain a large number of pollutions that are hazardous or even carcinogenic. Electroplating wastewater has many components, including surface cleaners, HMs utilized for detailed plating, and plating process additives that vary based on the technology, kind of plant, and product. The pH of the effluent varies dramatically from acidic to neutral to basic (H. Lu et al., 2015; Muratov et al., 2020). Brief, it is separated into three mainstream wastewaters based on the requirements of electroplating wastewater production including:

- Cyanide-containing wastewater. This can be explained as the cyanide wastewater stream meets the acid wastewater stream, which will produce HCN gas, a very toxic gas that contaminates both the plating workshop and impacts the other parts, thus it is separated from wastewater stream.

- Electroplating wastewater contains high levels of inorganic salts and HMs. Those metals change depending on the plating layer, such as Cu, Zn, Cr, Ni, etc. Also, depending on the type of metal salts, the wastewater has different toxins such as cyanide, sulfate, ammonium, etc. This is the main wastewater stream that creates wastewater that contains HMs.

- In addition, a wastewater stream contains substances such as grease, oil in the cleaning/washing process for equipment.

According to a report by the Thailand Electroplating Industrial Network (TEPNET), Thailand has a reasonably large surface finishing industry, with thousands

of plating lines and strong chemical and equipment supply chains, which firmly supports various major industries both locally and internationally, including automotive, electronics, sanitary, and jewelry (TEPNET, 2024). Electroplating of precious metals, zinc and zinc alloys, nickel-chrome, hard chrome, anodizing, plating on plastics, and electroless deposition are among Thailand's most critical surface finishing techniques. To promote the electroplating industry in Thailand, which is to develop economic strategies for advancing the electroplating industry and to create products of high quality and with environmentally friendly and efficient energy consumption processes. Therefore, while searching for solutions for HMs removal, potential recovery of HMs and limiting second products is also necessary in treating wastewater.

Table 2.1 shows twelve HMs which must be measured in industrial wastewater following regulation by the Ministry of Industry in Thailand (2017). The limited concentration in wastewater reflects the level that protects human health, and the available technology can reach the water source (Fairbrother et al., 2007b) . Therefore, controlling the concentration of wastewater to satisfy government regulations and enhance the quality of effluent is an important responsibility and necessary for future.

Table 2.1 Values standards of heavy metal parameters on industrial wastewater in Thailand.

Parameter	Unit	Value
Zinc (Zn)	mg/L	5.00
Hexavalent Chromium (Cr(VI))	mg/L	0.25
Trivalent Chromium (Cr(III)	mg/L	0.75
Arsenic (As)	mg/L	0.25
Copper (Cu)	mg/L	2.00
Mercury (Hg)	mg/L	0.005

Cadmium (Cd)	mg/L	0.030
Barium (Ba)	mg/L	1.00
Selenium (Se)	mg/L	0.02
Lead (Pb)	mg/L	0.20
Nickel (Ni)	mg/L	1.00
Manganese (Mn)	mg/L	5.00

2.1.3 Impacts of heavy metal pollution

The environmental contamination caused by HMs has led to increasing concerns about ecological and public health, driven mainly by the increased use of HMs in industries, agriculture, and technology (Vardhan et al., 2019). The combined exposure to toxic metals and other xenobiotic substances can exacerbate the hazardous impact on human health (Witkowska et al., 2021). Toxic metals pose a threat to the human body due to several characteristics: HMs exhibit systemic toxicity, affecting cells and persisting for extended durations, while also displacing essential metals from protein and enzyme binding sites, thereby disrupting metal homeostasis and enzymatic pathways (Witkowska et al., 2021). Besides, trace amounts of certain elements, including cadmium, mercury, lead, and arsenic, can induce acute and chronic toxicities (Goyer et al., 2004). Moreover, the toxicity of HMs fluctuates based on their chemical form (organic or inorganic) and the route of exposure (Vardhan et al., 2019).

Heavy metals, such as copper, chromium, and nickel, have become major pollutants in wastewater, presenting significant environmental and public health challenges (Tchounwou et al., 2012). The presence of these metals in water bodies can have severe consequences due to their toxic properties, long-lasting effects, and ability to accumulate in organisms. Table 2.2 presents the permissible limits for HMs in drinking water and their associated health impacts.

Copper is a commonly utilized material in various industrial processes. When it is released into water sources, it can negatively affect aquatic ecosystems and human health. Increased copper concentrations have the potential to negatively impact aquatic ecosystems, as they can induce oxidative stress, harm gills, and hinder enzyme activities in various aquatic organisms (Q. Chen et al., 2018; Dermentzis et al., 2009). Excessive exposure to copper through contaminated water can lead to gastrointestinal distress, as well as damage to the liver and kidneys in humans (Baby et al., 2010). Neurodegenerative diseases are associated with chronic copper exposure.

Chromium, specifically in its hexavalent (Cr(VI)) form, is highly toxic and presents significant dangers when released into water systems. Cr(VI) is widely recognized as a carcinogen and has been linked to a range of health concerns, including skin irritation, respiratory issues, and liver damage (Sharma et al., 2008; Yoon et al., 2009). Within aquatic environments, the presence of chromium can have adverse effects on organisms, leading to the development of oxidative stress and disruption of reproductive systems. Ensuring the complete reduction of Cr(VI) to the less harmful trivalent chromium (Cr(III)) in water bodies is crucial in order to prevent long-lasting environmental contamination (Sharma et al., 2008).

Nickel is HMs that raises concerns because of its extensive utilization in various industrial applications, including electroplating and battery production (H. Lu et al., 2015; Osińska, 2016). The presence of nickel in water resources can accumulate this element in aquatic organisms (Tchounwou et al., 2012). This accumulation can have detrimental effects, causing toxicity and bioaccumulation within the food chain. Human exposure to nickel has been linked to various health concerns, including allergic reactions, respiratory problems, and an elevated risk of cancer (Singh & Ram, 2016; Wang et al., 2021). Effective removal strategies are necessary to address the long-term environmental threats posed by the persistence of nickel in water bodies.

Table 2.2 Permissible limits of heavy metals in drinking water and their health impacts.

Metals	Concentration limit (mg/L)		Impacts	Reference
	WHO	EPA (US)		
Nickel	0.07	-	- Cause skin irritation, nausea, persistent asthma, coughing, and is a known human carcinogen.	(EPA, 2024; WHO, 2022)
Copper	2.0	1.3	- Brief exposure can lead to stomach issues. - Prolonged exposure can result in liver or kidney harm. - Individuals with Wilson's Disease should seek medical advice if copper levels in their water exceed safe limits.	(EPA, 2024; WHO, 2022)
Chromium (total)	0.05	0.1	- Trigger skin allergies or rashes.	(EPA, 2024; WHO, 2022)
Lead	0.01	0.015	- Cause developmental delays and minor issues with focus, learning. - Cause kidney issues and elevated blood pressure.	(EPA, 2024; WHO, 2022)

Cadmium	0.003	0.005	- Contribute to kidney disease.	(EPA, 2024; WHO, 2022)
Selenium	0.04	0.05	- Cause hair and nail loss, numbness in extremities, and circulation issues.	(EPA, 2024; WHO, 2022)
Arsenic	0.01	0.01	- Skin damage, circulatory issues, and a higher cancer risk.	(EPA, 2024; WHO, 2022)
Barium	1.3	2.0	- Raise blood pressure.	(EPA, 2024; WHO, 2022)
Mercury	0.006	0.002	- Cause kidney damage.	(EPA, 2024; WHO, 2022)

2.2 Approaches for heavy metal removal

Various methods are utilized to remove heavy metals, such as chemical precipitation, ion exchange, adsorption, membrane separation, and electrodialysis, among others. Every approach offers distinct mechanisms for the metals of interest. Figure 2.1 presents an overview of techniques utilized for the removal of HMs.

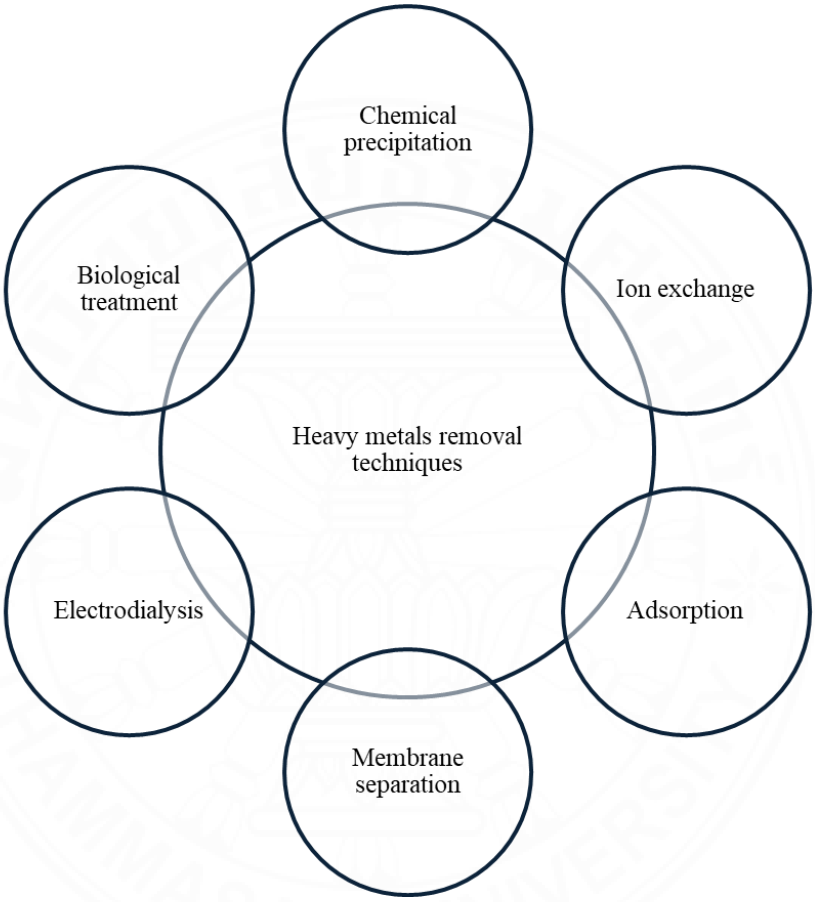

Figure 2.1 Various techniques for the removal of heavy metals.

2.2.1 Chemical precipitation

Chemical precipitation is one of the supported methods for HMs removal from wastewater because it provides simple methods, inexpensive operation, and potential for high concentrations (Fu & Wang, 2011). In chemical precipitation, there are two primary processes as hydroxide precipitation and sulfide precipitation.

a) Hydroxide precipitation

Hydroxide precipitation is popularly used in a chemical precipitation method because it is relatively simple, low cost, and pH control flexible (Fu & Wang, 2011).

By adding the amount of hydroxide to wastewater while being mixed, HMs in solutions such as Zn^{2+}, Cu^{2+}, Ni^{2+}, Pb^{2+}, and Cr^{3+} transfer insoluble metal hydroxide precipitating under pH values of 9 - 11 (Qasem et al., 2021). Many precipitants are used for hydroxide precipitation processes, among these, NaOH, CaO and $Ca(OH)_2$ use is more common (Fu & Wang, 2011; Qasem et al., 2021). For example, using $Ca(OH)_2$ to produce metal hydroxide precipitates:

$$M^{2+} + 2OH^- \Leftrightarrow M(OH)_2 \downarrow \quad (2.1)$$

where M^{2+}, $OH^-$and $M(OH)_2$ is the HMs, the precipitant, the insoluble metal hydroxide, respectively.

Although it is widely used, there are some drawbacks to the hydroxide precipitation technique. First, the hydroxide precipitation processes generate secondary product, which is expensive to process and manage with large sludge (Fu & Wang, 2011). Second, the pH value is adapted for one metal; therefore, the efficiency of separated metals can be reduced when wastewater contains amphoteric hydroxides or several metals in wastewater. Third, wastewater must be controlled by chemical agents to maintain a neutral pH before discharge, thereby increasing wastewater treatment costs.

b) Sulfide precipitation

In addition to the hydroxide precipitation process, sulfide precipitation removes HMs in wastewater. Sulfide precipitation provides more advantages than hydroxide precipitation, such as being applicable in a more comprehensive pH range, metal sulfide sludge being thicker, and better dewatering. Sulfur to supply for sulfide precipitation process can be obtained from many sources, including solids (FeS, CaS), water (Na_2S, NaHS, NH_4S), and gaseous sulfide sources (H_2S) (Lewis, 2010; Qasem et al., 2021)

$$M^{2+} + S^{2-} \Leftrightarrow MS \downarrow \quad (2.2)$$

where M^{2+}, S^{2-}, MS is HMs, precipitant, the insoluble metal sulfide, respectively.

The sulfide precipitation process has shown many benefits over the hydroxide precipitation procedure but has many drawbacks. Firstly, sulfide precipitants in acidic environments can cause the formation of H_2S, a toxic and malodorous gas. Secondly, it produces a process of secondary sludge as a hydroxide precipitation process, which is costly to fulfill. Thirdly, metal sulfide precipitates tend to form colloidal precipitates, making it more challenging to remove sludges from wastewater.

2.2.2 Ion exchange

Ion exchange for HMs removal is a reversible chemical reaction that separates HMs in wastewater and replaces them with neutral, non-toxic, and environmentally friendly ions (Budak, 2013; Dabrowski et al., 2004; Fu & Wang, 2011). This ion exchange mechanism is dependent on the type of resin, which can be natural/synthetic, and the different types of HMs (Dabrowski et al., 2004; Fu & Wang, 2011). The ion exchange resin may take on a variety of HMs including Pb^{2+}, Hg^{2+}, Cd^{2+}, Ni^{2+}, V^{4+}, V^{5+}, Cr^{3+}, Cr^{6+}, Cu^{2+}, Zn^{2+} and others, depending on the functional groups of the resins (Dabrowski et al., 2004). In this technique, solid ion exchange resin with carboxylic acid group (–COOH) or a robust sulfonic acid group ($–SO_3H$) is frequently utilized (Budak, 2013; Dabrowski et al., 2004). The following reaction explains the ion exchange method for HMs removal

$$M^{-}EC^{+} + WC^{+} \Leftrightarrow M^{-}WC^{+} + EC^{+} \quad (2.3)$$

where M^{-}, EC^{+}, WC^{+} is the fixed anion, the exchange cation, the wastewater cation, respectively.

Ion exchange technologies have several benefits such as quick kinetics, cost-effectiveness, and the ability to regenerate the ion exchange resin. However, they also have some disadvantages such as being difficult to use when there is a high concentration of HMs, being pH sensitive, and having low binding affinity due to free acids (Budak, 2013). In addition, since ion exchange resins are exhausted, they should be recovered by chemical reagents, which can result in significant secondary contamination.

2.2.3 Adsorption

The adsorption mechanism determined based on the properties of the adsorbent and HMs. In addition, other factors such as temperature, pH value, and adsorption time significantly influence adsorption (Kyaw et al., 2020). The benefits of the adsorption method are low costs, the efficiency of HMs removal capacity, and regenerating HMs which have been adsorbed on the material (Qasem et al., 2021; Singh et al., 2017).

HMs removal applications such as activated carbons, carbon nanotubes, and graphene are frequently used. Some modifications toward surface functional groups of adsorption material such as carboxyl, phenyl, and lactone groups aim to enhance HMs uptake to replace carbon-based nanoporous adsorbents has been widely researched (Qasem et al., 2021). However, based on adsorbent materials that can be expensive to operate in a long time. Furthermore, because adsorption is now an admitted technique for HMs removal in low concentration, thus it is necessary to improve more functions and material properties to improve the application in the future, which necessitates demonstrating efficiency through time (Chai et al., 2021)

While some adsorbents material is described above, adsorbent with original biology component, called is bio-adsorbent, has been confirmed as a potential material in HMs removal. Conventional bio-adsorbents are obtained from three sources as follows non-living biomass as bark, lignin, shrimp, krill, squid, crab shell; algal biomass; and microbial biomass as bacteria, fungi, and yeast (Chai et al., 2021; Singh et al., 2017). Furthermore, non-living plant materials such as potato peels, sawdust, eggshell, seed shells, coffee husks, have been extensively studied as possible bio-sorbents for HMs removal.

2.2.4 Membrane separation

Membrane filtration process with various types of membranes as ultrafiltration (UF), reverse osmosis (RO), nanofiltration (NF) showed potential for HMs removal because there are high efficiency, easy operation and limit area (Obotey Ezugbe & Rathilal, 2020; Zare & Kargari, 2018). Ultrafiltration (UF) is a membrane working at low transmembrane pressures for dissolved and colloidal material removal. Because dissolved metal ions are lower than the pore sizes of UF membranes as form of hydrated

ions or as low molecular weight complexes, so to obtain high removal efficiency of metal ions, the micellar enhanced ultrafiltration (MEUF) and polymer enhanced ultrafiltration (PEUF) introduced (Chai et al., 2021; Ravanchi et al., 2009). MEUF, created by combining UF and surfactant, has a high flux and selectivity, which means it uses less energy, has a higher removal efficiency, and takes up less space. However, MEUF is only suitable for wastewater with low levels of HMs. On the other hand, PEUF is formed through the integration of UF and binding polymers as sulfonate, phosphonic, carboxylate, or amine. PEUF process will prevent and take metal ions to link polymer, it is only permitted water and un-complexed components to permeate the UF membrane pores. However, the selection of water-soluble polymer macro-ligands remains challenging to create PEUF. Besides removing a wide range of dissolved species from water, HMs such as Cu^{2+}, Ni^{2+}, Zn^{2+}, Cr^{6+}, and others are removed via reverse osmosis (RO) (Chai et al., 2021). However, the major disadvantage of RO is the high-power consumption due to high pumping pressures, and the problematic membrane restoration process, which has prevented it from being widely used (Rajasulochana & Preethy, 2016). While nanofiltration (NF), which is a step between ultrafiltration (UF) and reverse osmosis (RO), is a potential method for HMs removal. While UF membranes require modifications and the hybrid addition of chemicals to achieve metal ion removal, NF membranes feature better with a selective film structure and small pore diameters, making them suitable for separating metallic ions.

2.2.5 Electrodialysis

Electrodialysis (ED) is another membrane technique for the separation of HMs across charged membranes by utilizing an electric field as the driving force (Fu & Wang, 2011). In ED model, a series of cation exchange membranes (CEMs) that allow cations to flow through and anion exchange membranes (AEMs) that allow anions to pass through are organized in parallel and interlaced to separate ionic solutes (Abdullah et al., 2019). In ED model, there are two streams of product water. In ED mode, half of the ED stack channels make the treated stream, while the other half is used to discharge the concentrated stream. Some of the results showed that ED was used to separate Ni^{2+} and Pb^{2+}, and K^{+} with efficiencies of 96.9% and 99.9%, respectively; As^{3+} and As^{5+}

were removed from metallurgical wastewater with a removal efficiency of 91.38 %; etc (Qasem et al., 2021). However, membrane fouling, high membrane expenses, and high demand for electric potential are some of the issues with ED that must be evaluated before being used (Yang et al., 2021).

2.3 Principle of capacitive deionization process

Generally, capacitive deionization (CDI) operates below 1.23 V to prevent water electrolysis. In a CDI cell, ions are captured within electric double layers on capacitive electrodes through electrostatic interaction or within the crystal structures of battery electrodes via Faradaic intercalation when voltage is applied to a pair of electrodes (Ahmed & Tewari, 2018; Zhang et al., 2018). Specifically, the principle of CDI consists of two phases: the charging phase and the discharge phase. During the charging phase, an electric field is generated by applying potential to electrode pairs, enabling the capture of opposite charges, similar to a supercapacitor. Under the influence of an electric field, ions in the solution move to the opposite electrode and store charges in the electrode material through electrostatic interaction. Notably, the negative electrode stores cations, while the positive electrode stores anions. During the discharging phase, electrode regeneration can occur through three possible methods: no voltage application, voltage reversal, or a combination of potential cut-off and reversed voltage. These methods facilitate the regeneration of electrodes and the release of captured charges into the concentrated solution. The next cycle will be performed after the discharge phase completed. The principle working of CDI is typically described in Figure 2.2.

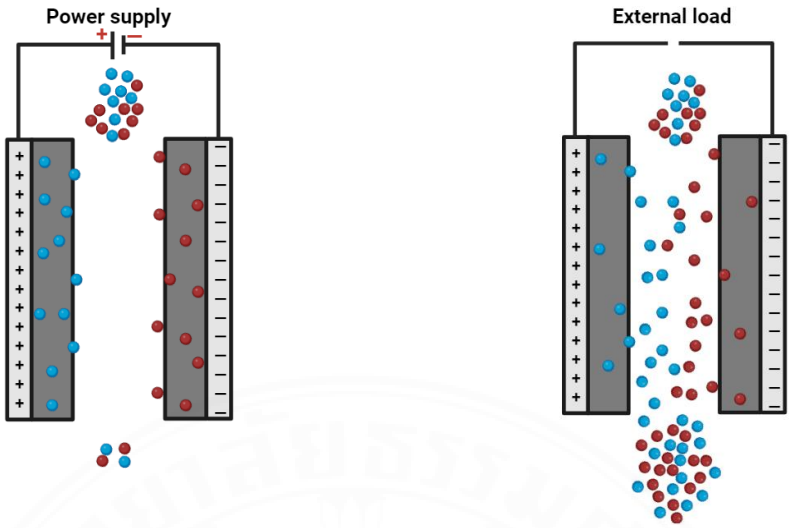

Figure 2.2 Principle working of CDI cell, showing (a) charging phase and (b) discharging phase.

2.4 Current progress in capacitive deionization

2.4.1 Capacitive deionization structures

The CDI, introduced in the 1960s, gained significant interest about two decades ago after progressing slowly for many years (Xing et al., 2020). The rapid development in recent times has been driven by advancements in membrane and electrode materials and an increasing variety of CDI cell architectures.

Flow-by CDI, also known simply as CDI, represents the conventional configuration for a CDI cell. The CDI cell comprises two electrodes, one positively charged, and one negatively charged, facilitating the sorption of cations and anions (Alvarado & Chen, 2014; Li & Zou, 2011). A separator is positioned between the electrodes to prevent short circuits and allowing the solution to flow. The potential applied across the electrodes generates an electric field, prompting ion migration towards the electrodes and accumulation in the electric double layers, thus yielding a fresh solution (Li & Zou, 2011). Saturated electrodes can be regenerated by desorbing ions through reverse voltage or short-circuiting mode, releasing ions and resulting in a concentrated solution. Energy recovery can also be utilized because stored charge is released during the discharging phase (Xing et al., 2020). Figure 2.3(a) presents the architecture of CDI cell.

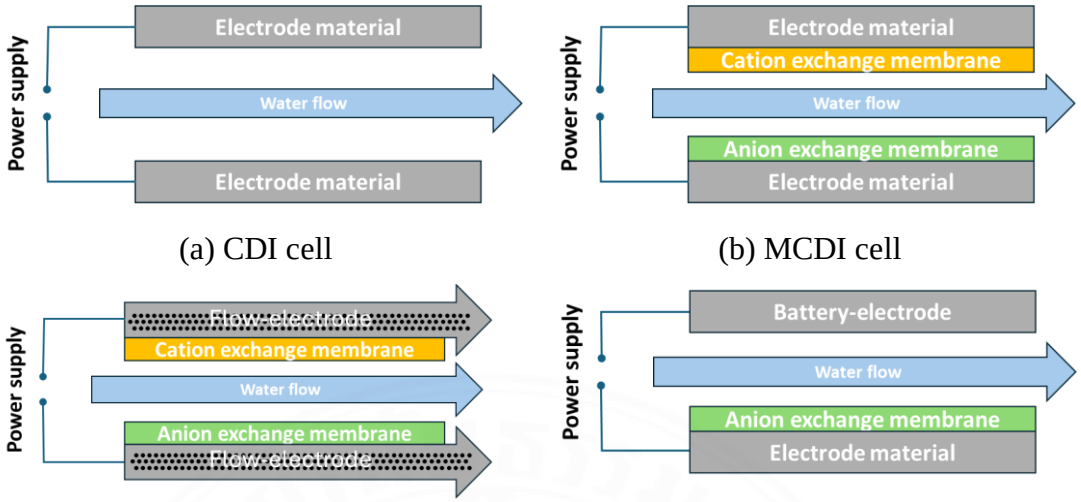

(a) CDI cell (b) MCDI cell

c) Flow-electrode CDI cell (d) Hybrid CDI cell

Figure 2.3 Typical cell architectures of various CDI: (a) CDI cell, (b) MCDI cell, (c) Flow-electrode CDI cell and (d) Hybrid CDI cell.

Membrane capacitive deionization (MCDI) is a modified version of CDI that uses ion exchange membrane (IEMs). It functions similarly to CDI but may achieve advancements using IEMs. The MCDI cell has a CEM strategically placed before the cathode, and an AEM similarly positioned before the anode. Using IEMs enhances ion migration velocity in the electrosorption process by reducing co-ion expulsion (P. M. Biesheuvel & A. van der Wal, 2010). Additionally, IEMs prevent the phenomenon of adsorptive reversal from happening during the discharge phase, enabling the thorough desorption of counter-ions that have been adsorbed (Li & Zou, 2011). Furthermore, installing IEMs acts as a barrier, effectively preventing oxygen diffusion toward the electrode, thus preventing the occurrence of Faradaic reactions that can impact the electrode's effectiveness (Tang et al., 2017). By this way, the MCDI cell demonstrates superior performance compared to the CDI cell in terms of ion removal efficiency and potential. However, evaluating price, efficiency, and lifetime is essential when considering the utilization of IEMs in MCDI. It was reported that IEMs significantly contribute to the overall water production costs caused by MCDI, constituting approximately 50% of the total price (Hand et al., 2019). Figure 2.3(b) provides the architecture of MCDI cell.

A significant advancement resulting from MCDI is the introduction of flow-electrode capacitive deionization (FCDI), which employs a flowable carbon solution instead of a solid porous carbon electrode, as depicted in Figure 2.3(c). The typical FCDI cell comprises current collectors, separators, and spacers, which are placed together by a set of end plates (Yu et al., 2022). The spacer chamber, where the feedwater passes, is created between the two separators. Electrode chamber is formed by positioning the separators onto the current collectors with flow-channels carved into them. A pump is used for pumping the flow-electrodes between the container and the electrode chambers. The FCDI facilitates the continuous removal of high-concentration feed water without requiring a traditional discharge process, as in a conventional CDI cell or MCDI cell (Yu et al., 2022). However, energy loss occurs when the electrode used as a slurry (powder) is recycled, causing ion transport resistance because of the poor conductivity of the flow electrode slurry, which negatively impacts performance (Ma et al., 2019; Yu et al., 2022). The highest energy recovery ratio achieved was 60% in the flow-electrode CDI (Ma et al., 2019).

Recently, hybrid capacitive deionization (HCDI) has been reported, opening a new stage in CDI technology (Lee et al., 2014). The HCDI represents an asymmetric system comprising two distinct types of electrodes: electrode material for the CDI process and a battery electrode, as illustrated in Figure 2.3(d). The battery electrode facilitates cation intercalation/deintercalation, while the capacitive electrode enables anion adsorption/desorption, accompanied by an anion exchange membrane, contributing to the large amount of electrical capacity (Leong et al., 2021; Tang et al., 2019b). Indeed, the HCDI exhibited a greater capacity for deionization when compared to the conventional CDI (Xing et al., 2020).

2.4.2 Electrode material properties

2.4.2.1 Activated carbon material

Carbon materials are commonly used in CDI electrodes because they are inexpensive, lightweight, large specific surface area, and porous structure (Ahmed & Tewari, 2018). Various types of carbon-based electrodes have been studied for CDI test, including activated carbon, 3D hierarchical carbon, 3D graphene,

nanofibers/activated carbon composite, mesoporous carbon, carbon aerogels, graphene, nanostructured electrodes, and polymer-coated electrodes (Ahmed & Tewari, 2018; Gaikwad & Balomajumder, 2017). Besides, carbon-based electrodes, such as activated carbon, carbon aerogel, and carbon nanotube, are being studied extensively for their controllable pore size distribution, and high specific surface area (Bharath et al., 2019). Regarding activated carbon-based materials, activated carbon shows high resistance, whereas carbon aerogel and graphene offer superior electrical conductivity but their widespread application has been restricted due to their high cost (Cheng et al., 2019). Villar et al. compared various activated carbon- based electrodes, including carbon aerogel, carbon cloth, carbon felt and carbon paper electrode, and found activated carbon to be the most suitable for the electrosorption (Villar et al., 2011). As a result, these properties make activated carbon material useful for electrochemical process and HMs removal.

2.4.2.2 Metal oxide decorated carbon composite

Metal oxides are recognized for being valuable materials in batteries, supercapacitors, and energy storage applications due to their high specific capacitance, availability, cost-effectiveness, and environmental friendliness (Cheng et al., 2019; Zhang et al., 2018). Carbonaceous material-based electrodes, which are grafted with metal oxide such as manganese dioxide (MnO_2), titanium dioxide (TiO_2), zinc oxide (ZnO), silicon dioxide (SiO_2), have been proposed to enhance the adsorption capacity of CDI systems (Cheng et al., 2019). Recent research has focused on developing metal oxide−carbon composite electrodes offering unique synergistic properties. For instance, titanium dioxide (TiO_2) surface modification has significantly improved wetting characteristics and enhanced capacitance precision (Liu et al., 2016). ACC electrodes coated with ZnO nanorods can improve desalination efficiency by facilitating ion collection (Laxman et al., 2018). The surface area and specific capacitance of the ACC surface are increased by the presence of MnO_2, which is essential for improving capacitive performance through its pseudocapacitive properties (Choi et al., 2020). Moreover, various metal oxide composite electrodes, including carbonaceous aerogels modified with CeO_2 and Fe_2O_3, carbon felt decorated with FeS

and ZnS, demonstrated enhanced performance as electrodes in CDI (Yang et al., 2017). Moreover, the hollow bowl-type carbon loaded with molybdenum sulfide (HBC-MoS2-0.02) showed great promise (Wu et al., 2023).

a) Zinc oxide

Researchers investigated a promising approach to enhance desalination processes by incorporating ZnO into AC, which results in a localized electric field enhancement at the electrode-nanoparticle interface (Laxman et al., 2018; Laxman et al., 2015). This property effectively concentrates electric field lines within the area covered by the nanorods, thereby locally amplifying the electric field. Laxman et al. found that coating ACC with ZnO nanorods resulted in a 40% increase in the efficiency of desalination compared to pristine ACC electrodes (Laxman et al., 2015). Yasin et al. reported that ZnO nanoparticles that co-incorporated AC had superior specific capacitance, enhanced salt removal efficacy, and electrosorption capacity (Yasin et al., 2021). Moreover, it was discovered that the morphology of ZnO structures like nanoparticles and nanorods on ACC surfaces impacts the salt removal capacity (Myint et al., 2014). Recently, some studies have demonstrated that the ZnO integrated carbon material may improve the adequate adsorption capacity of HMs.

b) Manganese dioxide

MnO_2 is currently regarded as one of the most advantageous materials for applying supercapacitors among the transition metal oxides, as it is associated with a high specific capacitance, low cost, and environmental compatibility. Furthermore, MnO_2 is widely regarded as the most promising candidate for grafting onto carbonaceous materials due to its inexpensive, chemical stability, and high capacitance (Cheng et al., 2019; Liu et al., 2016). To synthesize MnO_2 nanostructures, various techniques, including sol-gel, hydrothermal, co-precipitation, and electrodeposition, were performed, with the hydrothermal method particularly notable for its ability to regulate material shape and its suitability for large-scale applications (Adorna Jr et al., 2020; Han et al., 2020; Liu et al., 2016). Unfortunately, the scope of research on layered MnO_2 has been limited to its desalination capabilities (i.e., the removal of Na^+ and Cl^-), with potential applications in HMs removal being overlooked (Liu et al., 2016)

2.4.3 Ion exchange membranes

IEMs are extensively employed in electrochemical applications such as electrodialysis, fuel cells, redox flow batteries, and CDI techniques. MCDI is a modified configuration of the CDI cell, which utilizes an AEM and CEM to enhance its performance. IEMs employed in MCDI improve salt removal efficiency (Robert McNair et al., 2020). By acting as a selective gateway, IEMs allow for the preferential migration of counter-ions while preventing co-ions from reaching and being absorbed into the electrodes (Dong et al., 2019; Luo et al., 2020). Additionally, IEMs are crucial in preventing adsorptive reversal, ensuring the thorough desorption of counter-ions during the discharge phase (Li & Zou, 2011). Besides, installing IEMs acts as a barrier, preventing oxygen diffusion towards the electrode, leading to a decrease in CDI performance (Tang & 2017). Through this approach, the MCDI cell demonstrates a higher performance level than the CDI cell in terms of ion removal efficiency and potential regeneration. In terms of MCDI's work, only a limited quantity of research has been carried out regarding the impact of IEMs on removing HMs (Zhao et al., 2019). On the other hand, heterogeneous IEMs make up a substantial proportion of the total expenses linked to MCDI, around 50% of the overall cost of MCDI water production (Hand et al., 2019).

Ion exchange membranes comprise a polymer matrix with ionic groups attached to its backbone. Depending on the charge of the ionic groups, IEMs are classified as either anion exchange membranes (AEMs) or cation exchange membranes (CEMs). AEMs typically possess positively charged groups such as $–NH_3^+$, $–NRH_2^+$, $–NR_2H^+$, and NR_3^+, facilitating anion transport while excluding cations (Li & Zou, 2011; Mudau et al., 2022). Conversely, CEMs incorporate negatively charged groups like $–SO_3^–$, –COO–, $PO_3^{2–}$, and $PO_3H^–$, enabling the selective transport of cations and the rejection of anions (R. McNair et al., 2020; Tong et al., 2016). Integrating cation and anion exchange membranes results in a bipolar ion-exchange membrane. IEMs can be categorized into two primary groups: homogeneous and heterogeneous (Volodina et al., 2005).

2.4.3.1 Homogeneous ion exchange membranes

Homogeneous membranes are synthesized by incorporating ionizable functional groups into polymeric films, requiring polymers that ensure uniform charge distribution, mechanical stability, and low electrical resistance while being cross-linked to minimize swelling in water (Van der Bruggen, 2015). Increasing charge density improves conductivity and reduces swelling, which cross-linking mitigates by chemically anchoring polymer chains. These membranes are thinner and mechanically more robust than heterogeneous membranes, with charge densities typically ranging from 1–2 meq/g. Functional groups enable ion transport, where fixed ions remain on the surface, and counter-ions dissociate and hydrate upon contact with aqueous solutions.

Anion exchange membranes often contain quaternary ammonium groups, while cation exchange membranes include sulfonyl or carboxyl groups, with color differences distinguishing them (Van der Bruggen, 2015; Yang et al., 2020). While some IEMs are non-selective, some anion membranes show selectivity for monovalent ions, allowing efficient nitrate removal while managing total dissolved solids (TDS). Recent research has expanded the variety of polymeric membranes, including those composed of novel materials like poly(vinyltrimethoxysilane), 4-vinylbenzyl chloride, cross-linked polystyrene, and glycidyl methacrylate (Tsehaye et al., 2023; Van der Bruggen, 2015). Besides, cation exchange membranes include blends like polystyrene/polyaniline and ceramic zirconium phosphate membranes for wastewater treatment. The potential for diverse materials in ion exchange membranes is vast, but commercialization is still developing. Table 2.2 presents selected commercially available IEMs suitable for use in MCDI processes.

Table 2.3 Typical commercial ion exchange membranes used in the CDI process.

Type of membrane	Code of membrane	Water uptake (wt %)	Ion exchange capacity (meq/g)	Electrical resistance ($\Omega.cm^2$)	Thickness (μm)	Permselectivity (%)
Cation exchange membrane	Fumasep FKS-PET-130	15 – 25	0.75 – 0.85	2.6 – 4.6	110 – 130	93 – 98
	Neosepta CMX	-	1.62	2.91	164	99
	CMI-7000S	-	1.5 – 1.7	< 30	450 ± 25	94
Anion exchange membrane	Fumasep FAA-3-PK-130	10 - 25	1.1 – 1.4	1.8 – 4.0	110 – 130	93 – 98
	Neosepta AMX	-	1.25	2.35	134	90.7
	AMI-7001S	-	1.2 – 1.4	< 40	450 ± 25	90

2.4.3.2 Heterogeneous ion exchange membranes

Heterogeneous IEMs are produced by blending ion-exchange domains, such as ion-exchange resin particles or inorganic materials with ion-exchange sites, including silicates and zirconium phosphates, into a non-functional polymer backbone (Mubita et al., 2020; Volodina et al., 2005). The binder used in heterogeneous membranes is typically an uncharged material, such as polyethylene, polystyrene, polyvinyl chloride, or polycarbonate (Robert McNair et al., 2020) .The capacity to modify the ion-exchange properties of polymer membranes allows for higher ion exchange capacity compared to composite electrodes, enabling more significant ion transfer into porous electrodes (Robert McNair et al., 2020; Millet, 2011). However, the primary limitation of heterogeneous IEMs lies in the non-uniform distribution of ion-exchange sites. As a result, for membranes of the same thickness, heterogeneous membranes exhibit higher electrical resistance compared to homogeneous membranes. Various approaches have been explored to improve heterogeneous IEMs, including the use of polymeric binder blends, adjusting the concentration of ion-exchange resins, applying an electric field to organize the distribution of ion-exchange resin particles, and incorporating binders with charged functional groups (Robert McNair et al., 2020; Mubita et al., 2020; Omosebi et al., 2017). While homogeneous membranes possess various advantageous properties, the lower cost of heterogeneous membranes predominantly contributes to their widespread application, particularly in electrodialysis and other fields (Shi et al., 2019). Similarly, the limited availability of flexible and cost-effective commercial membranes impedes the widespread adoption of CDI systems (R. McNair et al., 2020).

2.5 Recent advances for heavy metal removal in CDI

2.5.1 Modified carbon electrode materials

Numerous materials with varying porous structures have been used to enhance the capacity of HMs removal by CDI. Activated carbon (AC) and modified AC are regularly used in CDI studies because of their high specific surface area, good conductivity, and electrochemical stability (Kyaw et al., 2020; Xing et al., 2020). Some electrode materials are made from primary carbon including activated carbon cloth (ACC), carbon aerogel, graphene (Cao et al., 2019; L. Liu et al., 2017; Liu et al., 2019).

Liu et al. (2019) discovered that ACC may be used to remove Co ions from an aqueous solution with an efficiency of about 36.54 % at 1.2 V when used in CDI model (Liu et al., 2019). Other forms of carbon as aerogels used as electrode materials for HMs treat. Cao et al. used the adsorption effect of a carbon aerogel electrode on Cu^{2+} to remove a HMs in a solution. The author concluded that carbon aerogel has many opportunities for advancements in HMs treatment (Cao et al., 2019). A one-pot process was employed to fabricate highly porous N-doped graphene (CNG), resulting in a large pore volume and high surface area. CNG was utilized in an MCDI cell to efficiently remove Pb^{2+}, Cd^{2+}, Cu^{2+}, and Fe^{2+}, achieving high removal efficiency (about 90 – 100%) and rapid HMs removal rates (L. Liu et al., 2017).

Carbon-based composite materials, currently a focus of CDI electrode research, involve combining carbon with other materials such as polymers or metal oxides to enhance the electrosorption ability of the original carbon material (Liu & Wang, 2020). Kyaw et al. investigated the effect of ZnO nanostructures on ACC for HMs removal. Results showed that coating ACC electrodes with ZnO nanostructures enhanced electric field, increasing ion adsorption and improved electrosorption performance for Pb^{2+}, Cd^{2+}, and mixed ions. Compared to ACC electrodes, electrosorption efficiency increased from 17% to 33% for Pb^{2+}, 21% to 29% for Cd^{2+}, and 21% to 35% for mixed Pb^{2+} and Cd^{2+} (Kyaw et al., 2020). Liu & Wang (2020) utilized ACC/GO composite for electro-assisted adsorptive Co^{2+} and Cs^{+} removal. Results demonstrate ACC/GO composite electrode superior adsorption capacity over ACC due to increased specific surface area and oxygen-containing functional groups. The results demonstrate that the ACC/GO composite electrode exhibits superior adsorption capacity over ACC due to its increased specific surface area and oxygen-containing functional groups (Liu & Wang, 2020).

In addition to attempts to enhance capacitance or the electrical field of electrode material for HMs removal, there has been considerable focus on grafting functional groups onto electrode materials to facilitate Faradaic reactions. Unlike porous carbon electrodes, which use capacitance to store HM ions, Faradaic-electrodes store HM ion via intercalation or conversion reactions within the electrode. Carbon-based materials' capacitance and electrosorption properties are effectively improved by incorporating

metal oxides. This is achieved through the facilitation of HMs conversion, adsorption onto defects, and intercalation within the structure of the metal oxide layer (Bautista-Patacsil et al., 2020; Bharath et al., 2019; Lihu Liu et al., 2017). The reduction of Cr(VI) to Cr(III) was achieved using Fe(II) ions from Fe_3O_4, followed by direct electro-capture on composite material. The adsorption capacity of Cr(VI) was 24.5 m/g at a Cr(VI) concentration of 50 mg/L, indicating an estimated removal efficiency of 99% for Cr(VI) using the composite material in CDI cell (Bharath et al., 2019). The composite of synthesized reduced graphene oxide (rGO) with titanate nanotubes (TNT) at 3:1 mass ratio exhibits high electrosorption capacities due to induced oxygen and π electron interactions, enhancing the adsorption of Pb^{2+} and Cu^{2+} ions. The adsorption capacity values were 253.25 mg/g for Cu^{2+} and 241.65 mg/g for Pb^{2+} (Bautista-Patacsil et al., 2020).

Table 2.4 Carbon-based electrode performance for heavy metal removal in CDI system.

Heavy metal ions	Electrode material	Unit	Initial concentration (mg/L)	Adsorption amount (mg/g)	Operation Time	Reference
Cu^{2+}	Polyacrylonitrile-based ACC impregnated with chitosan solution	CDI	100	30.6	12 h	(Huang & Su, 2010)
Cu^{2+}	Carbonaceous aerogels (CAs)	CDI	200	30.35	150 – 160 min	(J. Li et al., 2017)
Cu^{2+}	CAs/CeO_2	CDI	200	49.28	150 – 160 min	(J. Li et al., 2017)
Cu^{2+}	CAs/Fe_2O_3	CDI	200	41.42	150 – 160 min	(J. Li et al., 2017)
Cu^{2+}	FeS-decorated carbon felt	CDI	100	18.0	100 min	(Jin & Hu, 2019)
Cu^{2+}	ZnS-decorated carbon felt	CDI	100	27.4	100 min	(Jin & Hu, 2019)
Cu^{2+}	rGO-TNT	CDI	80	253.25	2 h	(Bautista-Patacsil et al., 2020)
Cu^{2+}	3-Dimensional reduced graphene oxide	CDI	50	18.1	60 min	(You et al., 2020)

Cu^{2+}	HBC loaded with molybdenum sulfide (HBC-MoS_2-0.02)	CDI	25	28.97	12 h	(Wu et al., 2023)
Ni^{2+}	Multi-walled carbon nanotubes	CDI	-	8.49	-	(Iftekhar et al., 2017)
Ni^{2+}	Nitric acid-modified activated carbon	CDI	-	103.09	8 h	(Xue et al., 2022)
Ni^{2+}	α-MnO_2/Carbon Paper Composite	CDI	100	16.40	2 h	(P. Li et al., 2018)
Ni^{2+}	Nanostructured birnessite-type manganese oxide and birnessite/carbon nanotubes (HB/CNTs) nanocomposites	CDI	500	158.4	12 h	(Lihu Liu et al., 2017)
Ni^{2+}	N, S-co-doped carbon materials (NS-C) derived from PVC plastic wastes	CDI	50	55.2	210 min	(Chang et al., 2020)
Cr (VI)	Peanut shell-derived activated carbon and Fe_3O_4 nanocomposites	CDI	50	24.5	60 min	(Bharath et al., 2019)
Cr(VI)	Rice husk waste biomass activated carbon	CDI	100	2.83	120 min	(Gaikwad et al., 2020)
Cr(VI)	Activated carbon fiber felt	MCDI	500	155.7	55 min	(Chen et al., 2019)

2.5.2 Membrane capacitive deionization

MCDI cell has been widely applied in desalination process and removal of pollutants and holds considerable research potential for removing HMs. Some studies suggest that MCDI system can enhance both the recovery and removal efficiency of HMs (Yang et al., 2020). MCDI system offers several advantages over conventional CDI, particularly by improving charge efficiency by preventing co-ion repulsion near the electrodes. Furthermore, reverse voltage in MCDI enables desorption without the risk of adsorption on opposite electrodes, as IEMs block the transport of oppositely charged ions. This approach facilitates faster and more efficient regeneration of CDI electrodes and allows the system to maintain high performance, making it more suitable for large-scale applications. The extended operational time in deionization mode further increases freshwater production within the same period. Shi et al compared the performance of CDI and MCDI for the removal of Li^+ and Mg^{2+} ions. The results demonstrated that MCDI outperformed conventional CDI, achieving removal efficiencies of 9% for Li^+ and 12.77% for Mg^{2+}, compared to 0.52% and 4.16% for Li^+ and Mg^{2+}, respectively, in conventional CDI. Dong et al. examined the effects of IEMs on Pb^{2+} removal. The study found that Pb^{2+} removal efficiency was enhanced using IEMs. However, the presence of CEM slowed the release of Pb^{2+}, reducing its selectivity over other cations such as Ca^{2+} and Mg^{2+} in subsequent cycles. This behavior is attributed to the strong interaction between Pb^{2+} and the functional groups on carbon-based electrode materials (Dong et al., 2019). Wang et al. reported the use of activated carbon fiber in MCDI for the removal of Cu^{2+} and Zn^{2+}, demonstrating the feasibility of selective reduction and recovery in MCDI (Wang et al., 2019). A recent study reported that NF and MCDI achieved the highest Cu^{2+} removal, even when operated at low pressure in an integrated system (Cetinkaya & Bilgili, 2021).

Table 2.5 Carbon-based electrode performance for heavy metal removal in MCDI system.

Heavy metal ions	Electrode material	Unit	Initial concentration (mg/L)	Efficiency/Adsorption capacity	Operation Time	Reference
Pd^{2+}	Activated carbon	MCDI	100	98.38% and 11.99 mg/g	8 min	(Kim et al., 2018)
Chromium complexes (Cr(III)-EDTA)	AC@SiO_2-NH_2	MCDI	300	17.70 mg/g	110 min	(T. Feng et al., 2022)
Cu^{2+} and Zn^{2+}	Activated carbon fiber	MCDI	500	108.7 mg/g (Cu^{2+}) 122.6 mg/g (Zn^{2+})	55 min	(Wang et al., 2019)
Cu^{2+}	Carbon electrode	Nanofiltration membrane combined MCDI	50	96 %	10 min	(Cetinkaya & Bilgili, 2021)
Cr (total)	CNT@TiO_2 membrane electrodes	CDI	10	93.3 %	240 min	(J. Feng et al., 2022)

Pb^{2+}, Cu^{2+} , and Cd^{2+}	ZnO-modified N-doped porous carbon nanofiber membrane (ZnO@N-PCNM)	CDI	50	32.87 mg/g (Pb^{2+}), 23.81 mg/g (Cu^{2+}) and 20.85 mg/g (Cd^{2+})	180 min	(Li et al., 2022)

2.6 Application of CDI for desalination and pollutants elimination

CDI effectively removes charged species from wastewater by utilizing electrically charged electrodes to attract and capture ions. The CDI process reduces contaminant concentrations, enhancing water quality and supporting environmental sustainability. Figure 2.4 illustrates the diverse applications of CDI in wastewater treatment.

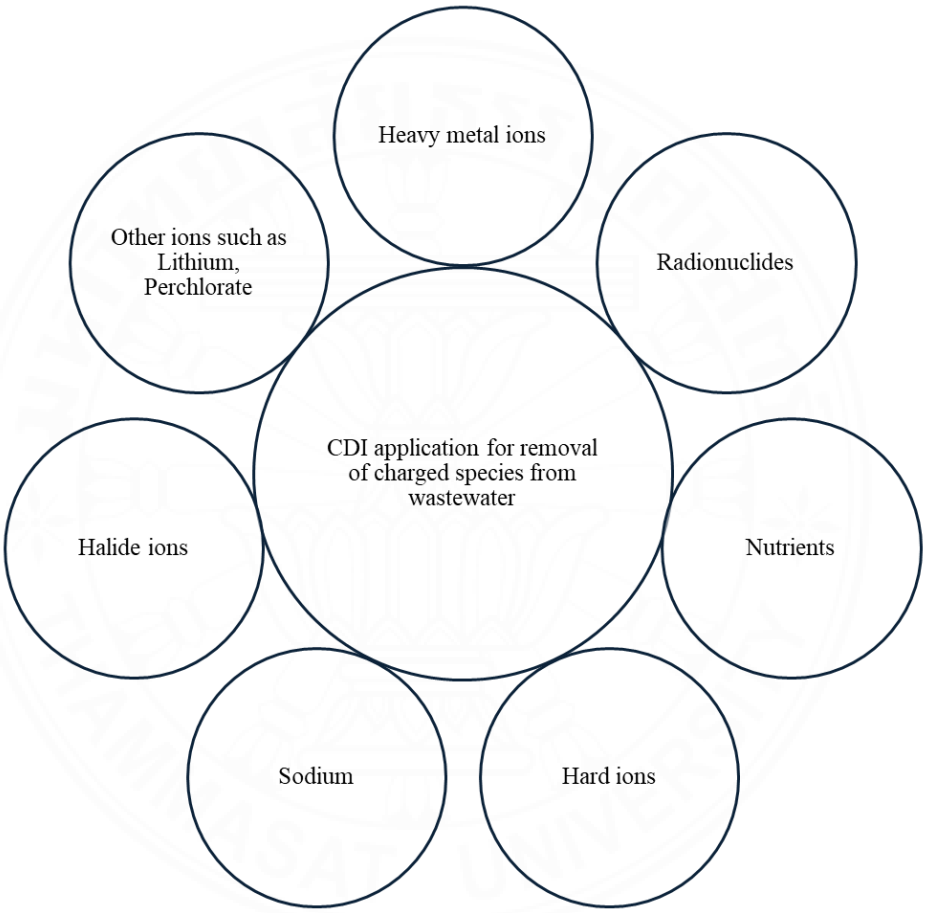

Figure 2.4 Applications of CDI for charged species removal from wastewater.

2.6.1 Desalination

The idea of electrochemical for desalination established the groundwork for advancing CDI technology. Initial electrodes utilized porous-activated carbon; however, challenges related to conductivity, wettability, and adsorption capacity prompted researchers to investigate diverse modifications to enhance their effectiveness (AL-Rajabi et al., 2024). Ryoo et al. improved activated carbon electrodes

by incorporating TiO_2, leading to a notable increase in Na^+ adsorption (Ryoo et al., 2003). Alternative carbon materials have been explored to overcome the limitations of traditional activated carbon. For example, MnO_2, a type of transition metal oxide, exhibits a high theoretical capacitance (> 1300 F/g), yet it faces challenges due to its limited conductivity (P. Li et al., 2018; C. Zhang et al., 2024). MnO_2 is frequently integrated with activated carbon to address this challenge, improving its electro-adsorption performance. Adorna et al. produced activated biochar from coconut shells, which, when combined with MnO_2, exhibited remarkable performance in the field of deionization, with a specific electro-sorption capacity of 68.4 mg/g for Na^+ removal (Adorna Jr et al., 2020).

Besides, graphene, known for its remarkable conductivity and extensive surface area (2630 m^2/g), has surfaced as an auspicious electrode material in CDI technology in desalination (Bao et al., 2023). Zhang et al. created graphene electrodes that exhibit exceptional desalination capabilities by utilizing core-shell composites (Zhang et al., 2022). Moreover, carbon nanotubes (CNTs), whether single-walled or multi-walled, exhibit exceptional mechanical strength and stability, rendering them ideal for use in this field. Hu et al. made significant progress in research by incorporating cobalt and cobalt oxide nanoparticles into carbon nanotubes, leading to improved desalination performance (Hu et al., 2022). The electrode material has a significant desalination capacity of 66.91 mg/g NaCl.

The electro-adsorption capacity of carbon materials no longer satisfies the demands of the rapidly advancing CDI technology. Researchers have combined MOF-derived carbon, Prussian blue (PB), and its analogues (PBAs) to develop electrode materials with enhanced electro-sorption capabilities with various carbon-based materials. These include MOF-derived carbon-graphene composites, PBA-CNTs, MOF-derived carbon-carbon nanofiber composites, and MOF-derived carbon-carbon nanotube composites. For instance, Shi et al. synthesized Fe-MOF and graphene, which displayed an electro-adsorption capacity of 37.6 mg/g with stable desalination performance (Shi et al., 2018). Graphene provides conductive pathways, while Fe-MOF contributes a porous carbon structure, enhancing the material's overall effectiveness. Furthermore, PB and PBAs are intercalation materials known for their high theoretical

specific capacity, safety, low toxicity, and ease of synthesis. However, they suffer from poor electronic conductivity, particle aggregation, and limited cycling stability, which restrict their practical use in CDI (Bao et al., 2023). Combining PBAs with carbon materials effectively enhances their desalination performance (Nai & Lou, 2019). Gong et al. developed a stepwise hollow Prussian blue/carbon nanotubes (SHPB/CNTs) composite with a high desalination capacity of 103.4 mg/g and excellent cycle stability (Gong et al., 2022).

2.6.2 Water softening

Hard water, characterized by high concentrations of soluble calcium and magnesium compounds, does not pose direct health risks but can cause significant problems in daily life and industrial applications. While advanced carbon materials like carbon aerogels, graphene, and carbon nanotubes (CNTs) offer high performance in water softening, their high cost and complex production processes drive researchers to investigate more economical and renewable biomass-derived materials (Bao et al., 2023). Deng et al. synthesized laminated activated carbon from chestnut inner shells, achieving an impressive specific surface area of 1943.2 m^2/g that demonstrated adsorption capacities of 21.0 mg/g for $CaCl_2$ and 17.7 mg/g for NaCl (Deng et al., 2022). However, the low selectivity and electro-adsorption capabilities of carbon-based electrodes limit the effectiveness of CDI technology in water softening. Pseudocapacitive materials, which interact selectively with specific ions through Faradaic redox reactions or ion (de)intercalation, offer high selectivity for Ca^{2+} in water. Xu et al. developed copper hexacyanoferrate (Cu-HCF) as a pseudocapacitive electrode, achieving a high electro-adsorption capacity of 42.8 mg/g for Ca^{2+} and a selectivity ratio of 3.05 compared to Na^+ and Mg^{2+} (Xu et al., 2020). Yoon et al. prepared a Ca-alginate-coated electrode, which enhanced Ca^{2+} removal by 44% compared to CDI and exhibited comparable performance to MCDI (Yoon et al., 2016). Moreover, Xu et al. also fabricated a manganese spinel ferrite (MFO) electrode that demonstrated selective hardness ion adsorption with a selectivity factor of 34.76 due to its unique crystal structure and pseudocapacitive properties(Xu et al., 2020) . This

research provides valuable insights into the redox mechanisms and ion selectivity of pseudocapacitive materials, guiding future advancements in CDI technology.

Despite the application of CDI to hard water, additional research is required in water softening. Additionally, most of the research is currently in the laboratory. The water quality may be compromised by the scaling that develops during the operation of the CDI device, a matter that requires additional investigation. Consequently, it is imperative to pursue in-depth research on the sustainable operation of CDI in practical applications and to create electrode materials that are low-cost, pollution-free, and possess high selectivity.

2.6.3 Organic contaminants

Non-Faradaic and Faradaic processes are the two main mechanisms for explaining ions storage during CDI (Zhang et al., 2018). While the non-Faradaic process, which is dependent on the creation of EDL, is reported as a critical electrochemical process for ions removal, where ions are stored in EDL generated inside the electrode pores (Xing et al., 2020; Zhang et al., 2018). Faradaic processes happening in CDI have both advantages and disadvantages, depending on the target of the utilization of CDI in the pollution removal. Besides ion removal, CDI technology based on positive results of the Faradaic process used to treat organic contaminants and water disinfection (Zhang et al., 2018).

Holey graphene hydrogel (r-HGH) electrodes exhibit significant advantages in the electrosorption of charged organic ions during CDI system. The r-HGH electrodes demonstrate a 57 mg/g electrosorption capacity for methyl orange, with adsorption and desorption equilibrium times of 200 seconds and 100 seconds, respectively (Liu et al., 2021). Besides, activated carbon has also been employed to treat sulfadimethoxine (SDM), ciprofloxacin (CIP), and clarithromycin (CLA) in water. The results indicate that these antibiotics were removed with 99.9% efficiency in surface water, reducing antibiotic concentrations to 580 ng/L trace levels. Effluent concentrations were successfully lowered to between 0.4 and 1.2 ng/L. Additionally, the recovery efficiency of activated carbon used for SDM adsorption reached 96.35 % (S. Wang et al., 2018). Research by Shim et al. (2021) investigated the effects of natural organic matter (NOM)

on the performance of MCDI. This study examined the effects of humic acid (HA) and tannic acid (TA) on MCDI with NaCl and $CaCl_2$ feed waters. HA reduced salt removal by up to 68% in NaCl but had minimal impact on $CaCl_2$ due to complex formation with Ca^{2+}. With its smaller molecular size, TA reduced removal rates by 37% for NaCl and 60% for $CaCl_2$, increasing resistance and energy consumption (J. Shim et al., 2021).

2.6.4 Nutrients contaminants

Ammonia, nitrate (NO_3^-) and nitrite (NO_2^-) are products of the nitrogen cycle commonly found in aquatic environments, such as lakes, streams, and drinking water sources. Various studies have utilized CDI systems to remove NO_3^- and NO_2^- from wastewater. Li et al. developed ion-exchange polymer and carbonized bacterial cellulose (CBC) electrodes treated with cation-exchange polymers, glutaric acid (GA), and sulfosuccinic acid (SSA) for an asymmetric CDI (p-CDI) cell (Li et al., 2020). The AC/CBC-SSA electrode demonstrated the high salt adsorption capacity (14.56 mg/g) and NO_3^- removal efficiency (71.01%) in comparison to the AC/AC electrode, which showed a salt adsorption capacity of 4.81 mg/g and a NO_3^- removal efficiency of 12.74%. The order of adsorption capacity recorded $NO_2^- > SO_4^{2-} > NO_3^- > F^- \approx Cl^-$ (Li et al., 2020). Mubita et al. observed that Cl^- was initially adsorbed on microporous carbons, but NO_3^- gradually displaced Cl^- during electrosorption (Mubita et al., 2019). NO_3^- selectivity increased over time but declined at higher voltages due to increased Cl^- absorption. Another study demonstrated that a CDI system with AC electrodes achieved 48% NO_3^- removal and 21% recovery rate from low-salinity domestic wastewater (Pastushok et al., 2019). Recently, Su et al. introduced an electrochemical flow-through system utilizing a titanium cathode and a granular-activated carbon (GAC)-filled anode. This system combined electrochemical redox reactions with electrosorption, achieving high NO_3^- removal efficiency. NO_3^- ions were electro-adsorbed on the positively charged GAC, followed by electroreduction to NH_4^+ at the cathode and oxidation to N_2 by anodically generated chlorine, resulting in nearly 100% N_2 selectivity (Su et al., 2021). Moreover, Fang et al. evaluated FCDI system for ammonia removal, finding minimal impact from AC content, while initial ammonia concentration significantly influenced removal efficiency, likely due to disparities

between ion availability and adsorption site limitations (Fang et al., 2021). It reported that FCDI systems with MXene ($Ti_3C_2T_x$) electrodes achieved high ammonia removal efficiency, low energy consumption (0.45 kWh/kg), and substantial ammonia adsorption (460 mg/g), with a 60% removal efficiency (Mansoor et al., 2022).

Removing phosphate and sulfur is crucial for protecting water quality and controlling pollution. Hong et al. demonstrated that layered double hydroxide/reduced graphene oxide (LDH/rGO) composite electrodes in CDI selectively removed phosphate, maintaining high efficiency even in chloride-rich environments (Hong et al., 2020). ZnFe-PANI/CNT composite electrodes were used for phosphate removal in sewage, efficiently removing phosphate at concentrations of 2–10 mg/L across a pH range of 3–10, reducing effluent phosphate to 0.095 mg/L (H. Zhang et al., 2024). Additionally, asymmetrical electrode system with $Na_{0.7}MnO_2$ as the negative electrode and activated carbon as the positive electrode achieved electrosorption capacities of 0.183 mmol/g in NaCl, 0.178 mmol/g in $NaNO_3$, and 0.124 mmol/g in Na_2SO_4. The order of electrosorption capacity was $SO_4^{2-} > Cl^- > NO_3^-$, indicating preferential ion adsorption based on hydrated radius and valence (Zhou et al., 2018).

2.6.5 Water disinfection

Wang et al. demonstrated that at 1.2 V, a contact-active activated carbon electrode functionalized with a quaternary ammonium compound may kill 99 % of *Escherichia coli* or *Pseudomonas aeruginosa*. After five regeneration cycles, E. coli killed at a rate of around 90% (J. Wang et al., 2018). For mixed microbial communities in groundwater, Laxman et al. (2020) used ACC electrode to evaluate the influence of ion concentrations on the electrosorption and disinfection. The results revealed that for both synthetic and groundwater, up to 75% of microbial cells could be eliminated through CDI cell while preserving salt removal capability (Laxman et al., 2020). Hydrogen peroxide (H_2O_2) and hydronium ions (H_3O^+) are produced at the CDI cathode and anode. It was explained that faradaic reactions were taking place at the electrodes. These chemical oxidants kill E. coli cells during deionization, then release them into the water stream during electrode regeneration (Laxman et al., 2020). Research by Janpoor et al. showed that the GO/G5/Ag nanocomposite electrodes showed promise

in desalination and disinfection applications. CDI system kills 99.9% of coliforms in a NaCl solution (500 mg/L) containing 1,000, 10,000, and 100,000 MPN of coliforms in 30 min, 60 min, and 120 min, respectively (Janpoor et al., 2021).

2.7 Evaluation of adsorption capacity of materials

Adsorption capacity, defined as the amount of adsorbate retained by the adsorbent per unit mass or volume under specific operating parameter, such as time and temperature, is a critical parameter in adsorption process (Sahoo & Prelot, 2020). It is typically expressed in terms of adsorbate mass per mass of adsorbent.

Kinetic models are employed to evaluate the adsorption rates of ions, and the duration required to reach equilibrium, facilitating the characterization of ion adsorption on electrode materials during the CDI process. Experimental data are analyzed for optimal fitting to kinetic models, including pseudo first order, pseudo second order, Elovich, and intra-particle diffusion models, with the model exhibiting the highest linear regression coefficient (R^2) considered most appropriate (Sahoo & Prelot, 2020). Several studies have predominantly utilized the pseudo first order model and pseudo second order model to analyze kinetic data in CDI system (Chen et al., 2019; Deng et al., 2022; Wang et al., 2019). The pseudo first order model assumes that the adsorption rate is proportional to the difference between the saturation concentration and the amount of material uptake over time. The pseudo second order model identifies chemical sorption as the rate-limiting step in adsorption.

2.8 Evaluation of the characteristics and properties of materials

Several characterization techniques evaluate materials and membranes, providing critical insights into their properties. Commonly applied techniques include those detailed in Tables 2.5 and 2.6. These techniques are essential for understanding the efficiency of materials and membranes properties.

Table 2.6 Summary of the characterization techniques for electrode materials.

Technique	Measurement	Purpose	Reference
Fourier transform infrared spectroscopy (FTIR)	- FTIR measures the absorption spectrum of a sample by directing an IR beam through an interferometer to generate an interferogram and subsequent spectrum. - Sample preparation techniques, including transmission, ATR, diffuse reflectance, and reflection absorption, are used to analyze molecular bonds and functional groups.	- To analyze the molecular fingerprints and functional groups of materials, which can reveal details about their chemical composition and performance in applications like gas separation, water treatment, and fuel cells.	(Mohamed et al., 2017)
X-ray diffraction (XRD)	- XRD analyzes the crystallographic structure and chemical composition of materials. - It directs collimated X-rays onto a crystalline sample, where the interaction produces a diffracted signal. - The intensity of diffracted rays at various angles is recorded to generate a diffraction	- To identify and quantify the crystalline phases of a material through its diffraction pattern. - To analyze the atomic arrangement, crystallinity, and detect structural defects or imperfections in the sample.	(Raja et al., 2022)

	pattern, unique to each phase of the material.		
Scanning electron microscopy (SEM) with energy dispersive X-ray spectroscopy (EDX)	- In SEM, an electron beam with energies ranging from a few hundred eV to 40 keV is directed across the sample surface. - SEM image is constructed pixel by pixel as the electron beam systematically scans the sample. - EDX, commonly coupled with SEM, facilitates the analysis of the sample's elemental composition.	- SEM image offers detailed insights into the surface texture, particle size, and morphological features of materials. - EDX provides supplementary chemical composition data, enhancing the information obtained from SEM. - SEM-EDX technique is widely used to comprehensively analyze surface characteristics and elemental composition at the micro- and nanoscale.	(Barhoum & Luisa García-Betancourt, 2018)
Porosity (surface area and pore volume)	- Gas adsorption analysis determines surface area and porosity by measuring weight uptake or sample volume with gases or vapors.	- To assess the impact of surface area and porosity on material properties before and after modification.	(Thommes et al., 2015b)

	- The Brunauer, Emmett, and Teller (BET) technique uses nitrogen gas to measure surface area based on monolayer capacity and the probe molecule's cross-sectional area.		
Cyclic voltammetry (CV)	- CV measures electrochemical reactions and kinetics by applying a linearly varying potential to a static working electrode and recording the resulting current. - The CV profile is constructed from the current-potential plot, known as the cyclic voltammogram, which reveals redox behavior, reaction kinetics, and adsorption processes.	- To determine the electrochemical active surface area, reduction peak potential, and current for evaluating electrocatalyst performance, particularly for oxygen reduction reactions. - To analyze the adsorption/ desorption and oxidation/ reduction of oxygen species on the catalyst surface based on peak appearances in the CV profile.	(Bhuvanendran et al., 2022)
Electrochemical impedance spectroscopy (EIS)	- EIS applies a sinusoidal signal to an electrochemical system and measures the response over a range of frequencies.	- To provide detailed kinetic and mechanistic data on various electrochemical processes, including	(Lazanas & Prodromidis, 2023)

	- EIS analyzes the relationship between the input signal (ac voltage or current) and output signal (AC or voltage) to model the system's behavior.	resistance, conductivity, and charge-transfer kinetics. - To differentiate and analyze various electrical and electrochemical phenomena, including those with varying time constants.	
Galvanostatic charging and discharging (GCD)	- GCD tests apply constant currents to charge and discharge a material within set potential limits, often cycling the process multiple times. - GCD profiles assess capacitive response, identify irreversible Faradaic reactions, and determine critical figures of merit such as capacitance, capacity, energy, and power.	- To evaluate the quality of energy storage systems and materials by analyzing their charge and discharge behavior. - To investigate the effects of charge redistribution within the material, which can influence the measured performance and self-discharge characteristics.	(Licht et al., 2020)

Table 2.7 Summary of the characterization techniques for membranes.

Technique	Measurement	Purpose	Reference
Fourier transform infrared spectroscopy (FTIR)	- FTIR measures the absorption spectrum of a sample by directing an IR beam through an interferometer to generate an interferogram and subsequent spectrum. - Sample preparation techniques, including transmission, ATR, diffuse reflectance, and reflection absorption, are used to analyze molecular bonds and functional groups.	- To identify and characterize various chemical components and functional groups within a membrane and monitor surface functionalization and stability.	(Mohamed et al., 2017)
Hydrophilicity property (water contact angle)	- Contact angle measures the wetting property of a surface by evaluating the angle between a water droplet and the membrane surface. - A high contact angle indicates hydrophobicity (poor wetting), while a low contact angle indicates hydrophilicity (good wetting).	- To assess the membrane's hydrophilicity or hydrophobicity, influencing its fouling resistance. - To determine the membrane's potential for anti-fouling by analyzing how well it resists the accumulation of contaminants during filtration.	(Jhaveri & Murthy, 2016)

Porous structure of membrane surface by scanning electron microscopy (SEM)	- SEM provides two-dimensional images of membrane surfaces, showing pore structures and surface defects. - SEM can reveal various pore sizes, such as those in polysulfone membranes, but often underestimates pore diameters due to metal coating and other factors.	- To characterize the surface morphology and pore structure of membranes. - To identify and analyze defects and pore sizes, despite potential underestimation and structural changes due to SEM processing.	(Khulbe et al., 2008)
Porous structure of membrane surface by atomic force microscopy (AFM)	- AFM provides high-resolution, three-dimensional images of membrane surfaces, revealing details not visible with SEM. - AFM shows changes in pore size and surface structure under different conditions.	- To analyze and compare membranes' surface structure and porosity with high detail. - To observe how surface morphology and pore size distribution change in different environments	(Khulbe et al., 2008)
Ion exchange capacity (IEC)	- IEC quantifies the amount of charged functional groups per unit volume in a membrane. - IEC can be determined using titration.	- To assess the quantity of charged functional groups interacting with water and mediating ion transport.	(Tsehaye et al., 2023)
Water content (WC)	- WC is measured by comparing wet and dry mass.	Correlate WC with ion mobility and membrane performance.	(Elozeiri et al., 2024)

CHAPTER 3

METHODOLOGY

Various approaches in CDI architectures were employed for enhance HMs removal. Overall experimental plan is shown in Figure 3.1. The first experiment focused on integrating MnO_2 nanostructures into activated carbon fiber felt (ACC/MnO_2) to improve the capacitive properties of the ACC/MnO_2 electrode compared to pristine ACC, specifically for Cr(III) and Cr(VI) ions. The second experiment shifted to the fabrication of heterogeneous cation exchange membranes, emphasizing the fabricated membrane's improved ion selectivity and adsorption capacity compared to commercial counterparts in an MCDI cell, specifically for Ni(II). The third experiment examined ZnO nanostructures on ACC, where ZnO nanoparticles (ACC/ZnO-nPs) and ZnO nanorods (ACC/ZnO-nRs) amplified the local electric field to enhance Cu(II) adsorption in CDI cell and MCDI cell. The fourth experiment aimed to identify the optimal fabricated electrode materials for removing single ions and mixtures of HMs, including Ni(II), Cu(II), and Cr(III), to determine whether ACC/MnO_2 or ACC/ZnO-nRs offered the best adsorption capacity. The final experiment explored the potential of the prepared CDI architectures for treating real electroplating wastewater.

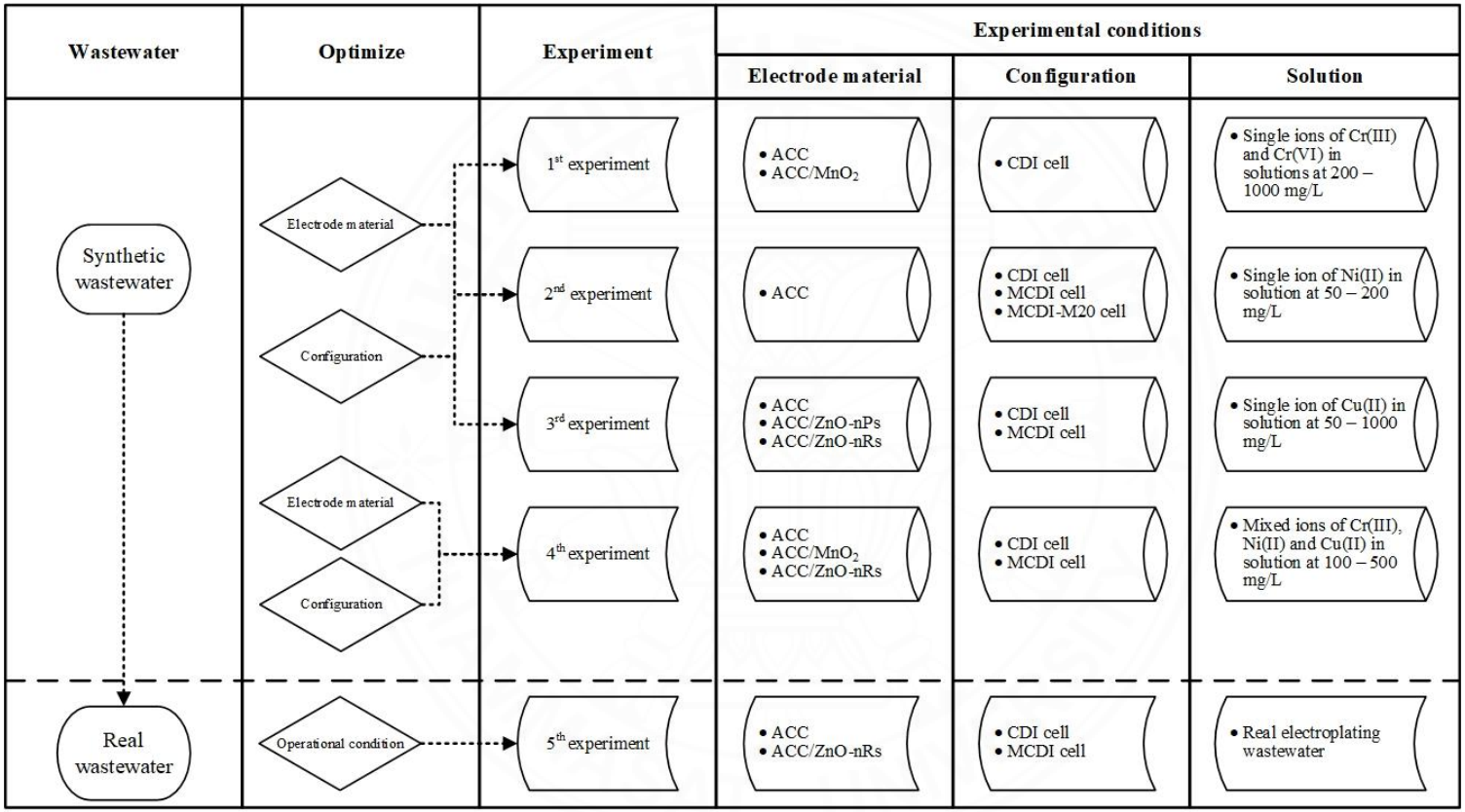

Note:

- CDI cell: no uses ion exchange membranes
- MCDI cell: uses commerial CEM & commerial AEM
- MCDI-M20: uses fabricated CEM & commerial AEM

Figure 3.1 Summary of different experiments and experimental conditions employed.

3.1 Preparation of materials

In this study, each experiment was conducted separately to evaluate the impact of different approaches on removal of HMs. The preparation of chemicals and materials for each experiment is described in detail.

3.1.1 Experiment 1: Integrating MnO_2 nanostructures into activated carbon fiber felt for enhanced chromium ions removal in capacitive deionization

3.1.1.1 Chemicals and materials

Potassium permanganate ($KMnO_4$) was ordered from Ajax Finechem Pty company (Australia), Chromium (III) nitrate nonahydrate, hydrochloric acid (HCl), Sodium chloride (NaCl) and sulfuric acid (H_2SO_4) were bought from Loba (India), Potassium dichromate ($K_2Cr_2O_7$) was required from KemAus (Australia), sodium hydroxide (NaOH) was gain from Merck Chemicals, Germany. The compounds were not subjected to any additional purification processes before use.

In this study, activated carbon cloth (ACC) served as the substrate for grafting MnO_2 nanostructures. Before use, ACC underwent a cleansing process involving immersion in 5% HCl at 95 °C for 12 h, followed by thorough rinsing with deionized (DI) water until achieving a neutral pH. ACC was then cooled down to room temperature. Subsequently, it was subjected to a drying in an oven set at 95 °C for 24 h before use in the experiments.

3.1.1.2 Preparation of ACC/MnO_2

This method was carried out as described by Xiao et al. to obtain MnO_2 nanorods grafted onto ACC (ACC/MnO_2) (Xiao et al., 2010). Initially, 0.395 g of potassium permanganate were dissolved in 100 mL of DI water under continuous magnetic agitation for 30 min. Subsequently, the ACC was immersed in the solution and agitated lightly for 15 min. Then, 1.25 mL of hydrochloric acid (37 wt%) were introduced dropwise into the solution with ongoing agitation. After 15 min of stirring, the mixed solution was transferred into a 150-mL Teflon-lined stainless-steel autoclave and subjected to a thermal process at 140 °C for 12 h in a furnace oven. The prepared

material was extensively cleaned with DI water several times until the washed water reached a neutral pH after naturally cooling to reach room temperature. The prepared material was then dried at 80 °C for at least 24 h before use.

3.1.2 Experiment 2: Enhancing the removal of Ni^{2+} through the fabrication of heterogeneous membranes as cation exchange membranes in membrane capacitive deionization

3.1.2.1 Chemicals and materials

The chemicals employed in the study are hydrochloric acid, sodium chloride, N, N-Dimethylacetamide, sodium hydroxide from Loba. Nickel sulfate hexahydrate from Carlo Erba. Polyvinylidene fluoride (molecular weight of 180,000 by GPC) from Merck. Polyethene glycol (molecular weights of 400 Da) from Tokyo Chemical Industry Co., Ltd (Japan). No additional purification steps were performed for any chemicals before being utilized in the study.

The electrode material utilized in the CDI system was ACC (CM−1300) with a specific surface area between 1150 and 1250 m^2/g. Before utilization, the ACC was submerged in a 5% hydrochloric acid solution at 95 °C for 12 h to remove contaminants generated from the manufacturing process and ensure uniform electrochemical stability. The ACC was thoroughly washed with DI water after being naturally cooled to room temperature until the pH of the cleaning solution became neutral (7.0 ± 0.2). The ACC was subsequently dried at 95 °C for 24 h before employed in the study.

This study utilized the anion exchange membrane (AMI-7001S) and cation exchange membrane (CMI–7000S) obtained from Membranes International Inc. (USA). They underwent a pretreatment to prepare membranes for application in the CDI cell. Initially, these membranes were immersed in DI water to ensure proper wetting and the expansion of their structure. After 48 h of immersion in DI water, they were engaged in a 5% (m/v) sodium chloride solution to facilitate hydration and ion exchange equilibration.

The cation exchange resin was procured from Purolite (USA) to produce heterogeneous membranes. Before utilizing resins, several essential steps were

implemented. Initially, the resins were immersed in two separate solutions for 2 h each: a 5% (v/v) hydrochloric acid solution and a 5% (m/v) sodium hydroxide solution. The resins were then thoroughly cleaned with DI water until reaching a near-neutral pH to remove any remaining acid or base. Subsequently, the resins were dried at 60 °C in a vacuum oven to ensure homogeneity. The particle size of resin reduction was achieved using a grinder, followed by sieving to obtain resin particles with a diameter smaller than 53 μm.

3.1.2.2 Heterogeneous cation exchange membrane fabrication

In this study, a total of five membranes were employed as membrane M0 (without resin) and four cation exchange membranes (M5, M10, M15, and M20), representing 5%, 10%, 15%, and 20% weight percentages of resins incorporated into the dope solution. The composition of the dope solution in cation exchange membranes encompassed dimethylacetamide, polyethene glycol, polyvinylidene fluoride, and cation exchange resin, all determined by the mass of elements. Each dope solution used in the membrane casting process has a total weight of 5 grams. The preparation of the membranes involved three stages: the initial stage was the preparation of the membrane casting solutions, the subsequent step was the casting of the polymer solution sheets, and the final stage was the phase inversion in the water bath.

a) Polymer solution preparation

Every flask designated for membranes M0, M5, M10, M15, and M20 contained 0.25 g of polyvinylidene fluoride (PVDF) and 0.1 g of polyethylene glycol (PEG). Subsequently, 4.65 g, 4.4 g, 4.15 g, 3.9 g, and 3.65 g of N, N-Dimethylacetamide (DMAc) were added to M0, M5, M10, M15, and M20, respectively. The mixture was then mixed at 60 ^{o}C for 4 h until a homogeneous solution was obtained. Following that, resin amounts of 0.25 g, 0.5 g, 0.75 g, and 1.0 g were respectively incorporated into the mixed solutions of flasks M5, M10, M15, and M20, while the mixture solution for M0 was prepared without the addition of resins. The mixture was stirred at 60 °C for 2 h, forming the dope solution.

b) Preparation of membranes

The polyester fabric, employed as a substrate for the prepared membrane (membrane M0 and membranes M5, M10, M15, and M20), was firmly attached to the glass support. Subsequently, the dope solution was poured onto the fabric sheet and uniformly distributed to a gap of 400 μm by a casting applicator. The membrane attached to the glass support was promptly submerged in a DI water bath for at least 30 min before further use.

3.1.3 Experiment 3: Removal of Cu^{2+} ion utilizing enhanced zinc oxide nanostructures on activated carbon cloth as electrode material in different configurations of capacitive deionization

3.1.3.1 Chemicals and materials

Zinc acetate dihydrate, zinc nitrate hexahydrate, cupric nitrate trihydrate, hydrochloric acid, and sodium chloride were ordered from Loba (India), hexamethylenetetramine was bought from Alfa Aesar (USA), sodium hydroxide was required from Merck (Germany), and absolute ethanol was received from RCI Labscan (Thailand). No additional purification had been performed on the chemicals before their use.

The ACC with a thickness of approximately 1 mm was used as a base to develop ZnO nanostructures. The ACC was maintained in 5% hydrochloric acid at 95 ^{o}C for 12 h to remove contamination. After cooling naturally to room temperature, it was extensively cleaned with DI water until the wash solution gained neutral pH (7.0 ± 0.2). Following that, it was dried at 95 °C for 24 h.

Two IEMs, including an anion exchange membrane (AMI-7001S) and a cation exchange membrane (CMI-7000S), were obtained from Membranes International Inc. (New Jersey, USA). Before use, the membranes were pretreated before being immersed in DI water for 48 h. Subsequently, these membranes were engaged in a 5% sodium chloride solution for 12 h to allow for membrane hydration and expansion.

3.1.3.2 Preparation of ACC/ZnO

A process similar to that described by Baruah and Dutta (2009) and Laxman et al. (2015) was used to grow ZnO nanoparticles and nanorods on ACC (S. Baruah & J. Dutta, 2009; Laxman et al., 2015).

To synthesize ZnO nanoparticle colloids, 5 mM NaOH was added to a solution of 5 mM zinc acetate in absolute ethanol in a 1:1 ratio with consistent mixing. They were then hydrolyzed at 60 °C for 2 h, forming a colloidal solution of ZnO nanoparticles. Subsequently, the ZnO nanoparticles were deposited onto a cleaned ACC sheet using a solution dipping approach. The ACC sheet was immersed in the ZnO nanoparticle colloidal solution for 10 min at 60 °C and then dried for 20 min in an oven heated to 95 °C. This procedure was repeated five times to ensure the coating was uniform. Finally, the coated samples were annealed at 250 °C for 1 h in an ambient environment to get ACC/ZnO nanoparticles material (ACC/ZnO-nPs).

The ZnO nanoparticles grafted onto ACC were used to prepare modified ZnO nanorods. ACC/ZnO nanorods (ACC/ZnO-nRs) were produced using a hydrothermal technique at 90 °C for 10 h. In a Teflon-coated stainless-steel autoclave, these materials were immersed in a hydrothermal solution containing 100 mL of 20 mM zinc nitrate hexahydrate and 20 mM hexamethylenetetramine in a ratio of 1:1. To achieve an initial pH level of 6.8 – 6.9, 1 M NaOH was added to the hydrothermal solution. The hydrothermal solution was refreshed every 5 h. After the hydrothermal growth process ended, these materials were cleaned with DI water and then air annealed at 250 °C for 1 h.

3.1.4 Experiment 4: Removal of individual and mixed HMs solution in different configurations of capacitive deionization

3.1.4.1 Chemicals and materials

Chemicals used in this study were prepared according to the procedures outlined in Experiments 1 and 3. For chemical oxygen demand (COD) analyses, potassium dichromate ($K_2Cr_2O_7$) was required from KemAus (Australia). Silver sulphate (Ag_2SO_4), sulfuric acid (H_2SO_4), 1, 10-phenanthroline monohydrate, ferrous sulphate

heptahydrate ($FeSO_4.7H_2O$), mercuric sulphate ($HgSO_4$), ammonium ferrous sulphate hexahydrate ($Fe(NH_4)_2SO_4.6H_2O$) were bought from Loba (India).

Materials, including activated carbon fiber felt and ion exchange membranes, were pretreated as described in Experiment 1 and 3. No additional purification was performed on any of the compounds.

3.1.4.2 Preparation of ACC/MnO_2 and ACC/ZnO

The electrode materials used include ACC, ACC/MnO_2, and ACC/ZnO-nRs. The ACC/MnO_2 electrode was prepared following the method detailed in Experiment 1, while the ACC/ZnO-nRs electrode was prepared according to the procedure described in Experiment 3. Both electrodes were prepared without additional modifications.

3.1.5 Experiment 5: Potential of capacitive deionization for removal of heavy metals from electroplating wastewater

3.1.5.1 Electroplating wastewater

Real wastewater for this study was collected from the Samut Sakhon metal electroplating plant in Thailand, which discharges about 960 m^3/day of wastewater from electroplating process. The flow diagram of the wastewater treatment plant is depicted in Figure 3.2. At the site, wastewater originated from two sources: electroplating processes and another source related to industrial operations. The wastewater was grabbed from the equalization tank of the wastewater treatment system. Wastewater was then pre-filtered using Whatman Grade 4 with a 20 – 25 μm pore size to remove solids and debris before conducting CDI tests. The concentration of elements from wastewater is presented in Table E.1.

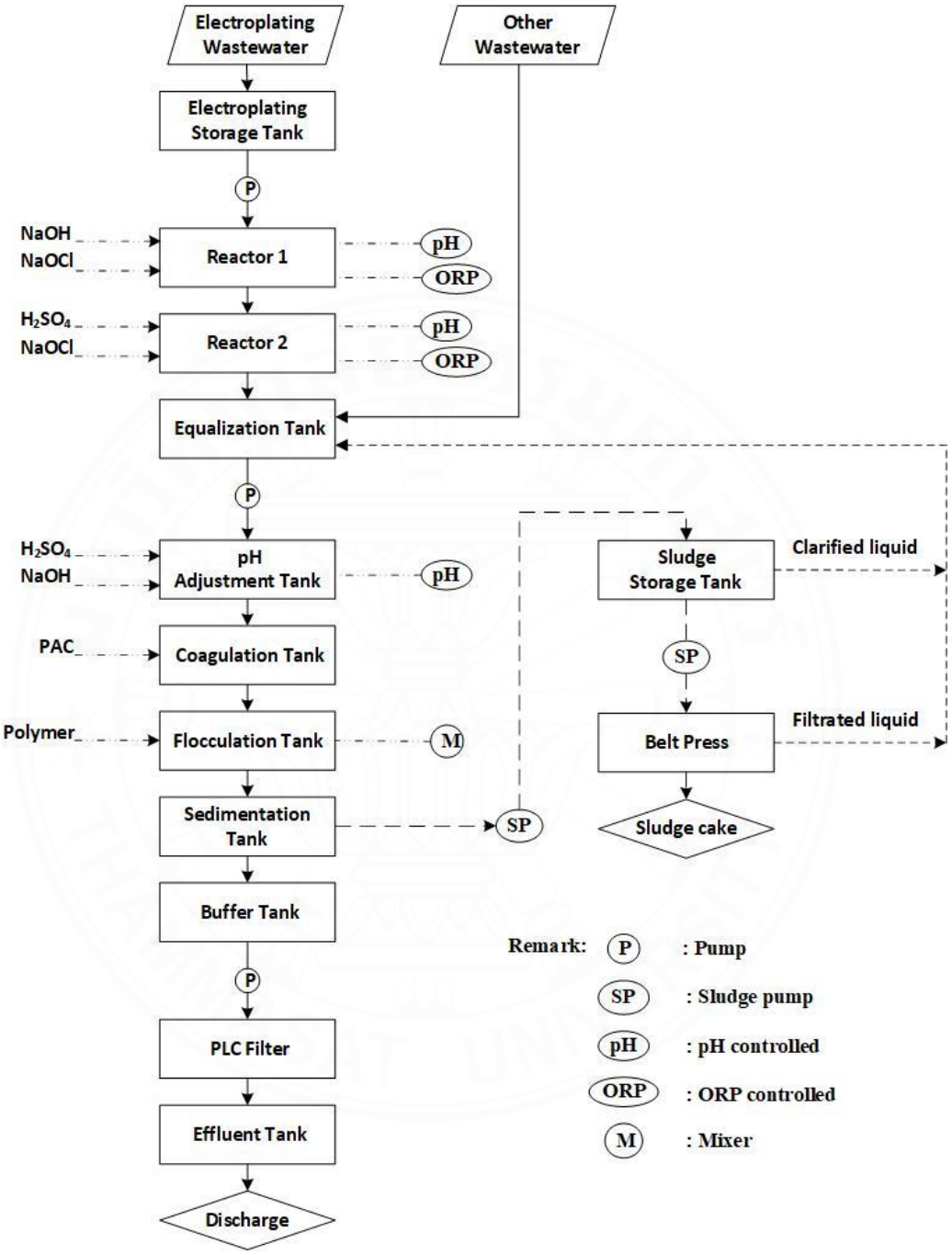

Figure 3.2 Flow diagram of electroplating wastewater treatment plant.

3.1.5.2 Chemical and preparation of electrode

Chemicals used in this study were prepared according to the procedures outlined in Experiments 3. The chemicals preparation for COD analyses followed as outlined in

Standard Method 5220 D (Baird et al., 2017). The suspended solid (SS) analysis protocol was conducted as outlined in Standard Method 2540 D (Baird et al., 2017).

The electrode materials used in this experiment include ACC and ACC/ZnO-nRs. The materials, such as commercial activated carbon fiber felt and ion exchange membranes, are pretreated as described in Experiments 3. The ACC/ZnO-nRs electrode is prepared using a method similar to that described in Experiment 3, without any additional modifications.

3.2 Configuration of capacitive deionization cell

This study was conducted in two configurations: CDI cell and MCDI cell operated continuously as presented in Figure 3.3(a). The laboratory-scale CDI cell was equipped with two electrodes, each electrode with a surface area of 3.8 cm × 3.8 cm. On the interior side of each electrode, an anion exchange membrane was placed in front of the anode, while the cation exchange membrane in front of the cathode. A spacer is installed between the electrodes to prevent a short circuit and ensure an equal portion of the feed flows to the electrodes. On the exterior side of each electrode, a graphite sheet is affixed to the electrode, which is then connected to the DC power supply. The current profile of the reactor during the experiment was monitored using a data logger (ADC-20, Pico Technology, The United Kingdom). Nuts and bolts are used to firmly attach the framework of the CDI cell after it is covered with a polyacrylic sheet. The configuration of the MCDI cell is presented in Figure 3.3(b). The structure of CDI cell was identical to the MCDI cell, but the CDI cell lacked both the cation exchange membrane (CEM) and anion exchange membrane (AEM), as presented in Figure 3.3(c).

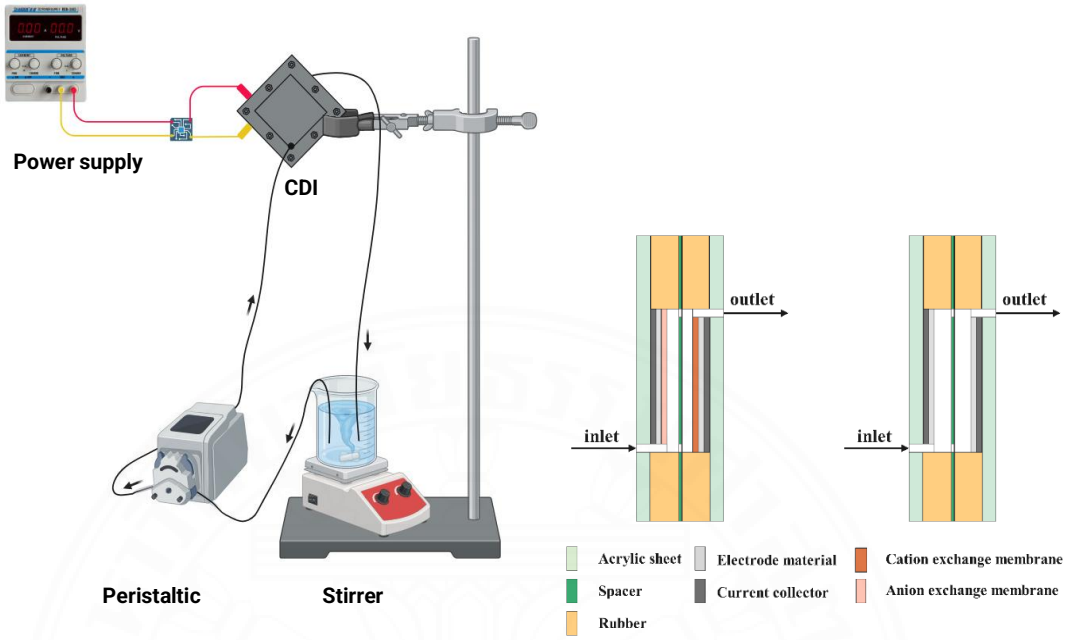

(a) Schematic representation of test (b) MCDI cell (c) CDI cell

Figure 3.3 (a) Schematic representation of the test, (b) configuration of MCDI cell, and (c) configuration of CDI cell.

3.3 Capacitive deionization tests

3.3.1 Electrosorption tests

During the electrosorption tests, a 100 mL solution with predetermined concentrations was consistently introduced into the CDI reactor at an instant flow rate and then returned to the feed tank. All studies were conducted at room temperature (22 - 25 °C) with potential less than 1.2 V to avoid hydrolysis phenomena in the CDI process. The evaluation was conducted in both CDI cell and MCDI cell at various concentrations of HMs.

The experimental design is as follows: In experiment 1, Cr^{3+} and Cr^{6+} concentrations were varied from 200 to 1000 mg/L, while experiment 2 examined Ni^{2+} concentrations ranging from 50 to 200 mg/L. Experiment 3 involved Cu^{2+} concentrations between 50 and 1000 mg/L. For experiment 4, single ion tests were conducted using solutions with an initial concentration of 500 mg/L for Cu^{2+}, Ni^{2+}, and Cr^{3+}. Subsequently, experiments were conducted with a mix of different metal ions to

see the effect of competitive ions on CDI and MCDI performance. For this, SA mixture comprised of 500 mg/L Cu^{2+}, 500 mg/L Ni^{2+}, 500 mg/L Cr^{3+}, SB mixture (500 mg/L Cu^{2+}, 200 mg/L Ni^{2+}, 100 mg/L Cr^{3+}), and SC mixture (500 mg/L Cu^{2+}, 100 mg/L Ni^{2+}, 200 mg/L Cr^{3+}). Additionally, the SA-COD mixture consisted of 500 mg/L Cu^{2+}, 500 mg/L Ni^{2+}, 500 mg/L Cr^{3+}, and 500 mg/L COD. Finally, real electroplating wastewater was employed in CDI tests without modification in experiment 5.

3.3.2 Charge/discharge tests for evaluating the performance of the CDI system

The consecutive charging/discharging tests followed the same protocol as the electrosorption tests. Many different potentials were applied to the CDI reactor to determine the impact of potential on the removal and recovery of HMs in the CDI system. Additionally, the experiment comprised multiple cycles, each cycle consisting of two phases: a charging phase and a discharging phase.

3.4 Analysis and calculation

3.4.1 Electrodes characterization

Multiple characterization methods were employed to analyze the prepared electrode materials. The X-ray diffraction (XRD) patterns of the electrodes ACC, ACC/ZnO-nPs, and ACC/ZnO-nRs were acquired by a Bruker AXS Model D8 Advance instrument using a Cu Kα X-ray source (wavelength ~ 0.154 nm) at a voltage of 40 kV with an increment of 0.02 degree/step. The morphology was analyzed using a Field Emission Scanning Electron Microscope (FE-SEM) (JEOL JSM7800F, JAPAN). Energy dispersive spectroscopy (EDS) was performed to check the presence of various elements in the sample. Specific surface area (SSA) and total pore volume (TPV) were analyzed using the Brunauer–Emmett–Teller (BET) method. The pore-size distribution (PSD) was calculated using combined method of NLDFT (Non-Localized Density Functional Theory) and GCMC (Grand Canonical Monte Carlo), known as the NLDFT/GCMC method. They were calculated based on the amount of nitrogen gas absorbed by the surface of the samples relative to the total mass of the samples measured using the BET analyzer (Belsorp Mini-X, Microtrac BEL Corp, Japan). The

nitrogen adsorption temperature was 77 K, with a saturated vapor pressure of 102.95 kPa. The samples were pretreated and heated to 423 K for 6 h while nitrogen gas flowed through the chamber.

3.4.2 Membranes characterization

The functional groups in the prepared membranes were examined by Fourier transform infrared spectroscopy (FTIR) with a NicoletTM iS50 analyzer (Thermo Fisher Scientific, USA). The FTIR measurement was conducted between 400 and 4000 cm−1. The hydrophilicity property of the membrane surface was analyzed via the water contact angle method, which required using the OCA 15 Plus analyzer (DataPhysics Instruments GmbH, Germany) with Pico droplet measurement. A 2 µL DI water droplet was dropped onto the surface of a dried membrane sample with a micro syringe for each measurement. The contact angle between the membrane surface and water was then recorded. Three measurements were taken on each membrane at different points, and the values were averaged. The membrane surface roughness was assessed using Atomic Force Microscopy (SPI3800N/SPA400, Seiko Instruments, Germany), with the membrane surfaces being imaged at a scan size of 50 µm × 50 µm. The membrane surface roughness is represented in this study using the RMS (root mean square of a surface) and Ra (roughness average). R_{MS} is computed as the root mean square of the recorded microscopic peaks and valleys on the membrane's surface, whereas Ra is found as the roughness average of those microscopic peaks and valleys. The membrane morphology was studied using a field emission scanning electron microscope (FE-SEM) (Jeol JSM7800F, Japan).

The ion exchange capacity (IEC) is an essential parameter used to determine a membrane's ability to exhibit ionic conductivity properties with the solution, whereas the water content of the membrane contributes to the transfer of electrical current structure. The membrane's ion exchange capacity was determined using an acid-base titration method. A membrane measuring approximately 40 mm × 40 mm was initially dried for 2 h at 60 °C in a vacuum oven. Consequently, the membrane was placed for 24 h in 100 mL of 1 M HCl solution to convert any salt form of sulfonate groups to

SO_3H groups, followed by thorough cleaning with DI water. The membrane was then submerged for 24 h in 10 mL of 0.1 M NaOH solution, and after collecting the supernatant, three droplets of phenolphthalein were applied. Finally, a 0.1 M HCl solution was used for the titration procedure.

The prepared membrane's water content (WC) was calculated based on the mass difference between dry and wet membranes. The mass of the membrane (size of 40 mm × 40 mm) was determined after undergoing a 2 h drying process at 60 °C in a vacuum oven. Subsequently, the membrane was immersed in DI water. After 24 h, any remaining DI water on the membrane surface was removed, and the membrane mass was measured.

To separate the static adsorption amount of ion on the used heterogeneous cation exchange membrane in the MCDI cell, the adsorption amount of ion on the prepared membrane was recorded. The prepared membrane was immersed for 24 h in 100 mL of 1 M HCl solution to convert any salt form of sulfonate groups to SO_3H, followed by a thorough cleaning with DI water. Next, the mass of the prepared membrane, approximately 40 mm × 40 mm in size, was measured following a 2h drying process at 60 °C in a vacuum oven. Finally, the prepared membrane was submerged in 100 mL of solution contained HMs without any applied voltage.

3.4.3 Electrochemical properties of electrodes

The electrochemical property of materials was analyzed through cyclic voltammetry (CV) using PalmSens4 potentiostat (Netherlands). The area of the prepared materials was held at 3 cm^2. The CV was performed using a system of three electrodes with HMs solution as the electrolyte. The prepared materials were utilized as the working electrodes, a KCl-saturated Ag/AgCl electrode was employed as the reference electrode, and a platinum plate served as the counter electrode. The prepared materials were observed at different scan rates. The prepared material's electrochemical impedance spectroscopy (EIS) was analyzed using a three-electrode system, similar to CV tests. The frequency ranges from 0.001 Hz to 10^6 Hz, with equivalent electrolyte

concentrations utilized for CV analysis, is also used for EIS measurement. During the EIS test, an AC amplitude of 10 mV was applied.

3.4.4 Analysis of elements in wastewater

The concentration of ions such as Cr, Cu, Ni, Zn, Cd, Pb, Fe, Se, As, Mn was determined by Inductively Coupled Plasma Optical Emission Spectrometry (Avio 200, PerkinElmer, USA). The analysis of SS and COD were determined following Standard Method 2540 D and 5220 D, respectively (Baird et al., 2017). The pH value was measured by a portable pH Starter300 meter (Ohaus Instruments, China).

3.4.5 Calculation

Adsorption amount (q, mg/g) of HMs and fabricated membrane was calculated as Equation 3.1.

$$q = \frac{(C_o - C_t).V}{m} \tag{3.1}$$

where C_o (mg/L) and C_t (mg/L) are a concentration of the initial time and a collected time of ion, respectively, V (mg/L) is the total volume of solution, and m (g) is the weight of both electrodes.

Pseudo-first order kinetic model for adsorption process in its nonlinear form is shown in Equation 3.2.

$$q_t = q_e.(1 - e^{k_1.t}) \tag{3.2}$$

Pseudo-second order kinetic model for adsorption process in its nonlinear form is shown in Equation 3.3.

$$q_t = \frac{q_e^2.k_2.t}{q_e.k_2.t + 1} \tag{3.3}$$

where q_e (mg/g) is adsorption amount of ion at equilibrium time and q_t (mg/g) is adsorption amount of ion at time t (min), k_1 (1/min) is a rate constant of pseudo-first order and k_2 (g/mg/min) is the rate constant of pseudo-second order.

Ion exchange capacity (IEC, meq/g) of the fabricated membrane was calculated as Equation 3.4.

$$IEC = \frac{(V_{NaoH}.C_{NaOH}) - (V_{HCl}.C_{HCl})}{m_{dry}} \quad (3.4)$$

where (V_{NaOH} (mL) and V_{HCl} (mL) are the used volume of NaOH and HCl, respectively, and C_{NaOH} (M) and C_{HCl} (M) are the concentrations of NaOH and HCl, respectively. While m_{dry} (g) is weight of the dry membrane.

Water content (WC, %) of the fabricated membrane was computed from Equation 3.5.

$$WC = \frac{m_{wet} - m_{dry}}{m_{dry}}.100 \quad (3.5)$$

where m_{dry} (g) and m_{wet} (g) are the mass of the membrane before and after swelling, respectively.

Specific capacitance (C_s, F/g) of prepared material was determined from the CV curve as Equation 3.6.

$$C_S = \frac{1}{2.m.v.\Delta V}.\int_{V_A}^{V_C} idV \quad (3.6)$$

where m (g) is weight of the prepared material, ν (V/s) is scan rate, ΔV (V) is recorded potential window, ∫idV is the integrated area of CV curve, and i (A) is the current.

Charge efficiency (CE, %), defined as the ratio of electrosorbed ions to the equivalent total charge, was calculated as Equation 3.7.

$$CE = 100\frac{q.n.F}{\int Idt.M} \tag{3.7}$$

where I (A/g) is the current density at time t, n is number of electron equivalents per mole ion, F is Faraday's constant (F = 96,485 C/mol e^{-}) and M is molar mass of ion.

Specific energy consumption (EC, J/g), which indicates the amount of energy used to produce a unit of product, is calculated as shown in Equation 3.8

$$EC = \int \frac{i.U}{q.m} dt \tag{3.8}$$

where U is the applied voltage (V), i (A) is current.

CHAPTER 4

RESULTS AND DISCUSSIONS

This chapter provides the results and discussions from experiments to improve the removal of HMs. Each test explored a different approach of HMs based on different CDI architectures. Furthermore, this chapter evaluates the feasibility of optimized CDI structures for practical use, particularly in electroplating wastewater treatment.

4.1 Removal of Cr ions utilizing integrated manganese dioxide nanostructures on activated carbon felt as electrode material in capacitive deionization

4.1.1 Physical properties of materials

4.1.1.1 Porosity and pore size distribution

The deposition of nano-MnO_2 on ACC via the hydrothermal method is supported by Figure 4.1. In Figure 4.1(a), the N_2 isotherms of both ACC and ACC/MnO_2 exhibit a distinctive S-shaped curve with no apparent hysteresis loop. According to the IUPAC classification, both prepared materials exhibit typical type-I isotherm, suggesting many micropores within the materials (Thommes et al., 2015a). Though the microporous surface area of materials exhibited type I isotherm by IUPAC classification, which is an essential factor in the adsorption process, it was observed that the adsorption behavior of these materials depends on the accessible micropore volume rather than the microporous surface area (Liu et al., 2016; Thommes et al., 2015a).

To explore the growth mechanism of nano-MnO_2 on ACC, Table A.1 (Appendix A) provides SSA and TPV values for MnO_2, ACC, and ACC/MnO_2. The BET analysis reveals that ACC has a significant specific surface area (SSA) and total pore volume (TPV), with values of 1316.2 m^2/g and 0.5638 cm^3/g, respectively. Notably, the pristine nano-MnO_2 indicates an impressively high TPV of 0.2427 cm^3/g. After the deposition process of nano-MnO_2 on ACC, ACC/MnO_2 exhibits a decrease in both SSA and TPV, measured at 1017.4 m^2/g and 0.4537 cm^3/g, respectively.

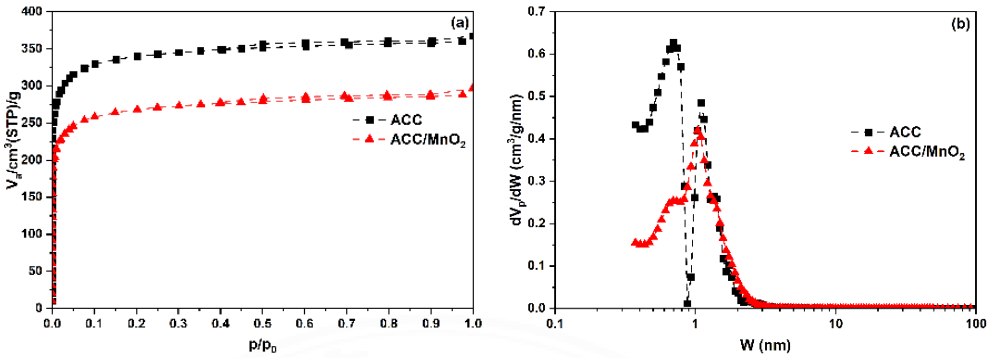

Figure 4.1 Characteristics of ACC and ACC/MnO_2 through (a) N_2 adsorption/ desorption isotherms, (b) Pore size distributions based on NLDFT/GCMC analysis.

The NLDFT/GCMC method was used to analyze the pore features of the material to explain the observed reduction in SSA and TPV of ACC/MnO_2 compared to ACC. The dVp/dW value, which exhibits the derivative of the pore volume concerning the pore width in NLDFT calculation, supports characterizing the PSD of materials based on N_2 adsorption/desorption isotherms data. Figure 4.1(b) shows that ACC/MnO_2 exhibits an extensively distinct dVp/dW value compared to ACC. The results indicated that pore volume varied with pore size among the prepared samples, corresponding to changes in SSA and TPV, as discussed. This occurrence is explained by the deposition and overlapping of nano-MnO_2 on the surface of carbon fiber. This process contributed to the occlusion of micropores within the material, consequently reducing TPV as observed by BET method. Besides, Figure 4.1(b) illustrates peak changes as supplementary characteristics in observing ACC/MnO_2 compared to ACC, which resulted in additional pores on the carbon fiber surface. Significantly, Table A.1 (Appendix A) reveals a decline in the TPV value based on NLDFT/GCMC method of ACC/MnO_2 compared to ACC in the microporous range (pore size < 2 nm), decreasing from 0.475 (cm^3/g) to 0.364 (cm^3/g). However, the TPV value in the non-microporous range increases notably from 0.040 cm^3/g (ACC) to 0.049 cm^3/g (ACC/MnO_2), which can be attributed to the presence of MnO_2 nanostructures. This phenomenon can be explained by the deposition of MnO_2 nanostructures, which forms a tunnel-like structure, as previously reported (Muraoka et al., 1999). This structure blocks certain

positions while also opening new active sites, resulting in increased pore volume in non-microporous regions and decreased volume in microporous regions. According to Deng et al. (2021), this structural feature created more active sites, making it easier for ions to stick to the surface fiber (Deng et al., 2021). Maintaining a controllable mesoporous pore distribution in electrode materials for electrosorption is crucial to enhance ion adsorption and stabilize the electrical double layer (Pengju Li et al., 2018). Despite their smaller specific surface areas, ACC/MnO_2 composites exhibit a more favorable pore morphology for adsorption performance than ACC.

The analysis of pore texture features supports the impact of MnO_2 nanostructure deposition on carbon fiber. The reduction in pore volume and specific surface area observed, along with the appearance of new pores in the non-microporous range of ACC/MnO_2, suggested that the addition of nano-MnO_2 has changed the pore properties of ACC. The nature of MnO_2 nanostructures is also explored by evaluating changes in the morphological and crystal structural characteristics of nano-MnO_2 deposited on ACC.

4.1.1.2 Morphological properties

Figure 4.2(a) presents the clear surface of carbon fiber, which is highly suitable to achieve improved adhesion and uniform coverage when grafting substrates or nanomaterials (Tan & Babel, 2023). Figure 4.2(b) displays the structural characteristics of pure MnO_2 nanorods generated using the hydrothermal technique without grafting on ACC. The shape of MnO_2 has a rod form, with sizes ranging from 60 to 90 nm and lengths reaching 750 to 1000 nm. The hydrothermal procedure yielded MnO_2 nanorods, showcasing its exceptional capability to control material morphology and its viability for extensive implementation. In addition, Figure 4.2(c) demonstrates the process of depositing MnO_2 nanorods onto carbon fiber using the hydrothermal method. It shows noticeable changes to the carbon fiber surface with a roughened structure caused by MnO_2 features.

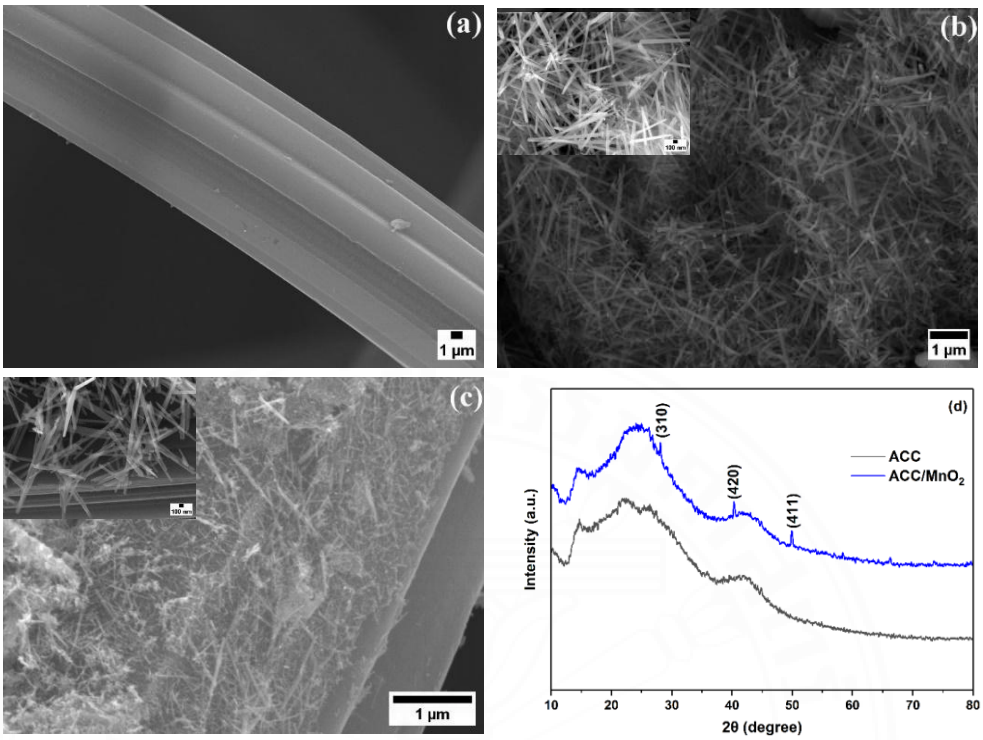

Figure 4.2 SEM image of (a) ACC, (b) MnO_2, (c) ACC/MnO_2, and (d) XRD patterns of ACC and ACC/MnO_2.

Figure 4.2(c) reveals densely packed MnO_2 nanorods covering the surface of carbon fiber, creating a highly porous network that significantly enhances the electrochemical properties of a material, as discussed in section 3.1.1. Figure 4.2(b and c), at high magnification (scale bar indicating 100 nm), shows that the MnO_2 structure resembles nanoneedles with numerous overlapping nanorods in multiple layers. Additionally, it demonstrates that adding MnO_2 nanorods to the carbon fiber does not alter the shape of MnO_2, as observed by comparing Figure 4.2(b and c). The structure of MnO_2 nanoneedle suggests that the deposition process is diffusion-controlled, typically resulting in the formation of dendritic nanostructures (Chen et al., 2012). Equation 4.1 illustrates the potential growth mechanism of MnO_2 nanoparticles during the hydrothermal process. Adding HCl to the carbon fiber surface activates nucleation sites, facilitating the formation and growth of MnO_2 crystallites. As the reaction proceeds, the length and porosity of the nanoneedles increase, causing internal stresses and subsequent detachment (Pengju Li et al., 2018).

$$2KMnO_4 + 8HCl \rightarrow 2MnO_2 + 2KCl + 3Cl_2 + 4H_2O \quad (4.1)$$

4.1.1.3 Crystal Structure Analysis

The crystal structural characteristics of both ACC and ACC/MnO_2 were studied by X-ray diffraction (XRD) patterns, as depicted in Figure 4.2(d). A peak at $2\theta \approx 24.0°$ indicates the existence of the (002) reflection, which shows the graphite crystallographic plane in the carbon fiber structure of ACC. Additionally, the broadened peak at $2\theta \approx 43°$, indicative of the (101) reflection, suggests a notable interlayer carbon condensation. The peak of ACC lacks a clear definition and shape, implying a significant degree of disorder in the carbon fiber within the structure of carbon material (Liu et al., 2016).

There are three distinct peaks visible in the XRD profile of ACC/MnO_2 at $2\theta \approx 29°$, 41°, and 49°. These peaks are associated with the (310), (420), and (411) reflections, which suggest the presence of the tetragonal crystalline phase related to α-MnO_2 (JCPDS Card no # 44 – 141) (Davoglio et al., 2018). Although the three minor peaks observed in the ACC/MnO_2 are small, they are attributed to the crystallographic planes of MnO_2. These observations suggest that the MnO_2 structure obtained via the hydrothermal method when combined with carbon fiber, either possesses minimal crystallinity or is predominantly amorphous in carbon fiber (Liu et al., 2016). As illustrated in Figure 4.2(a and c), grafting MnO_2 onto ACC via the hydrothermal method exhibits characteristics indicative of amorphousness on the surface of carbon fiber, which holds utility for capacitive charge storage. This is attributed to its ability to facilitate ion diffusion within the electrode materials by creating a mesoporous layer that directs ions to the microporous regions (Ahmed G. El-Deen et al., 2014; Liu et al., 2016). As mentioned in the previous section, this layer facilitates ion diffusion within the microporous regions of materials by establishing a mesoporous layer on carbon fiber to efficiently transport ions.

4.1.2 Electrochemical properties of materials

The presence of a specific Cr(VI) species in water is affected by chromium concentration and pH (Agrawal et al., 2008). In acidic conditions (pH < 6), bichromate ($HCrO_4^-$) prevails when Cr(VI) is less than 20 mM, shifting to dichromate ($Cr_2O_7^{2-}$) when Cr(VI) exceeds 20 mM. $Cr_2O_7^{2-}$ anion has less ability to reach all adsorption centers due to its larger volume than $HCrO_4^-$. Besides, the distribution of Cr(III) species is approximately 40% for Cr^{3+} and 60% for $Cr(OH)^{2+}$ at a pH of 4 (Leyva-Ramos et al., 1995). Consequently, a 50 mM Cr ion electrolyte at pH 4.0 was used to ensure comparable performance in CV and EIS tests.

The electrochemical behavior of ACC and ACC/MnO_2 in Cr solutions is presented in Figure 4.3, which displays the CV curves, a computed value of specific capacitance, and their impedance spectra (Nyquist plot). The CV curves derived from ACC/MnO_2 in Figure 4.3(a) exhibit distinct characteristics compared to those of pristine ACC, thereby emphasizing the notable influence of the grafted MnO_2 compared to ACC in both Cr(III) and Cr(VI). Figure 4.3(a) illustrates that the capacitance of ACC grafted with MnO_2, as indicated by the area of the CV curves, is more remarkable for ACC/MnO_2 than ACC. As discussed previously, the phenomenon is attributed to a larger mesoporous surface area with well-distributed and interconnected pores, enhancing ion storage capacity. This observation correlates with increased electrochemical activity, driven by MnO_2 nanorods that offer extra active sites [20]. Moreover, the electrochemical properties of electrodes are significantly influenced by the shape of the CV curve (Tan & Babel, 2023). As depicted in Figure 4.3(a), the CV curves at a scan rate of 1 mV/s display a leaf shape, indicating the absence of redox peaks. Results suggest that the capacitive behavior of materials is beneficial for ion storage.

Figure A.1 (Appendix A) presents CV curves at various scan rates for the prepared materials and Cr ions, revealing the presence of symmetric curves, indicating the high reversibility and reliability of the capacitive process. Noticeable changes in the leaf form were observed as the scan rate was improved. These changes were accompanied by a reduction in the area of the leaves regardless of the observed CV, as

presented in Figure A.1 (Appendix A). The shift in CV shapes can be explained by the reduced time available for Cr ions to be absorbed into the pores of both ACC and ACC/MnO_2 as the scan rate increases, leading to alterations in the CV shape. Furthermore, the presence of micropores on ACC limits the extent of ionic diffusion needed to reach these micropores. Because micropores restrict the amount of space available, they also limit the mobility of ions, making it harder for them to get in. Therefore, the Cr ions cannot spread widely into the pores of ACC and ACC/MnO_2, causing an overlapping electric double layer at the pore's entrance. As a result, it is observed in Figure 4.3(c) that the specific capacitance of the prepared material decreased as the scan rate was enhanced. As depicted in Figure 4.3(b), the specific capacitance of ACC/MnO_2 is 65.8 F/g, whereas ACC reached 31.5 F/g at a scan rate of 1 mV/s for Cr(VI). Additionally, ACC/MnO_2 demonstrates a greater capacitance than ACC at all scan rates for Cr solutions. The enhancement is attributed to the increased surface capacitance caused by the arrangement of MnO_2 nanorods on carbon fiber.

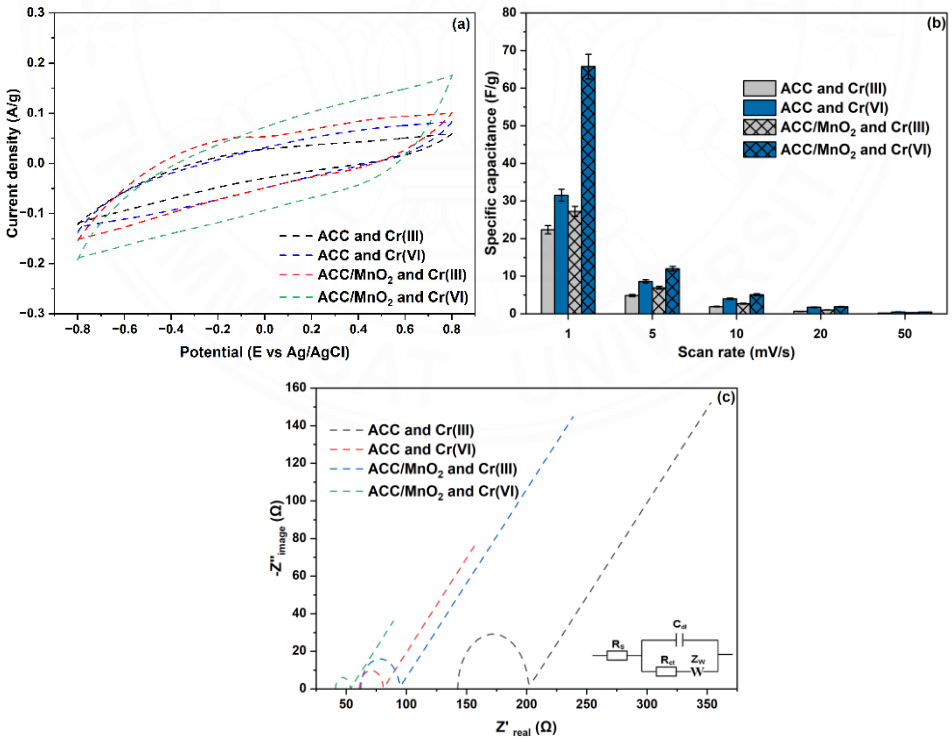

Figure 4.3 (a) Comparison of CV curves for ACC and ACC/MnO_2 electrodes in Cr(III) and Cr(VI) solution at a scan rate of 1 mV/s, (b) Specific capacitance of the

prepared electrodes and Cr ions at various scan rates, and (c) Impedance spectra (Nyquist plots) of the ACC, ACC/MnO_2 electrodes and Cr ions.

Despite the lack of detectable redox peaks in the CV test, the grafting of MnO_2 into ACC could participate in Faradaic charge transfer at the material's surface. It acts as a pseudocapacitor for H^+ ions existing in a Cr solution, as described by Equation 4.2 (Pengju Li et al., 2018). This study suggests that capacitive behaviors rather than Faradaic processes affect the electrochemical capacities. This positively impacts eliminating Cr(III) and Cr(VI) ions despite potential detrimental effects from Faradaic processes.

$$(MnO_2)_{surface} + H^+ + e^- \leftrightarrow (MnOO^-H^+)_{surface} \quad (4.2)$$

In Figure 4.3(c), the Nyquist diagram of ACC and ACC/MnO_2 for Cr(III) and Cr(VI) was used to plot the real and imaginary impedances. The charge transfer resistance (Rct) is the collective term for the combined resistance in the semi-circle, which includes the electrode resistance, the electrode and current collector contact resistances, and the electrolyte resistance within the electrode's porous structure (Liang et al., 2013). Figure 4.3(c) illustrates a reduction in charge transfer resistance (Rct) for ACC/MnO_2 compared to ACC in Cr solutions. The decrease in resistance was significant for Cr(III), going from 58.3 Ω to 31.7 Ω, and slight for Cr(VI), reducing from 19.6 Ω to 15.2 Ω. It suggests that MnO_2 nanostructures on the carbon surface resulted in a reduction in Rct. Moreover, the intersection of Zreal and Zimage aids in determining the series resistance (Rs), encompassing bulk electrolyte, electrode, and electrode-current collector contact resistances. Based on the data presented in Figure 4.3(c), it is evident that the prepared material exhibits a significant series resistance of more than 40 Ω. There is a significant ionic resistance for Cr(III) and Cr(VI), while the contact resistance between the active material and current collectors is likewise high. On the other hand, ACC/MnO_2 exhibits a noticeably lower intercept with the Zreal at high frequency when compared to ACC in both Cr solutions. Therefore, ACC/MnO_2

exhibits excellent capacitive behavior, resulting in a highly efficient CDI process with less energy consumption. Moreover, the superior interfacial contact and increased contact area significantly improve the electrode's electrical conductivity, effectively compensating for the low conductivity of carbon. A straight line in the low-frequency region resembles Warburg diffusion.

Based on the EIS measurements, it is evident that ACC exhibits a high Rct in the Cr solution. When MnO_2 is grafted onto ACC, there is a noticeable decrease in Rct for Cr solutions. This decrease is more significant for Cr ions, indicating improved ion transfer because of MnO_2 nanostructures. ACC/MnO_2 exhibits superior charge transfer resistance to pristine ACC in Cr solutions. Moreover, MnO_2 deposition on carbon fiber enhances Cr(III) transfer more effectively than Cr(VI) due to the cationic nature of Cr(III) compared to the anionic properties of Cr(VI).

4.1.3 Adsorption experiments for Cr

pH is a crucial parameter that influences both adsorbent surface properties and the ionic forms of ions in the solution (Gheju et al., 2016; Jain et al., 2009). Figure A.2(a) (Appendix A) presents the PZC of ACC and ACC/MnO_2. It reported that the adsorbent surface is positively charged when Δ pH is lower than the solution pH and negatively charged when Δ pH exceeds the solution pH (Cristiano et al., 2011). In Figure A.2(a) (Appendix A), ACC exhibited a PZC at a pH of 4.7, whereas ACC/MnO_2 displayed a PZC of 5.1. Integrating MnO_2 into ACC resulted in a significant alteration of the surface material properties. Notably, the Δ pH of ACC was – 0.19, whereas ACC/MnO_2 exhibited – 0.83 at a pH of 4.0. The higher Δ pH value of ACC/MnO_2 compared to ACC at a pH of 4.0 indicates more significant proton (H^+) absorption due to MnO_2 integration. This is attributed to increased H^+ intercalation sites facilitated by MnO_2, altering surface properties and enhancing H^+ attraction, as presented in Equation 4.2.

4.1.3.1 Effects of pH and initial concentration of Cr(VI) ions

pH fluctuations substantially influence critical parameters of adsorption, including surface charge, ionization degree, and adsorbate speciation, profoundly impacting the adsorption capacity of Cr species (Bharath et al., 2019; Wang et al., 2013). Figure 4.4(a) presents the impact of pH changes on Cr(VI) adsorption capacity at 1000, 500, and 200 mg/L over 24 h. The influence of the adsorbent's surface characteristics on the Cr(VI) adsorption is apparent. As previously mentioned, ACC displayed a cationic charge when the pH was between 2 and 4.7, then converted to an anionic charge when the pH was more significant than 4.7. As a result, the adsorption favorability of Cr(VI) on ACC increased from pH 2 to 4.7 but later declined. At a pH of 2, the adsorption capacity on ACC for Cr(VI) at a concentration of 1000 mg/L was 33.8 mg/g. It increased to 39.4 mg/g at pH 4 but declined to 19.9 mg/g and 13.4 mg/g at pH 6 and 8, respectively. ACC material's adsorption capacity peaked at a pH of 4, consistent with its highest PZC value, enhancing its ability to adsorb anionic Cr(VI) species via electrostatic interaction. At pH levels 6 and 8, ACC material's surface charge became negatively charged, diminishing its ability to adsorb Cr(VI).

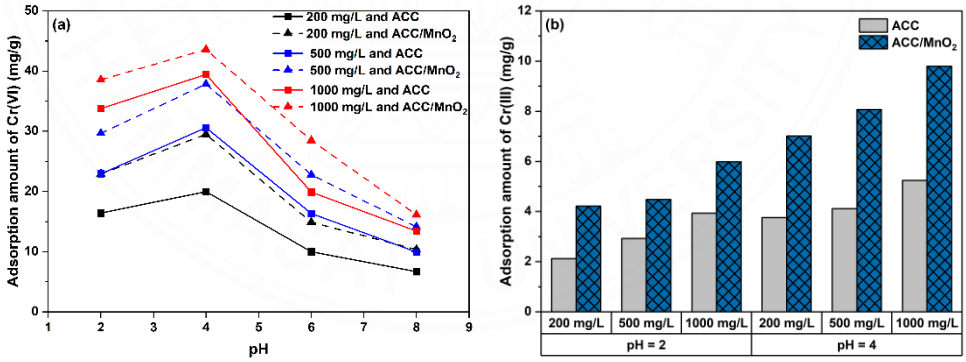

Figure 4.4 Adsorption capacity of (a) Cr(VI), (b) Cr(III) by ACC and ACC/MnO_2 at different pH.

The adsorption capacity of ACC/MnO_2 was shown to be pH-dependent, complying with a similar trend as ACC. At a Cr(VI) concentration of 1000 mg/L, ACC/MnO_2 exhibited an adsorption capacity of 38.6 mg/g at pH 2, increasing to 43.6 mg/g at pH 4. Subsequently, the adsorption capacity dropped to 28.5 mg/g and 16.1

mg/g at pH 6 and 8, respectively. This trend remained constant in all experiments involving different ACC and ACC/MnO_2 at concentrations. The adsorption efficiency was highest at the initial pH of 4.0 for both ACC and ACC/MnO_2. This trend can be attributed to several factors. First, the shift in solution pH from 2.0 to 8.0 promotes the reaction, as shown in Equation 4.3 (Gheju et al., 2016), resulting in a change in the surface charge of the material from quasi-neutral to strongly negative. As a result, the electrostatic repulsion forces between Cr(VI) oxyanions and the negatively charged MnO_2 surface rise with higher pH, which reduces the adsorption capacity.

$$MnOH + HO^- \Leftrightarrow MnO^- + H_2O \quad (4.3)$$

Second, the reduced efficiency of Cr(VI) removal in both ACC and ACC/MnO_2 becomes worse by the weakened electrostatic forces between the adsorbent and adsorbate caused by the abundance of OH^- ions at a higher pH solution. H^+ ions enhance adsorbent surface protonation in acidic conditions, facilitating electrostatic attraction with Cr (VI) as $HCrO_4^-$ ions. When the pH increases, fewer H^+ ions lead to less adsorbent protonation. As a result, the adsorption capacity of Cr (VI) decreases. Third, adsorption efficiency is impacted by the specific types of Cr(VI) anions in the solution. At pH levels ranging from 2 to 6, when the concentration of Cr(VI) is less than 20mM, the bichromate ion ($HCrO_4^-$) becomes more dominant than $Cr_2O_7^{2-}$ (Agrawal et al., 2008). Due to their higher volume than $HCrO_4^-$, $Cr_2O_7^{2-}$ has a reduced ability to access all adsorption centers. Besides, chromate (CrO_4^{2-}) becomes increasingly common near pH 8.0. Because certain anions require different numbers of positively charged centers for adsorption in both ACC and ACC/MnO_2, it becomes clear that a higher pH level reduces the number of available positive centers, affecting adsorption capacity.

The adsorption capacity of ACC and ACC/MnO_2 improved as the initial Cr(VI) concentration increased, ranging from 200 mg/L to 1000 mg/L. According to Gheju et al. (2011), the $HCrO_4^-$ oxyanion can undergo dimerization to produce the dichromate oxyanion, $Cr_2O_7^{2-}$, within a pH range of 2 to 6, which is represented by Equation 4.4

(Gheju, 2011). Based on Le Châtelier's principle, when the $HCrO_4^-$ concentration increases, the equilibrium (4) is shifted to the right, leading to a higher concentration of $Cr_2O_7^{2-}$. However, the higher concentration of Cr(VI) increased the concentration gradient at the interface between the Cr(VI) solution and the material (Baral et al., 2006). As a result, this raised the likelihood of collisions and mass transfer, leading to a higher adsorption capacity with increased concentrations.

$$HCrO_4^- + HCrO_4^- \Leftrightarrow Cr_2O_7^{2-} + H_2O \quad (4.4)$$

This study reveals that ACC/MnO_2 exhibits a superior adsorption capacity, regardless of concentrations and pH, compared to pure ACC. Figure A.2(b) (Appendix A) shows the presence of hydroxyl and carboxyl groups on ACC via FTIR measurements. Notably, some functional groups, like hydroxyl and carboxyl groups, were found to have a pronounced effect on the adsorption of Cr(VI) (Du et al., 2015). They could facilitate the exchange or interaction with $Cr_2O_7^{2-}$ or $HCrO_4^-$ ions in Cr(VI) solutions. Du et al. (2015) discovered that the adsorbed Cr(VI) behaves similarly to CrO_3 on MnO_2–deposite- based material (Du et al., 2015). Additionally, Li et al. (2023) found that nano-MnO_2 involves the reduction of Cr(VI) to yield Cr(III) through reduction, electrostatic adsorption, and complexation precipitation mechanisms (Li et al., 2023). Cr(VI) predominantly presents as an anion attracted by abundant H^+ ions via electrostatic forces. Nano-MnO_2 serves as electron donors, reducing Cr(VI) to Cr(III), which then complexes with oxygen-containing functional groups for immobilization. Consequently, $Cr(OH)_3$ precipitates may form on material surfaces during Cr(VI) removal. These processes can be represented by the following Equation from (4.5) to (4.9) (Li et al., 2023).

$$Cr_2O_7^{2-}(aq) + 14H^+ + 6e^- \rightarrow 2Cr^{3+}(aq) + 7H_2O \quad (4.5)$$

$$3Mn^{2+} + CrO_4^{2-} + 6H^+ H_2O = 3Mn^{3+} + Cr^{3+} + 8OH^- \quad (4.6)$$

$$3Mn^{3+} + CrO_4^{2-} + 6H^+ H_2O = 3Mn^{4+} + Cr^{3+} + 8OH^- \quad (4.7)$$

$$3Cr^{3+} + 6OH^- = Cr_2O_3 + 3H_2O \quad (4.8)$$

$$3Cr^{3+} + 6OH^{-} = Cr(OH)_3 + 3H_2O \quad (4.9)$$

4.1.3.2 Effects of pH and initial concentration of Cr(III) ions

Cr(III) ions may result in various complexes in aqueous solution, including Cr^{3+}, $Cr(OH)^{2+}$, $Cr(OH)_2^{+}$, $Cr(OH)_3^{0}$, $Cr(OH)_4^{-}$, and $Cr_3(OH)_4^{5+}$ (Fahim et al., 2006; Leyva-Ramos et al., 1995). When the pH is below 2, chromium primarily exists as Cr^{3+}, while both Cr^{3+} and $Cr(OH)^{2+}$ coexist as the pH rises to 4, and chromium precipitates as $Cr(OH)_3$ at near neutral pH (Blázquez et al., 2009; Fahim et al., 2006). Leyva-Ramos et al. (1995) reported that activated carbon material effectively adsorbs Cr(III) within the pH range of 2 to 6.4, with minimal adsorption at a pH of 2 (Leyva-Ramos et al., 1995). This study observed precipitation in the Cr(III) solution at all concentrations when the pH was adjusted to 6.0 without the absorbent. Besides, it was observed that Cr(III) did not adsorb to the activated carbon matrix in a strongly acidic solution (Fahim et al., 2006; Leyva-Ramos et al., 1995). Then, adsorption experiments for Cr(III) were conducted at pH of 2.0 and 4.0.

Figure 4.4(b) shows that ACC adsorbed 2.1 mg/g of Cr(III), while ACC/MnO_2 exhibited a higher capacity of 4.2 mg/g at 200 mg/L and pH 2. This consistent trend was maintained at all levels of concentration. They enhanced the pH and improved adsorption for both ACC and ACC/MnO_2, with ACC/MnO_2 exhibiting improved adsorption abilities compared to ACC. As previously explained, both ACC/MnO_2 and ACC exhibited a net positive charge at a pH of 4, while the pH of 2 displayed a neutral charge. This observation can be attributed to several factors in the adsorption capacity of Cr(III). Firstly, the adsorption capacity of carbon material is impacted by the distribution of Cr(III) species (Fahim et al., 2006). In aquatic environments, Cr^{3+} was recorded at a pH of 2, yet the primary form in which Cr(III) is adsorbed is Cr^{3+} and $Cr(OH)^{2+}$ at a pH of 4. A change in pH causes an increase in adsorption capacity due to the prevalence of the $Cr(OH)^{2+}$ species in the Cr(III) solution. Secondly, excess H_3O^{+} ions in solution at a low pH level compete with Cr(III) for surface space on ACC and ACC/MnO_2, resulting in reduced Cr(III) ion adsorption compared to a pH of between 2 and 4. Thirdly, as the pH increases from 2.0 to 4.0, both ACC and ACC/MnO_2 acquire

a more positive charge, which weakens their attraction to positively charged Cr(III) ions. However, the increase in pH could potentially boost the deprotonation of specific functional groups on ACC and ACC/MnO_2, resulting in negatively charged sites that can attract Cr(III) ions (Dehouli et al., 2010). Notably, Blázquez et al. (2009) found that the retention of Cr(III) ions on absorbent is primarily due to the ionic attraction between metal ions and the carboxylic group of absorbent (Blázquez et al., 2009). Additionally, integrating MnO_2 nanostructures onto ACC reduced the surface area, concomitantly leading to new pores on the ACC/MnO_2 surface, as previously mentioned. Through this change, the adsorption process of ACC/MnO_2 becomes more efficient, which could increase the adsorption capacity of modified ACC, as previously discussed.

4.1.4 Studies on capacitive deionization for Cr

4.1.4.1 Electrosorption kinetics models of Cr

Kinetic models, pseudo-first order (PFO) and pseudo-second order (PSO), were utilized to assess the adsorption process of Cr ions on the prepared electrodes in the CDI cell, providing insights into equilibrium time and adsorption mechanisms. Figure 4.5(a and b) illustrate the adsorption amounts of Cr ions on ACC and ACC/MnO_2 at 200, 500, and 1000 mg/L, respectively, under a potential of 1.2 V in the CDI cell for 120 min. Figure 4.5 indicates a significant rise in the adsorption capacity with improving concentrations of Cr ions. Moreover, it reveals that Cr(VI) has a more incredible adsorption amount than Cr(III), and ACC/MnO_2 composite has a greater adsorption capacity than ACC regardless of concentration. Specifically, at 200 mg/L of Cr(III), ACC/MnO_2 removed 8.4 mg/g, surpassing ACC's adsorption amount of 6.1 mg/g. Similarly, the adsorption amount of ACC/MnO_2 achieved 30.6 mg/g compared to ACC's 25.3 mg/g at 1000 mg/L of Cr(VI). Moreover, higher concentrations led to increased adsorption amounts for both materials. For instance, at 1000 mg/L of Cr(III), adsorption amounts of ACC and ACC/MnO_2 reached 8.8 mg/g and 13.2 mg/g, respectively, while adsorption amounts of ACC and ACC/MnO_2 reached 50.0 mg/g and 71.6 mg/g, respectively, at 1000 mg/L of Cr(VI).

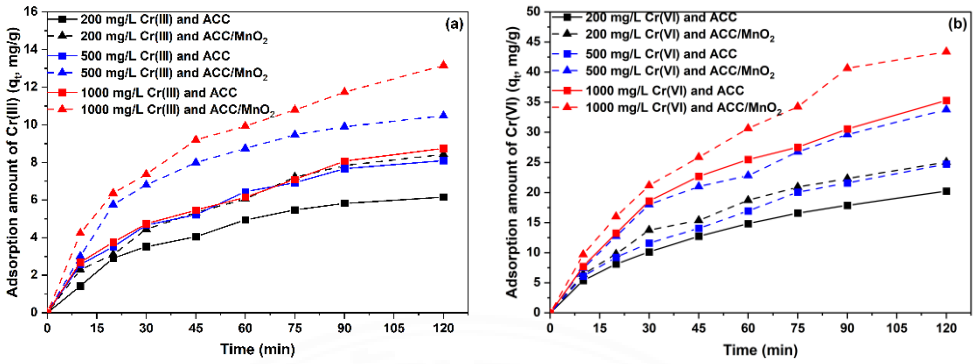

Figure 4.5 Adsorption amount of (a) Cr (III), (b) Cr(VI) in CDI cell at different concentrations at 1.2 V.

Additionally, Table A.2 (Appendix A) shows a strong correlation between the PSO model and the experimental data for Cr solutions on ACC and ACC/MnO_2. This provides evidence of potential chemical sorption or chemisorption. In contrast to the PFO model, the PSO model showed exceptional performance in describing the results of the CDI tests. This was evident from the high R-squared (R^2) values, which approached 0.99. This finding is consistent with previous observations, indicating that the PSO model offers a more comprehensive representation of the entire adsorption process of HMs (Wu et al., 2009). The results presented here confirm the reliable adsorption capacities discussed previously. The result supports previous research on the characterization of PSO for the adsorption of Cr species (Gheju et al., 2016; Li et al., 2023; Samaraweera et al., 2020).

Both ACC and ACC/MnO_2 exhibit distinct characteristics in their ability to adsorb Cr ions. The discrepancy primarily arises from ion charges and the involvement of other surface oxides in the elimination of ions. Several factors contribute to the efficiency of the adsorption process, including the charge and size of the ions being exchanged, along with the presence of surface oxides possessing distinctive properties (Blázquez et al., 2009). Additionally, the ionic radii of Cr(III) and Cr(VI) are measured as 0.0615 nm and 0.044 nm, respectively (Coskun et al., 2018). At pH of 4, Cr(III) species exist as Cr^{3+} and $Cr(OH)^{2+}$, whereas Cr(VI) species are present as $Cr_2O_7^{2-}$ and $HCrO_4^-$. This leads to the Cr(VI) species having a higher propensity to infiltrate

microporous materials in the presence of an electric field in the charging phase, in contrast to their Cr(III) counterparts. Furthermore, the enhanced adsorption capacity for Cr(VI) resulting from its reduction to Cr(III) through reduction mechanisms, as previously stated in this study.

4.1.4.2 CDI tests for electrosorption and regeneration of Cr

Figure 4.6 reveal that ACC/MnO_2 consistently outperforms ACC, showing higher adsorption amounts under all potentials for Cr solutions. At 0.6 V, the adsorption capacity of Cr(III) is 2.0 mg/g for ACC/MnO_2 and 1.4 mg/g for ACC; for Cr(VI), the adsorption amount is 7.4 mg/g for ACC/MnO_2 and 6.4 mg/g for ACC. This superior performance is attributed to MnO_2 nanorod grafting onto carbon fiber, enhancing adsorption capacity. Additionally, the recovery rates also favor ACC/MnO_2, with Cr(III) recovery rates of 70.5% and 67.5% and Cr(VI) recovery rates of 62.7% and 68.3% at 1.2 V for ACC/MnO_2 and ACC, respectively, as shown in Figure 4.7. The adsorption capacity and recovery rate of prepared materials were improved by increasing the potential. A stronger electric field at higher voltages enhances ion mass transfer to the electrode surfaces, increasing the likelihood of contact between Cr ions and the electrode surface (Liu et al., 2016). Due to this, there is a notable improvement in adsorption efficiency. Results suggest the potential of ACC/MnO_2 for efficient removal and recovery of Cr ions, offering promising applications in carbon fiber using MnO_2 nanostructures.

Unfortunately, the adsorption capacity and recovery rate with ACC and ACC/MnO_2 decreased from the 5th cycle to the 10th cycle in Cr solutions. The adsorption amount and recovery rate for Cr(VI) of ACC/MnO_2 in the 5th cycle were 8.5 mg/g and 68.3%, respectively, while these values in the 10th cycle had decreased to 7.9 mg/g and 63.3%, respectively. The decline in performance can be attributed to the incomplete recovery of active sites on the electrode, potential alterations in structure, or degradation caused by the sorption or chemisorption of Cr ions onto the carbon fiber's surface, as previously discussed.

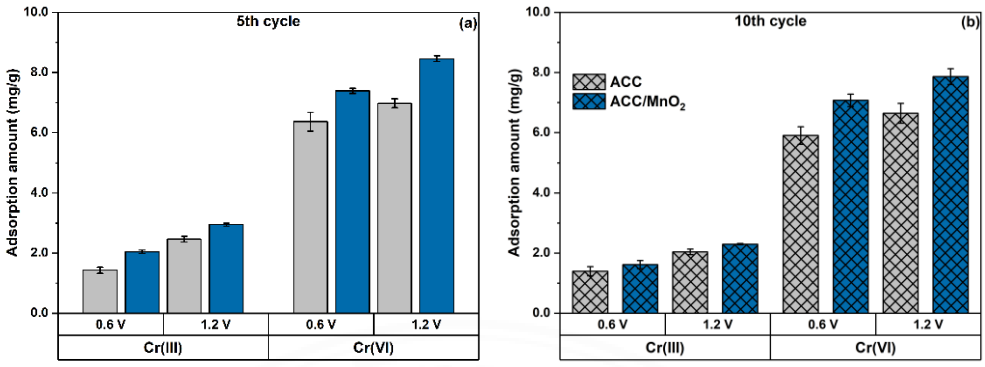

Figure 4.6 Adsorption amount of Cr(III) and Cr(VI) at a) 5th cycle, b) 10th cycle of ACC and ACC/MnO_2.

Figure 4.7 exhibits consistently higher recovery rates for Cr(III) compared to Cr(VI) despite the variation not being notable. For instance, the recovery rates for Cr(III) with ACC and ACC/MnO_2 were 67.4% and 70.5%, respectively, while Cr(VI) recorded recovery rates of 62.5% and 68.3%, respectively. The inherent properties of the Cr species account for the difference in recovery rates. Cr(VI) tends to undergo reduction reactions in favorable conditions, which can result in the formation of Cr(III) precipitates or their incorporation into the adsorbent matrix, as mentioned before (Du et al., 2015; Li et al., 2023). This delays the release or renewal of Cr ions, which impacts the overall recovery process. Reducing Cr(VI) to Cr(III) minimizes the amount released from the adsorbent surface, decreasing the recovery efficiency. Additionally, the adsorption capacity of Cr(III) is mainly influenced by electrostatic interactions between Cr(III) species and the adsorbent, contributing to its higher recovery rate compared to Cr(VI). The presence of MnO_2 in the ACC matrix holds promise for an enhanced recovery rate due to its pristine properties. These enhancements, such as changes in the surface area of the mesoporous region and improved modified surface, enhance the recovery rate (Hou & Huang, 2013; Liu et al., 2016). Highly porous activated carbon captures ions through its capacitance, with pseudocapacitive charge storage reaction of MnO_2 nanostructures further enhancing this process (Guo et al., 2016; Xiao et al., 2010).

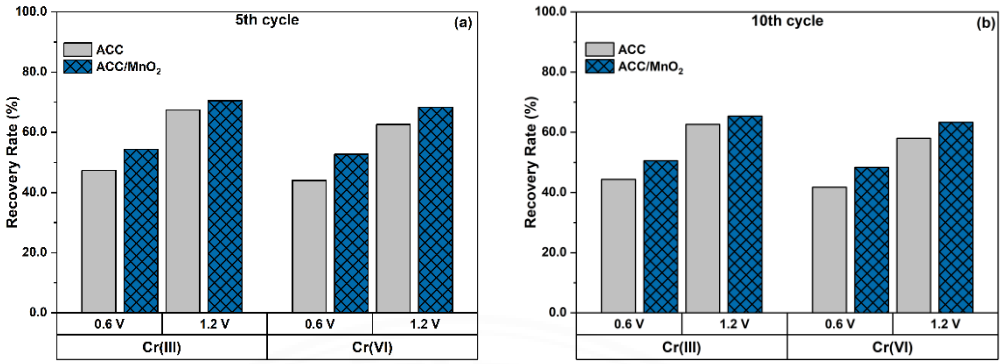

Figure 4.7 Recovery rate of Cr(III) and Cr(VI) at a) 5th cycle, (b) 10th cycle of ACC and ACC/MnO_2.

4.1.5 Conclusions for Cr removal

Using hydrothermal method, the ACC/MnO_2 material was successfully synthesized by grafting MnO2 nanorods onto activated carbon cloth (ACC). The material's capacitance is significantly increased by grafting MnO_2 nanostructures onto the activated carbon fiber. Results exhibit a noteworthy enhancement in the capacitance of ACC/MnO_2 (65.8 F/g) compared to pristine ACC (31.5 F/g) when employed in a Cr(VI) solution. The enhanced performance is attributed to the substantial presence of MnO_2 nanostructures on the surface of the carbon fiber, which provides an extra number of active sites for ion storage. The alteration resulted in increased effectiveness in getting rid of both Cr species. Both ACC and ACC/MnO_2 demonstrated excellent results in removing Cr(VI) compared to Cr(III) under identical circumstances. In the 5th cycle, ACC/MnO_2 showed a higher adsorption amount for Cr(VI) (8.5 mg/g) compared to Cr(III) (3.0 mg/g). Additionally, the ACC/MnO_2 adsorption amount in the charging phase reached 7.9 mg/g, which was more significant than pristine ACC (6.7 mg/g) to eliminate Cr(VI) during the 10th cycle at a voltage of 1.2 V. Furthermore, the recovery rate for Cr(III) with ACC is higher at 67.4% compared to Cr(VI), which recorded a recovery rate of 62.5%. As the potential increased, the Cr species' adsorption capacity and recovery rate increased.

4.2 Enhancing the removal of Ni^{2+} through the fabrication of heterogeneous membranes as cation exchange membranes in membrane capacitive deionization

4.2.1 Properties of fabricated membranes

4.2.1.1 Functional groups on the membranes

FTIR analysis identified functional groups on the membranes, as illustrated in Figure 4.8. Some peaks were observed due to chemical elements by PEG and PVDF. The peak characteristics of PVDF are identified by peaks at wavenumbers of 1400 cm^{-1} (the deformation vibration of CH_2 linked with CF_2), 1180 cm^{-1} (stretching vibration of CF_2), and 875 cm^{-1} (C–H wagging) (Daems et al., 2018). Additionally, the recognition at 840 cm^{-1} band of CH_2 rocking of PEG, PVDF (Vrandečić et al., 2010).

Upon grafting resins onto the mixture solution, four identifiable peaks appear visible compared to membrane M0 and other membranes (M5 - M20). The identifiable peaks observed at wavenumbers of 1007 cm^{-1} and 1035 cm^{-1} for symmetric stretching vibrations and 1128 cm^{-1} for asymmetric stretching vibrations can be attributed to the identifiable O=S=O bond vibration (Daems et al., 2018; Strasheim & Buijs, 1961). Furthermore, an additional peak is observed at a wavenumber of 675 cm^{-1}, implying the existence of the S–O stretching mode (Strasheim & Buijs, 1961). A relatively broad band followed at approximately 3460 cm^{-1}, as shown in Figure 4.8, was assigned to the bending vibration of the OH^- group, forming a noticeable membrane M20. This contribution was caused by the hydrogen bond interaction between the H_2O molecule and the oxygen atom of the sulfonic acid group (Gonzalez et al., 2010). The results provided compelling evidence for the existence of sulfonic acid functional groups within the cation exchange resins, and the intensity of these peaks heavily increased as the resin proportion in the membrane increased.

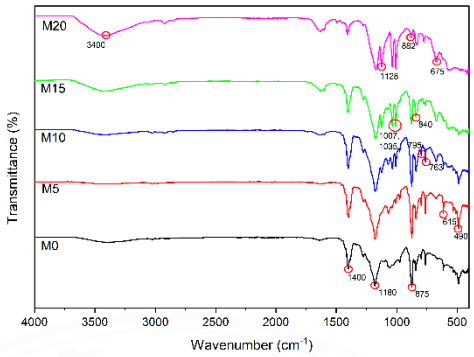

Figure 4.8 FTIR spectra of the prepared membranes (M0, M5, M10, M15 and M20).

Besides, distinct peaks existed in the prepared membranes, particularly at 615 cm^{-1} and 490 cm^{-1} wavenumber. The intensities of these peaks exhibited a decrease from membrane M0 to the absence of these two peaks in membrane M20, as presented in Figure 4.8. The peak at 615 cm^{-1} is attributed to a mixed mode of CF_2 bending and CCC skeletal vibration, whereas the 490 cm^{-1} band is associated with bending and wagging vibrations of the CF_2 group, ascribed to the α phase PVDF (Lanceros-Méndez et al., 2007). Also, the bending vibration peak of CF_2 at 875 cm^{-1}, present in membranes M0 to M15, shifted to a higher wavenumber of 882 cm^{-1} in membrane M20, implying that there was the dipole interaction between the SO_3^- group in cation exchange resins and CF_2 dipoles. In addition, it observed that PVDF, with a molecular formula of $(–CH_2–CF_2–)_n$, is a polymer existing in various crystalline phases. In this study, PVDF is attributed to the α phase, characterized by a non-polar crystalline structure. The IR spectra presented in Figure 4.8 illustrate α phase PVDF backbone peaks, including the 840 cm^{-1} band corresponds to CH_2 rocking, which arose from the rocking vibrations of CH_2 groups, and the CF_2 symmetric stretching of CF_2 groups within the α phase PVDF backbone (at 763 cm^{-1}) (Cai et al., 2017). Furthermore, a peak at 795 cm^{-1} indicated CH_2 deformation, originating from the deformation vibrations of CH_2 groups in the α phase PVDF backbone (Cai et al., 2017); however, this peak is absent in membrane M20, similar to the CF_2 peak, which implied the dipole interactions between the sulfonic acid group in cation exchange resins and PVDF on the membrane.

Consequently, a membrane structure exhibiting interfacial bonding with the cation exchange resins was established.

The FTIR spectra revealed a strong proficiency in recognizing the presence of the sulfonic acid group in cation exchange resins and its interaction with basic chemicals within the membrane matrix structures. By combining this analysis with a study of the membrane's surface morphology, the impact of cation exchange resins on the membrane surface needs to be clarified, which will provide an adequate understanding of its role.

4.2.1.2 Membrane morphology

Images of the prepared membranes via SEM and AFM techniques were used to examine the surface features in various CER contents. Figure 4.9 depicts the surface morphology (SEM analysis) and the 3D surface profiles (AFM analysis) of the prepared membranes M0, M5, M10, M15, and M20.

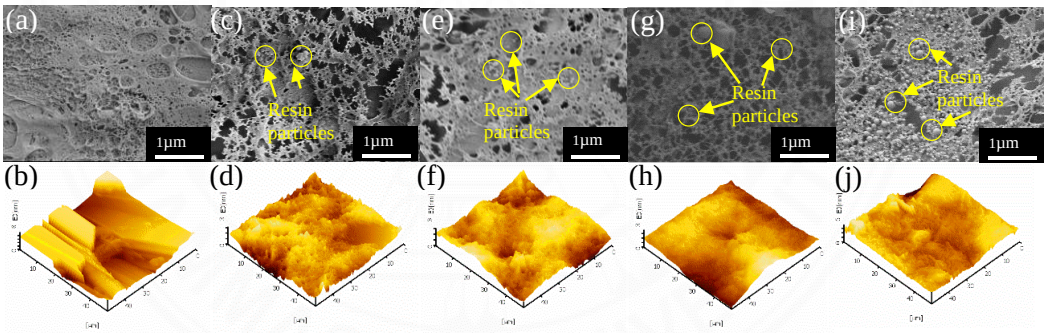

Figure 4.9 SEM image (scale bar = 1 µm) and the 3D surface profile of membrane M0 (a, b), membrane M5 (c, d), membrane M10 (e, f), membrane M15 (g, h), and membrane M20 (i, j), respectively.

In Figure 4.9(a), membrane M0 revealed an uneven surface with a wide range of hole sizes on the membrane surface and a spatially heterogeneous distribution of surface pores, represented as black holes. Once the resins were onto the membranes, ranging from 5% to 20% by weight for membranes M5 to M20, the density of CER particles on the surface increased noticeably, as demonstrated in Figure 4.9(c, e, g, and i). The prepared membranes' 3D surface profile (AFM measurement) exhibited

similarities to SEM results, as shown in Figure 4.9(b, d, f, h, and j). Increased CER loading resulted in the efficient filling of voids and a change in surface roughness, explored in the next section. Figure 4.9(i) revealed that the amount of cation exchange resins in the dope solution attained 20% by weight (membrane M20), and there was a substantial distribution of CER particles per unit of area in comparison to membranes (M0 – M15). The CER particles on the membrane performed exceptionally well as conducting regions compared to membrane M0 (without resins), thereby efficiently facilitating ion transfer and limiting co-ion phenomena across the membrane.

The topography parameters, including R_a (roughness average of a surface) and R_{MS} (root mean square of a surface), were measured to gain the surface roughness of the membranes. Table 4.1 indicated that membrane M0 (without cation exchange resins) had exhibited significantly larger R_a and R_{MS} values, measuring 1852 nm and 2199 nm, respectively, than the other membranes (membrane M5, M10, M15, and M20), indicating its rough membrane surface characteristics, as presented in Figure 4.9. The integration of PEG into the matrix of the dope solution resulted in enhanced porosity and pore formation on the membrane (Fadaei et al., 2014; Pei et al., 2010). While PVDF is recognized as the polymer-rich phase, the introduction of hydrophilic PEG reduces the thermodynamic stability of the dope solution, thereby facilitating phase separation into a polymer-poor phase (PEG), forming valleys, and a polymer-rich phase (PVDF) surrounding these valleys as peaks (Pei et al., 2010). This phase separation phenomenon led to peak and valley areas forming on the membrane surface, contributing to the surface roughness. The rise in cation exchange accompanied the increase in R_a and R_{MS} values resin loading from 5% to 20% by weight, attributed to the integration of resins into the membrane matrix. As depicted in Figure 4.9, the resin particles significantly escalated the irregularity of the membrane surface. Notably, the surface roughness of the membranes M5, M10, M15 and M20 was less than that of the membrane M0, as shown in Table 4.1. As discussed, cation exchange resins, a crosslinked polymer with negatively charged structural moieties, tended to interact with the CH_2 dipoles of the PVDF. Furthermore, the utilization of PEG resulted in forming a pore-like structure, as discussed in the phase separation phenomenon, which exerted

a force compelling the deposition of resins onto these pores. With the deposit of cation exchange resins on the membrane, a portion of resin particles filled the pores formed by PEG, resulting in a roughness of the manufactured resins lower than that of membrane M0. An increase in membrane roughness was reported due to the excessive inclusion of resins, as exhibited in Table 4.1.

Table 4.1 Roughness average, root mean square of a membrane surface, water content, and ion exchange capacity value of the prepared membranes (M0, M5, M10, M15 and M20).

Membrane	Roughness average (R_a, nm)	Root mean square (R_{MS}, nm)	Water content (%)	Ion exchange capacity (meq/g)	Water contact angle (^{o})
M0	1852	2199	40.28	0.12	$77.86^o \pm 1.85^o$
M5	342.8	439.6	58.99	0.88	$102.43^o \pm 2.19^o$
M10	414.4	509.1	69.27	1.20	$103.45^o \pm 1.35^o$
M15	514.9	656.7	72.43	1.43	$106.01^o \pm 1.28^o$
M20	757.1	970.9	76.58	1.62	$113.52^o \pm 2.16^o$

4.2.1.3 Wettability property of membrane surface

The wettability property of the membrane surface is determined using the water contact angle to obtain the formation of resins on the membrane surface, as provided in Table 4.1. The combination of PEG and PVDF in the membrane structure causes the membrane surface to become hydrophilic (Pei et al., 2010); this study shows that membrane M0 has a hydrophilic feature on the membrane surface. The water contact angle of membrane surface M0 was $77.86^o \pm 1.85^o$. As observed in Table 4.1, upon the resins being added to the dope solution, the water contact angle of the prepared

membrane increased considerably, higher than 90º. The water contact angles on the membrane surface of M5, M10, M15, and M20 were 102.43º ± 2.19º, 103.45º ± 1.35º, 106.01º ± 1.28º, and 113.52º ± 2.16º, respectively. The grafting of cation exchange resins into a membrane containing sulfonic acid groups was known to enhance the hydrophilic properties of the membrane, as discussed in the following section; however, an unexpected increase in the water contact angle measurement on the membrane surface was observed. The origin of the increased water contact angle in measurement on the membrane surface might be related to many factors. Firstly, as discussed, a portion of the resin particles occupied the pores formed by PEG, impacting the membrane surface's wettability. A greater amount of resin resulted in the greater filling of the pores, resulting in a higher water contact angle. Secondly, as discussed in the previous section, the interaction between cation exchange resins and PVDF may lead to the emergence of hydrophobic elements on the membrane surface, resulting in an enhanced water contact angle. Thirdly, according to the data in Table 4.1, introducing cation exchange resins caused peaks and valleys in the topography, thereby influencing the water contact angle measurement.

4.2.1.4 Water content and ion exchange capacity of the membrane

Table 4.1 shows the prepared membranes' ion exchange capacity and water content values. Membrane M0 revealed a comparatively low level of water content (40.28%) and ion exchange capacity (0.12 meq/g). The PEG incorporation in the dope solution created holes or microvoids in the membrane matrix, enabling the membrane to retain more water molecules than the pristine PVDF's inherent hydrophobic nature (Hosseini et al., 2014). The ion exchange capacity and the water content of the prepared membrane (M5, M10, M15 and M20) increased proportionally to the amount of resin present on the membranes, with ion exchange capacity values increasing from 0.88 meq/g to 1.62 meq/g and the water content increasing from 58.99% to 76.58% as the quantity of cation exchange resins risen from 5% to 20% by weight. Introducing resin particles into the membrane matrix resulted in the formation of polymer structure irregularities, creating additional water pockets, which increased the ion exchange

capacity and the water content (Kumar et al., 2014). Increasing the ratio of cation exchange resins resulted in a higher density of ionic functional groups, specifically the sulfonic acid group, facilitating an enhanced ion exchange capacity and making it more straightforward for ions to migrate through the membrane.

4.2.2 Electrode material properties

The activated carbon cloth (ACC) material possesses a complex structure consisting of several functional groups and interconnected pores. The FTIR measurement was conducted to analyze the presence of functional groups in the ACC material, as shown in Figure 4.10(a). A prominent peak was observed in the wavenumber range of 3200 – 3650 cm^{-1}, displaying an extensive transmission band with its highest intensity at 3430 cm^{-1}. The broad transmission band was likely caused by the O – H stretching mode attached to the ACC structure or moisture adsorbed on its surface. An observable low-intensity transmission band was consecutively detected at 3780 cm^{-1} and 3710 cm^{-1}, attributed to free O–H functional groups (Ali et al., 2020). Additionally, there were two consecutive small peaks at approximately 2919 cm^{-1} and 2851 cm^{-1}, suggesting the existence of asymmetric and symmetric C–H stretching vibrations(Pradhan & Sandle, 1999). Notably, the most substantial peak at 2354 cm^{-1} was attributed to the –OH bond of carboxylic groups (Lota et al., 2016), whereas the peak at 1587 cm^{-1} represented the stretching vibration of the C = O group in carboxylic groups (Lota et al., 2016; Pradhan & Sandle, 1999). The recorded peak at 1220 cm^{-1} corresponded to the C – O stretching band found in acids and esters (Lota et al., 2016). Further, broadband associated with the coupled vibrations of C-H bending in the carbon structure and physiosorbed CO_2 appeared at around 618 – 676 cm^{-1} (Ali et al., 2020).

The adsorption process is significantly influenced by surface area, pore diameter, and pore volume. These factors can impact the quantity of sites available for ions to be adsorbed on the electrode, thereby influencing the electrosorption performance. As classified by IUPAC, the ACC material exhibits a type-I isotherm in Figure 4.10(b), with no hysteresis in nitrogen adsorption-desorption observed. This result implies the abundant presence of micropores in the ACC material. Moreover,

Figure 4.10(b) illustrates that most of the total pore volume is derived from micropores, as indicated by the pore size distribution (inset). The value of total pore volume and specific surface area of the ACC material were determined to be 272.7 cm^3/g and 1187 m^2/g, respectively. It was reported that the absorption process is influenced by the volume of micropores rather than the internal surface area within the context of a typical type-I isotherm (Thommes et al., 2015b). The ACC material primarily comprises micropores and a high surface area. This aspect could restrict ion diffusion within the electrode structure, leading to a prolonged duration required to reach equilibrium (Han et al., 2019; Peng et al., 2011). Thus, the electrochemical properties of the ACC material are analyzed to gain insights into its interactions with Ni^{2+} using a CV test and EIS test.

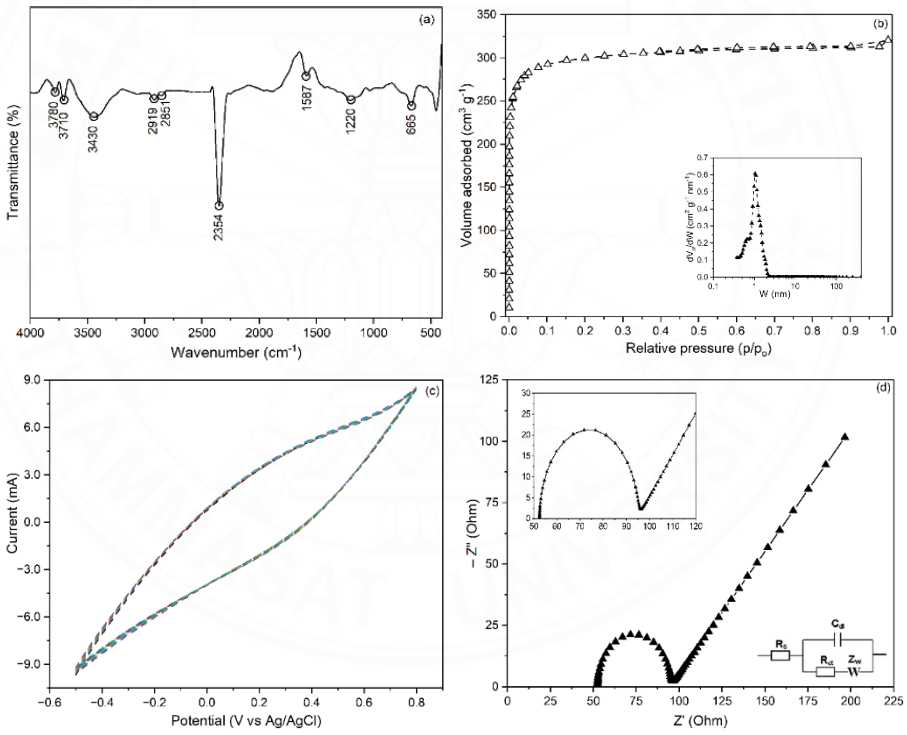

Figure 4.10 (a) FTIR spectra of ACC, (b) N_2 adsorption/desorption isotherm and the pore size distribution (inset) of ACC, (c) Cyclic voltammetry of ACC at a scan rate of 5 mV/s, and (d) Nyquist plot of electrochemical impedance spectroscopy spectra of ACC with circuit diagram.

Figure 4.10(c) illustrates CV curve obtained with a scan rate of 5 mV/s for 20 scan cycles. The shape of the CV curve was known to have a considerable effect on the

electrochemical properties of the electrodes. The CV leaf-shaped pattern observed in Figure 4.10(c) provides strong evidence of a highly reversible electrochemical process. The leaf-shaped pattern is caused by the carbon material's high porosity and internal resistance (Singh et al., 2021). As known, the ion capture mechanisms on the electrode material play an essential role in the CDI process. No notable electrochemical responses were observed at a scan rate of 5 mV/s for the reduction of Ni^{2+} to Ni, as observed in Figure 4.10(c). The CV curve at this scan rate exhibits a consistent and continuous pattern, indicating non-Faradaic reactions on the ACC material. The ACC material used in this study indicates capacitive properties in accordance with the electric double-layer mechanism rather than involving intercalation or deintercalation processes associated with Faradaic reactions. It implies that it is favourable to consider employing it for HMs removal. Alternatively, the recorded capacitance of Ni^{2+} on the ACC material is of interest. At scan rates of 5 mV/s, 10 mV/s, and 25 mV/s, specific capacitance values were measured as 10.61 F/g, 4.19 F/g, and 1.23 F/g, respectively. With a higher scan rate, the contact time for Ni^{2+} ions to enter the micropores of ACC material is shortened, leading to their inability to reach the active sites of the material. Thus, the incomplete utilization of the porous space leads to decreased specific capacitance.

Besides, EIS analysis yields crucial information about the behavior of the interface between the ACC material and Ni^{2+} solution. Figure 4.10(d) displays the Nyquist plot of the ACC material, accompanied by an inset showing the fitted equivalent circuit. The primary two regions of the plot are a semi-circular in the high-frequency region and a straight line in the low-frequency region. First, the solution resistance, represented as the x-intercept in the region with the highest frequency, is known as the bulk electrolyte resistance (Yang et al., 2017). The value of the solution resistance was found to be 52.5 Ω, which was ascribed to the aspects of the Ni^{2+} solution integrated into the ACC material. Next, a charge transfer resistance, consisting of electronic and ionic resistance components, occurs in the semi-circular region (Yang et al., 2017). While the electronic resistance consists of the intrinsic resistance of the ACC material and the contact resistance between the active layer and current collector, the ionic resistance is the resistance to the movement of the ionic electrolyte inside the

inter-particle pores structures of ACC material (Mei et al., 2017; Yang et al., 2017). This study revealed the value of a charge transfer resistance to be 42.4 Ω. Finally, the linear trend in the low-frequency region is similar to the ion diffusion process referred to as Warburg diffusion. The result reveals that the ACC material exhibited a relatively high charge transfer resistance, which can be explained as follows. Under the impact of an electric field, ions migrate towards the porous structures of the electrode material through macropores, functioning as reservoirs to minimize the space between ions and micropores. Afterwards this, the ions undergo mesopores, which includes several activity sites, prior to entering micropores (Han et al., 2019). As discussed earlier, there is a significant existence of micropores within the ACC material. Therefore, it could reduce the transport of Ni^{2+} ions going to micropores in ACC material. The small number of macropores and mesopores within the electrode material, acting as a bridge, poses a challenge in facilitating ion access to micropores. Due to the limited access of ions to the micropore, there is a competition among numerous ions for the available space, which ultimately restricts charge transfer. As a result, the resistance for charge transfer increased, and the specific capacitance of the electrode was not very impressive as observed. This phenomenon becomes visible at high scan rates due to the limited diffusion caused by an abundant presence of micropores.

The CV test in the potential window of -0.5 V to 0.8 V revealed the absence of Ni^{2+} reduction peaks. However, it was found a tiny deposition of Ni^{2+} on the surface of the activated carbon fiber during the electrosorption (Xue et al., 2022). The presence of $Ni(OH)_2$ species on carbon fiber was confirmed by the equation 4.10. Furthermore, it was noted that the functional groups on activated carbon fiber are likely responsible for the Ni^{2+} adsorption. The formation of chemical bonds between Ni^{2+} ions and oxygen functional groups on ACC material, such as R−O, −COO, and C−O−C, was found after the adsorption process (Liu et al., 2015). In addition, the H^+ ions in carboxylic and phenolic groups could participate in ion exchange activities, leading to the formation of carbonyl-Ni complexes by the exchange reaction of Ni^{2+} with H^+ (He et al., 2022; Liu et al., 2015). In this study, the FTIR analysis revealed the presence of surface oxygen-containing functional groups of the ACC material. Despite the absence of

specific peaks related to the reduction of Ni^{2+} in the CV result, it is noteworthy that the existence of functional groups, as discussed earlier on the activated carbon fiber, potentially influences the adsorption process of Ni^{2+}.

$$Ni^{2+} + 2OH^{-} \rightarrow Ni(OH)_2\downarrow \quad (4.10)$$

4.2.3 Studies on capacitive deionization for Ni^{2+}

As previously mentioned, a comprehensive examination of the membrane parameters revealed that membrane M20 exhibits superior characteristics compared to the other membranes. Hence, membrane M20 was chosen in the MCDI cell. The CDI cell and MCDI cell were compared to understand the roles of the prepared membrane (M20) and a commercial anion exchange membrane (MCDI-M20) in the CDI process.

To determine whether membrane M20 facilitated enhanced Ni^{2+} mobility in the MCDI system or Ni^{2+} adsorption onto the membrane, the adsorption capacity of Ni^{2+} on the membrane was tested without applied voltage. Figure B.1 (Appendix B) revealed a Ni^{2+} adsorption amount on a membrane of 1.55 mg/g membrane. Results with the applied voltage, as shown in Table B.1 (Appendix B), suggested that the utilization of membrane M20 facilitated the promotion of the Ni^{2+} across the membrane in the MCDI system, contributing to the improvement of CDI performance, which was superior to the adsorption mechanism of Ni^{2+} caused by the resin onto the membrane (zero voltage).

In Figure 4.10(a), the CV test observes no peaks relating to a redox process between the ACC electrode and the Ni^{2+} solution at a scan rate of 5 mV/s. Furthermore, interactions between Ni^{2+} and the charged functional groups on the prepared membrane M20 occur via a non-electron transfer process. Therefore, the kinetic model was utilized to understand the equilibrium time and the adsorption mechanism, with a particular emphasis on the role played by the prepared membrane. This study employed a PFO model to determine parameters for the adsorption of Ni^{2+} by an ACC electrode in the CDI cell and the MCDI-M20 cell. The results in Table B.1 (Appendix B) suggest the PFO model was a good fit for describing the CDI tests, as evidenced by the high R-

squared (R^2) values approaching 0.99. This result is consistent with findings from prior studies (Iftekhar et al., 2017; Xue et al., 2022). Consequently, it was used to determine the estimated equilibrium adsorption value in both the CDI cell and MCDI-M20 cell, as integrated in Figure 4.11.

4.2.3.1 Electrosorption kinetics models of Ni^{2+}

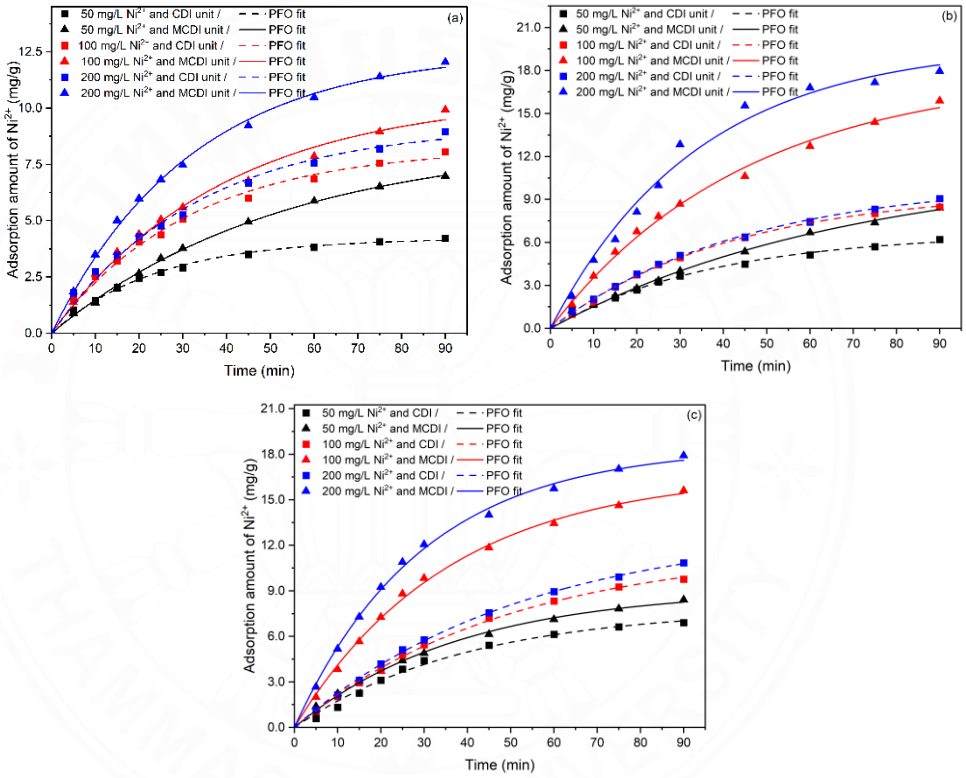

Figure 4.11 Adsorption behaviour of Ni^{2+} at flow rates of (a) 5 mL/min, 10 mL/min (b), and (c) 15 mL/min for Ni^{2+} concentrations of 50 mg/L, 100 mg/L, and 200 mg/L in the CDI cell and MCDI-M20 cell.

Figure 4.11 exhibits the adsorption amount of Ni^{2+} at various flow rates (5 mL/min, 10 mL/min, and 15 mL/min) for different Ni^{2+} concentrations (50 mg/L, 100 mg/L, and 200 mg/L) in the CDI cell and MCDI-M20 cell. Based on the experimental data in Figure 4.11 and the estimated equilibrium Ni^{2+} adsorption value in Table B.1 (Appendix B), an enhancement in the Ni^{2+} adsorption amount was found as the increased Ni^{2+} concentration in the observed CDI cells at the same flow rate. Figure

4.11 exhibited notable differences between the CDI cell and MCDI-M20 cell in the adsorption process and efficiency over time. Both the CDI cell and the MCDI-M20 cell exhibit an evident increase in adsorption capacity, with the MCDI-M20 cell continually showing higher adsorption levels than the CDI cell. This trend became notably apparent when the concentration of Ni^{2+} reached 200 mg/L during the experiments. The comparative analysis of the CDI cell and the MCDI-M20 cell reveals a difference in the adsorption process at the same observed time, as presented in Figure 4.11(a). At the point of 20 min, the adsorption amount for the CDI cell was 2.45 mg/g ACC, 4.05 mg/g ACC, and 4.29 mg/g ACC while the MCDI-M20 cell exhibited adsorption amounts of 2.65 mg/g ACC, 4.40 mg/g ACC, and 5.99 mg/g ACC for initial Ni^{2+} concentrations of 50 mg/L, 100 mg/L, and 200 mg/L at flow rate of 5 mL/min, respectively. This consistent trend demonstrates that the ion exchange membranes incorporated into the MCDI-M20 cell result in superior adsorption efficiency and stability compared to the CDI cell. Figure 4.11(a) illustrates that at Ni^{2+} concentrations of 50 mg/L and 100 mg/L, there were no significant differences in adsorption amount between the CDI cell and the MCDI-M20 cell during the initial 20-min interval. In contrast, the MCDI-M20 cell's adsorption amount significantly surpassed that of the CDI cell at the concentration of 200 mg/L before the end of 20 min. This phenomenon can be attributed to the Ni^{2+} concentration in solution, which was influenced by numerous causes. Initially, a limitation factor observed in utilizing ion exchange membranes concerns the restriction of ion transport. This limitation encompasses the resistance posed by the diffusion boundary layer and the membrane resistance itself (Długołęcki et al., 2010). It was proved that the resistance of the ion exchange membranes exhibited a significant rise as the molar concentration gradually decreased, particularly at low NaCl concentration (lower than 0.1 M), which is attributed to the resistance of the diffusion boundary layer (Długołęcki et al., 2010). In this study, the Ni^{2+} concentrations of 50 mg/L, 100 mg/L, and 200 mg/L were converted to molar concentrations of 0.323 mM, 0.646 mM, and 1.292 mM Ni^{2+}, respectively. Secondly, the absence of ion exchange membranes in the CDI cell may facilitate the easy access of Ni^{2+} to the surface of the ACC electrode at low concentrations compared to the MCDI-M20 cell. The CDI cell facilitated rapid ion

transport and direct adsorption on the electrode surface in the initial stage instead of overcoming the resistance of the membrane. Thirdly, once the ions concentration in the solution was enhanced, a large number of ions rapidly reached the ion exchange membranes, thereby improving their capacity to efficiently convey ions to the electrode under the impact of the electric field in the CDI system, which contributed to an improvement in adsorption time in the initial stage, as observed. Similar to the flow rate of 5 mL/min as presented in Figure 4.11(a), the results obtained from Figure 4.11(b) and Figure 4.11(c) also demonstrated consistent findings about the impact of concentrations on adsorption performance at flow rates of 10 mL/min and 15 mL/min, respectively. It is consistently observed that the MCDI-M20 cell employing an ion exchange membrane displays a better adsorption amount than the CDI cell when subjected to the same testing circumstances. Nevertheless, significant differences emerged in the duration, mainly when dealing with more significant concentrations and an increased flow rate.

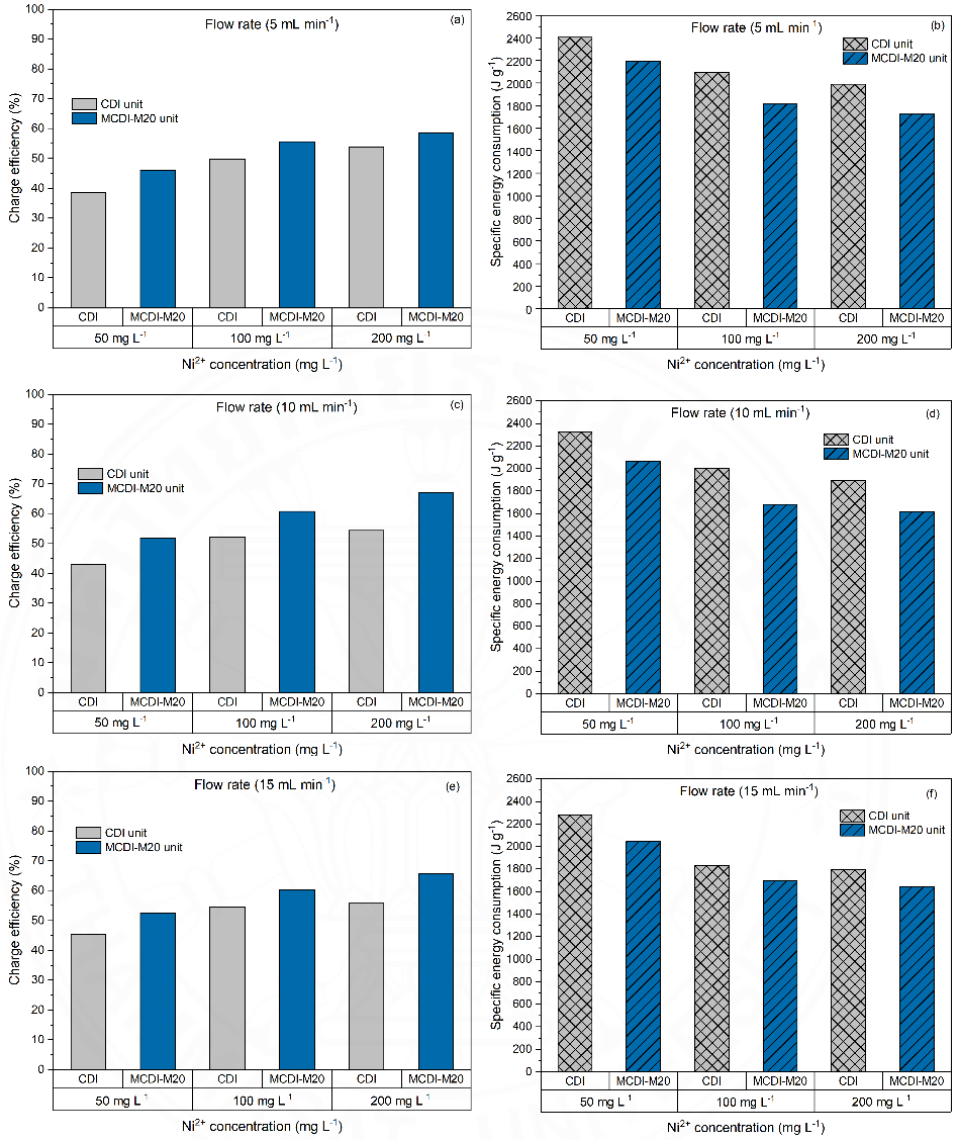

Figure 4.12 Charge efficiency and specific energy consumption at flow rates of 5 mL/min (a, b), 10 mL/min (c, d), and 15 mL/min (e, f) for Ni^{2+} concentrations of 50 mg/L, 100 mg/L and 200 mg/L in the CDI cell and MCDI-M20 cell.

Besides, the success of ion removal in the MCDI system is affected by flow rates (Pastushok et al., 2019). Table B.1 (Appendix B) reveals that the MCDI-M20 cell consistently exhibits higher adsorption levels than the CDI cell across various flow rates while maintaining the same Ni^{2+} concentration. For example, when operated at a flow rate of 5 mL/min for 90 min, the MCDI-M20 cell exhibited an adsorption amount of

8.57 mg/gACC, while the CDI cell achieved a lower adsorption amount of 4.22 mg/gACC at the 50 mg/L. It implies that the addition of ion exchange membranes enhanced the adsorption efficiency of the MCDI cell. On the other hand, the enhanced flow rate resulted in improved MCDI-M20 cell adsorption performance. For instance, at a concentration of 100 mg/L, the Ni^{2+} adsorption amount was 10.55 mg/gACC at a flow rate of 5 mL/min, while the Ni^{2+} adsorption amounts were 17.87 mg/gACC and 16.75 mg/gACC at a flow rate of 10 mL/min and 15 mL/min, respectively. The diffusion boundary layer resistance decides the significant resistance of the membrane instead of its membrane resistance at low concentrations (Długołęcki et al., 2010). As a result, an enhancement in the flow rate reduces the thickness of the diffusion boundary layer that forms at the interface of the ion exchange membrane (Choi et al., 2002; Długołęcki et al., 2010). The observed enhancement in adsorption amount at different concentrations in the MCDI-M20 cell can be ascribed to an increase in flow rates, implying an increase in the ion mobility across the membrane. However, a few studies found a relationship between the increase in flow rate and the resulting alteration in adsorption efficiency (Mossad & Zou, 2012; Pastushok et al., 2019), and it was found in this study. A slight alteration in adsorption efficiency was observed after the expansion of the flow rate from 10 mL/min to 15 mL/min. Specifically, the adsorption amount of Ni^{2+} was 12.56 mg/gACC at a flow rate of 5 mL/min, and at a flow rate of 10 mL/min was 19.80 mg/gACC, whereas it measured 18.49 mg/gACC at a flow rate of 15 mL/min. The phenomenon ascribed to an increased flow rate, which led to less contact time for the essential mass transfer processes between the membrane and the Ni^{2+} ions.

Some studies have focused on enhancing the adsorption efficiency in removing Ni^{2+} through the CDI process. Integrating a multi-walled carbon nanotube electrode into a CDI cell achieved an adsorption capacity of 8.49 mg/g (Iftekhar et al., 2017). Another study utilized modified activated carbon treated with nitric acid, resulting in an adsorption amount of 14.91 mg/g (Xue et al., 2022). Using the nanostructured α-MnO_2/Carbon paper composite electrode in CDI cell achieved an adsorption amount of 16.40 mg/g (Pengju Li et al., 2018). This study, employing the membrane M20 in MCDI cell, revealed an extensive enhancement in adsorption capacity to 19.80

mg/gACC. The findings indicate the promising potential of using a membrane M20 in the MCDI cell, which improves the adsorption capacity compared to modified electrode materials.

Figure 4.12(a, c, and e) shows values of the charge efficiency obtained under different Ni^{2+} concentrations (50 mg/L, 100 mg/L, and 200 mg/L) at flow rates of 5 mL/min, 10 mL/min, and 15 mL/min for CDI cell and MCDI-M20 cell, respectively. It reveals that the charge efficiency of the CDI cell and MCDI-M20 cell is affected by flow rates and Ni^{2+} concentrations. Figure 4.12(a) reveals a distinct shift in charge efficiency trends for the CDI cell and MCDI-M20 cell as Ni^{2+} concentration increased. For example, the charge efficiency of the CDI cell was increased from 38.5% to 53.8%, and the MCDI-M20 cell was improved from 45.9% to 58.6% as Ni^{2+} concentration enhanced from 50 mg/L to 200 mg/L. This trend remained consistent at flow rates of 10 mL/min and 15 mL/min, as depicted in Figure 4.12(c and e). Notably, the MCDI-M20 consistently exhibited superior charge efficiencies compared to the CDI cell across various concentrations. At 10 mL/min, the charge efficiency of MCDI-M20 attained 66.9% at 200 mg/L Ni^{2+}, outperforming 54.3% of the CDI cell. It implies that higher Ni^{2+} concentrations enhance charge efficiency when combined with the prepared membrane in the MCDI cell. Results suggest that controlling the flow rate and concentration enhances charge efficiency in CDI cells.

The charge efficiency in CDI cell was significantly less than the MCDI-M20 cell in this study. There are several pathways influencing the charge efficiency in the CDI system (Shang et al., 2017). They reported that the primary cause of inefficiency in the CDI cell was the effect of co-ion repulsion, severely restricting the total amount of used charge. Utilizing ion exchange membranes in the MCDI cell selectively allows cations to pass through the membrane toward the electrodes, effectively preventing the co-ion effect (Shang et al., 2017). Although introducing ion exchange membranes in the MCDI cell leads to increased internal resistance system and energy consumption (Kalfa et al., 2020; Zhao et al., 2013), charge efficiency in the MCDI-M20 shows improvement. Apart from the co-ion phenomenon in the CDI cell, various factors could contribute to the loss of charge efficiency, such as current leakage due to Faradaic

reactions, ion residue in the flow channel and effluent (Shang et al., 2017). Therefore, a further comparison of specific energy consumption in the CDI cell and MCDI-M20 cell was conducted to clarify the performance difference.

The specific energy consumption for different Ni^{2+} concentrations (50 mg/L, 100 mg/L, and 200 mg/L) at flow rates of 5 mL/min, 10 mL/min, and 15 mL/min in the CDI cell and MCDI-M20 cell is illustrated in Figure 4.12(b, d, and f), respectively. The specific energy consumption between the MCDI-M20 and CDI cells is a noticeable distinction. The MCDI-M20 cell consumed 1616.0 J/g, whereas the CDI cell consumed 1894.9 J/g at a Ni^{2+} concentration of 200 mL/L and a flow rate of 10 mL/min. The energy required to address the "co-ion phenomenon" exceeds the energy loss caused by the ion exchange membranes (Zhao et al., 2013). While integrating ion exchange membranes into the MCDI-M20 cell contributes to increased internal resistance in the reactor, the specific energy consumption of the MCDI-M20 cell is lower than that of the CDI cell, which is an economic advantage of the system. The CDI system's feed concentrations and flow rates influence the specific energy consumption. With the Ni^{2+} concentration changing from 50 mg/L to 200 mg/L, the MCDI-M20's specific energy consumption changed from 2279.0 J/g to 1642.3 J/g at a flow rate of 15 mL/min.

A study of adsorption amount, charge efficiency, and specific energy consumption reveals differences in the CDI cell and the MCDI-M20 cell. The MCDI-M20 cell offers significantly superior performance compared to the CDI cell. This indicates that integrating the prepared membrane into the CDI cell potentially enhances efficiency.

4.2.3.2 CDI tests for electrosorption and regeneration of Ni^{2+}

Figure 4.13 displays the Ni^{2+} adsorption amount and recovery rate in CDI cells, as determined by different potentials across several cycles. Figure 4.13(a and c) indicates that the CDI cell consistently has the lowest Ni^{2+} adsorption compared to a commercial cation exchange membrane used in membrane capacitive deionization (MCDI-CEM) cell and membrane M20 used in membrane capacitive deionization (MCDI-M20) cell, regardless of the applied voltages (0.6 V and 1.2 V). This trend

remained consistent in the following cycles from the 3rd cycle to the 6th cycle and 9th cycle for both observed potentials. As shown in Figure 4.13(a), during the 3rd cycle at a potential of 0.6 V, the CDI cell recorded 2.15 mg/gACC of Ni^{2+}, whereas the MCDI-CEM and MCDI-M20 cells achieved much higher adsorption amounts of 4.06 mg/gACC and 3.42 mg/gACC, respectively. Similarly, the same trend was observed at potentials of 1.2 V, as shown in Figure 4.13(c). The adsorption capacities increased with increasing voltage. By increasing the applied voltage, the electric field in a pair of electrodes became much more potent, which led to a noticeable increase in ion movement from the Ni^{2+} solution to the interfaces of the electrode material, resulting in higher adsorption capacity. During the 9th cycle at an applied voltage of 1.2 V, the adsorption capacities were 2.96 mg/gACC, 4.84 mg/gACC, and 5.57 mg/gACC, for the CDI cell, MCDI-M20 cell and MCDI-CEM cell, respectively. Figure 4.13(a and c) indicates an enhancement in the adsorption efficiency of the MCDI-M20 cell compared to the CDI cell at both potentials.

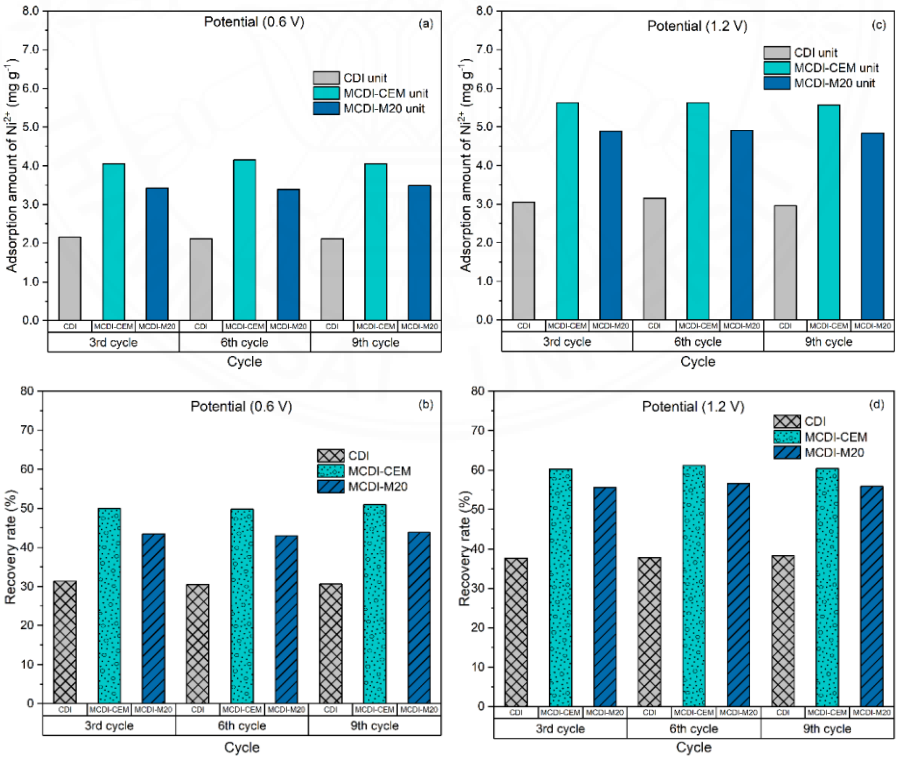

Figure 4.13 Adsorption amount and recovery rate of Ni^{2+} at potential of 0.6 V (a, b) and 1.2 V (c, d) in CDI cell, commercial cation exchange membrane used in

membrane capacitive deionization (MCDI-CEM) cell and membrane M20 used in membrane capacitive deionization (MCDI-M20) cell at 3rd, 6th and 9th cycle.

Figure 4.13(b and d) depicts the Ni^{2+} recovery rate from the tests at potential 0.6 V and 1.2 V over several cycles. Consistent trends in recovery rates were observed for each CDI cell at both potentials. In Figure 4.13(b), the average recovery rate of the CDI cell achieved 30.8%, whereas MCDI-CEM demonstrably outperformed with 50.2% and MCDI-M20 exhibited 43.4%. Furthermore, Figure 4.13(b and d) depicts that higher applied voltage corresponds to an increased Ni^{2+} recovery rate in CDI cells.

The performance of both MCDI-CEM and MCDI-M20 cells surpasses that of the CDI cell, which is attributed to ion exchange membranes. In the MCDI process, ion exchange membranes may act as barriers, impeding co-ions' access to the electrodes and preventing adsorptive reversal during the discharge phase (Yang et al., 2020). Using ion exchange membranes in the MCDI cell increases the required energy and hinders the release of Ni^{2+} back into the solution during the discharge phase. On the other hand, the MCDI-M20 cell presents lower adsorption capacity and recovery rate results than the related MCDI-CEM cell. The possible reason may be that the prepared membrane exhibits substantial water uptake, and the water molecules occupy a portion of the membrane volume. This impedes the rate at which other ions can be absorbed during the charging phase or regenerated in the discharging phase in the MCDI-M20 cell. Furthermore, the membrane's mechanical properties could change due to water uptake, subsequently affecting the membrane's electrical resistance. As a result, the extraction of ions from a heterogeneous membrane demands more energy than its counterpart. These factors may explain why the adsorption amount and recovery rate of Ni^{2+} did not match its counterpart. However, it was observed that the prepared membrane contributed to an enhanced performance of the CDI process, with the adsorption capacity and recovery rate of the MCDI-M20 cell being higher than that of the CDI cell. Furthermore, the findings suggest that the performance of the MCDI-M20 cell remained stable during the observed 9 cycles for the adsorption and recovery of Ni^{2+}.

4.2.4 Conclusions for Ni^{2+} removal

In summary, membranes were prepared under different weight percentages of resins added to the dope solution using the non-solvent-induced phase inversion technique, precisely at 5%, 10%, 15%, and 20% weights, and without resins. After optimizing cation exchange resins grafting into the membrane matrix, the resulting membrane was utilized for the CDI system. It was revealed that resin loading substantially affected the membrane structural properties and considerably enhanced the efficiency of Ni^{2+} removal in the CDI system. The identification of peaks corresponding to sulfonic acid groups served as evidence for the existence of cation exchange resins in the membrane structure, and the intensity of these peaks increased directly in proportion to the weight of the resins added to the membrane. The arithmetic mean roughness increased from 342.8 nm to 757.1 nm, corresponding to resin loadings from 5 to 20 wt%. In conjunction with the increased resin concentration, ion exchange capacity and membrane surface water content were increased. The analysis of the effect of Ni^{2+} concentrations and flow rates on the CDI system using membrane M20 revealed its roles in the CDI cell. The MCDI-M20 cell consistently exhibited higher adsorption levels than the CDI cell. Notably, Ni^{2+} concentrations and flow rates had a discernible effect on the duration of the adsorption process due to the transport of ions associated with forming a diffusion boundary layer on the membrane surface. This study showed that incorporating a heterogeneous cation exchange membrane within the CDI system can potentially remove Ni^{2+} from the solution, thereby providing a novel method for enhancing the efficacy of removing HMs from wastewater effluent. Future studies should consider the costs of the fabricated membrane process, and the various elements present in mixed solutions to unlock the potential of employing heterogeneous membranes in CDI systems. Moreover, to fully understand the binding mechanism of Ni^{2+} on an electrode surface, it is essential to employ X-ray photoemission spectroscopy in further studies.

4.3 Removal of Cu^{2+} ion utilizing enhanced zinc oxide nanostructures on activated carbon cloth as electrode material in different configurations of CDI

4.3.1 Physical properties of materials

4.3.1.1 Surface area analysis

Figure 4.14 presented data obtained from N_2 adsorption/desorption isotherms and pore-size distribution (PSD) analyses, offering valuable insights into the porous structure of the prepared electrodes for ACC, ACC/ZnO-nPs, and ACC/ZnO-nRs. According to the IUPAC classification, the three samples displayed typical type-I isotherms with well-defined characteristics, and no hysteresis loop was detected in the Nitrogen adsorption-desorption curves (Figure 4.14(a)), indicating the presence of significant micropores in materials (Thommes et al., 2015b). This finding was supported by the suitable PSD observed in Figure 4.14(b). It can be inferred that the uptake was determined by the available micropore volume rather than the interior surface area (Liu et al., 2016; Thommes et al., 2015b).

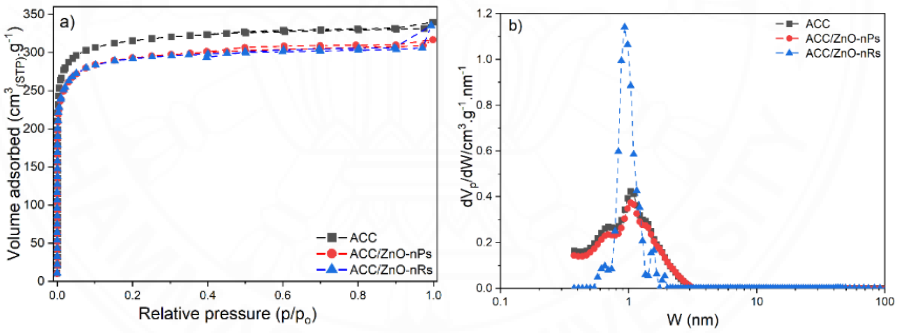

Figure 4.14 a) N_2 adsorption/desorption isotherms and b) Pore-size distribution of ACC, ACC/ZnO-nPs, and ACC/ZnO-nRs.

The value of dVp/dW ($cm^3/g/nm$) represents the derivative of pore volume to pore size in the NLDFT/GCMC method, which describes the adsorption by porous materials well. In Figure 4.14(b), dVp/dW decreased slightly compared to ACC, whereas it was higher for ACC/ZnO-nRs than ACC and ACC/ZnO-nPs. Results revealed a modification in pore volume compared to pore size among the samples. To comprehend this alteration, the specific surface area (SSA) and total pore volume (T_{PV}) of the three prepared materials were examined and are presented in Table 4.2. Overall,

the deposition of ZnO nanostructures changed the material's properties, decreasing the modified material's SSA and T_{PV} compared to ACC. Their departure may have resulted from several factors (Kyaw et al., 2020; Laxman et al., 2015). The formation and overlapping of these nanoparticles could have led to nanoparticles covering pores in materials and reducing the size of porous. Notably, Figure 4.14(b) shows that ACC/ZnO-nRs have two additional peaks compared to ACC and ACC/ZnO-nPs, implying the incorporation of ZnO nanorods on the external surface of ACC. This incorporation most likely triggers reorganization and the formation of a new pore network, which may improve the adsorption process. The abundance of micropores in activated carbon materials restricts the diffusion of ions on surface materials, making it difficult for these ions to enter the microporous. It led to the formation of a double layer that overlaps at the pore entrance. By forming larger pores on the external surface of the ACC/ZnO-nRs, Cu^{2+} ions initially come to these pores, which serve as ion storage sites that shorten the distance between the Cu^{2+} solution and the electrodes. After that, the ions diffuse into micropores after migrating into mesopores. The presence of these mesopores facilitates ion transport into the micropores inside the material.

Surface area and the localized electric field are two scenarios that can be addressed in depth to understand the adsorption material deeply [19, 21]. Since no significant changes in the surface area were observed, it is difficult to explain the adsorption solely on this parameter. Therefore, enhancing the specific capacitance of samples becomes essential, precisely the localized electric field, which is measured by CV.

Table 4.2 Specific surface area and total pore volume of the ACC, ACC/ZnO-nPs, and ACC/ZnO-nRs.

Materials	Specific surface area (m^2/g)	Total pore volume (cm^3/g)
ACC	1226.5	0.5206
ACC/ZnO-nPs	1130.9	0.4860
ACC/ZnO-nRs	1133.0	0.5103

4.3.1.2 Morphological analysis

Figure 4.15 displayed scanning electron microscope (SEM) images and results of energy dispersive X-ray spectroscopy (EDS) of prepared materials, each obtained at a magnification of 10,000 times.

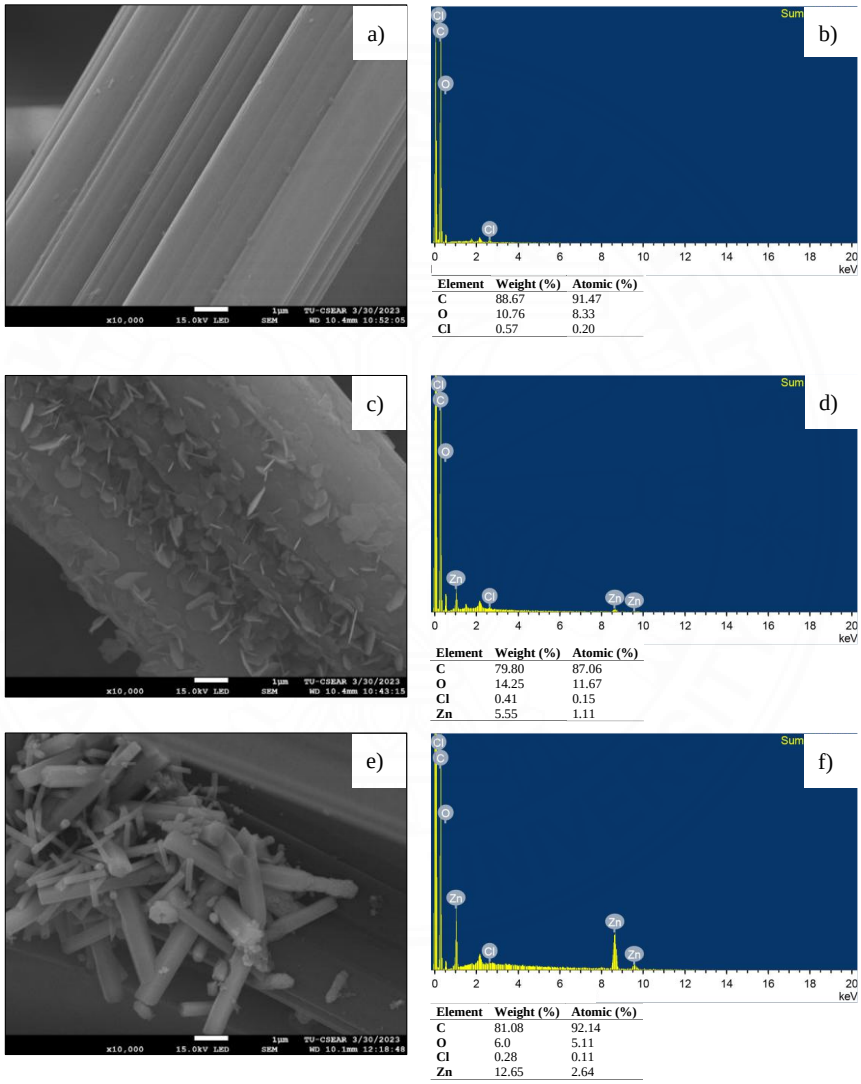

Figure 4.15 SEM images and EDS analysis of ACC (a, b), ACC/ZnO-nPs (c, d), and ACC/ZnO-nRs (e, f).

The analysis of the surface morphology of ACC (Figure 4.15(a)), ACC/ZnO-nPs (Figure 4.15(c)), and ACC/ZnO-nRs (Figure 4.15(e)) by SEM images revealed

essential details. It clarified the nanostructure growth images of ZnO on the surfaces of ACC fibers after being seeded with ZnO nanoparticles or nanorods. The feature of carbon fiber shown in Figure 4.15(a) depicted that it has a relatively smooth surface, making it a candidate for development with other materials on the surface of them. ACC/ZnO-nPs and ACC/ZnO-nRs exhibited rougher surfaces with ZnO sharpened features, indicating the deposition of ZnO onto the ACC substrate (Figure 4.15(c and e)). Figure 4.15(c) presents the formation of ZnO nanoparticles onto ACC fibers, whereas Figure 4.15(e) shows how ZnO nanorods with a rod-like structure grew on the surface of the ACC fibers. ZnO nanoparticle growth on ACC fibers (Figure 4.15(c)) was suggested at the establishment, with horizontal surface diffusion (non-polar facets) predominating over vertical gain along the polar facets (Laxman et al., 2015). Myint et al. discovered that when ZnO nanorods were synthesized using a hydrothermal process with an initial pH of 6.8, the resulting hexagonal ZnO crystals exhibited a preferred orientation in the (0001) direction (Myint et al., 2014). However, using a carbon sheet and employing a hydrothermal technique in an autoclave might cause an uneven distribution of ZnO nanorods on carbon fiber, as presented in Figure 4.15(e). EDS analysis was performed since it is difficult to ascertain the chemical elements on the surface of materials. The results confirmed the presence of carbon and oxygen in all samples, while minute traces of chlorine were also detected in trace amounts as presented in Figure 4.15(b, d, and f). The EDS elemental mapping pictures of ACC, ACC/ZnO-nPs and ACC/ZnO-nRs are presented in Figure C.1, C.2 and C.3 (Appendix C), respectively. Using a hydrochloric acid solution for cleaning trace amounts of ACC could result in Cl^- being found in three samples. The apparent presence of zinc in the ACC/ZnO-nPs and ACC/ZnO-nRs confirms the successful deposition of ZnO nanoparticles and nanorods onto the ACC substrate without other elements. This finding provides compelling evidence supporting the efficient integration of ZnO within the ACC substrate, which holds significant promise for enhancing the substrate's surface properties and the properties of ZnO on the ACC substrate.

The SEM analysis offered valuable insight into the continual growth of ZnO structures on carbon fibers. It explained the successful deposition of ZnO nanoparticles

and nanorods on the ACC substrate. The structural morphology of materials helps to acquire an in-depth knowledge of the direction of ZnO structures on the surface (Laxman et al., 2015).

4.3.1.3 Crystal structures

Figure 4.16 revealed significant findings from XRD measurements conducted on prepared samples. The results of XRD analysis help gain more clarity on the structural characteristics of prepared material.

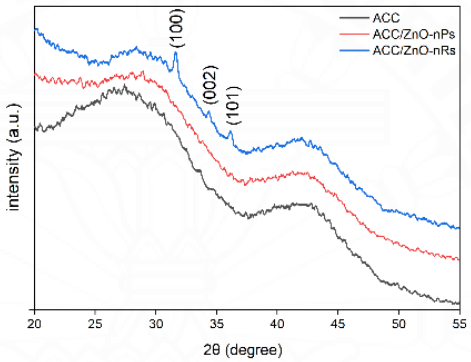

Figure 4.16 X-ray diffraction patterns of ACC, ACC/ZnO-nPs, and ACC/ZnO-nRs.

In Figure 4.16, broad peaks observed at 2θ ~ 26° and 2θ ~ 43° in all samples corresponded to the (002) and (100)/(101) planes typically associated with graphitic carbon materials derived from the activated carbon utilized (Elazari et al., 2011). Notably, the XRD analysis of ACC/ZnO-nPs revealed an absence of distinct peaks related to crystalline zinc, suggesting a high dispersion of zinc on the carbon surface without the presence of discernible crystal planes, which is also confirmed in the SEM image (Figure 4.15(c)). Conversely, upon depositing ZnO nanorods onto ACC, the XRD analysis exhibited characteristic peaks at 2θ angles of 31°, 34°, and 36°, corresponding to the diffraction of (100), (002), and (101) planes (JCPDS card No. 00–001–1136). These peaks signify a preferential orientation of the as-grown nanorods along the c-axis and the observed anisotropic growth (Figure 4.15(e)), which is a defining feature of ZnO nanorods (Kyaw et al., 2020; Laxman et al., 2015). These findings provided valuable insights into the crystal structural properties of the ZnO-

modified samples, thereby supporting further investigation into their potential applications for Cu^{2+} removal.

4.3.2 Electrochemical properties of materials

Figure 4.17 illustrates CV curves, and a computed value of specific capacitance obtained from the prepared materials, including ACC, ACC/ZnO-nPs, and ACC/ZnO-nRs depicting their electrochemical behavior. In Figure 4.17(a), CV curves obtained from ACC/ZnO-nPs and ACC/ZnO-nRs revealed different properties than pristine ACC, highlighting the significant impact of the added ZnO. Notable are the current peaks observed in ACC/ZnO-nPs and ACC/ZnO-nRs, which are higher than those in pristine ACC, which confirmed the favorable impact that ZnO has on the electric field and is the result of enhanced peak currents. This observation suggested an increase in electrochemical activity, predominantly attributable to the additional active sites supplied by ZnO nanoparticles and nanorods (Kyaw et al., 2020). In addition, the shape of electrodes, as seen in Figure 4.17(a, b, c, and d), significantly influences the electrochemical behavior of the electrodes. CV curves exhibit a leaf-like structure, which shows the presence of a significant number of active sites than a rectangular structure. The CV curves were reported to exhibit a quasi-rectangular shape (no evidence of redox peaks), implying that double-layer capacitive behavior is advantageous for energy storage (Ma et al., 2016). During this process, electrons from the electrode and ions from the electrolyte endure attractive and repulsive forces to form the electrical double layer (EDL). Once a substantial number of ions approach the electrode, it generates a force capable of propelling co-ions. The formation of a leaf-shaped structure reveals intermediary active sites that facilitate improved ion transfer, subsequently contributing to the increased efficiency of the electrode material. In this study, the current behavior of the prepared electrodes was different, with the ACC exhibiting an increasing line from -0.3 V to 0.5 V, then the current line in the x-axis direction to 0.9V, which appears as EDL. While the current line of ACC/ZnO-nPs and ACC/ZnO-nRs samples gradually increased with a slope towards 0.9 V. To gain a greater insight into the electrochemical properties, the samples were analyzed using a

variety of scan rates of 2, 5, 10, 20, 50, and 100 mV/s, as shown in Figure 4.17(b, c, and d). Figure 4.17(e) compares the computed value of specific capacitances corresponding to each value. In general, each CV curve has the shape of a leaf, which agrees with the findings from the earlier observations. No significant electrochemical responses were observed at low scan rates for reducing Cu^{2+} to Cu^{+} or Cu.

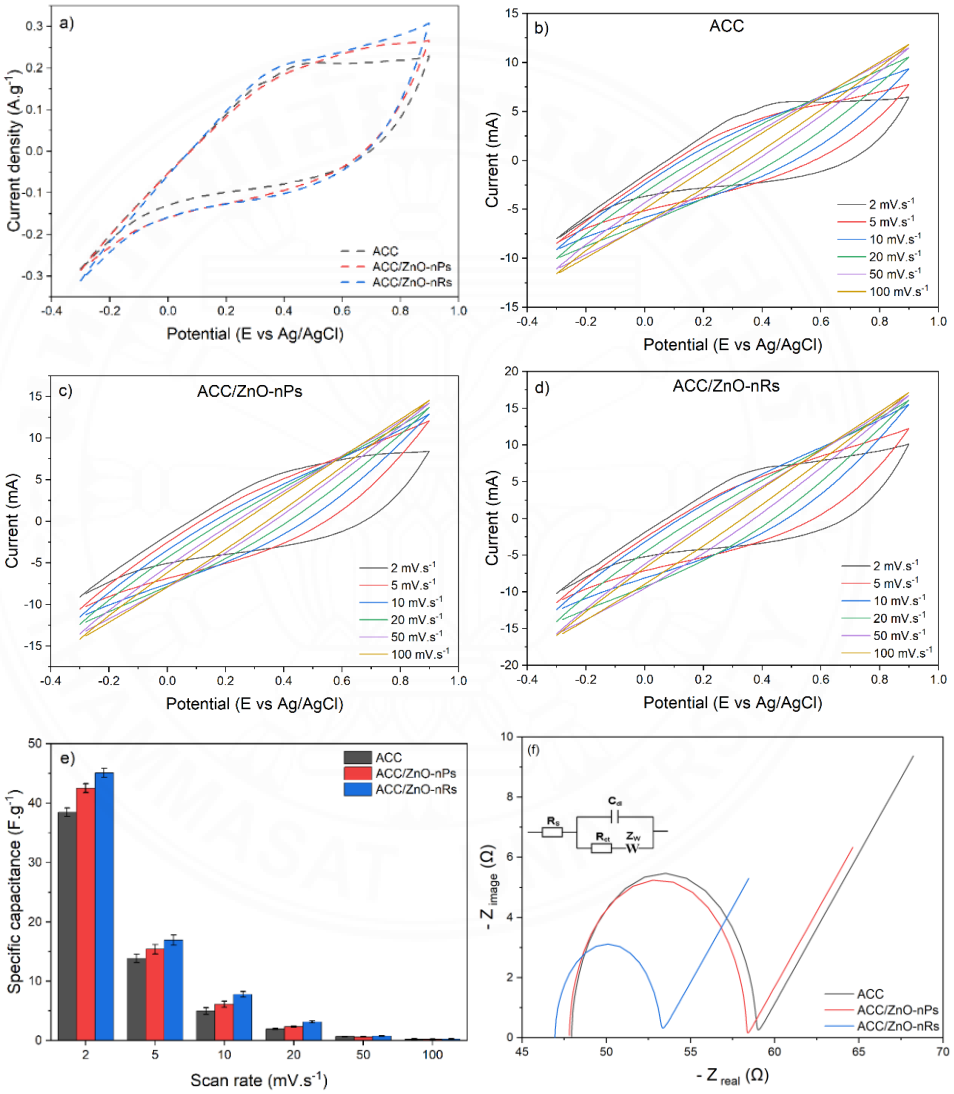

Figure 4.17 Comparison of cyclic voltammetry curves for a) the prepared electrodes at a scan rate of 2 mV/s, Cyclic voltammetry curves at various scan rates of b) ACC, c) ACC/ZnO-nPs, d) ACC/ZnO-nRs, e) Specific capacitance of prepared electrodes at various scan rates, and f) Impedance spectra (Nyquist plots) plot of ACC, ACC/ZnO-nPs, and ACC/ZnO-nRs.

Figure 4.17(b, c, and d) revealed that it is possible to locate symmetric curves, which provides evidence that the capacitive process is very reversible and reliable. It was possible to notice some modest variations in the leaf's shape when the scan rate changed from 10 mV/s to 100 mV/s. These changes coincided with a reduction in the leaf area. The changes in CV shapes can be attributed to the fact that as scan rates increase, Cu^{2+} ions have less time to be absorbed into the pores of the materials, resulting in CV shape alterations. Additionally, the size limitation of micropores on cloth imposes restrictions on the extent of ionic diffusion necessary to access the tiny pores. The minimized spatial capacity by micropores caused limitations on the efficient mobility of ions, consequently decreasing their ability to enter. As a result, ions exhibited a propensity to gather near the entrance region and in the proximity of pore spaces, leading to a noticeable growth in the charge density. Consequently, the limited diffusion of ions into the pores leads to an overlapping EDL at the pore entrance, as observed in the case of ACC (Kyaw et al., 2020). As depicted in Figure 4.17(e), the specific capacitance of ACC/ZnO-nPs and ACC/ZnO-nRs is 42.52 F/g and 45.08 F/g, respectively, at a scan rate of 2 mV/s, whereas the ACC reached 38.43 F/g. Additionally, the specific capacitance of ACC/ZnO-nPs and ACC/ZnO-nRs is more significant than that of pristine ACC at all scan rates. This improvement in specific capacitance can be attributed to the enhancement in the electric field distribution at the material's surface due to the deposition of ZnO nanoparticles on carbon fibers.

In this study, CV test in the potential range of – 0.3 V to 0.9 V did not reveal any identifiable peaks of Cu^{2+} reduction. This result is consistent with findings from prior studies that reported similar results (Wang et al., 2019; Wu et al., 2021). However, they confirmed that when a cathode was treated with a Cu^{2+} solution at a potential higher than 0.8 V, a distinct reddish-brown layer was observed through SEM images [24]. This layer indicated the presence of deposits like copper. Consequently, these results strongly suggested the potential participation of Cu^{2+} reduction in the electrochemical reactions occurring at the cathode, resulting in a decrease in copper removal rate during the experiment. Moreover, functional groups of the activated carbon fibers were found to be essential electron donors that gave electrons for reducing

Cu^{2+} to Cu or Cu^{+} (Wang et al., 2019; Wu et al., 2021). As reported by Wang et al., the two primary reduction products of Cu^{2+} included the formation of Cu, Cu^{+}, and Cu_2O, which were represented by Equation 4.11 to 4.13 (Wang et al., 2019).

$$Cu^{2+} + e^{-} \rightarrow Cu^{+} \quad (4.11)$$

$$2Cu^{+} + H_2O \rightarrow Cu_2O + 2H^{+} \quad (4.12)$$

$$Cu_2O + H_2O + 2e^{-} \rightarrow 2Cu + 2OH^{-} \quad (4.13)$$

The dynamic behavior of ions transferring from Cu^{2+} solution to prepared materials was investigated using EIS measurement. Real and imaginary impedances were plotted in the Nyquist diagram of ACC, ACC/ZnO-nPs, and ACC/ZnO-nRs in Figure 4.17(f).

In Figure 4.17(f), two elements appeared: a semi-circle at the high-frequency zone and a straight line at the low-frequency range. The combined resistance in the semi-circle, encompassing the electrolyte resistance within the electrode's porous structure, the electrode resistance, and the contact resistance of the electrode and the current collector, is collectively referred to as the charge transfer resistance (R_{ct}) (Mei et al., 2017). Figure 4.17(f) revealed a decrease in R_{ct} in the semi-circle of ACC/nPs and ACC/ZnO-nRs compared to ACC. Notably, the R_{ct} of ACC/ZnO-nPs decreased slightly from 10.92 Ω to 10.49 Ω, and ACC/ZnO-nRs significantly reduced from 10.92 Ω to 6.205 Ω. It suggested that the coating of ZnO nanorods on the surface of ACC caused a decrease in R_{ct}. Furthermore, the intersection of the real axis (Z_{real}) with the image axis (Z_{image}) can be used to calculate the series resistance (R_s). It defined the total resistance of the series resistance, which included the resistance of the bulk electrolyte, the resistance of the electrode, and the resistance of contact between the electrode and the current collector (Mei et al., 2017). The R_s was lower for modified ACC by ZnO nanostructures when compared to ACC. The linear trend observed in the low-frequency zone is comparable to the ion diffusion process known as Warburg diffusion (Kyaw et al., 2020).

4.3.3 Studies on capacitive deionization for Cu^{2+}

4.3.3.1 Electrosorption kinetics models of Cu^{2+}

Kinetic models are commonly used to understand equilibrium time and the mechanism of adsorption of electrolytes and materials (Wu et al., 2009). The experimental data of the prepared electrode have been assessed by employing PFO and PSO as kinetic models in both CDI cells. Figure 4.18(a, b, c, d, and e) depicts the adsorption amount of Cu^{2+} ions on the prepared electrodes at concentrations of 50, 100, 200, 500, and 1000 mg/L, while Figure 4.18(f) provides a comparison of Cu^{2+} adsorption amount for various concentrations under 1.2 V in CDI and MCDI cells after 120 minutes. Table C.1 and Table C.2 (Appendix C) depict the parameters of both kinetic models applied to ACC, ACC/ZnO-nPs, and ACC/ZnO-nRs, evaluating their impact on CDI cell and MCDI cell under 1.2 V at various concentrations. The adsorption amount of the prepared materials increased from ACC to ACC/ZnO-nPs, then ACC/ZnO-nRs for both cells, as revealed in Figure 4.18(a, b, c, d, and e) at all concentrations. The results presented in Figure 4.18(f) and the estimated adsorption amount (Table C.1 and Table C.2 in Appendix C) in both kinetic models indicated that the elevation in the concentration of Cu^{2+} in both CDI cell and MCDI cell led to an enhancement in the quantity of adsorption for the prepared electrode. Additionally, it is revealed that the MCDI cell has been found to exhibit a better ability for the adsorption of Cu^{2+} compared to the CDI cell. From Table C.1 (Appendix C) and Table C.2 (Appendix C), the PSO model for the prepared materials in both CDI cells offered a good fit for all concentrations, thereby supporting the concept suggested by Sahoo and Prelot that the rate-limiting step within the framework of the PSO model was likely due to chemical sorption or chemisorption (Sahoo & Prelot, 2020). Moreover, the calculated $q_{e,cal}$ value from the PSO were near the determined data from experiments, but the calculated $q_{e,cal}$ value from the PFO was higher than the experimental data. While the PFO equation typically relates to the first 20 to 30 minutes of the adsorption process, the PSO model predicts the behavior over the entire range of adsorption (Sahoo & Prelot, 2020). Wang et al. indicated that the PSO kinetic fit better on the physical adsorption of HMs during the experiment (Wang et al., 2013). This could be because

ions can quickly capture the active sites on the surface of the electrode at a high concentration. The adsorption process may be slowed because free ions must overcome electrostatic repulsion with already adsorbed ions (Wang et al., 2013; Wu et al., 2009). In addition, the potential participation of Cu^{2+} reduction in the electrochemical reactions occurring at the cathode may have happened, as discussed in the previous part. Therefore, fitting experimental data with the PSO is acceptable. It showed that the adsorption amount of Cu^{2+} improved with the concentration, and it varied depending on the configuration of the CDI cell. The application of IEMs in MCDI cell demonstrated an increasing proportion of Cu^{2+} adsorption compared to CDI. In addition, the adsorption amount of Cu^{2+} increased when ZnO nanoparticles and nanorods modified ACC. It also revealed that the adsorption amount of Cu^{2+} by ACC/ZnO-nRs is more significant than that of ACC/ZnO-nPs and ACC.

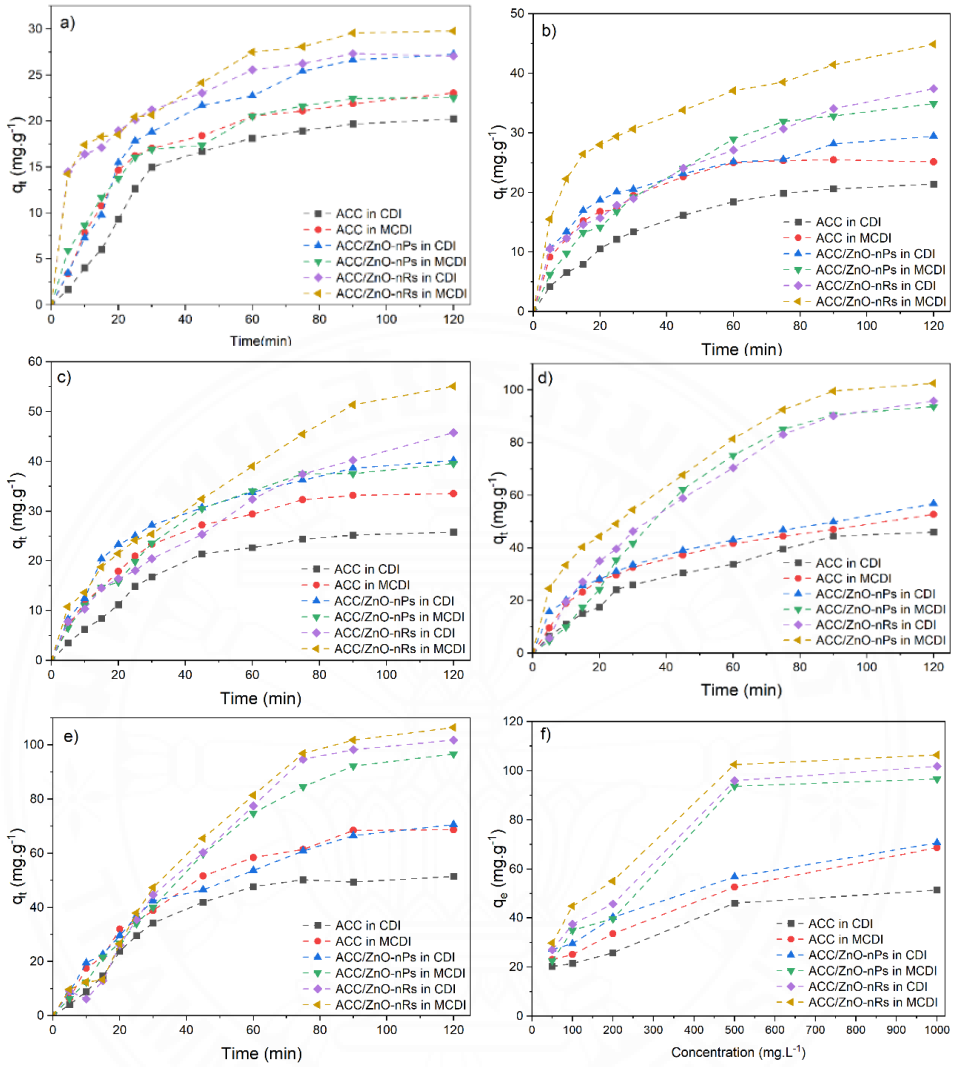

Figure 4.18 Adsorption amount of Cu^{2+} ions on the prepared electrodes (ACC, ACC/ZnO-nPs, ACC/ZnO-nRs) under 1.2 V in CDI cell and MCDI cell at a) 50 mg/L, b) 100 mg/L, c) 200 mg/L, d) 500 mg/L, e) 1000 mg/L, and f) Comparison of the adsorption amount of the prepared electrodes (ACC, ACC/ZnO-nPs, ACC/ZnO-nRs) at 1.2 V in CDI cell and MCDI cell.

Table 4.3 compares the electrosorption performance related to Cu^{2+} for various created electrode materials. The results revealed the significant effectiveness of integrating ZnO nanostructures onto ACC (ACC/ZnO-nPs and ACC/ZnO-nRs) to enhance the adsorption capacity of Cu^{2+} compared to other materials. Comparing

material rGO-TNT (the reduced graphene oxide with titanate nanotubes at a 3:1 mass ratio), it displayed a remarkable adsorption capacity at 253.25 mg/g, but rGO-TNT exhibited a recovery rate of only 5.28 % in the discharge phase (Bautista-Patacsil et al., 2020). The research conducted by Li et al. (J. Li et al., 2017) on the utilization of carbonaceous aerogels (CAs) modified with CeO_2 (CAs/CeO_2) and Fe_2O_3 (CAs/Fe_2O_3) revealed that CAs/CeO_2 and CAs/Fe_2O_3 exhibited a Cu^{2+} adsorption amount of 49.28 mg/g and 41.42 mg/g, respectively, whereas our research revealed a Cu^{2+} adsorption amount of 33.52 mg/g for ACC/ZnO-nPs and 40.18 mg/g for ACC/ZnO-nRs. The ratios of enhanced adsorption capacities for CAs/CeO_2 and CAs/Fe_2O_3 relative to CAs are 1.624 and 1.36, respectively, whereas the enhancement ratios for adsorption capacities in the case of ACC/ZnO-nRs and ACC/ZnO-nPs, in relation to ACC, are 1.556 and 1.298, respectively, observed at a concentration of 200 mg/L. The differences in adsorption amount can be ascribed to variations in the pore size structure of materials, including the difference between microporous materials (activated carbon cloth used in this study) and mesoporous materials (carbonaceous aerogels). This distinction by pore size structures has been recognized to impact the adsorption capacity, as reported by Peng et al. (Peng et al., 2011). Furthermore, some studies have reported higher adsorption capacities with time, as illustrated in Table 4.3 (Huang & Su, 2010; Wu et al., 2023).

Table 4.3 Electrosorptive performance of the ACC, ACC/ZnO-nPs and ACC/ZnO-nRs compared to other materials in the CDI system.

Electrode materials	Electrosorption of Cu^{2+} ions				Reference
	Unit	Initial concentration (mg/L)	Adsorption amount (mg/g)	Operation Time	
Polyacrylonitrile-based ACC impregnated with chitosan solution	CDI	100	30.6	12 h	(Huang & Su, 2010)
CAs	CDI	200	30.35	150 – 160 min	(J. Li et al., 2017)
CAs/CeO_2	CDI	200	49.28	150 – 160 min	(J. Li et al., 2017)
CAs/Fe_2O_3	CDI	200	41.42	150 – 160 min	(J. Li et al., 2017)
FeS-decorated carbon felt	CDI	100	18.0	100 min	(Jin & Hu, 2019)
ZnS-decorated carbon felt	CDI	100	27.4	100 min	(Jin & Hu, 2019)
rGO-TNT	CDI	80	253.25	2 h	(Bautista-Patacsil et al., 2020)

3-Dimensional reduced graphene oxide	CDI	50	18.1	60 min	(You et al., 2020)
Hollow bowl-type carbon (HBC)	CDI	25	18.5	6 h	(Wu et al., 2023)
HBC loaded with molybdenum sulfide (HBC-MoS_2-0.02)	CDI	25	28.97	12 h	(Wu et al., 2023)
ACC	CDI	50 100 200 500 1000	20.22 21.41 25.82 46.03 51.42	120 min	This study
ACC/ZnO-nPs	CDI	50 100 200 500 1000	23.02 25.14 33.52 52.68 68.65	120 min	This study
ACC/ZnO-nRs	CDI	50 100	27.24 29.47	120 min	This study

		200	40.18		
		500	56.78		
		1000	70.62		
ACC	MCDI	50	22.51	120 min	This study
		100	34.94		
		200	39.59		
		500	93.68		
		1000	96.63		
ACC/ZnO-nPs	MCDI	50	27.06	120 min	This study
		100	37.42		
		200	45.75		
		500	95.88		
		1000	101.84		
ACC/ZnO-nRs	MCDI	50	29.77	120 min	This study
		100	44.85		
		200	55.08		
		500	102.54		
		1000	106.43		

4.3.3.2 CDI tests for electrosorption and regeneration of Cu^{2+}

The electrosorption performance and recovery rate of Cu^{2+} for various electrode materials and configurations at different voltages are presented in Figure 4.19, with their corresponding values recorded in Table C.3 (Appendix C) and Table C.4 (Appendix C). Figure 4.19(a, b) depicts the amount of Cu^{2+} adsorption on the 5th cycle and 10th cycle of ACC, ACC/ZnO-nPs, and ACC/ZnO-nRs in CDI and MCDI cells. ACC/ZnO-nRs had the most significant Cu^{2+} adsorption amount in three samples for CDI cell (6.4 mg/g), and it also had the highest adsorption amount for MCDI cell (7.1 mg/g) at a voltage of 0.4 V on the 5th cycle. Similarly, at higher potentials (0.8 V and 1.2 V), ACC/ZnO-nRs consistently exhibited more significant adsorption amounts than ACC/ZnO-nPs and ACC for two cells, with ACC/ZnO-nPs outperforming ACC for both the 5th cycle and 10th cycle. It demonstrated that ACC modified with ZnO nanoparticles and ZnO nanorods has tremendous removal potential than ACC, with ACC/ZnO-nR exhibiting the highest adsorption performance, followed by ACC/ZnO-nP and ACC. At a more significant voltage, the mass transfer of ions in solution and the surface of electrode materials was enhanced by the electric field, and the contact probability between Cu^{2+} ions and the electrode surface were markedly increased, resulting in a significant improvement of adsorption performance.

Figure 4.19(c and d) provided the Cu^{2+} recovery rate for each material at the 5th cycle and 10th cycle for two cells. For instance, the Cu^{2+} recovery rate in ACC/ZnO-nRs increased from 51.8% at 0.4 V to 67.2% at 1.2 V in the CDI cell; similarly, the recovery rate of Cu^{2+} in the MCDI cell improved from 31.6% to 35.6% with the same voltage and prepared material. The recovery rate of Cu^{2+} must be enhanced as the applied potential improves. When the applied voltage is increased, the Cu^{2+} adsorption amount is higher in MCDI cells than in CDI cells; however, the Cu^{2+} recovery rate in MCDI cells is lower than in CDI cells. By comparing cycles at the 5th cycle and 10th cycle, results in Figure 4.19(c, d) revealed that the MCDI configuration consistently outperformed the CDI configuration cycles at various voltages and materials. The examination of variations in the adsorption amount (Figure 4.19(a and b)) and the recovery rate (Figure 4.19(c and d)) at the 5th cycle and 10th cycle yielded valuable

observations regarding the stability and efficacy of the system. The results indicated that the performance of both CDI cells exhibited a slight improvement across successive cycles, potentially attributable to the conditioning and activation of the electrodes, which contribute to stability and cyclability. In the examined conditions, the Cu^{2+} adsorption amount and recovery rate results exhibited stability and the ability to undergo repeated cycles.

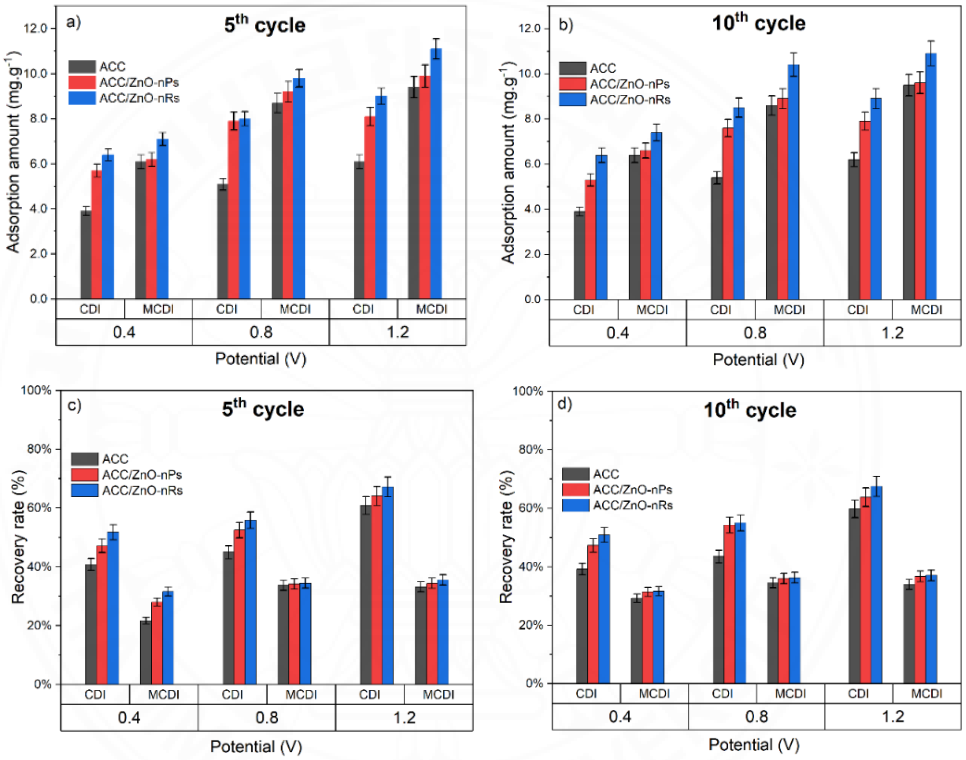

Figure 4.19 Adsorption amount of Cu^{2+} at a) the 5th cycle, b) the 10th cycle, and recovery rate of Cu^{2+} at c) the 5th cycle and d) the 10th cycle of the prepared material in both CDI cell and MCDI cell at 0.4, 0.8, and 1.2 V.

Based on the data in Figure 4.19(a and b) and Table C.3 (Appendix C), it is suggested that the existence of IEMs in MCDI cells improves the adsorption of Cu^{2+} more than in CDI cells. For example, the adsorption amount of Cu^{2+} of ACC/ZnO-nRs in CDI is 8.9 mg/g, while MCDI cell is 10.9 mg/g with the potential of 1.2V at the 10th cycle. IEMs prevent co-ions from reaching the electrodes and improve ion transport by generating a concentration gradient across the membrane (Yang et al., 2020).

Furthermore, IEMs help limit the reverse diffusion of ions into the electrolyte solution when the applied voltage is cut off. However, the lesser Cu^{2+} recovery rate in MCDI than in CDI may also be due to the presence of the membrane. The Cu^{2+} recovery rates in CDI and MCDI cells are 67.5% and 33.8% of ACC/ZnO-nRs with a potential of 1.2V after ten cycles, respectively, as presented in Figure 4.19(c, d) and Table C.4 (Appendix C). IEMs as a barrier can inhibit the transport of Cu^{2+} ions from the electrode compartment, which built up between electrode and membrane, to the solution channel, resulting in a lower recovery rate in the regeneration phase. In addition, the presence of IEMs can raise the system's resistance during the discharge phase, resulting in a decrease in the volume of energy supplied to the electrode and an associated decrease in the Cu^{2+} recovery rate.

The results demonstrated that increasing the potential of the prepared materials in two cells led to a notable rise in the Cu^{2+} adsorption amount and recovery rate. Cu^{2+} adsorption and recovery performance revealed that the ACC/ZnO-nRs were better than ACC/ZnO-nPs, and pristine ACC. By utilizing IEMs, the Cu^{2+} adsorption amount in the MCDI cell increased significantly compared to the CDI cell under the same conditions. It was also observed that the recovery rate decreased when IEMs were used in MCDI cell. In addition, the stability of the adsorption amount and recovery rates over ten cycles indicated the potential for additional applications of the prepared material for further studies.

4.3.4 Conclusions for Cu^{2+} removal

ACC/ZnO-nPs and ACC/ZnO-nRs were successfully produced by modifying ACC with ZnO via a hydrothermal method. The results revealed that the specific capacitance of ACC/ZnO-nPs (42.52 F/g) and ACC/ZnO-nRs (45.08 F/g) was more significant than pure ACC (38.43 F/g), which strongly contributed to electrosorption. In addition, charge transfer resistance (R_{ct}) and series resistance (R_S) have improved in the modified sample. It was found that elevating the potential of materials by ZnO nanostructures resulted in a notable enhancement in both the adsorption amount and recovery rate of Cu^{2+}, with the ACC/ZnO-nRs outperforming the ACC/ZnO-nPs and

ACC exhibiting the lowest performance. On the other hand, utilizing IEMs increased the Cu^{2+} adsorption amount in the charge phase but lowered the Cu^{2+} recovery rate in the discharge phase. This research indicated that the ZnO-modified ACC electrode was an acceptable candidate for enhancing the performance of Cu^{2+} removal in CDI and MCDI. Further studies should be conducted at extended-cycles in order to assess the stability and performance trends in the long run. Understanding voltage during the discharge phase is crucial for optimizing system performance and improving HMs recovery rates. Utilizing X-ray photoemission spectroscopy should be conducted to understand binding mechanism of elements on surface comprehensively. Furthermore, investigating the effects of various HMs should be carried out to understand the application of the system.

4.4 Removal of individual and mixed metals solution in different configurations of capacitive deionization

4.4.1 Physical properties of materials

4.4.1.1 Morphological analysis

Figure 4.20 illustrates the synthesis and characterization of ACC composites with ZnO and MnO_2 by FE-SEM images at scale bar = 1µm. Figure 4.20(a) exhibits that the pure carbon fibers had a smooth and uniform surface, making them ideal for grafting nanomaterials. When adding ZnO and MnO2, remarkable changes were observed on the carbon surface, revealing an abundant number of nanostructures on the carbon surface, as depicted in Figure 4.20(b and c). Figure 4.20(b) presents that the ZnO nanorods are evenly distributed, forming a thick overlay across the carbon fibers with diameters of 70 – 100 nm and lengths of 500-700 nm. It found that an initial pH of 6.8 optimizes ZnO nanorod formation in the hydrothermal process, resulting in hexagonal ZnO crystals with a (0001) preferential orientation, as inserted in Figure 4.20(b) (Sunandan Baruah & Joydeep Dutta, 2009). Additionally, using carbon sheets in the autoclave during hydrothermal growth led to uneven distribution of ZnO nanoparticles on the carbon cloth (Kyaw et al., 2020). Figure 4.20(c) illustrates that the MnO_2 nanorods form a substantial overlay, creating a network-like structure on the

carbon surface. Extending the hydrothermal reaction duration beyond 8 h significantly influences the formation of MnO_2 rod-like and wire-like nanostructures (Hlaing & Win, 2012). Figure 4.20(c) corroborates this, showing distinct rod-like nanostructures and aggregated wire-like nanoparticles forming bulk products. The composition of elements on the carbon fiber surface was observed using EDS spectra, as observed in Figure D.1 (Appendix D). The presence of Zn and Mn and increased oxygen content is confirmed in Figure D.1(b and c) (Appendix D). Incorporating ZnO and MnO_2 leads to a significant concentration of Zn and Mn on the fiber's surface. The presence of potassium (K) and chlorine (Cl) in Figure D.1(c) (Appendix D) can be attributed to the deposition of KCl on the carbon, which was generated during the hydrothermal process. Furthermore, it reported that α-MnO_2, discussed in the next part, has a tunnel structure with large cations, such as K^+, Ba^{2+}, or Pb^{2+}, embedded in its tunnel cavity (Muraoka et al., 1999). As a result, a tiny quantity of K, probably added from $KMnO_4$ during the reaction, is found within the tunnels of α-MnO_2 as resulted in Figure D.1(c) (Appendix D). Moreover, a tiny amount of HCl may have been adsorbed on the carbon fibers during preparation. Checking SEM images combined with EDS spectra provides compelling evidence for the efficient integration of ZnO and MnO_2 within the ACC substrate, highlighting their potential to improve the substrate's surface properties. The successful incorporation of ZnO and MnO_2 onto the carbon fibers has meant an enhancement in surface area and the creation of additional active sites for ion adsorption. While SEM analysis demonstrated the successful deposition of ZnO nanorods and MnO_2 nanorods on the ACC substrate, XRD patterns were also used to identify the crystallographic structures of the fabricated materials.

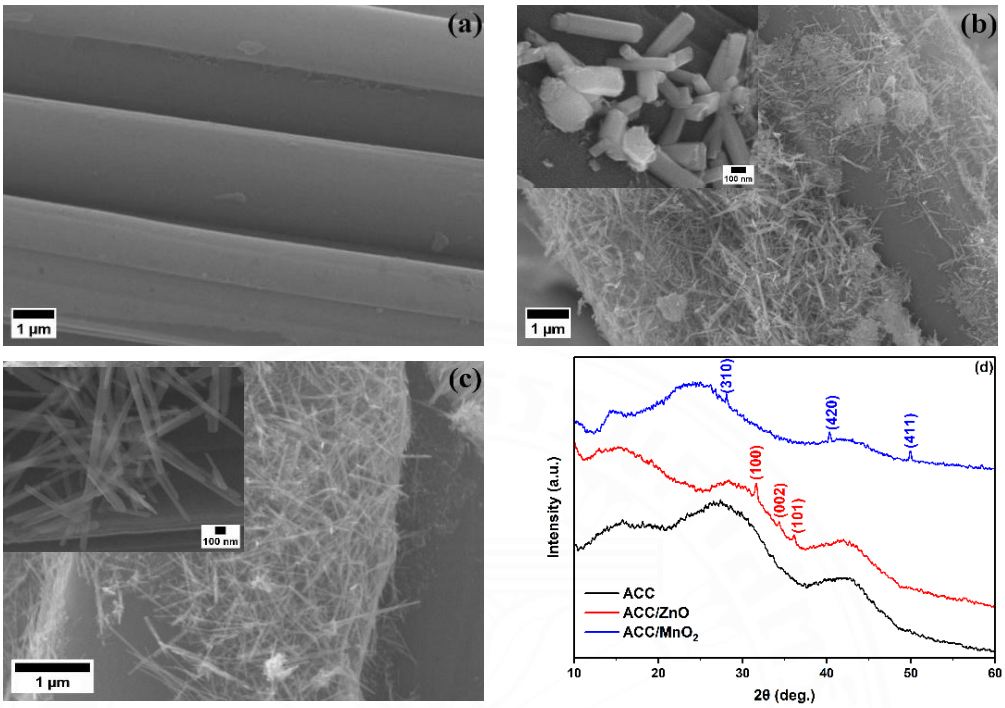

Figure 4.20 Analysis of FE-SEM image for (a) ACC, (b) ACC/ZnO, (c) ACC/MnO_2, and (d) XRD patterns of the prepared materials (ACC, ACC/MnO_2 and ACC/ZnO).

Figure 4.20(d) reveals significant findings from XRD patterns conducted on ACC, ACC/ZnO, and ACC/MnO_2. Figure 4.20(d) displays broad peaks at $2\theta \sim 25°$ and $2\theta \sim 43°$ in all samples, indicating the presence of (002) and (100)/(101) planes commonly found in carbon materials. The XRD patterns of ACC/ZnO and ACC/MnO_2 showed clear peaks corresponding to crystalline Zn and Mn, suggesting a significant amount of Zn and Mn on the carbon surface with visible crystal planes. After depositing ZnO nanostructures onto ACC, the XRD pattern of ACC/ZnO shows distinct peaks at 2θ of 31°, 34°, and 36°, corresponding to the diffraction planes (100), (002), and (101) as per JCPDS card no. 00–001–1136. These peaks indicate a specific alignment of the ZnO nanorods during their growth, resulting in a distinct directional growth pattern despite being mostly amorphous, as presented in Figure 4.20(b). On the other hand, the XRD profile of ACC/MnO_2 reveals three distinct peaks at $2\theta \approx 29°$, 41°, and 49°, corresponding to the (310), (420), and (411) reflections, indicating the presence of the tetragonal crystalline phase of α-MnO_2 (JCPDS card no. 00-044-0141) (Davoglio et al.,

2018; Hlaing & Win, 2012). The peaks observed are attributed to the crystallographic planes of MnO_2 exhibiting minimal crystallinity or predominantly amorphous (Davoglio et al., 2018). The sharp and intense peaks indicate good crystallinity for ZnO and MnO_2 nanostructures, with no impurity peaks observed. This study reveals that grafting MnO_2 and ZnO onto ACC via the hydrothermal method results in amorphous nanorods on the carbon fiber, which is beneficial for capacitive charge storage. This amorphous layer facilitates ion diffusion within the electrode materials by establishing a mesoporous layer, enhancing ion transport to the microporous regions of the material (Ahmed G El-Deen et al., 2014; Han et al., 2020). Results provide valuable insights into the crystal structural properties of the ACC modified with ZnO and MnO_2, thereby supporting further research on their potential applications in HMs removal. The materials' porosity and pore size distribution were investigated to obtain an in-depth knowledge of the alteration caused by the amorphous layer on the carbon fiber surface.

4.4.1.2 Porosity property, pore size distribution

The adsorption process is greatly influenced by surface area, pore diameter, and pore volume (NguyenTan et al., 2024a). These factors collectively determine the availability of adsorption sites on the electrode, affecting its electrosorption performance. Based on the IUPAC classification, the pristine ACC and fabricated materials display a type-I isotherm without any noticeable hysteresis in N_2 adsorption-desorption, as illustrated in Fig. 3(a). The adsorption process is more affected by the volume of micropores than the internal surface area, specifically in the context of a type-I isotherm (Thommes et al., 2015a).

Furthermore, Table 4.4 compares ACC and its composites with ACC/ZnO and ACC/MnO_2 regarding specific surface area, pore volume, and pore diameter by BET and NLDFT/GCMC method. It reveals that the specific surface areas of ACC, ACC/ZnO, and ACC/MnO_2 are 1140 m^2/g, 1133 m^2/g, and 1146.8 m^2/g, respectively, with only slight variation observed. However, the fabricated materials exhibit a notable increase in pore volume, with ACC having 0.4664 cm^3/g, which rises to 0.5103 cm^3/g for ACC/ZnO and 0.4986 cm^3/g for ACC/MnO_2. Consistent with BET results, using

the NLDFT/GCMC method yields total pore volumes of 0.4640 cm^3/g for ACC/ZnO and 0.4508 cm^3/g for ACC/MnO_2, which are higher than the 0.4197 cm^3/g for ACC. To account for the significant increase in pore volume despite the relatively stable surface area, pore size distribution data obtained using the NLDFT/GCMC method are presented in Figure 4.21(b). It exhibits that the derivative of pore volume concerning pore size (dVp/dW) decreased for ACC/MnO_2 compared to ACC, with ACC/ZnO showing the highest value, affecting pore volume changes relative to pore size. The deposition of ZnO and MnO_2 has significantly modified the material properties, leading to noticeable enhancements in pore diameter and total pore volume compared to ACC. The interaction and arrangement of nanorods could potentially block micropores or reduce their number. However, this integration is likely to result in the organization and formation of an additional pore network, which could enhance the adsorption process. Figure 4.21(b) reveals that the ACC/MnO_2 pattern shows two separate peaks, while the base of the ACC/MnO_2 graph is broader than ACC. Moreover, the average pore diameters for ACC, ACC/ZnO, and ACC/MnO_2 are 1.6366 nm, 1.8016 nm, and 1.7836 nm, respectively, which supports the findings presented in Figure 4.21(b) as determined by BET analysis.

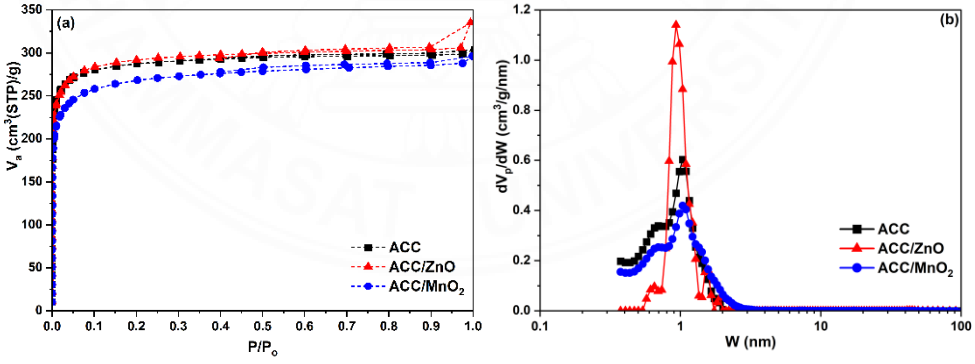

Figure 4.21 (a) N_2 adsorption-desorption isotherms of the prepared materials (ACC, ACC/MnO_2 and ACC/ZnO), (b) NLDFT/GCMC pore size distribution of the prepared materials (ACC, ACC/MnO_2 and ACC/ZnO).

Table 4.4 indicates that the total pore volume of the microporous region, as determined by NLDFT/GCMC analysis, remains unchanged for both ACC and

ACC/ZnO. However, the total pore volume of the non-microporous region increased significantly from 0.0064 cm^3/g for ACC to 0.0487 cm^3/g for ACC/ZnO. Conversely, while the total pore volume of the microporous region in ACC/MnO_2 decreased significantly to 0.3642 cm^3/g, the total pore volume of the non-microporous region markedly increased to 0.0866 cm^3/g, which is approximately 13 times higher than that of ACC in the non-microporous region. As discussed previously, Figure 4.21(b and c) exhibit the distinct deposition characteristics of ZnO and MnO_2. ZnO deposits as nanorods with a uniform distribution, forming an overlay on the carbon fibers that introduces new non-microporous layers. In contrast, MnO_2 grafted onto ACC forms a substantial overlay with a network-like structure called a tunnel structure. This formation covers a significant portion of the carbon fiber surface, reducing microporosity, but tunnel structures create numerous non-microporous regions. The increased non-microporous regions of ACC/MnO_2, due to the properties of MnO_2 nanorods, enhance its capacitive applications. This makes ACC/MnO_2 well-suited for comparison with ACC/ZnO, which exhibits enhanced electric field properties due to ZnO nanorods.

Table 4.4 Characteristics of the ACC, compared to ACC/ZnO and ACC/MnO_2.

Parameters	Unit	Value		
		ACC	ACC/ZnO	ACC/MnO_2
Specific surface area - using BET	m^2/g	1140	1133	1146.8
Total pore volume - using BET	cm^3/g	0.4664	0.5103	0.4986
Average pore diameter - using BET	nm	1.6366	1.8016	1.7836
Total pore volume - using NLDFT & GCMC	cm^3/g	0.4197	0.4640	0.4508

Total pore volume microporous (pore size < 2 nm) - using NLDFT & GCMC	cm^3/g	0.4133	0.4153	0.3642
Total pore volume non-microporous (pore size > 2 nm) - using NLDFT & GCMC	cm^3/g	0.0064	0.0487	0.0866

4.4.2 Electrochemical properties of materials

Figure 4.22 presents the results of CV and EIS analyses, comparing ACC with ACC/MnO_2 and ACC/ZnO in the SA mixture containing 500 mg/L of Cu^{2+}, Ni^{2+}, and Cr^{3+} ions. Figure 4.22(a) illustrates the CV profiles for prepared electrodes recorded at a scan rate of 1 mV/s. The CV curve for ACC exhibits a nearly fusiform shape without distinct redox peaks, signifying a purely capacitive process dominated by non-Faradaic reactions. These observed results can be attributed to the ACC electrode's incomplete charge/discharge process. In this study, the CV curve of ACC typically displays asymmetrical and non-linear profiles, indicating unfavorable adsorption behaviors of mixed ions. However, the CV curves for ACC/MnO_2 and ACC/ZnO exhibit a leaf shape and symmetry without redox peaks, but they reveal that the area enclosed by these curves is significantly larger than that of ACC. The ACC exhibits an asymmetrical fusiform shape due to its high porosity and internal resistance. However, adding MnO_2 and ZnO to the carbon surface causes it to become symmetrical and acquire a leaf-like shape. From the observations, it appears that the characteristics of the substrate material primarily influence the leaf-shaped structures on the modified electrode. These features are primarily impacted by the surface carbon structures rather than by the change in porosity of the pristine ACC. Even though the modified electrode does not have the expected rectangular shape, it indicates that both ACC/MnO_2 and ACC/ZnO materials possess capacitive properties resembling the EDL mechanism, likely due to their leaf-like form. Creating an EDL can be challenging due to competing ions in a mixture and the influence of co-ion phenomena. Unlike intercalation/deintercalation processes associated with Faradaic reactions in electrolytes such as K^+, Na^+, Li^+, H^+, or protons

(H_3O^+) in MnO_2 materials (Davoglio et al., 2018; Pargoletti et al., 2019), this study suggests that employing MnO_2 nanostructures on ACC for HMs removal may not be favorable for intercalation/deintercalation mechanism due to the lack of distinct Faradaic processes.

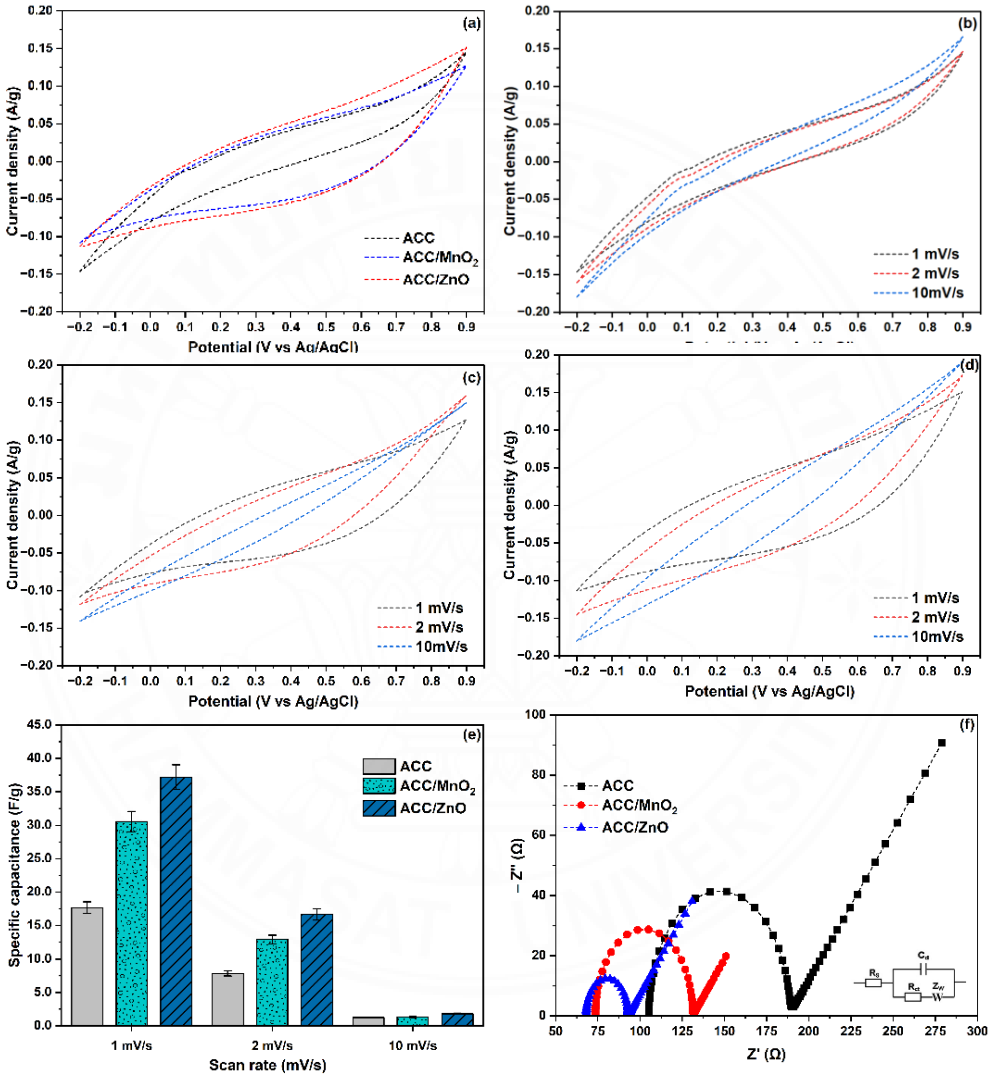

Figure 4.22 Comparison of CV profiles for (a) a scan rate of 1 mV/s of prepared electrodes (ACC, ACC/MnO_2, and ACC/ZnO), (b) ACC at different scan rates, (c) ACC/MnO_2 at different scan rates, (d) ACC/ZnO at different scan rates, (e) specific capacitance at various scan rates of prepared electrodes (ACC, ACC/MnO_2, and ACC/ZnO), and (f) Nyquist plot of EIS spectra with equivalent circuit diagram of prepared electrodes (ACC, ACC/MnO_2, and ACC/ZnO).

Figure 4.22(b, c, and d) compare CV profiles by ACC, ACC/MnO_2, and ACC/ACC/ZnO at scan rates of 1 mV/s, 2 mV/s, and 10 mV/s. The leaf-shaped pattern observed is a result of carbon-based electrodes. Additionally, as the scan rate increased from 1 mV/s to 10 mV/s, there were slight changes in the leaf shape, corresponding to a decrease in leaf area. As presented in Figure 4.22(e), the specific capacitance values calculated from the CV curves show that ACC, ACC/MnO_2, and ACC/ZnO exhibit capacitances of 17.7 F/g, 30.6 F/g, and 37.2 F/g, respectively, at a scan rate of 1 mV/s. At a scan rate of 2 mV/s, the specific capacitances of ACC, ACC/MnO_2, and ACC/ZnO are recorded as 7.9 F/g, 12.9 F/g, and 16.6 F/g, respectively. At higher scan rates, the contact time for ions to enter the micropores of the material is shortened, preventing them from reaching the active sites within the material (Tan & Babel, 2023). Consequently, the incomplete utilization of the porous space leads to decreased specific capacitance. ACC/MnO_2 and ACC/MnO_2 exhibit higher specific capacitance than ACC at the observed scan rates, attributed to their enhanced activity area of MnO_2 and support by the local electrical field of ZnO nanorods, respectively.

EIS analysis of the prepared electrodes is presented as a Nyquist plot in Figure 4.22(f) to assess the electrical conductivity. The EIS data were collected to evaluate the resistance of the ACC electrode in comparison to ACC/MnO_2 and ACC/ZnO. Figure 4.22(f) presents the Nyquist plot of the prepared material, with an inset displaying the fitted equivalent circuit. As expected, the ACC material exhibits higher resistance than the modified electrodes, corroborating previous analysis results. Figure 4.22(f) shows the Nyquist plots, where the high-frequency impedance spectrum forms a semicircle, mainly controlled by charge transfer. The semicircle's diameter represents the charge transfer resistance (Rct), while the intercept on the real axis indicates the resistance between the electrode and the electrolyte (Rs) (Mei et al., 2018). The observed linear trend in the low-frequency zone is like the ion diffusion process called Warburg diffusion. It demonstrates that both ACC/MnO_2 and ACC/ZnO exhibit lower Rct and Rs than ACC. This proves that grafting nanostructures onto ACC materials can significantly enhance their performance. The recorded Rct value for ACC is 83.0 Ω. According to the results, the ACC has a relatively high charge transfer resistance. This

can be further elucidated as follows. Under the influence of an electric field, ions are drawn toward the porous structures of the electrode, utilizing macropores as reservoirs to reduce the distance between ions and micropores. The ions flow through mesopores, which house multiple active sites, before entering the micropores. As mentioned earlier, the ACC has an abundance of micropores compared to non-microporous regions. Ion access to the micropores is hindered by the limited number of macropores and mesopores in ACC, which serve as bridges. Because of the limited access, many ions compete for active sites, ultimately hampering charge transfer. Furthermore, the coexistence of numerous ionic forms of Cr^{3+}, Ni^{2+}, and Cu^{2+} in solution exacerbates their adverse effects. Adding MnO_2 and ZnO nanostructures to ACC led to a remarkable reduction in Rct, resulting in 57.6 Ω and 24.8 Ω for ACC/MnO_2 and ACC/ZnO, respectively. In addition, the high Rs value of the prepared materials indicates the presence of intrinsic properties of the carbon material. The improved resistance can be attributed to the deposition of nanoparticles on the carbon fibers. ACC/MnO_2 and ACC/ZnO reported an increased total pore volume in the non-microporous region compared to ACC. While grafting MnO_2 nanostructures onto ACC significantly improved the non-microporous region, ZnO nanorods also contributed to its expansion in ACC/ZnO. However, the decrease in resistance observed in ACC/ZnO is even more remarkable, possibly due to the intensified local electrical field and the inherent hydrophilicity of ZnO nanorods (Kyaw et al., 2020; Laxman et al., 2015).

4.4.3 Electrosorption experiments for removal of individual and mixed metals solution

4.4.3.1 Electrosorption kinetics models in individual ions

The initial experiment used a set of single-ion electrolytes in a CDI cell to evaluate the effect of prepared materials on the removal of Ni^{2+}, Cu^{2+}, and Cr^{3+}. It aimed to compare the adsorption mechanisms of pristine ACC with those of modified materials for operational conditions. As higher voltages were found to enhance the electrosorption capacity of electrodes by improving electrostatic contacts, all tests in this study were conducted at a potential of 1.2V to avoid electrolysis. This study

investigated the influence of particular ion features by analyzing divalent ions (Cu^{2+} and Ni^{2+}) and a trivalent ion (Cr^{3+}) at a concentration of 500 mg/L without any other cations. Figure 4.23 illustrates the adsorption capacities of three distinct electrode materials (ACC, ACC/ZnO, and ACC/MnO_2) for Ni^{2+}, Cu^{2+}, and Cr^{3+}.

Figure 4.23 shows that the adsorption capacity for Cu^{2+}, Ni^{2+}, and Cr^{3+} based on the electrodes used increases with contact time, though the rate slows over time. Additionally, Cu^{2+} consistently exhibited the highest adsorption capacity, followed by Ni^{2+}, with Cr^{3+} having the lowest. After 120 minutes, the adsorption capacity for Cr^{3+} on ACC was 8.1 mg/g, while Ni^{2+} and Cu^{2+} were 19.3 mg/g and 42.0 mg/g, respectively. For ACC/ZnO, the adsorption capacity for Cr^{3+} was 12.8 mg/g; for Cu^{2+} and Ni^{2+}, it was 27.4 mg/g and 56.8 mg/g, respectively. Various factors can account for the observed differences in adsorption capacity. Firstly, it reported that the electrosorption of smaller ions, which occupy less space, is more effective at screening the surface charge of carbon-driven electrodes (Hou & Huang, 2013). Hou et al. (2008) found that ions with a larger hydrated radius cause a more pronounced overlap of the EDL, hindering the movement of similarly charged ions toward the electrode surface (Hou et al., 2008). Among the ions studied, Cr^{3+} has a larger hydrated radius of 4.61 Å, compared to Ni^{2+} (4.04 Å) and Cu^{2+} (4.19 Å) (Nightingale Jr, 1959). Hence, the adsorption capacity of Cr^{3+} (trivalent) was lower than that of divalent ions of Cu^{2+} and Ni^{2+}. Secondly, the ionic radius is an essential metric for comprehending ion adsorption behavior and electrochemical reactions (Faur-Brasquet et al., 2002; Hou & Huang, 2013). The radii of Ni^{2+} and Cu^{2+} ions are 70 pm and 72 pm, respectively. It was reported that for ions with the same charge, the larger ionic radius of Cu^{2+} than Ni^{2+} leads to rapid occupancy of adsorption sites due to steric overcrowding, resulting in more available surface area for Cu^{2+} (Faur-Brasquet et al., 2002). This finding was corroborated by studies on ion removal using oxidized carbon nanotubes, where the uptake amount of Cu^{2+} was higher than Ni^{2+} (Gao et al., 2009). Thirdly, the metal ions' properties and the adsorbent's physical-chemical characteristics influence the adsorption affinity and capacity. While electrostatic attraction in the CDI process significantly impacts ion adsorption, functional groups (e.g., – OH, – COOH) on

surface electrode materials also affect the removal efficiency of metal ions (Y. Li et al., 2018; L. Liu et al., 2017). For divalent metal ions, the primary adsorption mechanism involves chemical interactions with the adsorbent's surface functional groups (Y. Li et al., 2018). A trade-off between these parameters leads to efficiency and adsorption capacity variations during the adsorption/recovery.

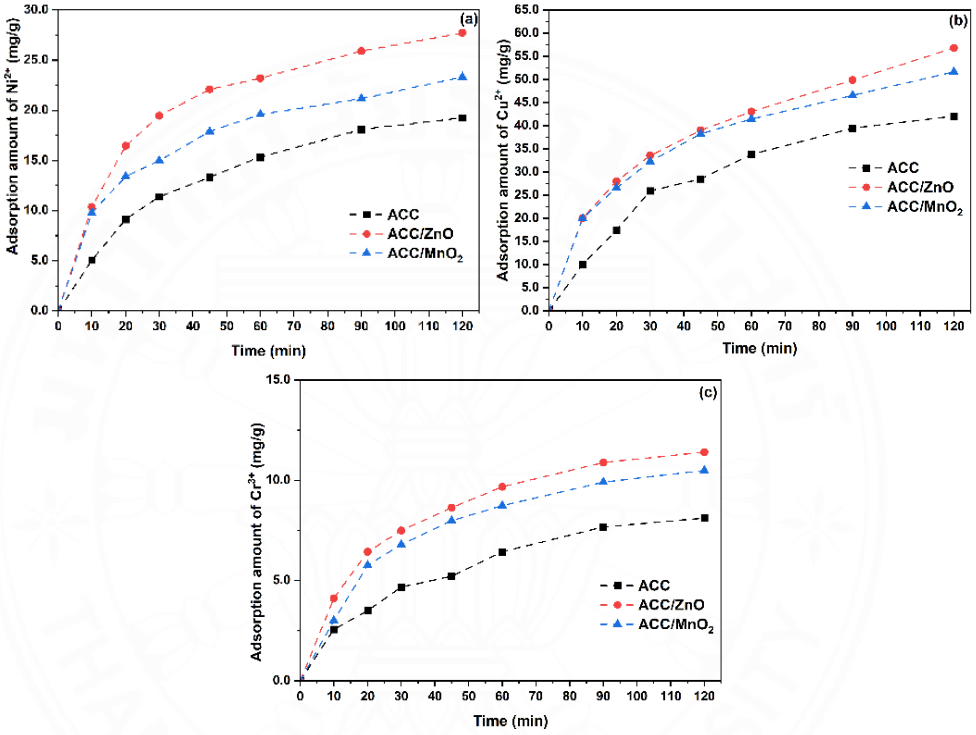

Figure 4.23 Adsorption capacity at various electrode materials of ACC, ACC/ZnO, and ACC/MnO_2 for (a) Cu^{2+} solution, (b) Ni^{2+} solution, and (c) Cr^{3+} solution.

Ni^{2+}, Cu^{2+}, and Cr^{3+} adsorption mechanisms are discussed for a deeper understanding. Figure 4.23 indicates that Cu^{2+} is adsorbed better than Ni^{2+} and Cr^{3+} across different prepared materials. Studies reported that chemical bonds were formed between Ni^{2+} ions and oxygen functional groups on activated carbon material after adsorption (Liu et al., 2015). Additionally, H^{+} ions in carboxylic and phenolic groups can exchange ions, forming carbonyl-Ni complexes (Liu et al., 2015; L. Liu et al., 2017). Similarly, the retention of Cr^{3+} ions on the adsorbent is mainly due to the ionic attraction between metal ions and the carboxylic groups of the adsorbent (Blázquez et al., 2009). However, compared to Ni^{2+} and Cr^{3+}, enhanced Cu^{2+} removal by the CDI

process can be influenced by several factors. Firstly, functional groups on carbon electrodes were identified as essential electron donors, promoting the reduction of Cu^{2+} to Cu or Cu^{+} (Y. Li et al., 2018; Wang et al., 2019). Secondly, it was reported that the electrodeposition of Cu^{2+} at the cathode increased when the voltage exceeded 0.8 V (Wang et al., 2019). These may be the possible reasons for enhanced copper removal.

A deep understanding of kinetic models is crucial for determining the equilibrium time and the adsorption mechanisms between electrolytes and prepared materials. This study employed PFO and PSO as kinetic models to examine the electrosorption process, and the results are presented in Table D.1 (Appendix D). It is evident that both the PFO model and PSO model exhibited high correlation coefficient values ($R^2 > 0.98$), and the fitting data of the PSO model outperformed that of the PFO model. It suggests that the rate-limiting step in this study is most likely attributed to chemisorption. It is widely recognized that the PFO model typically applies to the first 20 to 30 minutes of adsorption, whereas the PSO model characterizes the adsorption behavior throughout the entire adsorption process (Deng et al., 2021; Wang et al., 2019). Furthermore, it was observed that the PSO model is more suitable for describing the physical adsorption of HMs [43]. The results confirm the reliable adsorption capacities as previously discussed and support previous studies on the PSO characterization for the adsorption of Cu^{2+}, Ni^{2+}, and Cr^{3+} (Z. Lu et al., 2015; Wang et al., 2019; Xue et al., 2022; Zhong et al., 2015). According to a recent study by Xue et al. (2022), the cathode underwent a reaction with OH^{-} ions, resulting in the deposition of Ni^{2+} ions and the formation of $Ni(OH)_2$ during the electrosorption process (Xue et al., 2022). Additionally, possible Cu^{2+} reduction in cathodic electrochemical reactions may also influence the results of the kinetic model (Wang et al., 2019). Thus, fitting the experimental data with the PSO model is appropriate. The ions were initially attracted to the electrode surface due to the EDL and were subsequently deposited through hydrolysis and redox reactions.

In addition, the order of adsorption capacity remains consistent for all prepared materials under the same operational conditions. The adsorption capacity of ACC is lowest. However, the adsorption performance can be enhanced by grafting MnO_2

nanostructures and ZnO nanostructures onto ACC. For example, the adsorption amount of Cr^{3+} that may be adsorbed on ACC is 8.1 mg/g. This value increases to 10.5 mg/g and 12.8 mg/g for ACC/MnO_2 and ACC/ZnO, respectively. Similarly, the adsorption capacity of Ni^{2+} increased from 19.3 mg/g on ACC to 22.2 mg/g with ACC/MnO_2 and 27.4 mg/g with ACC/ZnO.

4.4.3.2 Electrosorption kinetics models in competitive ions

Figure 4.24 illustrates the adsorption capacities of various electrode materials (ACC, ACC/ZnO, and ACC/MnO_2) for a mixed solution under different scenarios. Computational results of the SA, SB, and SC mixture derived from the kinetic model are detailed in Table D.2, D.3, and D.4 (Appendix D), respectively.

SA mixture was designed to investigate the competitive behavior of Cu^{2+}, Ni^{2+}, and Cr^{3+} in a solution at equal concentrations. It reveals that the adsorption capacity of the prepared electrode on each element in the SA mixture was lower than that observed in single-ion solutions. For instance, the adsorption capacities of Cr^{3+}, Ni^{2+}, and Cu^{2+} for ACC/ZnO in CDI cells were recorded at 12.8 mg/g, 27.4 mg/g, and 56.8 mg/g, respectively, in individual ion tests, but dropped to 10.0 mg/g, 23.8 mg/g, and 34.1 mg/g in the mixed ion solution. This reduction in adsorption capacity can be attributed to the competition among ions in the solution. In a single-ion solution, the electrode surface is exposed to only one type of ion, which optimizes adsorption efficiency and capacity. However, when Cr^{3+}, Ni^{2+}, and Cu^{2+} coexist in the solution, these ions compete for the same limited adsorption sites, inherently reducing the adsorption capacity for each ion. Additionally, different ions may have varying affinities for the electrode surface, further complicating the adsorption process and diminishing overall adsorption efficiency in mixed ion solutions (Hou & Huang, 2013).

This study found the electrosorption order to be $Cu^{2+} > Ni^{2+} > Cr^{3+}$ in a mixed solution at equal concentrations. Several factors influence this adsorption order, with the intrinsic properties of the metal ions playing a pivotal role. In a mixed solution with equal concentrations, the adsorption capacity of Cu^{2+}, Ni^{2+}, Cr^{3+} is primarily determined by their ionic properties, such as ionic radius, hydration radius, and valence. Among

the ions studied, Cr^{3+} has the largest hydrated radius (4.61 Å) compared to Ni^{2+} (4.04 Å) and Cu^{2+} (4.19 Å), which explains the lower adsorption capacity of Cr^{3+}, a trivalent ion, compared to the divalent ions, Cu^{2+} and Ni^{2+}. The adsorption efficiency of Cr^{3+} is hindered by its larger size, which limits access to the adsorption sites. Additionally, the ionic radii of Ni^{2+} and Cu^{2+} are 70 pm and 72 pm, respectively, suggesting that Ni^{2+} could have an advantage over Cu^{2+} during adsorption. However, the performance of the electrosorption process is heavily influenced by the applied electric field. Despite having a similar charge to Ni^{2+}, Cu^{2+} exhibits a higher adsorption capacity due to enhanced electrosorption on the cathode. This study reveals that the removal of metal ions in the CDI process is governed by ionic radius, hydration radius, valence, and electrostatic interactions between ions and electrode materials.

The prepared electrode was further evaluated to study the influence of initial ion concentration on selectivity and adsorption capacity, as illustrated in Figure 4.24 (d, e, and f) and Figure 4.24(g, h, and i) for the SB mixture and the SC mixture, respectively. Compared to the SA mixture, the SB mixture included a solution with concentrations of 500 mg/L of Cu^{2+}, 200 mg/L of Ni^{2+}, and 100 mg/L of Cr, which showed exciting features. In the SB mixture, the adsorption capacities of Ni^{2+} and Cr^{3+} were lower compared to the SA mixture, whereas Cu^{2+} demonstrated a higher adsorption capacity. This behavior can be attributed to the competition between Ni^{2+} and Cu^{2+}, which are similarly charged. In the SA mixture, there was a notable competition between divalent ions with the same concentration. However, reducing the concentration of Ni^{2+} from 500 mg/L to 200 mg/L increased the ability of Cu^{2+} to be adsorbed. It can be inferred that the adsorption of Cu^{2+} was preferred when the presence of Ni^{2+} was not as significant. Additionally, the decrease in concentrations of specific ions in the SB mixture may have led to a decrease in the efficiency of electrosorption of Cr^{3+} and Ni^{2+}. This could be attributed to the reduction between contact time and mass transfer processes of ions from electrolyte to electrode. The results highlight the significance of the initial ion concentration when maximizing the selective adsorption of metal ions in CDI. Additionally, the SC mixture was conducted by maintaining the concentration of Cu^{2+} at 500 mg/L while adjusting the concentrations of Ni^{2+} and Cr^{3+}

to 100 mg/L and 200 mg/L, respectively, further, to explore the relationship between initial concentration and adsorption capacity. This test aimed to determine whether the observed effects on CDI performance were driven by ion concentration or the intrinsic properties of these ions. When the concentrations of competing ions were altered in the SC mixture, there was a noticeable change in the adsorption capacity. The adsorption capacity of Cu^{2+} increased even further compared to both the SA mixture and the SB mixture, which can be explained by reduced competition between Cu^{2+} and Ni^{2+}. The lower concentration of Ni^{2+} in the SC mixture resulted in less intense competition, thereby enhancing the adsorption capacity of Cu^{2+}, which shares the same divalent charge. Interestingly, the adsorption capacity of Cr^{3+} appeared similar to that of Ni^{2+}, with a slight advantage in favor of Cr^{3+} in the SC mixture. There is a trade-off between ion concentration and the inherent properties of the ions, including ionic charge, ionic radius, and hydration energy. Cr^{3+} faces challenges in adsorption due to its larger ionic and hydrated radii, which hinder its approach to porous surface on the electrode. However, when the concentration of competing ions such as Ni^{2+} is reduced, Cr^{3+} increases adsorption capacities compared to Ni^{2+}, possibly due to increased contact time and mass transfer. Furthermore, the SA mixture demonstrates that the MCDI cell enhances adsorption performance compared to the CDI cell. For example, the adsorption capacities of Cr^{3+}, Ni^{2+}, and Cu^{2+} for ACC/ZnO in the CDI cell were 10.0 mg/g, 23.8 mg/g, and 34.1 mg/g, respectively, while in the MCDI cell, they were 15.3 mg/g, 31.2 mg/g, and 42.7 mg/g for the SA mixture. Similarly, in the SB mixture and the SC mixture, the MCDI cell outperformed the CDI cell under identical conditions. This improvement is attributed to integrating IEMs in the MCDI cell, which increases ion selectivity and reduces co-ion effects (L. Chen et al., 2018; Shen et al., 2021). This mechanism enhances the adsorption capacity by ensuring that more target ions are adsorbed, even in the presence of competing ions, and mitigates the co-ion repulsion effects that lower adsorption efficiency in conventional CDI systems.

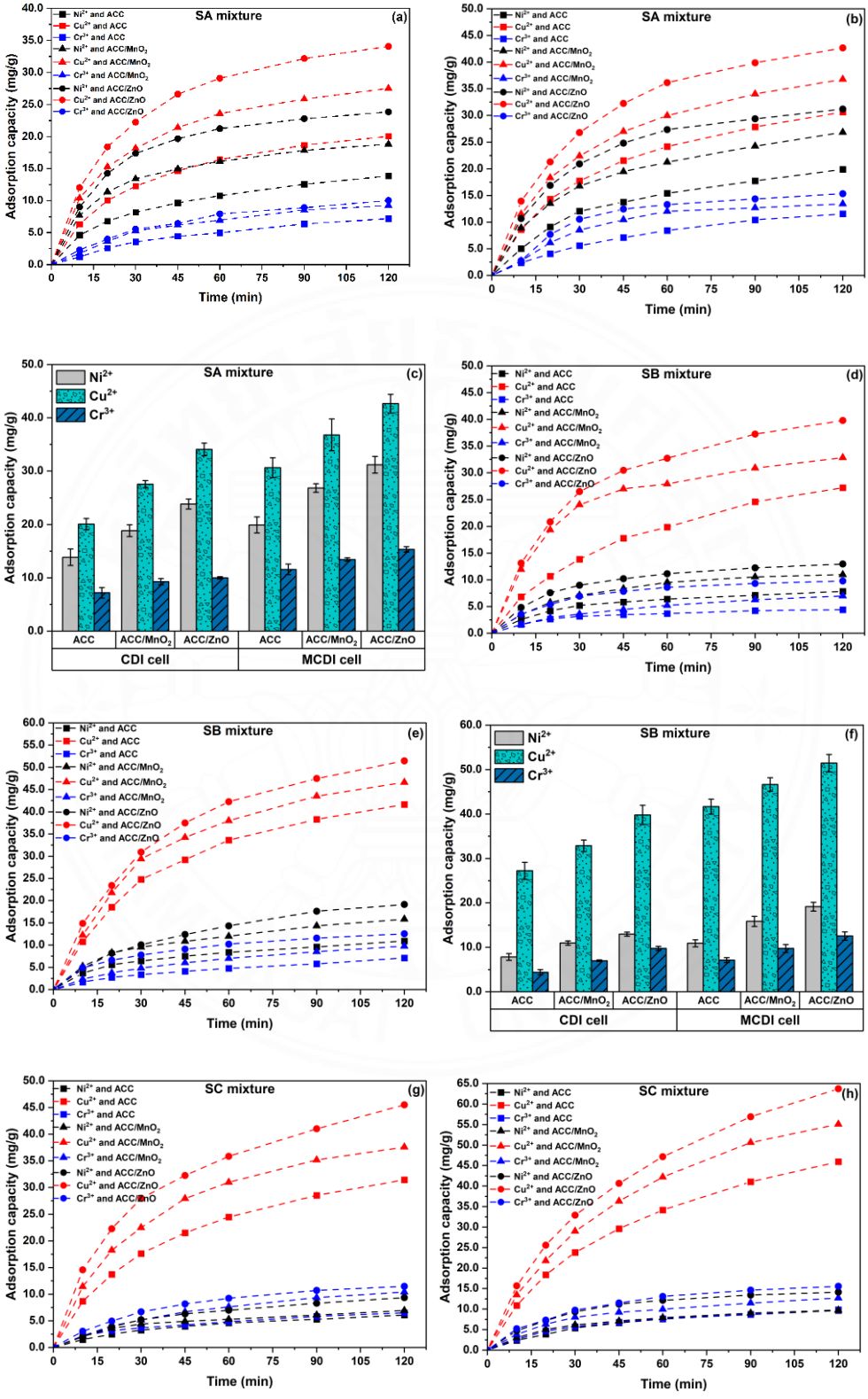
SA mixture
(a)
SA mixture
(b)
SA mixture
(c)
SB mixture
(d)
SB mixture
(e)
SB mixture
(f)
SC mixture
(g)
SC mixture
(h)
Adsorption capacity (mg/g)
Time (min)
Ni2+ and ACC
Cu2+ and ACC
Cr3+ and ACC
Ni2+ and ACC/MnO2
Cu2+ and ACC/MnO2
Cr3+ and ACC/MnO2
Ni2+ and ACC/ZnO
Cu2+ and ACC/ZnO
Cr3+ and ACC/ZnO
Ni2+
Cu2+
Cr3+
ACC
ACC/MnO2
ACC/ZnO
CDI cell
MCDI cell

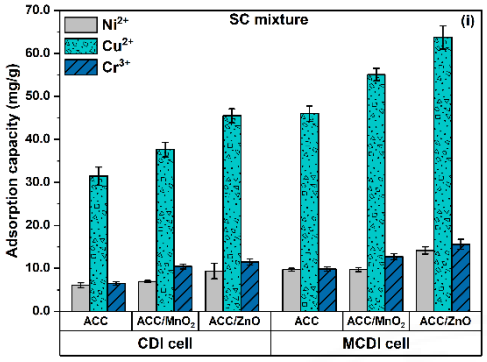

Figure 4.24 Adsorption capacity of Cu^{2+}, Ni^{2+}, and Cr^{3+} on prepared materials (ACC, ACC/MnO_2, and ACC/ZnO) with SA mixture (a-c): (a) CDI cell, (b) MCDI cell, (c) comparison of equilibrium adsorption capacity values, SB mixture (d-f): (d) CDI cell, (e) MCDI cell, (f) comparison of equilibrium adsorption capacity values, SC mixture (g-i): (g) CDI cell, (h) MCDI cell, (i) comparison of equilibrium adsorption capacity values.

To better understand the effectiveness of modified electrodes compared to pristine ACC for removing Ni^{2+}, $Cu^{2+,}$ and Cr^{3+}, it is crucial to analyze the performance adsorption under various scenarios. In the SA mixture, ACC exhibits adsorption efficiencies of 13.9 mg/g for Ni^{2+}, 20.1 mg/g for Cu^{2+}, and 7.2 mg/g for Cr^{3+}. The adsorption capacity of the pristine ACC in the CDI cell can be attributed to its inherent properties, which result from its high surface area and porosity. Once MnO_2 nanostructures are added to ACC, there is a noticeable enhancement in adsorption efficiency. The removal capacity for Cu^{2+} increases to 27.5 mg/g, Ni^{2+} to 18.8 mg/g, and Cr^{3+} to 9.3 mg/g. This improvement can be ascribed to many factors. As previously discussed, grafting MnO_2 onto ACC modified its surface properties, increased porosity, and introduced additional active sites, enhancing performance. Additionally, the inherent properties of MnO_2 enhance the material's pseudocapacitive behavior through the intercalation cations, including K^+, Na^+, Li^+, H^+, and protons (H_3O^+). However, the enhanced adsorption capacity of Ni^{2+}, $Cu^{2+,}$ and Cr^{3+} on ACC/MnO_2 can be explained by the intercalation/deintercalation mechanisms associated with $MnO_{2,}$ as some reports (Hu et al., 2020; Lihu Liu et al., 2017; C. Zhang et al., 2024). Although the mechanism

of oxidation of Cr^{3+} by MnO_2 remains unclear, a general reaction has been suggested as Equation 4.14, which may partially explain the observed increase in adsorption capacity (Zhong et al., 2015).

On the other hand, introducing ZnO into ACC further enhanced removal efficiencies, particularly for Cu^{2+}, which sees a substantial increase to 34.1 mg/g. The amphoteric nature of ZnO, combined with its ability to interact with metal ions through surface hydroxyl groups, likely underpins this superior performance (Kyaw et al., 2020; Laxman et al., 2015). Grafting ZnO nanostructures onto ACC has been observed to create more favorable adsorption sites for storing ions than omly ACC. In addition, the presence of ZnO nanorods has been widely acknowledged for generating localized electric field enhancement at the electrode-nanoparticle interface (Laxman et al., 2015; Tan & Babel, 2023). As a result, the unique properties of ZnO nanorods allowed for a more focused electric field, leading to enhanced adsorption capacity and faster ion removal. Besides, ACC/ZnO also shows a marked increase in the removal of Ni^{2+} (23.8 mg/g) and Cr^{3+} (10.0 mg/g). The increase in adsorption capacity for Cu^{2+}, Ni^{2+}, and Cr^{3+} indicates that adding ZnO nanostructures on ACC not only provides an effective solution for the removal of these ions but also enhances the reactivity of the electrode's surface compared to ACC and ACC/MnO_2, making it a highly effective material for multi-ion removal scenarios.

$$3MnO_2 + 2Cr^{3+} + 2H_2O = 2HCrO_4^- + 3Mn^{2+} + H^+ \quad (4.14)$$

In the SB mixture, the concentrations of Ni^{2+} and Cr^{3+} were adjusted from 500 mg/L to 200 mg/L and 100 mg/L, respectively, while Cu^{2+} remained at 500 mg/L. The efficiency of Cu^{2+} removal increased between the SA mixture and the SB mixture, while the removal of Ni^{2+} and Cr^{3+} decreased. Furthermore, the adsorption amount of Cu^{2+} by ACC/MnO_2 increased from 27.2 mg/g (ACC) to 32.9 mg/g, whereas the adsorption amount of Ni^{2+} and Cr^{3+} were 11.0 mg/g and 7.0 mg/g, respectively. Consistently, ACC/ZnO material achieved better outcomes compared to ACC and ACC/MnO_2, with a Cu^{2+} removal rate of 39.8 mg/g, as well as removal rate of 12.9 mg/g for Ni^{2+} and 9.8

mg/g for Cr^{3+}. The data in the SC mixture demonstrates the greater effectiveness of ACC/ZnO compared to ACC and ACC/MnO_2. In general, modification of ACC with MnO_2 and ZnO significantly improved the removal of Cu^{2+}, Ni^{2+}, and Cr^{3+} by enhancing performance by adding active sites. While MnO_2 nanostructures on ACC improved performance through capacitive behavior, ZnO nanostructures amplified local electric fields, resulting in higher adsorption capacity.

Figure 4.24 shows the adsorption amounts of Cu^{2+}, Ni^{2+}, and Cr^{3+} on various prepared electrodes under different scenarios, while Table D.2, D.3, and D.4 (Appendix D) present the parameters of the applied kinetic models. Adsorption capacity increased sequentially from ACC to ACC/MnO_2 and then to ACC/ZnO in CDI and MCDI cells. Using ACC in CDI cells exhibited adsorption capacities of 13.9 mg/g for Ni^{2+}, 20.1 mg/g for Cu^{2+}, and 7.2 mg/g for Cr^{3+}, while MCDI cells improved these capacities to 19.9 mg/g for Ni^{2+}, 30.6 mg/g for Cu^{2+}, and 11.6 mg/g for Cr^{3+}. Although ACC is effective in the CDI cell, it faces limitations in competitive environments with multiple ions due to varying ionic charges and radii. The MCDI cell mitigates these limitations through the selectivity of IEMs, thereby enhancing overall performance. The use of the MCDI cell also improved the adsorption amounts for ACC/MnO_2, increasing from 18.8 mg/g to 26.8 mg/g for Ni^{2+}, 27.5 mg/g to 36.8 mg/g for Cu^{2+}, and 9.3 mg/g to 13.4 mg/g for Cr^{3+}. Similarly, the ACC/ZnO electrode exhibited the highest adsorption capacities among the materials tested, with 23.8 mg/g for Ni^{2+}, 34.18 mg/g for Cu^{2+}, and 10.0 mg/g for Cr^{3+} in CDI cells, and 31.2 mg/g for Ni^{2+}, 42.7 mg/g for Cu^{2+}, and 15.33mg/g for Cr^{3+} in MCDI cell. The SB mixture and the SC mixture revealed the order of adsorption capacity as ACC/ZnO > ACC/MnO_2 > ACC in both CDI and MCDI cells. Overall, the enhancement of electrode properties led to improved adsorption in CDI and MCDI cells, with MCDI consistently showing superior ion adsorption performance due to the IEMs.

4.4.3.3 CDI tests for electrosorption and regeneration

As previously indicated, an in-depth understanding of the electrosorption parameters revealed that ACC/ZnO highlights superior characteristics regarding the

prepared electrodes. Therefore, ACC/ZnO was selected to test the adsorption capacity and regeneration rate of the mixed ion solution over several cycles compared to ACC. The comparison between a CDI cell and an MCDI cell provided a better understanding of the presence of organics in the removal of multiple ions.

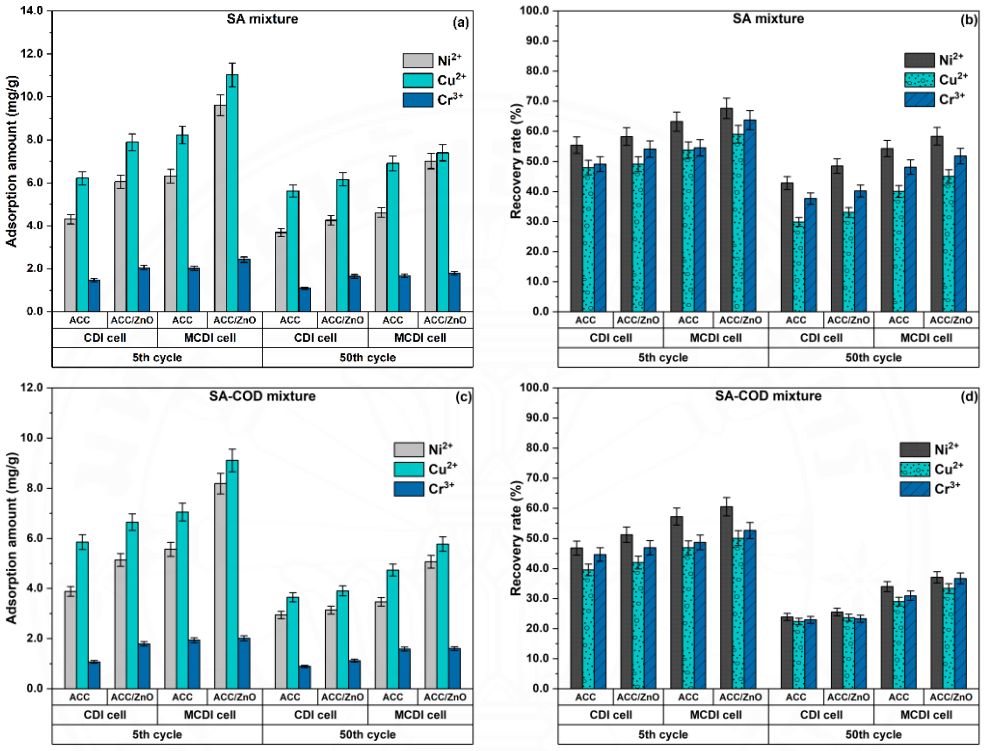

Figure 4.25 Comparison of adsorption performance for Cu^{2+}, Ni^{2+}, and Cr^{3+} on ACC and ACC/ZnO in CDI and MCDI cells under SA mixture for (a) adsorption amount, (b) recovery rate, and under the SA-COD mixture for (c) adsorption amount, (d) recovery rate.

Figure 4.25 presents a detailed examination of the adsorption efficiency during the 5th and 50th cycles of a 50-cycle test on ACC and ACC/ZnO in both CDI and MCDI cells under two different conditions: a mixed solution (SA mixture) and the same solution with 500 mg/L organic matter added (SA-COD mixture). As presented in Figure 4.25(a), the adsorption amount varies depending on how each metal ion interacts with the electrode materials in different CDI configurations. The results are consistent with our previous discussion. CDI cells show that ACC/ZnO has a higher adsorption

capacity for Cu^{2+} and Ni^{2+} than ACC, with Cu^{2+} adsorbed in more significant amounts than Ni^{2+}. For instance, the adsorption amounts of Cu^{2+} and Ni^{2+} by ACC/ZnO electrode were recorded at 7.9 mg/g and 6.1 mg/g, respectively, while ACC recorded 6.2 mg/g and 4.3 mg/g for Cu^{2+} and Ni^{2+} at the 5th cycle. However, the adsorption amount for Cr^{3+} is less significant, possibly due to the properties of Cr^{3+} as described in the report. Incorporating IEMs into MCDI cells significantly enhances selectivity and adsorption efficiency (P. Biesheuvel & A. Van der Wal, 2010; NguyenTan et al., 2024a). The effectiveness of ACC/ZnO in the removal of various metal ions in the MCDI cell compared to the CDI cell has been proven, with recorded values of 9.6 mg/g and 11.0 mg/g for Ni^{2+} and $Cu^{2+,}$ respectively, at the 5th cycle. The improvement in MCDI cells under no organic matter can be attributed to decreased co-ion expulsion, which allows for better adsorption capacity. When adding a mixed solution with organic matter, Figure 4.25(c) shows that organic matter significantly affects adsorption capacity. Besides, the presence of Na^{+} ions in sodium acetate (CH_3COONa), employed for simulating organic matter in synthetic wastewater, may reduce the adsorption capacity in the CDI process by competing for active sites on the electrode surface, thereby limiting the removal of target ions. Additionally, the increased ionic strength can alter the electrical double layer, affecting adsorption efficiency of HMs in solution. Compared to the SA mixture, there is a noticeable decrease in adsorption for all metal ions in the SA-COD mixture. For instance, Ni^{2+} and Cu^{2+} adsorption amounts on ACC/ZnO electrode decreased to 5.1 mg/g and 6.7 mg/g in CDI cells and to 8.2 mg/g and 9.1 mg/g in MCDI cells at the 5th cycle in the SA-COD mixture. A significant decrease in adsorption was observed in the reduction performance under the presence of organics (L. Chen et al., 2018; Mossad & Zou, 2013). This leads to a reduction in its free concentration and, as a result, its adsorption on the electrodes is decreased (Jaegyu Shim et al., 2021). Still, the adsorption capacity of the prepared electrode decreased significantly between the 5th cycle and the 50th cycle in both the CDI cell and MCDI cell, which are discussed in the recovery rate of ion.

The recovery rate, depicted in Figure 4.25(b and d), provides more insight into the differences in performance across the prepared electrodes and CDI configurations

in presence of organics and no organics in wastewater. Unlike the adsorption capacity, the recovery rates of Cu^{2+} are the lowest, while the recovery rates of Ni^{2+} are higher than Cr^{3+} in tests. For example, the recovery rate of Ni^{2+} and Cu^{2+} for ACC was recorded at 55.4% and 47.9%, respectively, while ACC/ZnO showed slightly higher recovery rates of 58.3% and 49.1%. The recovery rate of Ni^{2+} with Cu^{2+} was observed to be higher, as previously expected. During the charging phase, prepared ions were adsorbed at the cathode while an electrodeposition of Cu^{2+} took place at the electrode. As a result, the recovery rate of Cu^{2+} is lower than that of Ni^{2+} in the same charge conditions. MCDI cell was reported to improve adsorption efficiency significantly due to the perm-selectivity of IEMs, shielding the electrode from dissolved oxygen (Lee et al., 2010). Besides, using IEMs has improved the recovery rate, as several previous studies have reported (Hassanvand et al., 2018; Jaegyu Shim et al., 2021). At the 5th cycle, the recovery rates for Ni^{2+} and Cu^{2+} using ACC/ZnO in MCDI cells were 67.7% and 59.1%, respectively. Figure 4.25(d) shows that the recovery rates for ions are generally lower under conditions involving organic matter (SA-COD mixture) compared to a mixed solution without the presence of organic matter (SA mixture). This highlights the difficulties presented by organic substances in the solution. The recovery rates in the SA-COD mixture exhibit a comparable pattern to that observed in the SA mixture, with Ni^{2+} displaying the highest recovery rate, followed by Cr^{3+} and Cu^{2+}. During the 5th cycle, it was noted that the utilization of IEM resulted in enhanced recovery rates in the SA-COD mixture.

The recovery rates for Ni^{2+}, Cr^{3+}, and Cu^{2+} were recorded as 60.6%, 52.6%, and 50.1%, respectively. However, there was a noticeable decrease in recovery rates at the 50th cycle. The recovery rates for Ni^{2+}, Cr^{3+}, and Cu^{2+} using ACC/ZnO in CDI cells decreased from 51.2% to 25.5%, 46.9% to 23.3%, and 42% to 23.6%, respectively. In contrast, the recovery rates in the SA mixture also declined, though the extent of reduction was less significant. The recovery rates for Ni^{2+} decreased from 58.3% to 48.5%, for Cr^{3+} from 54.1% to 40.2%, and for Cu^{2+} from 49.1% to 33.0%. The presence of organic matter significantly affected the performance of the electrode material and IEMs in the CDI process (Mossad & Zou, 2013). Consequently, the accumulation of

contaminants on the electrode and membrane increased over time, leading to reduced ion recovery rates. Simultaneously, the adsorption capacity of the electrode also decreased.

The recovery rate for ions in this study is notably lower than expected, which could be attributed to several factors. First, the strong electrostatic binding of ions to functional groups on the electrode surface and the carbon material's inherent properties may inhibit ions' release (Chen et al., 2023; Lee et al., 2010). Second, the reduced recovery rate could be due to the blockage and partial regeneration of co-ions at zero voltage (L. Chen et al., 2018). When the potential is cut off, the counter-ions, which have an opposite charge to the electrode during adsorption, are repelled. However, their concentration in the carbon's pores only decreases to match the feed solution (Hou & Huang, 2013; Hou et al., 2008).

Figure 4.26(a) shows the electrosorption performance over 50 consecutive charge-discharge cycles with peak value on the x-axis shifts to the right as the number of process hours increased. In Figure 4.26(a), it can be observed that the current density of ACC/ZnO in the CDI cell with the SA-COD mixture went through a significant decrease from 1st cycle to the 50th cycle, whereas ACC/ZnO in the CDI cell with SA mixture showed a less rapid decline. A decreasing current density over time was reported due to the incomplete release of ions from the electrode surface (Shen et al., 2021; Zhang et al., 2020). After extended operation, the electrodes lost their ability to effectively contribute to the electrosorption capacity. Fouling caused a significant decrease in potential at the electrode surface. As a result, the driving force on ions was reduced, leading to a slower movement of ions during the charging/discharging process. The different current densities between ACC/ZnO in the CDI cell with the SA-COD mixture and ACC/ZnO in the CDI cell with the SA mixture can be attributed to organic matter in the SA-COD mixture. Nevertheless, the IEM demonstrated remarkable stability in the MCDI cell, remaining consistent from the 5th cycle to the 50th cycle.

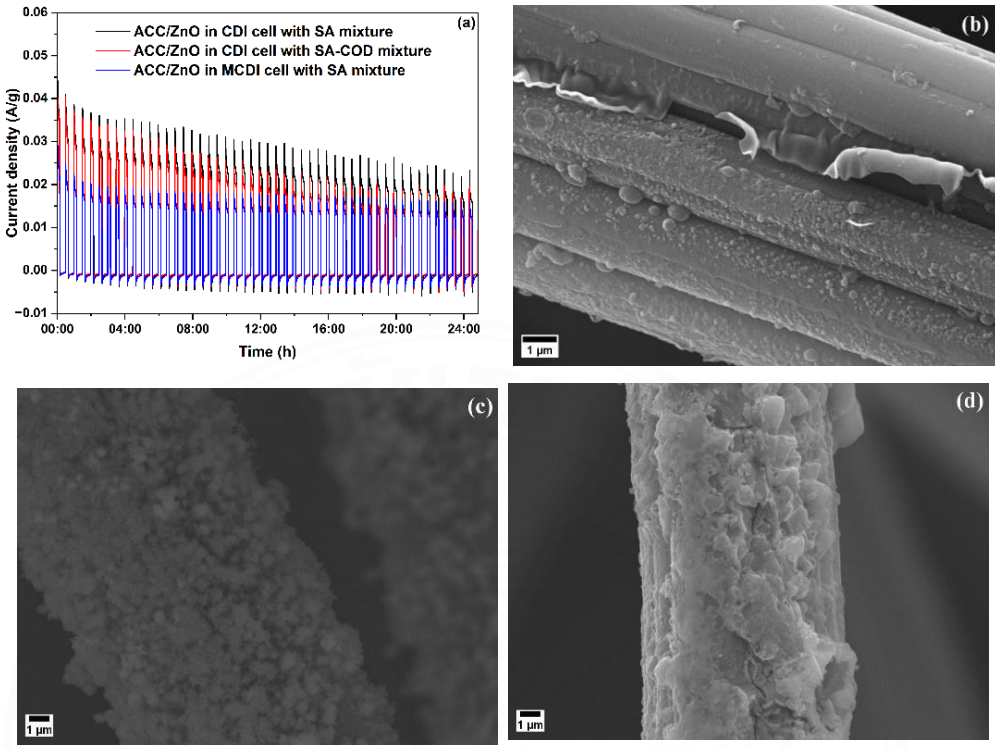

Figure 4.26 (a) Current density profile for 50 consecutive charge-discharge cycles, SEM images of the surface cathode of b) ACC in CDI cell with SA mixture, (c) ACC/ZnO in CDI cell with SA mixture, and (d) ACC/ZnO in CDI cell with SA-COD mixture after 50 cycles.

To verify the cause of the decrease in adsorption efficacy, FE-SEM images were analyzed in conjunction with EDS spectra following a 50-cycle test, as illustrated in Figure 4.26(b, c, and d) and Figure D.2 (Appendix D). No cleaning methods were used to study electrode degradation in the CDI cell. Figure 4.26(b) presents the image of the surface cathode of ACC in a CDI cell with the SA mixture. It exhibits the appearance of deposits as the binding of ions used on the surface of carbon fibers. Additionally, the surface exhibits notable texture and irregularities, likely due to the deposition of these metals on the carbon fibers during 50 cycles. Figure 4.26(c) shows that the carbon fiber surface is covered with dense particles, likely metal oxides. The uniformity and density of the particles suggest good dispersion and attachment of ZnO and metal ions used on the ACC/ZnO surface. In contrast, Figure 4.26(d) shows a surface with more irregular

structures than the ACC/ZnO in the CDI with SA mixture. This suggests that adding organic matter in the solution significantly influenced the surface morphology, leading to larger aggregates or a more complex surface texture. The more rugged surface could be attributed to a deposit of metal oxides on the surface ACC/ZnO contributing to fouling caused by organic matter.

4.4.4 Conclusions for removal of individual and mixed metals solution

This study highlights the enhanced performance of ACC/ZnO and ACC/MnO_2 electrodes compared to ACC in removing HMs (Cu^{2+}, Ni^{2+}, and C^{r3+}) using CDI and MCDI cells. This enhancement is primarily due to the increased surface area and the formation of active sites, which are crucial for efficient HM removal. ACC/ZnO electrode exhibited superior adsorption capacities, with the highest values recorded in the CDI cell, such as 34.1 mg/g for ACC/ZnO, 27.5 mg/g for ACC/MnO_2, and 20.1 mg/g for ACC for Cu^{2+} removal. These figures significantly surpassed those of pristine ACC and ACC/MnO_2 electrodes, underscoring ZnO's effectiveness in enhancing adsorption through local electric field amplification and increased surface reactivity. Besides, the MCDI cell consistently outperformed the CDI cell across all electrode materials, primarily due to integrating IEMs that enhance ion selectivity and mitigate co-ion expulsion effects. While the ACC/ZnO electrode in the CDI cell showed an adsorption capacity of 34.1 mg/g for Cu^{2+}, this increased to 42.7 mg/g in the MCDI configuration. Similarly, the adsorption capacities for Ni^{2+} and Cr^{3+} also saw significant improvements in the MCDI cell compared to the CDI cell. Furthermore, the study also highlights the influence of organic matter on HMs removal efficiency, noting that organic matter can hinder ion diffusion and adsorption due to pore blockage and fouling. These findings highlight the potential of ZnO and MnO_2 modifications to ACC in improving the efficiency of CDI and MCDI systems for HMs ion removal, offering a promising approach for water purification technologies. Future research should further explore these modified electrodes' long-term stability and regeneration capabilities, especially under varying environmental conditions and in the presence of complex organic contaminants.

4.5 Potential of capacitive deionization for removal of heavy metals from electroplating wastewater

4.5.1 Electrosorption kinetics models in electroplating wastewater

Figure 4.27 illustrates the adsorption capacity of ions removed utilizing ACC and ACC/ZnO in both the CDI cell and the MCDI cell. In Figure 4.27(a), the adsorption amount of Cr, Ni, Cu, and Mn was recorded at 0.17 mg/g, 0.23 mg/g, 0.22 mg/g, and 0.29 mg/g, respectively, after 10 minutes, whereas the other ions displayed a slight increase to around 0.1 mg/g. Notably, the adsorption capacity of Zn significantly rose to 6.1 mg/g. The differences in adsorption capacity of cations can be attributed to the difference in their initial concentrations. Several studies have reported that the ionic charge, hydrated radius, and initial concentration of ions significantly impact the adsorption capacity of carbon-based electrodes in CDI process (Chen et al., 2015; Hou & Huang, 2013). It was reported that the adsorption capacity of cations in the CDI process is highly dependent on the initial concentration rather than the hydrated radius in a competitive multi-ionic environment of alkali- and alkaline-earth cations, resulting from the more vital driving force caused by a higher concentration gradient (Hou & Huang, 2013). At the same time, higher initial concentrations result in a greater abundance of ions, which accelerates their interaction with the electrode in the CDI cell when exposed to the electric field generated by the electrode pair. Moreover, Figure 4.27(a) reveals a trend in which ion removal efficiency improves over time across all ions, underscoring the significance of extended operational periods in achieving optimal performance.

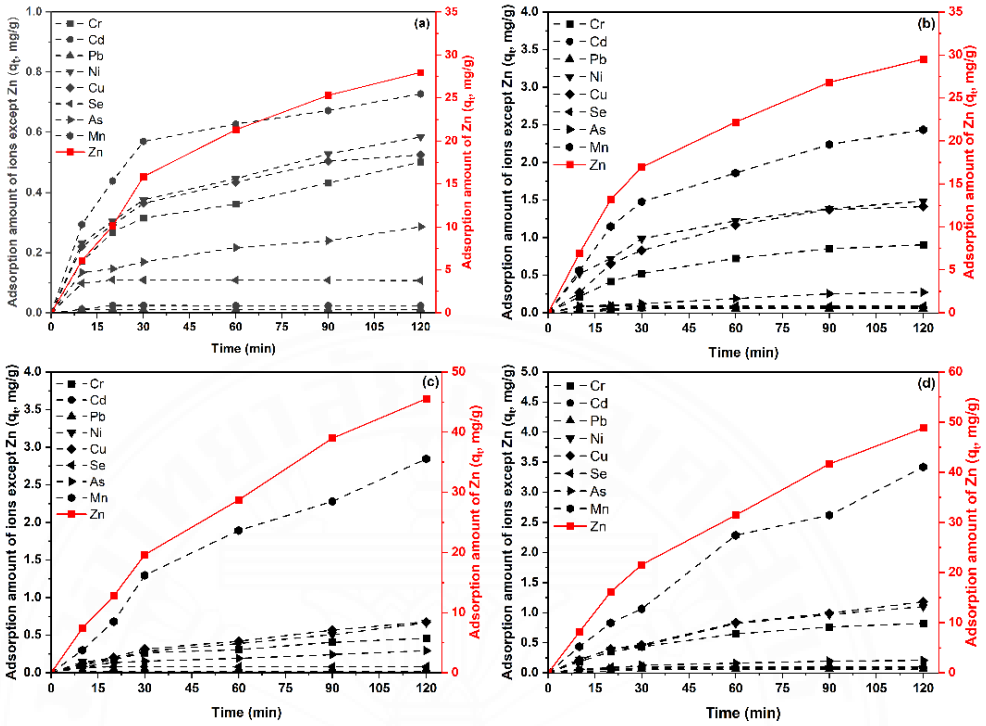

Figure 4.27 Adsorption capacity of ions in electroplating wastewater utilizing (a) ACC in the CDI cell, (b) ACC/ZnO in the CDI cell, (c) ACC in the MCDI cell, and (d) ACC/ZnO in the MCDI cell.

Figure 4.27(b) illustrates the role of ZnO nanostructures attached to carbon fiber in the CDI tests by adsorption capacity. The ACC/ZnO electrodes have a higher adsorption capacity for ions removal than the ACC electrodes in the CDI cell. The removal efficacy of metals such as Cr, Zn, Ni, Cu, and Mn is significantly improved by introducing ZnO nanostructures. For example, the ACC/ZnO electrode adsorbed 0.90 mg/g of Cr, 29.52 mg/g of Zn, 1.49 mg/g of Ni, 1.41 mg/g of Cu, and 2.44 mg/g of Mn after 120 minutes in CDI test, whereas the ACC electrode removed only 0.50 mg/g of Cr, 27.97 mg/g of Zn, 0.58 mg/g of Ni, 0.53 mg/g of Cu, and 0.73 mg/g of Mn. The enhanced adsorption of ACC/ZnO can be attributed to several factors, including improved electron transfer properties resulting from ZnO modification and an enhanced local electric field (Kyaw et al., 2020; Laxman et al., 2015). Additionally, more active sites and an expanded surface area in ACC/ZnO contribute to this improvement as

explained in detail above. On the other hand, both ACC and ACC/ZnO electrode in the CDI cell showed promising trends in improved ion removal efficiency over time. There was a significant increase in the capacity adsorbed by ACC/ZnO compared to ACC. For Zn removal, the adsorption capacity of ACC/ZnO increased from 6.93 mg/g at 10 min to 29.52 mg/g at 120 min, while ACC's adsorption capacity increased from 6.10 mg/g at 10 min to 27.97 mg/g at 120 min. For Cu removal, ACC/ZnO reached 1.41 mg/g, while ACC achieved 0.53 mg/g. The ACC/ZnO electrode reached 2.44 mg/g of Mn, compared to 0.73 mg/g by the pristine ACC electrode. The time-dependent adsorption trends observed in ACC and ACC/ZnO indicate that ion removal efficiency generally improves with extended operation periods. ZnO nanostructures facilitate a more efficient interaction between the electrode surface and the metal ions, leading to a more pronounced adsorption effect over time. Adsorption capacity of materials is influenced by the properties of metal ions and the adsorbent's physical-chemical characteristics. In CDI processes, metal ion removal efficiency is affected by electrostatic attraction and surface functional groups (e.g., –OH, –COOH) on the electrode materials (Y. Li et al., 2018; L. Liu et al., 2017). Additionally, the primary adsorption mechanism for divalent metal ions involves chemical interactions with the adsorbent’s surface functional groups (Y. Li et al., 2018). The superior performance of ZnO is attributed to its amphoteric nature and interaction with metal ions through surface hydroxyl groups (Kyaw et al., 2020; Laxman et al., 2015). Additionally, ZnO nanorods generate localized electric field enhancement at the electrode-nanoparticle interface, resulting in a more focused electric field, which enhances adsorption capacity and accelerates ion removal (Kyaw et al., 2020)

The effect of ZnO modification is particularly significant for metals with larger hydrated radii, such as Cu and Ni, where the enhanced electrode surface properties provided by ZnO likely facilitate improved ion transport and adsorption. This is evident from the superior performance of ACC/ZnO in removing these metals compared to ACC alone. For instance, at 120 minutes, ACC/ZnO removed 1.41 mg/g of Cu and 1.49 mg/g of Ni, compared to 0.53 mg/g and 0.58 mg/g, respectively, for ACC. This suggests that the ZnO modification helps to overcome the limitations associated with the

hydrated radius of larger metal ions, enabling more efficient adsorption in competitive multi-ionic environments.

The adsorption capacity of ACC and ACC/ZnO in CDI and MCDI cells is observed in Figure 4.27(c and d), respectively. These figures reveal the impact of prepared material on various CDI configurations and their effectiveness in eliminating metal ions, such as Cr, Zn, Ni, and Mn, from real wastewater samples. Using IEMs in the MCDI cell resulted in enhanced adsorption capacity of ions compared to the CDI cell for both electrode materials, as presented in Figure 4.27(c and d). There is a significant enhancement in the adsorption capacity observed in MCDI cell compared to CDI cell. For instance, the adsorption capacity of Zn in the CDI cell was 27.97 mg/g, while it reached 45.56 mg/g in the MCDI cell. ACC/ZnO in the CDI cell displayed adsorption capacity of 29.52 mg/g, achieving an adsorption amount of 48.81 mg/g in the MCDI cell. The adsorption amount of Mn reached 2.44 mg/g in CDI cell, while it reached 3.42 mg/g in MCDI cell. Additionally, the adsorption capacity of Cr with ACC was 0.50 mg/g and 0.53 mg/g in the CDI cell and MCDI, respectively, while ACC/ZnO exhibited amount of 0.86 mg/g in CDI cell and 0.88 mg/g in MCDI cell. The enhanced adsorption in the MCDI cell compared to the CDI cell is attributed to the IEMs, which reduce co-ion phenomena during electrosorption process and enhance selective ion removal (P. M. Biesheuvel & A. van der Wal, 2010; NguyenTan et al., 2024b). Among the metal ions investigated, Cr^{3+} exhibits the largest hydrated radius (4.61 Å) compared to others (e.g., Ni^{2+} (4.04 Å), Cu^{2+} (4.19 Å), and Zn^{2+} (4.30 Å)) (Nightingale, 2002). In this case, using IEMs in MCDI cell for Cr removal slightly improves the adsorption capacity compared to CDI for both ACC and ACC/ZnO. However, the larger hydrated radius of Cr presents difficulties when it comes to effective adsorption on prepared materials and IEMs, especially when several metal ions are present in wastewater.

Figure 4.27 exhibits that ion selectivity in CDI and MCDI cells depends more on the initial ion concentration than ionic charge, ionic radius or hydrated radius. When the adsorption selectivity of ion i ($S_{i,t}$) is higher, indicating that ion i is more likely to be adsorbed onto the electrode material than other co-existing ions in wastewater. In general, the selectivity order in CDI cell is Zn > Mn > Ni > Cu > Cr > As > Se > Cd >

Pb, whereas it is Zn > Mn > Cu > Ni > Cr > As > Se > Cd > Pb in MCDI cell. The critical difference is the switch in selectivity between Ni and Cu. Although Cu has a slightly higher initial concentration (4.46 mg/L of Cu vs. 4.31 mg/L of Ni), Ni adsorption capacity is more significant in CDI cell due to its smaller ionic (70 pm) and hydrated radius (4.04 Å) compared to Cu (72 pm and 4.19 Å) (Nightingale, 2002). The smaller size of the Ni ions enables it to efficiently reach and occupy adsorption sites within a porous material, outperforming the Cu ions. In MCDI, however, Cu shows higher selectivity than Ni, likely due to the presence of IEMs that reduce co-ion interference and enhance Cu removal. Additionally, Cu adsorption increases at the cathode when the voltage exceeds 0.8 V as previously reported (Wang et al., 2019), further favoring Cu over Ni in electrode material.

4.5.2 Effect of flow rate on CDI tests for electrosorption and regeneration

The electrosorption/regeneration process in CDI test involved consecutive 50 cycles without cleaning method for flow rate of 10, 15, and 25 mL/min. Each cycle comprised a 10-min charging phase at a potential of 1.2 V and a 20-min discharging phase under short-circuit mode. Improved adsorption capacity and recovery rate of ions were shown to be correlated with enhanced potential (Tan & Babel, 2023; Wang et al., 2019). However, elevated voltage may induce unstable side reactions, such as water electrolysis, which can reduce efficiency and increase energy consumption (Rathi & Kumar, 2020; Wang et al., 2015). To mitigate these effects, an applied voltage of 1.2 V was employed in this work to prevent electrolysis and optimize performance. Additionally, a short-circuit mode was implemented during the discharge phase to limit adsorptive reversal and ensure complete desorption of adsorbed counter-ions from the electrode.

The adsorption amount and recovery rate of ACC and ACC/ZnO in CDI cell and MCDI cell at flow rates of 10 mL/min, 15 mL/min, and 25 mL/min are presented in Table E.2, Table E.3, and Table E.4 (Appendix E), respectively. The results suggest that higher flow rates increase the efficacy of metal removal from wastewater. Additionally, varying trends in ion selectivity and recovery rates in effluent samples

are observed at different flow rates. As shown in Table E.2, Table E.3, and Table E.4 (Appendix E), the adsorption amounts for metal ions such as Ni, Cu, Cr, As, Se, Cd, and Pb in both CDI and MCDI cells remain below 0.1 mg/g at all flow rates during the observed 5th cycle and 50th cycle. This low adsorption capacity can be attributed to the low concentration of these metal ions and weak recovery rates, leading to a significant amount of ions remaining on the electrodes without being released back into the feed solution. It appears that the grafting of ZnO nanostructures onto carbon fiber is not adequate for these metal ions under the conditions of studied wastewater combined with the discharging phase without voltage. Additionally, though Mn shows the second highest selectivity among metal ions in wastewater, as previously discussed, its adsorption capacity in the electrosorption/regeneration process remains low at around 0.1 mg/g in the CDI cell. However, the presence of ion IEMs in the MCDI cell improved both Mn adsorption capacity and recovery rate. For instance, at a flow rate of 10 mL/min, the adsorption amounts for Mn in the MCDI cell with ACC and ACC/ZnO are 0.1 mg/g and 0.13 mg/g, respectively, with recovery rates of 37.5% and 40%.

Among the metal ions detected in wastewater, Zn^{2+} exhibits the highest concentration and specific selectivity. In Table E.2 (Appendix E), the ACC/ZnO electrode at a flow rate of 10 mL/min in a CDI cell demonstrated an adsorption capacity of 2.67 mg/g for Zn^{2+} at the 5th cycle compared to pristine ACC, which showed 2.55 mg/g at the 5th cycle. This trend is consistent with the results in Table E.3 and E.4 (Appendix E), indicating that ZnO nanostructures enhance adsorption efficiency compared to ACC. The recovery rates for ACC/ZnO were generally higher, suggesting improved desorption and recyclability, which are critical for sustainable CDI operations. For instance, at a flow rate of 15 mL/min, the recovery rate for ACC/ZnO was 48.4% and 40.5% whereas ACC recorded at 47.3 % and 38.8 % at the 5th cycle, 50th cycle respectively. The introduction of IEMs in the MCDI cell further enhanced the performance of both ACC and ACC/ZnO electrodes by selectively allowing counter-ions to pass while rejecting co-ions, thereby minimizing ion recombination and improving charge efficiency. For example, in the MCDI cell at a flow rate of 10 mL/min, ACC/ZnO exhibited a significant adsorption capacity of 3.13 mg/g for Zn at

the 5th cycle and 2.81 mg/g at the 50th cycle, compared to 2.94 mg/g and 2.69 mg/g in CDI cekk. Similar trends were observed at flow rates of 15 mL/min and 25 mL/min, as presented in Table E.3 (Appendix E) and E.4 (Appendix E). In this study, a slightly higher recovery rate is observed in the MCDI cell compared to the CDI cell. For instance, the recovery rate of ACC/ZnO at flow rate of 10 mL/min in MCDI recorded at 50.5 % and 37.4 % at 5th cycle and 50th cycle respectively, but CDI cell only recorded at 42.2 and 30.4 %. As presented in Table E.2, Table E.3, and Table E.4 (Appendix E), the recovery rate of the MCDI cell was slightly higher than that of the CDI cell due to the presence of IEMs. A trade-off is linked to the existence of IEMs in the CDI system when no reverse voltage is used in the discharge phase (Yang et al., 2020; Zhao et al., 2013). Ions that have been adsorbed onto the electrodes diffuse back into the feed solution, which may result in adsorptive reversal during the discharging phase in the CDI cell. Using IEMs in the MCDI cell avoids the adsorptive reversal process, but it may also hinder the release of ions during regeneration.

A faster flow rate in the CDI process accelerates adsorption, leading to more ions being adsorbed onto the electrode surfaces (Liang et al., 2013; Wang et al., 2015). In this work, when the flow rate increased from 10 mL/min to 15 mL/min, the adsorption capacity of ACC and ACC/ZnO improved in both CDI cell and MCDI cell. For instance, in CDI cell the adsorption amount of ACC increased from 2.55 mg/g (10 mL/min) to 3.60 mg/g (15 mL/min), ACC/ZnO recorded 2.67 mg/g (10 mL/min) and 4.04 mg/g (15 mL/min). ACC/ZnO increased from 3.13 mg/g (10 mL/min) to 5.19 mg/g (15 mL/min) in MCDI cell. Lower flow rates reduce removal capacitance while increasing energy consumption and treatment time. However, higher flow rates can also cause ions to pass through the CDI reactor before they can be effectively adsorbed. For example, at a 25 mL/min flow rate, both ACC and ACC/ZnO recorded lower adsorption and recovery rates compared to a 10 mL/min flow rate. For example, in the CDI cell, ACC and ACC/ZnO showed adsorption capacity of 2.04 mg/g and 2.42 mg/g, respectively. Similarly, the recovery rate for ACC and ACC/ZnO in the CDI cell were 30.1% and 33.9%, respectively.

When comparing the 5th and 50th cycles across various configurations, including ACC, ACC/ZnO in both CDI cell and MCDI cell, there is a decrease in adsorption performance and recovery rate as time progresses. In CDI cell, the recovery rate of Zn in the 5th cycle tends to be higher, but it decreases significantly by the 50th cycle at all flow rates. For example, when the flow rate is set at 10 mL/min, the recovery rate experiences a decline from 35.7% in the 5th cycle to 24.3% in the 50th cycle. This suggests a decrease in the efficiency of the ACC electrode over time, possibly due to fouling, degradation of the electrode material, or incomplete regeneration. While ACC shows superior performance in MCDI cells compared to CDI cells, there is still a noticeable decrease in recovery rate over time. For instance, at a flow rate of 15 mL/min, the recovery rate drops from 45.4% in the 5th cycle to 34.6% in the 50th cycle. However, this decline is less significant in MCDI cells, highlighting their advantage in maintaining performance over extended cycles. Additionally, ACC/ZnO in CDI cell exhibits higher recovery rate than pristine ACC in CDI cell. However, over 50 cycles at a 25 mL/min flow rate, the recovery rate decreases from 33.9% in the 5th cycle to 23.5% in the 50th cycle. Despite this degradation, the performance decline is slightly less severe than that of ACC alone. In the CDI cell, ACC/ZnO consistently outperforms ACC in maintaining a stable recovery rate throughout the cycles. These results imply that the ZnO nanostructures grafting onto carbon fibers might provide certain degree of protection against prolonged wear. At a flow rate of 15 mL/min, the recovery rate of ACC/ZnO in MCDI cell was 50.5% in the 5th cycle and decreased to 37.4% in the 50th cycle. The observed performance decline over cycles indicates the challenges of long-term operation in removing ions in real wastewater, such as damage and foul of the electrode or membrane in the CDI system.

4.5.3 Properties of electrode material in CDI tests

Figure 4.28 shows the current density of ACC and ACC/ZnO in both CDI and MCDI cells, revealing the prepared materials' reliability and effectiveness. It exhibits an initial increase in current density, stabilizing after the 3rd cycle. This result indicates the accumulation of charges and the subsequent saturation of the electrode surface with

ions. Fluctuations in current density during subsequent cycles could arise from factors such as electrode degradation or incomplete recovery which are discussed in the next part. As presented in Figure 4.28, the MCDI cell exhibits superior stability to the CDI cell, primarily attributed to IEMs that improve ion selectivity and reduce co-ion repulsion. Additionally, the electrode's performance, stability, and durability are significantly enhanced when grafting ZnO nanostructures onto carbon fiber. This improvement is consistently observed during the 5th and 50th cycles, where ACC/ZnO outperforms ACC. Additionally, there is a decrease in current density from the 5th cycle to the 50th cycle, as a result, the adsorption capacity and recovery rate are reduced, as previously discussed.

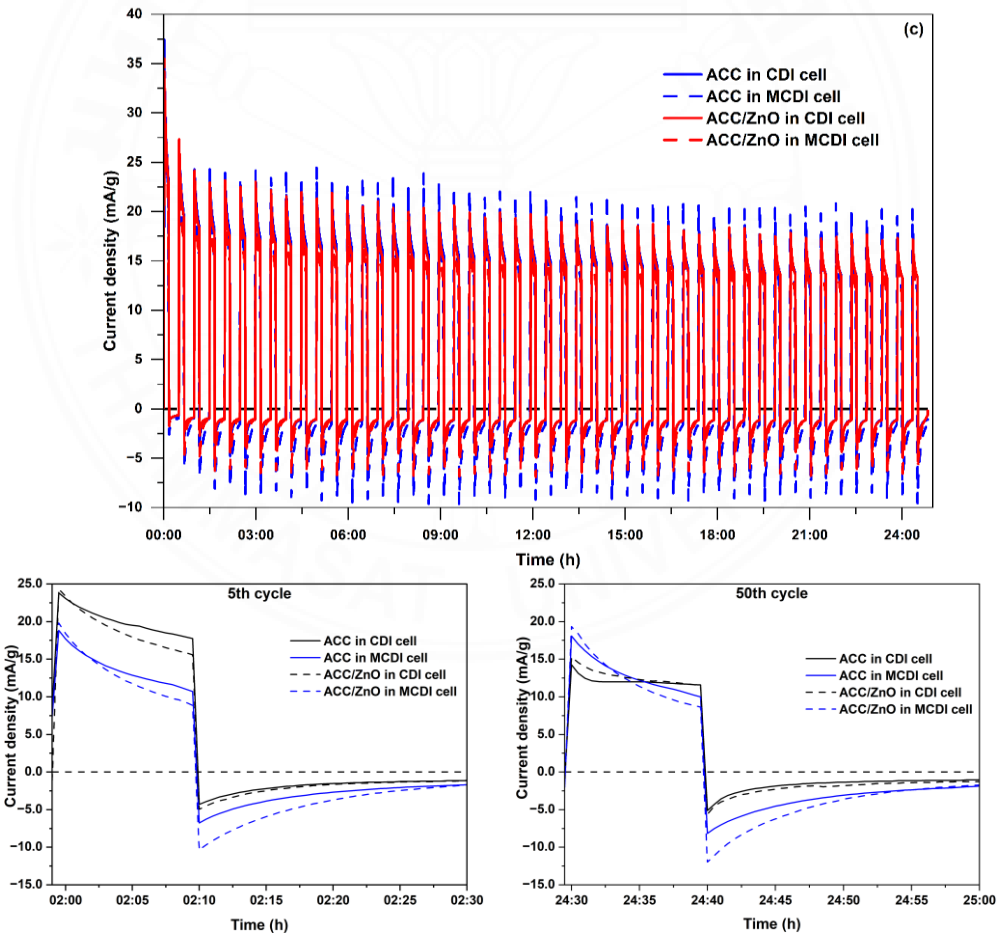

Figure 4.28 Current density at flow rate of 15 mL/min of ACC and ACC/ZnO in CDI cell and MCDI cell over consecutive 50 cycles, with inset showing current density at the 5th cycle and 50th cycle.

The study of electrode degradation in the CDI system did not involve any cleaning methods during the entire CDI process. SEM images and EDS spectra were analyzed to assess the condition of the electrodes after 50 cycles, as shown in Figure 4.29. This analysis aimed to confirm the cause of the decline in adsorption efficiency and recovery under electroplating wastewater. The rough surface may appear to be caused by electrodeposition of metal ions on the cathode surface, which can lead to fouling electrode. In Figure 4.29(a), the electrode surface displays noticeable texture and irregularities, possibly resulting from the deposition of metals on the carbon fibers over 50 cycles. Deposits are observed when ions bind to the surface of carbon fibers. In addition, Figure 7(c) shows a surface wholly coated with a thick layer of particles, which are most likely metal oxides. The particles' uniform distribution and close packing suggest that bonding of ZnO nanostructures and metal ions on the ACC/ZnO surface has been achieved.

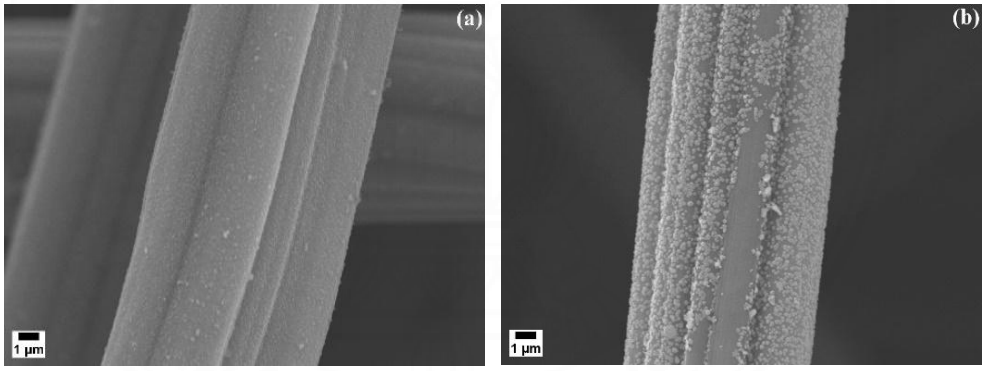

Figure 4.29 SEM images of (a) ACC and (b) ACC/ZnO after 50 cycles testing.

4.5.4 Conclusions of electroplating wastewater treatment

This study evaluated the performance of ACC and ACC/ZnO electrodes in both CDI and MCDI cells over 50 electrosorption/regeneration cycles for electroplating wastewater treatment. The adsorption capacity and recovery rates of the ACC/ZnO electrodes were superior to those of pristine ACC, especially in MCDI cells. At a flow rate of 10 mL/min, the ACC/ZnO electrode in the CDI cell showed a slightly higher adsorption capacity for Zn^{2+} compared to ACC, with 2.67 mg/g at the 5th cycle. The improvement was particularly noticeable in the MCDI cell, with ACC/ZnO reaching a

value of 3.13 mg/g by the 5th cycle. Unfortunately, there was a noticeable decrease in performance as time went on. At the 50th cycle, the recovery rate of ACC/ZnO in the CDI cell experienced a decrease from 33.9% to 23.5% with a flow rate of 25 mL/min. Similarly, in the MCDI cell, the recovery rate dropped from 50.5% to 37.4% with a flow rate of 15 mL/min. The electrodes underwent degradation, specifically due to the electrodeposition of metal ions. This degradation was evident from the SEM images, which revealed a roughened surface. The results highlight the significance of optimizing electrode materials and operational conditions to reduce fouling and enhance the durability of capacitive deionization systems for wastewater treatment.

4.6 Performance degradation in CDI systems and possible solutions for improving efficiency

This study shows that the adsorption capacity and recovery rate of HMs diminished over time across the prepared electrodes (ACC, ACC/MnO_2, and ACC/ZnO), regardless of the CDI architectures, in both synthetic wastewater and electroplating wastewater. Several factors contribute to performance reduction, including electrode material degradation, electrochemical processes, and electrode and ion exchange membrane fouling. The active surface area of carbon-based electrodes may diminish over time due to physical factors, affecting their structural integrity (Xing et al., 2020). A decrease in adsorption capacity can be attributed to the degradation of electrode materials caused by Faradaic reactions, a challenge frequently encountered in CDI processes when using carbon electrodes (Zhang et al., 2018; Zhang & Kong, 2020). Carbon electrodes in CDI system experience anodic oxidation and cathodic reduction or hydrogenation (Zhang et al., 2018; Zhang et al., 2020). Tang et al. reported that the concentration of H_2O_2 in CDI process increased rapidly before declining during charging phase, whereas no H_2O_2 was generated in MCDI cell due to the absence of oxygen to penetrate IEMs (Tang et al., 2017). In addition, it was found that the degradation of MnO_2 nanostructures on carbon fibers during the CDI process (Pengju Li et al., 2018). Similarly, ZnO nanostructures could degrade in acidic environments, compromising their structural integrity and effectiveness on the electrodes (Myint et

al., 2014; Yasin et al., 2021; Baruah and Dutta, 2009b). On the other hand, Cu^{2+}, Ni^{2+}, and Cr^{3+} may accumulate on the electrode surface or within its porous structure by electrodeposition, as discussed. Over time, this accumulation can lead to blocking, obstructing active adsorption sites and thereby reducing performance. Metal ions may also precipitate as insoluble compounds (e.g., metal hydroxides), further diminishing adsorption capacity (Q. Chen et al., 2018; Kalfa et al., 2020). The presence of organic matter exacerbates this problem by blocking adsorption sites on the electrode in CDI system and limiting active sites on the IEMs in MCDI cells, consequently reducing the electrode's ion capture capacity (Chen et al., 2023; Wang et al., 2015).

Several potential solutions aim to mitigate performance degradation by optimizing the electrode properties or operating conditions to improve efficiency in CDI systems. Incorporating MnO_2 nanostructures into GO material or CNTs material has been shown to enhance the stability of the MnO_2 crystalline structure, reducing degradation of MnO_2 nanostructures over time (Ahmed G El-Deen et al., 2014; Y. Li et al., 2017). Some studies have been developed nanostructure-modified carbon-based materials, hybrid membranes, or introduced hybrid materials such as ZnO-TiO_2 and MnO_2-SnO_2, which may enhance durability while preserving substantial adsorption capability (Dai et al., 2014; Li et al., 2022; Manikandan et al., 2022). To address electrodeposition, polarity reversal during the discharging phase can enhance recovery rate in CDI, with further improvement achieved by applying a higher potential (Arar et al., 2014; Tang et al., 2019a; Zhang & Kong, 2020). However, this poses challenges due to reversal adsorption in CDI cell (Li & Zou, 2011). Besides, pre-treating the feedwater to reduce a concentration of metal ion before entering the CDI system is an effective method to diminish metal oxides deposition on electrodes that degrades CDI performance. Adjusting the initial pH solution can also help mitigate electrode degradation and enhance CDI performance (Maheshwari et al., 2023). On the other hand, Wang et al. reported using water, NaOH, and HCl for cleaning electrodes, but the efficiency remained lower than expected in wastewater tests (Wang et al., 2015). The long-term operation effects of exposing carbonaceous materials to alkaline or acidic solutions require investigation, as these solutions may compromise membrane stability

despite their cleaning effectiveness for CDI system (Kalfa et al., 2020). Moreover, the performance of the CDI system is strongly influenced by the surface properties of the electrodes. Changes in the composition of functional groups on electrode, particularly the ratio of acidic to basic groups due to fluctuating pH environments, can significantly impact the efficiency of the CDI process (Gao et al., 2016). Consequently, conducting in-depth studies on cleaning and regeneration is essential to facilitate the comprehensive application of CDI processes to treat various water streams. Using membranes like ultrafiltration (UF) or nanofiltration (NF) as pretreatment before CDI system enhances performance by reducing fouling, improving efficiency, and extending electrode lifespan (Maheshwari et al., 2023; Shen et al., 2021). These membranes can effectively eliminate HMs, suspended solids, and organic molecules that hinder adsorption sites in the porous structure of carbon electrodes during the CDI process. While the suggested approaches offer potential solutions for improving performance efficiency, they also imply operational complexities and increased expenses related to their implementation.

4.7 Low-cost materials and solutions for enhancing their properties in CDI

This study exhibits the potential promise of low-cost materials for CDI applications, emphasizing the grafting of metal oxides such as MnO_2 and ZnO onto inexpensive ACC by hydrothermal techniques, which presents a cost-effective strategy for manufacturing high-performance CDI electrodes. In addition to ACC and metal oxides integration, various cost-effective materials have been explored to improve CDI systems (Cheng et al., 2019; Sayed et al., 2023; Zhang & Kong, 2020). Carbon-derived materials, such as activated carbon, graphite, and carbon nanotubes, are esteemed for their extensive surface area, electrical conductivity, and resilience, rendering them ideal for efficient ion adsorption. Sustainable materials like clay, graphene oxide, and carbon generated from bio-waste are viable alternatives that mitigate environmental impact while ensuring cost-effectiveness (Bautista-Patacsil et al., 2020; Lu et al., 2022; Wang et al., 2024). These materials facilitate the advancement of accessible, efficient, and eco-friendly CDI technologies. Nevertheless, inexpensive materials frequently

encounter issues related to quality variability, restricted ion selectivity, and durability challenges, especially in the case of naturally sourced or bio-waste-derived alternatives, which could affect the dependability and longevity of CDI systems. It is crucial to address these limitations to enhance the cost-effectiveness and long-term performance of CDI process.

To enhance the characteristics of inexpensive materials for CDI applications, several studies have reported methods that can be realized through the integration of advanced synthetic techniques and AI-driven optimization. Some synthetic techniques, including sol-gel processing, solvothermal synthesis, and chemical vapor deposition, play a crucial role in customizing material properties. For example, sol-gel processing facilitates meticulous regulation of particle size and pore distribution, resulting in highly porous structures that improve ion adsorption and charge storage capabilities (Liu et al., 2024; Ntakirutimana & Tan, 2021). Addionally, solvothermal synthesis demonstrates significant efficacy in generating uniform nanostructures of metal oxides such as MnO_2 and ZnO on carbon materials (Gao et al., 2023; Ma et al., 2024). This process enhances the electrochemical surface area and facilitates improved ion transport within the CDI system (Huo et al., 2023). Furthermore, chemical vapor deposition is utilized to apply conductive layers on surface carbon fibres, which markedly improves conductivity and the overall stability of the electrode (Vir Singh et al., 2023). Furthermore, the processes of doping and surface functionalization, including nitrogen doping or the incorporation of metal ions, modify the electronic structure of these economical materials (Gao et al., 2023). This enhancement leads to increased conductivity and surface reactivity, ultimately resulting in improved performance in low-cost materials.

The integration of AI tools facilitates predictive modeling and high-throughput screening, enabling machine learning algorithms to analyze extensive datasets to forecast material performance based on characteristics such as surface area, conductivity, and pore size distribution (Liu et al., 2023). The optimization of synthesis parameters, such as temperature, pH, and reaction duration, is enhanced through AI-driven reinforcement learning. This approach effectively reduces the number of

experimental iterations by pinpointing conditions that optimize both adsorption capacity and stability (Wang et al., 2025) . Moreover, AI improves the operational efficiency of CDI by forecasting the most effective voltage, flow rates, and cycle durations, facilitating energy-efficient and successful ion removal (Wang et al., 2025). The integration of synthetic and AI methodologies results in economical CDI materials that exhibit markedly enhanced structural and electrochemical characteristics, promoting efficient and scalable options for water treatment (Dian et al., 2024).

While these methods offer various benefits, they also possess specific limitations. The use of synthetic techniques such as sol-gel processing, solvothermal synthesis, and chemical vapor deposition often entails significant costs, extended timeframes, and substantial energy requirements. The sol-gel process typically requires precise conditions and extended processing durations, whereas solvothermal methods may necessitate elevated temperatures and pressures, thereby raising operational expenses (Cao et al., 2019; Huo et al., 2023; Ma et al., 2024). Furthermore, the use of hazardous precursor gases in chemical vapor deposition process can raise significant safety concerns and environmental risks (Vir Singh et al., 2023). Doping and surface functionalization techniques present certain challenges; if not meticulously controlled, they may result in inconsistent material properties, thereby impacting the reproducibility ofmaterial performance (Cheng et al., 2019; C. Zhang et al., 2024). Furthermore, although optimization powered by AI provides valuable predictive insights, it is significantly dependent on the quality of the input data and the availability of computational resources, which can often be restricted or expensive to obtain (Liu et al., 2023; Zaghloul & Achari, 2022). The interplay of these factors poses significant challenges in the development of economically viable CDI materials and methods, especially when considering large-scale applications.

CHAPTER 5

CONCLUSIONS AND RECOMMENDATIONS

5.1 Conclusions

This study found the successful performance in eliminating HMs through appropriately configured and operated capacitive deionization systems. The pivotal roles of ion exchange membranes and modifying activated carbon materials with MnO_2 and ZnO nanostructures have been highlighted as crucial in enhancing CDI performance for HMs removal. Furthermore, the study revealed the significance of operational parameters, including initial concentration, pH, and flow rate, affecting the efficacy of HMs removal in CDI configuration. Some factors such as charge/discharge time, discharge mode influenced CDI experiment outcomes. The integration of the electrode material of ACC/ZnO-nRs and a commercial ion exchange membrane in the MCDI cell resulted in significant enhancements in the efficacy of HMs removal from real electroplating wastewater compared to the CDI cell.

The following is a summary of the results and findings of this study.

Grafting MnO_2 nanostructures onto activated carbon fiber (ACC/MnO_2) significantly increased the material's capacitance due to the enhanced surface area and availability of more active sites for ion storage. This alteration has resulted in improved efficiency in the removal of chromium. When tested under the same initial concentration and pH conditions, it was observed that both ACC and ACC/MnO_2 perform better in eliminating Cr^{6+} compared to Cr^{3+}, which is evident in both adsorption and electrosorption tests. In the capacitive deionization test, ACC/MnO_2 material exhibited a higher adsorption capacity for Cr^{6+} (8.46 mg/g) than Cr^{3+} (2.95 mg/g). Furthermore, the adsorption amount of ACC/MnO_2 was 7.86 mg/g, more significant than that of pristine ACC (6.65 mg/g) for Cr^{6+} removal at the tenth cycle under a potential of 1.2 V.

Heterogeneous cation exchange membranes were prepared by grafting cation exchange resin onto a membrane, aiming to enhance the efficiency of Ni^{2+} removal. Grafting resins significantly impacted the membrane's structural properties, increasing

the density of cationic functional groups and enhancing the ion transport capacity. The ion exchange capacity of M20 membrane, with 20% resins by weight, reached to 1.62 meq/g. Using the fabricated membrane in a MCDI cell exhibited higher adsorption levels than the CDI cell, reaching 3.42 mg/g, while the CDI cell achieved 2.15 mg/g. However, the utilization of the synthesized membrane in the MCDI cell yields worse results in adsorption capacity and recovery rate compared to employing the commercial counterpart membrane.

Modifying the activated carbon fiber surface with ZnO nanostructures enhanced the electric field, leading to higher specific capacitance and reduced charge transfer resistance of the material. The ACC material presented a specific capacitance of 38.43 F/g, while ACC/ZnO-nRs demonstrated a higher value of 45.08 F/g. Furthermore, the charge transfer resistance of ACC/ZnO-nRs decreased significantly from 10.92 Ω to 6.21 Ω compared to ACC. By this way, incorporating ZnO nanorods onto the activated carbon fiber surface (ACC/ZnO-nRs) enhanced the efficiency in facilitating Cu^{2+} removal. ACC/ZnO-nRs demonstrated an electrosorption capacity of 8.9 mg/g, surpassing that of pristine ACC at 6.2 mg/g at tenth cycle in the capacitive deionization test.

The improvements in adsorption capacity and recovery rate of Cr^{6+}, Cr^{3+}, Cu^{2+}, and Ni^{2+} were noted with increasing potential. Additionally, initial concentrations, pH and flow rates had a noticeable impact on the adsorption capacity in studies.

Enhanced performance in the removal and recovery of HMs in synthesis wastewater is achieved by using IEMs in MCDI cell, which prevent reverse ion diffusion into the electrolyte solution during the charge phase and reduce co-ion expulsion.

The evaluation of the potential application of CDI for treating real electroplating wastewater involved a comprehensive analysis of their electrosorption performance, HMs removal efficiency, operational optimization, and long-term performance degradation. The utilization of ACC/ZnO-nRs and commercial ion exchange membranes resulted in promising outcomes for the MCDI cell, surpassing the performance of CDI cell utilizing activated carbon electrodes. Additionally, it revealed

great success in wastewater treatment with low concentrations of HMs, such as Cr, As, Se, Co, Cd, and Pb, fulfilling Thailand's requirements for industrial wastewater discharge within a 10-min test. HMs at high concentration from wastewater like Cu, Ni, Mn and Zn might require prolonged treatment durations for optimal efficacy. Furthermore, it was found that increasing the flow rate in the CDI system resulted in enhanced water quality. The adsorption capacity and regeneration of the activated carbon-based materials was impeded by the incomplete recovery of HMs throughout the 50-cycles observation.

5.2 Recommendations

Based on the findings of this study, the following recommendations are suggested to enhance the efficiency of CDI process in removal of HMs from wastewater.

This study presents the potential of using ZnO and MnO_2 nanostructures on ACC to enhance HM adsorption. Although these materials have demonstrated potential, the investigation of alternative materials like graphene oxide or metal-organic frameworks may offer additional improvements to the performance of CDI systems. Besides, further research should prioritize optimizing the synthesis process of these nanostructures to enhance their surface area and ion storage capacity. In addition, the efficiency of the CDI process can be positively impacted by the presence of various metal oxides. It is vital to conduct extended-cycle experiments to assess the long-term stability of a modified electrodes.

Although heterogeneous cation exchange membranes have shown potential, they are less effective than their counterparts. However, there are several opportunities for improving their performance. Further research should explore different fabrication techniques to enhance ion selectivity and adsorption capacity. Additionally, it is essential to evaluate the cost-effectiveness and durability of the prepared membranes compared to commercial ones in real wastewater applications.

This study presents the impact of various parameters, including flow rate and initial concentration, on CDI systems' adsorption capacity. Future experiments should

systematically explore the interaction of these parameters to develop more efficient operating protocols for different wastewater types. Besides, optimizing the pH of wastewater in CDI process is crucial for improving the removal efficiency of HMs such as Cu^{2+}, Ni^{2+}, Cr^{6+}, and Cr^{3+}. Reduced pH levels enhance the adsorption of Cu^{2+} and Ni^{2+} by maintaining these ions in their ionic states, whereas elevated pH may result in the generation of less adsorbable hydroxide species. Acidic circumstances enhance the adsorption of Cr^{3+} species, but increased pH may lead to precipitation, hence diminishing its removal effectiveness. For Cr^{6+} species, sustaining acidic conditions is essential to promote its reduction to Cr^{3+} species, which is more easily absorbed. Consequently, regulating the pH is essential for optimizing ion removal efficacy in CDI systems.

Sodium acetate is used to simulate organic matter in this study, while alternatives such as glucose, humic acids, and phenolic compounds can also be used in CDI studies. Humic acid is particularly recommended for further research as it effectively represents natural organic matter. Its complex structure, functional groups, and charge characteristics closely resemble real wastewater, providing valuable insights into fouling, scaling, and the impact of organic matter on performance of CDI system.

This study notes the performance degradation issue over extended cycles caused by the electrodeposition of metal ions. Developing strategies to minimize fouling and electrode degradation is crucial. This can be achieved through implementing periodic cleaning protocols or utilizing protective coatings.

To promote the practical implementation of CDI for the removal of metal ions from wastewater, it is crucial to improve electrode materials that exhibit excellent selectivity and adsorption capability for metal ions. Creating hybrid CDI systems that integrate selective ion-exchange membranes with improved carbon-based materials, including activated carbon or graphene composites, could enhance the targeting of specific pollutants. Moreover, enhancing operational parameters, including applied voltage and flow rate, may augment the efficiency and energy consumption of CDI, rendering it more viable for large-scale treatment. Subsequent study should concentrate on reducing fouling and scaling, which frequently impact CDI efficacy in actual

wastewater contexts. Incorporating CDI with pre-treatment processes or within a multi-stage treatment system may improve its effectiveness for the removal of heavy metals in industrial wastewater applications. Besides, balancing cost, durability, and efficiency is essential for CDI's practical industrial deployment. Combining cost-effective materials, machine learning and AI tools-assisted optimization, and strategic system design can establish CDI as a sustainable option for heavy metal remediation in industrial wastewater, enhancing its applicability and economic feasibility.

REFERENCES

Abdullah, N., Yusof, N., Lau, W. J., Jaafar, J., & Ismail, A. F. (2019). Recent trends of heavy metal removal from water/wastewater by membrane technologies. *Journal of Industrial and Engineering Chemistry*, *76*, 17-38. https://doi.org/10.1016/j.jiec.2019.03.029

Adorna Jr, J., Borines, M., & Doong, R.-A. (2020). Coconut shell derived activated biochar–manganese dioxide nanocomposites for high performance capacitive deionization. *Desalination*, *492*, 114602. https://doi.org/10.1016/j.desal.2020.114602

Agrawal, A., Pal, C., & Sahu, K. K. (2008). Extractive removal of chromium (VI) from industrial waste solution. *J Hazard Mater*, *159*(2-3), 458-464. https://doi.org/10.1016/j.jhazmat.2008.02.121

Ahmed, M. A., & Tewari, S. (2018). Capacitive deionization: Processes, materials and state of the technology. *Journal of Electroanalytical Chemistry*, *813*, 178-192. https://doi.org/10.1016/j.jelechem.2018.02.024

AL-Rajabi, M. M., Abumadi, F. A., Laoui, T., Atieh, M. A., & Khalil, K. A. (2024). Capacitive deionization for water desalination: Cost analysis, recent advances, and process optimization. *Journal of Water Process Engineering*, *58*, 104816.

Ali, R., Aslam, Z., Shawabkeh, R. A., Asghar, A., & Hussein, I. A. (2020). BET, FTIR, and RAMAN characterizations of activated carbon from waste oil fly ash. *Turk J Chem*, *44*(2), 279-295. https://doi.org/10.3906/kim-1909-20

Alvarado, L., & Chen, A. (2014). Electrodeionization: Principles, Strategies and Applications. *Electrochimica Acta*, *132*, 583-597. https://doi.org/10.1016/j.electacta.2014.03.165

Arar, Ö., Yüksel, Ü., Kabay, N., & Yüksel, M. (2014). Various applications of electrodeionization (EDI) method for water treatment—A short review. *Desalination*, *342*, 16-22. https://doi.org/10.1016/j.desal.2014.01.028

Baby, J., Raj, J. S., Biby, E. T., Sankarganesh, P., Jeevitha, M., Ajisha, S., & Rajan, S. S. (2010). Toxic effect of heavy metals on aquatic environment. *International Journal of Biological and Chemical Sciences*, *4*(4).

Baird, R., Rice, E., & Eaton, A. (2017). Standard methods for the examination of water and wastewaters. *Water Environment Federation, Chair Eugene W. Rice, American Public Health Association Andrew D. Eaton, American Water Works Association*, *1*, 71-90.

Bao, S., Xin, C., Zhang, Y., Chen, B., Ding, W., & Luo, Y. (2023). Application of capacitive deionization in water treatment and energy recovery: a review. *Energies*, *16*(3), 1136.

Baral, S. S., Das, S. N., & Rath, P. (2006). Hexavalent chromium removal from aqueous solution by adsorption on treated sawdust. *Biochemical engineering journal*, *31*(3), 216-222.

Barhoum, A., & Luisa García-Betancourt, M. (2018). Physicochemical characterization of nanomaterials: size, morphology, optical, magnetic, and electrical properties. In A. Barhoum & A. S. H. Makhlouf (Eds.), *Emerging Applications of Nanoparticles and Architecture Nanostructures* (pp. 279-304). Elsevier. https://doi.org/10.1016/b978-0-323-51254-1.00010-5

Baruah, S., & Dutta, J. (2009). Hydrothermal growth of ZnO nanostructures. *Sci Technol Adv Mater*, *10*(1), 013001. https://doi.org/10.1088/1468-6996/10/1/013001

Baruah, S., & Dutta, J. (2009). pH-dependent growth of zinc oxide nanorods. *Journal of Crystal Growth*, *311*(8), 2549-2554. https://doi.org/10.1016/j.jcrysgro.2009.01.135

Bautista-Patacsil, L., Lazarte, J. P. L., Dipasupil, R. C., Pasco, G. Y., Eusebio, R. C., Orbecido, A., & Doong, R. (2020). Deionization utilizing reduced graphene oxide-titanium dioxide nanotubes composite for the removal of Pb2+ and Cu2+. *Journal of Environmental Chemical Engineering*, *8*(3). https://doi.org/10.1016/j.jece.2019.103063

Bharath, G., Rambabu, K., Banat, F., Hai, A., Arangadi, A. F., & Ponpandian, N. (2019). Enhanced electrochemical performances of peanut shell derived activated carbon and its Fe(3)O(4) nanocomposites for capacitive deionization of Cr(VI) ions. *Sci Total Environ*, *691*, 713-726. https://doi.org/10.1016/j.scitotenv.2019.07.069

Bhuvanendran, N., Ravichandran, S., Xu, Q., Maiyalagan, T., & Su, H. (2022). A quick guide to the assessment of key electrochemical performance indicators for the oxygen reduction reaction: A comprehensive review. *International Journal of Hydrogen Energy*, *47*(11), 7113-7138. https://doi.org/https://doi.org/10.1016/j.ijhydene.2021.12.072

Biesheuvel, P., & Van der Wal, A. (2010). Membrane capacitive deionization. *Journal of Membrane Science*, *346*(2), 256-262.

Biesheuvel, P. M., & van der Wal, A. (2010). Membrane capacitive deionization. *Journal of Membrane Science*, *346*(2), 256-262. https://doi.org/10.1016/j.memsci.2009.09.043

Blázquez, G., Hernáinz, F., Calero, M., Martín-Lara, M., & Tenorio, G. (2009). The effect of pH on the biosorption of Cr (III) and Cr (VI) with olive stone. *Chemical Engineering Journal*, *148*(2-3), 473-479.

Budak, T. B. (2013). Removal of Heavy Metals from Wastewater Using Synthetic Ion Exchange Resin. *Asian Journal of Chemistry*, *25*(8), 4207-4210. https://doi.org/10.14233/ajchem.2013.13902

Cai, X., Lei, T., Sun, D., & Lin, L. (2017). A critical analysis of the α, β and γ phases in poly(vinylidene fluoride) using FTIR. *RSC Advances*, *7*(25), 15382-15389. https://doi.org/10.1039/c7ra01267e

Cao, Z., Zhang, C., Yang, Z., Qin, Q., Zhang, Z., Wang, X., & Shen, J. (2019). Preparation of Carbon Aerogel Electrode for Electrosorption of Copper Ions in Aqueous Solution. *Materials (Basel)*, *12*(11). https://doi.org/10.3390/ma12111864

Cetinkaya, A. Y., & Bilgili, L. (2021). Removal of Cu(II) ions from aqueous solutions using membrane system and membrane capacitive deionization (MCDI)

technology. *Environ Monit Assess*, *193*(8), 460. https://doi.org/10.1007/s10661-021-09239-z

Chai, W. S., Cheun, J. Y., Kumar, P. S., Mubashir, M., Majeed, Z., Banat, F., Ho, S.-H., & Show, P. L. (2021). A review on conventional and novel materials towards heavy metal adsorption in wastewater treatment application. *Journal of Cleaner Production*, *296*, 126589.

Chang, Y., Dang, Q., Samo, I., Li, Y., Li, X., Zhang, G., & Chang, Z. (2020). Electrochemical heavy metal removal from water using PVC waste-derived N, S co-doped carbon materials. *RSC Adv*, *10*(7), 4064-4070. https://doi.org/10.1039/c9ra09237d

Chen, L., Wang, C., Liu, S., Hu, Q., Zhu, L., & Cao, C. (2018). Investigation of the long-term desalination performance of membrane capacitive deionization at the presence of organic foulants. *Chemosphere*, *193*, 989-997.

Chen, L., Wang, C., Liu, S., & Zhu, L. (2019). Investigation of adsorption/desorption behavior of Cr(VI) at the presence of inorganic and organic substance in membrane capacitive deionization (MCDI). *J Environ Sci (China)*, *78*, 303-314. https://doi.org/10.1016/j.jes.2018.11.005

Chen, Q., Yao, Y., Li, X., Lu, J., Zhou, J., & Huang, Z. (2018). Comparison of heavy metal removals from aqueous solutions by chemical precipitation and characteristics of precipitates. *Journal of Water Process Engineering*, *26*, 289-300. https://doi.org/10.1016/j.jwpe.2018.11.003

Chen, S., Zhai, T., Lu, X.-H., Zhang, M.-Z., Li, Z.-Y., Xu, C.-W., & Tong, Y. (2012). Large-area manganese oxide nanorod arrays as efficient electrocatalyst for oxygen evolution reaction. *International Journal of Hydrogen Energy*, *37*(18), 13350-13354.

Chen, W., He, X., Jiang, Z., Li, B., Li, X.-y., & Lin, L. (2023). A capacitive deionization and electro-oxidation hybrid system for simultaneous removal of heavy metals and organics from wastewater. *Chemical Engineering Journal*, *451*, 139071.

Chen, Z., Zhang, H., Wu, C., Wang, Y., & Li, W. (2015). A study of electrosorption selectivity of anions by activated carbon electrodes in capacitive deionization. *Desalination*, *369*, 46-50.

Cheng, Y., Hao, Z., Hao, C., Deng, Y., Li, X., Li, K., & Zhao, Y. (2019). A review of modification of carbon electrode material in capacitive deionization. *RSC Adv*, *9*(42), 24401-24419. https://doi.org/10.1039/c9ra04426d

Choi, J. H., Park, J. S., & Moon, S. H. (2002). Direct measurement of concentration distribution within the boundary layer of an ion-exchange membrane. *J Colloid Interface Sci*, *251*(2), 311-317. https://doi.org/10.1006/jcis.2002.8407

Choi, J. R., Lee, J. W., Yang, G., Heo, Y.-J., & Park, S.-J. (2020). Activated Carbon/MnO2 Composites as Electrode for High Performance Supercapacitors. *Catalysts*, *10*(2). https://doi.org/10.3390/catal10020256

Coskun, M., Polat, O., Coskun, F. M., Durmus, Z., Caglar, M., & Turut, A. (2018). The electrical modulus and other dielectric properties by the impedance spectroscopy of LaCrO(3) and LaCr(0.90)Ir(0.10)O(3) perovskites. *RSC Adv*, *8*(9), 4634-4648. https://doi.org/10.1039/c7ra13261a

Crini, G., & Lichtfouse, E. (2019). Advantages and disadvantages of techniques used for wastewater treatment. *Environmental Chemistry Letters*, *17*, 145-155. https://doi.org/10.1007/s10311-018-0785-9ï

Cristiano, E., Hu, Y.-J., Sigfried, M., Kaplan, D., & Nitsche, H. (2011). A comparison of point of zero charge measurement methodology. *Clays and Clay Minerals*, *59*(2), 107-115.

Dabrowski, A., Hubicki, Z., Podkoscielny, P., & Robens, E. (2004). Selective removal of the heavy metal ions from waters and industrial wastewaters by ion-exchange method. *Chemosphere*, *56*(2), 91-106. https://doi.org/10.1016/j.chemosphere.2004.03.006

Daems, N., Milis, S., Verbeke, R., Szymczyk, A., Pescarmona, P. P., & Vankelecom, I. F. J. (2018). High-performance membranes with full pH-stability. *RSC Adv*, *8*(16), 8813-8827. https://doi.org/10.1039/c7ra13663c

Dai, Y. M., Tang, S. C., Peng, J. Q., Chen, H. Y., Ba, Z. X., Ma, Y. J., & Meng, X. K. (2014). MnO2@SnO2 core–shell heterostructured nanorods for supercapacitors. *Materials Letters*, *130*, 107-110. https://doi.org/https://doi.org/10.1016/j.matlet.2014.05.090

Davoglio, R. A., Cabello, G., Marco, J. F., & Biaggio, S. R. (2018). Synthesis and characterization of α-MnO2 nanoneedles for electrochemical supercapacitors. *Electrochimica Acta*, *261*, 428-435.

Dehouli, H., Chedeville, O., Cagnon, B., Caqueret, V., & Porte, C. (2010). Influences of pH, temperature and activated carbon properties on the interaction ozone/activated carbon for a wastewater treatment process. *Desalination*, *254*(1-3), 12-16.

Deng, D., Luhasile, M. K., Li, H., Pan, Q., Zheng, F., & Wang, Y. (2022). A novel layered activated carbon with rapid ion transport through chemical activation of chestnut inner shell for capacitive deionization. *Desalination*, *531*, 115685.

Deng, X., Wang, L., Xiu, Q., Wang, Y., Han, H., Dai, D., Xu, Y., Gao, H., & Liu, X. (2021). Adsorption performance and physicochemical mechanism of MnO 2-polyethylenimine-tannic acid composites for the removal of Cu (II) and Cr (VI) from aqueous solution. *Frontiers of Chemical Science and Engineering*, *15*, 538-551.

Dermentzis, K., , Davidis, A., , Papadopoulou, D., , Christoforidis, A., , Ouzounis, K., & (2009). Copper removal from industrial wastewaters by means of electrostatic shielding driven electrodeionization Engineering Science and Technology Review. *2*, 131-136. www.jestr.org

Dian, X.-m., Hao, J.-y., Zhang, Z.-a., Chen, Z., & Yao, L. (2024). Heavy metal removal performance of capacitive deionization technology studied by machine learning. *Engineering Research Express*, *6*(3), 035002.

Długołęcki, P., Anet, B., Metz, S. J., Nijmeijer, K., & Wessling, M. (2010). Transport limitations in ion exchange membranes at low salt concentrations. *Journal of Membrane Science*, *346*(1), 163-171. https://doi.org/10.1016/j.memsci.2009.09.033

Dong, Q., Guo, X., Huang, X., Liu, L., Tallon, R., Taylor, B., & Chen, J. (2019). Selective removal of lead ions through capacitive deionization: Role of ion-exchange membrane. *Chemical Engineering Journal*, *361*, 1535-1542. https://doi.org/10.1016/j.cej.2018.10.208

Du, Y., Wang, L., Wang, J., Zheng, G., Wu, J., & Dai, H. (2015). Flower-, wire-, and sheet-like MnO2-deposited diatomites: Highly efficient absorbents for the removal of Cr(VI). *J Environ Sci (China)*, *29*, 71-81. https://doi.org/10.1016/j.jes.2014.06.047

El-Deen, A. G., Barakat, N. A., & Kim, H. Y. (2014). Graphene wrapped MnO2-nanostructures as effective and stable electrode materials for capacitive deionization desalination technology. *Desalination*, *344*, 289-298.

El-Deen, A. G., Barakat, N. A. M., & Kim, H. Y. (2014). Graphene wrapped MnO2-nanostructures as effective and stable electrode materials for capacitive deionization desalination technology. *Desalination*, *344*, 289-298. https://doi.org/10.1016/j.desal.2014.03.028

Elazari, R., Salitra, G., Garsuch, A., Panchenko, A., & Aurbach, D. (2011). Sulfur-impregnated activated carbon fiber cloth as a binder-free cathode for rechargeable Li-S batteries. *Adv Mater*, *23*(47), 5641-5644. https://doi.org/10.1002/adma.201103274

Elozeiri, A. A. E., Lammertink, R. G. H., Rijnaarts, H. H. M., & Dykstra, J. E. (2024). Water content of ion-exchange membranes: Measurement technique and influence on the ion mobility. *Journal of Membrane Science*, *698*, 122538. https://doi.org/10.1016/j.memsci.2024.122538

EPA. (2024). *National Primary Drinking Water Regulations*. United States Environmental Protection Agency. Retrieved 16 September 2024 from https://www.epa.gov/ground-water-and-drinking-water/national-primary-drinking-water-regulations

Fadaei, A., Salimi, A., & Mirzataheri, M. (2014). Structural elucidation of morphology and performance of the PVDF/PEG membrane. *Journal of Polymer Research*, *21*(9), 1-8. https://doi.org/10.1007/s10965-014-0545-x

Fahim, N. F., Barsoum, B. N., Eid, A. E., & Khalil, M. S. (2006). Removal of chromium(III) from tannery wastewater using activated carbon from sugar industrial waste. *J Hazard Mater*, *136*(2), 303-309. https://doi.org/10.1016/j.jhazmat.2005.12.014

Fairbrother, A., Wenstel, R., Sappington, K., & Wood, W. (2007a). Framework for metals risk assessment. *Ecotoxicol Environ Saf*, *68*(2), 145-227. https://doi.org/10.1016/j.ecoenv.2007.03.015

Fairbrother, A., Wenstel, R., Sappington, K., & Wood, W. (2007b). Framework for metals risk assessment. *Ecotoxicology and Environmental Safety*, *68*(2), 145-227. https://doi.org/10.1016/j.ecoenv.2007.03.015

Fang, K., Peng, F., San, E., & Wang, K. (2021). The impact of concentration in electrolyte on ammonia removal in flow-electrode capacitive deionization system. *Separation and Purification Technology*, *255*, 117337. https://doi.org/10.1016/j.seppur.2020.117337

Faur-Brasquet, C., Reddad, Z., Kadirvelu, K., & Le Cloirec, P. (2002). Modeling the adsorption of metal ions (Cu2+, Ni2+, Pb2+) onto ACCs using surface complexation models. *Applied Surface Science*, *196*(1-4), 356-365. https://doi.org/10.1016/s0169-4332(02)00073-9

Feng, J., Xiong, S., Ren, L., & Wang, Y. (2022). Atomic layer deposition of TiO2 on carbon-nanotubes membrane for capacitive deionization removal of chromium from water. *Chinese Journal of Chemical Engineering*, *45*, 15-21. https://doi.org/10.1016/j.cjche.2021.05.014

Feng, T., Liu, Q., Yang, C., Li, G., & Liu, J. (2022). Membrane capacitive deionization (MCDI) for removal of chromium complexes with AC@SiO2-NH2 electrode. *Journal of Environmental Chemical Engineering*, *10*(5), 108363. https://doi.org/10.1016/j.jece.2022.108363

Fu, F., & Wang, Q. (2011). Removal of heavy metal ions from wastewaters: a review. *J Environ Manage*, *92*(3), 407-418. https://doi.org/10.1016/j.jenvman.2010.11.011

Gaikwad, M. S., & Balomajumder, C. (2017). Simultaneous electrosorptive removal of chromium(VI) and fluoride ions by capacitive deionization (CDI): Multicomponent isotherm modeling and kinetic study. *Separation and Purification Technology*, *186*, 272-281. https://doi.org/10.1016/j.seppur.2017.06.017

Gaikwad, M. S., Balomajumder, C., & Tiwari, A. K. (2020). Acid treated RHWBAC electrode performance for Cr(VI) removal by capacitive deionization and CFD analysis study. *Chemosphere*, *254*, 126781. https://doi.org/10.1016/j.chemosphere.2020.126781

Gao, M., Yang, Z., Liang, W., Ao, T., & Chen, W. (2023). Recent advanced freestanding pseudocapacitive electrodes for efficient capacitive deionization. *Separation and Purification Technology*, *324*, 124577. https://doi.org/https://doi.org/10.1016/j.seppur.2023.124577

Gao, X., Porada, S., Omosebi, A., Liu, K. L., Biesheuvel, P. M., & Landon, J. (2016). Complementary surface charge for enhanced capacitive deionization. *Water Research*, *92*, 275-282. https://doi.org/https://doi.org/10.1016/j.watres.2016.01.048

Gao, Z., Bandosz, T. J., Zhao, Z., Han, M., & Qiu, J. (2009). Investigation of factors affecting adsorption of transition metals on oxidized carbon nanotubes. *J Hazard Mater*, *167*(1-3), 357-365. https://doi.org/10.1016/j.jhazmat.2009.01.050

Gheju, M. (2011). Hexavalent chromium reduction with zero-valent iron (ZVI) in aquatic systems. *Water, Air, & Soil Pollution*, *222*, 103-148.

Gheju, M., Balcu, I., & Mosoarca, G. (2016). Removal of Cr(VI) from aqueous solutions by adsorption on MnO2. *J Hazard Mater*, *310*, 270-277. https://doi.org/10.1016/j.jhazmat.2016.02.042

Gong, A., Zhao, Y., Liang, B., & Li, K. (2022). Stepwise hollow Prussian blue/carbon nanotubes composite as a novel electrode material for high-performance desalination. *Journal of Colloid and Interface Science*, *605*, 432-440.

Gonzalez, J., Torrent-Sucarrat, M., & Anglada, J. M. (2010). The reactions of SO3 with HO2 radical and H2O...HO2 radical complex. Theoretical study on the atmospheric formation of HSO5 and H2SO4. *Phys Chem Chem Phys*, *12*(9), 2116-2125. https://doi.org/10.1039/b916659a

Goyer, R., Golub, M., Choudhury, H., Hughes, M., Kenyon, E., & Stifelman, M. (2004). Issue Paper on the Human Health Effects of Metals.

Guo, M.-X., Bian, S.-W., Shao, F., Liu, S., & Peng, Y.-H. (2016). Hydrothermal synthesis and electrochemical performance of MnO 2 /graphene/polyester composite electrode materials for flexible supercapacitors. *Electrochimica Acta*, *209*, 486-497. https://doi.org/10.1016/j.electacta.2016.05.082

Han, B., Cheng, G., Wang, Y., & Wang, X. (2019). Structure and functionality design of novel carbon and faradaic electrode materials for high-performance capacitive deionization. *Chemical Engineering Journal*, *360*, 364-384.

Han, S., Park, S., Yi, S.-H., Im, W. B., & Chun, S.-E. (2020). Effect of potential and current on electrodeposited MnO2 as a pseudocapacitor electrode: Surface morphology/chemistry and stability. *Journal of Alloys and Compounds*, *831*, 154838.

Hand, S., Guest, J. S., & Cusick, R. D. (2019). Technoeconomic Analysis of Brackish Water Capacitive Deionization: Navigating Tradeoffs between Performance, Lifetime, and Material Costs. *Environ Sci Technol*, *53*(22), 13353-13363. https://doi.org/10.1021/acs.est.9b04347

Hassanvand, A., Chen, G. Q., Webley, P. A., & Kentish, S. E. (2018). A comparison of multicomponent electrosorption in capacitive deionization and membrane capacitive deionization. *Water Res*, *131*, 100-109. https://doi.org/10.1016/j.watres.2017.12.015

He, D., Zhang, J., Shang, Z., & Zhang, C. (2022). Adsorption of Ni 2+ on malic acid modified activated carbon from Phragmites australis. *Science Asia*, *48*(5).

Hlaing, A. A., & Win, P. P. (2012). The synthesis of α-MnO2 nanorods using hydrothermal homogeneous precipitation. *Advances in Natural Sciences: Nanoscience and Nanotechnology*, *3*(2), 025001.

Hong, S. P., Yoon, H., Lee, J., Kim, C., Kim, S., Lee, J., Lee, C., & Yoon, J. (2020). Selective phosphate removal using layered double hydroxide/reduced graphene oxide (LDH/rGO) composite electrode in capacitive deionization. *J Colloid Interface Sci*, *564*, 1-7. https://doi.org/10.1016/j.jcis.2019.12.068

Hosseini, S. M., Rahzani, B., Asiani, H., Khodabakhshi, A. R., Hamidi, A. R., Madaeni, S. S., Moghadassi, A. R., & Seidypoor, A. (2014). Surface modification of heterogeneous cation exchange membranes by simultaneous using polymerization of (acrylic acid-co-methyl methacrylate): Membrane characterization in desalination process. *Desalination*, *345*, 13-20. https://doi.org/10.1016/j.desal.2014.04.028

Hou, C.-H., & Huang, C.-Y. (2013). A comparative study of electrosorption selectivity of ions by activated carbon electrodes in capacitive deionization. *Desalination*, *314*, 124-129.

Hou, C. H., Taboada-Serrano, P., Yiacoumi, S., & Tsouris, C. (2008). Electrosorption selectivity of ions from mixtures of electrolytes inside nanopores. *J Chem Phys*, *129*(22), 224703. https://doi.org/10.1063/1.3033562

Hu, L., Gao, R., Zhang, A., Yang, R., Zang, X., Wang, S., Yao, S., Yang, Z., Hao, H., & Yan, Y.-M. (2020). Cu2+ intercalation activates bulk redox reactions of MnO2 for enhancing capacitive performance. *Nano Energy*, *74*, 104891.

Hu, X., Min, X., Li, X., Si, M., Liu, L., Zheng, J., Yang, W., & Zhao, F. (2022). Co-Co3O4 encapsulated in nitrogen-doped carbon nanotubes for capacitive desalination: Effects of nano-confinement and cobalt speciation. *Journal of Colloid and Interface Science*, *616*, 389-400.

Huang, C. C., & Su, Y. J. (2010). Removal of copper ions from wastewater by adsorption/electrosorption on modified activated carbon cloths. *J Hazard Mater*, *175*(1-3), 477-483. https://doi.org/10.1016/j.jhazmat.2009.10.030

Huang, S., Gu, L., Zhu, N., Feng, K., Yuan, H., Lou, Z., Li, Y., & Shan, A. (2014). Heavy metal recovery from electroplating wastewater by synthesis of mixed-Fe3O4@SiO2/metal oxide magnetite photocatalysts. *Green Chem.*, *16*(5), 2696-2705. https://doi.org/10.1039/c3gc42496k

Huo, Y., Xiu, S., Meng, L.-Y., & Quan, B. (2023). Solvothermal synthesis and applications of micro/nano carbons: A review. *Chemical Engineering Journal*, *451*, 138572.

Iftekhar, S., Farooq, M. U., Sillanpää, M., Asif, M. B., & Habib, R. (2017). Removal of Ni (II) using multi-walled carbon nanotubes electrodes: relation between operating parameters and capacitive deionization performance. *Arabian Journal for Science and Engineering*, *42*(1), 235-240.

Jain, M., Garg, V. K., & Kadirvelu, K. (2009). Chromium(VI) removal from aqueous system using Helianthus annuus (sunflower) stem waste. *J Hazard Mater*, *162*(1), 365-372. https://doi.org/10.1016/j.jhazmat.2008.05.048

Janpoor, F., Torabian, A., Panahi, H. A., & Baghdadi, M. (2021). Capacitive deionization and disinfection of water using graphene oxide-dendrimer-silver coated electrodes. *Desalination and Water Treatment*, *216*, 129-139. https://doi.org/10.5004/dwt.2021.26754

Jhaveri, J. H., & Murthy, Z. V. P. (2016). A comprehensive review on anti-fouling nanocomposite membranes for pressure driven membrane separation processes. *Desalination*, *379*, 137-154. https://doi.org/10.1016/j.desal.2015.11.009

Jin, W., & Hu, M. (2019). High-Performance Capacitive Deionization of Copper Ions at Nanoporous ZnS-Decorated Carbon Felt. *Journal of The Electrochemical Society*, *166*(2), E29-E34. https://doi.org/10.1149/2.1061902jes

Kalfa, A., Shapira, B., Shopin, A., Cohen, I., Avraham, E., & Aurbach, D. (2020). Capacitive deionization for wastewater treatment: Opportunities and challenges. *Chemosphere*, *241*, 125003. https://doi.org/10.1016/j.chemosphere.2019.125003

Khulbe, K., Feng, C., & Matsuura, T. (2008). Pore size, pore size distribution, and roughness at the membrane surface.

Kim, D. I., Gwak, G., Dorji, P., He, D., Phuntsho, S., Hong, S., & Shon, H. (2018). Palladium recovery through membrane capacitive deionization from metal plating wastewater. *ACS Sustainable Chemistry & Engineering*, *6*(2), 1692-1701.

Kumar, P., Dutta, K., Das, S., & Kundu, P. P. (2014). Membrane prepared by incorporation of crosslinked sulfonated polystyrene in the blend of PVdF-co-HFP/Nafion: A preliminary evaluation for application in DMFC. *Applied Energy*, *123*, 66-74. https://doi.org/10.1016/j.apenergy.2014.02.060

Kyaw, H. H., Myint, M. T. Z., Al-Harthi, S., & Al-Abri, M. (2020). Removal of heavy metal ions by capacitive deionization: Effect of surface modification on ions adsorption. *J Hazard Mater*, *385*, 121565. https://doi.org/10.1016/j.jhazmat.2019.121565

Lanceros-Méndez, S., Mano, J. F., Costa, A. M., & Schmidt, V. H. (2007). Ftir and Dsc Studies of Mechanically Deformed β-Pvdf Films. *Journal of Macromolecular Science, Part B*, *40*(3-4), 517-527. https://doi.org/10.1081/mb-100106174

Laxman, K., Kimoto, D., Sahakyan, A., & Dutta, J. (2018). Nanoparticulate Dielectric Overlayer for Enhanced Electric Fields in a Capacitive Deionization Device. *ACS Appl Mater Interfaces*, *10*(6), 5941-5948. https://doi.org/10.1021/acsami.7b16540

Laxman, K., Myint, M. T. Z., Khan, R., Pervez, T., & Dutta, J. (2015). Improved desalination by zinc oxide nanorod induced electric field enhancement in capacitive deionization of brackish water. *Desalination*, *359*, 64-70. https://doi.org/10.1016/j.desal.2014.12.029

Laxman, K., Sathe, P., Al Abri, M., Dobretsov, S., & Dutta, J. (2020). Disinfection of Bacteria in Water by Capacitive Deionization. *Front Chem*, *8*, 774. https://doi.org/10.3389/fchem.2020.00774

Lazanas, A. C., & Prodromidis, M. I. (2023). Electrochemical Impedance Spectroscopy-A Tutorial. *ACS Meas Sci Au*, *3*(3), 162-193. https://doi.org/10.1021/acsmeasuresciau.2c00070

Lee, J.-H., Bae, W.-S., & Choi, J.-H. (2010). Electrode reactions and adsorption/desorption performance related to the applied potential in a capacitive deionization process. *Desalination*, *258*(1-3), 159-163. https://doi.org/10.1016/j.desal.2010.03.020

Lee, J., Kim, S., Kim, C., & Yoon, J. (2014). Hybrid capacitive deionization to enhance the desalination performance of capacitive techniques. *Energy & Environmental Science*, *7*(11), 3683-3689.

Leong, Z. Y., Zhang, J., Vafakhah, S., Ding, M., Guo, L., & Yang, H. Y. (2021). Electrochemically activated layered manganese oxide for selective removal of calcium and magnesium ions in hybrid capacitive deionization. *Desalination*, *520*, 115374. https://doi.org/10.1016/j.desal.2021.115374

Lewis, A. E. (2010). Review of metal sulphide precipitation. *Hydrometallurgy*, *104*(2), 222-234. https://doi.org/10.1016/j.hydromet.2010.06.010

Leyva-Ramos, R., Fuentes-Rubio, L., Guerrero-Coronado, R. M., & Mendoza-Barron, J. (1995). Adsorption of trivalent chromium from aqueous solutions onto activated carbon. *Journal of Chemical Technology & Biotechnology: International Research in Process, Environmental AND Clean Technology*, *62*(1), 64-67.

Li, D., Ning, X. A., Yuan, Y., Hong, Y., & Zhang, J. (2020). Ion-exchange polymers modified bacterial cellulose electrodes for the selective removal of nitrite ions from tail water of dyeing wastewater. *J Environ Sci (China)*, *91*, 62-72. https://doi.org/10.1016/j.jes.2020.01.002

Li, H., & Zou, L. (2011). Ion-exchange membrane capacitive deionization: A new strategy for brackish water desalination. *Desalination*, *275*(1-3), 62-66. https://doi.org/10.1016/j.desal.2011.02.027

Li, J., Wang, X., Wang, H., Wang, S., Hayat, T., Alsaedi, A., & Wang, X. (2017). Functionalization of biomass carbonaceous aerogels and their application as electrode materials for electro-enhanced recovery of metal ions. *Environmental Science: Nano*, *4*(5), 1114-1123. https://doi.org/10.1039/c7en00019g

Li, M., Kuang, S., Dong, J., Ma, H., & Kang, Y. (2023). Performance and mechanisms of Cr (VI) removal by nano-MnO2 with different lattices. *Journal of Molecular Structure*, *1275*, 134624.

Li, P., Gui, Y., & Blackwood, D. J. (2018). Development of a Nanostructured alpha-MnO(2)/Carbon Paper Composite for Removal of Ni(2+)/Mn(2+) Ions by

Electrosorption. *ACS Appl Mater Interfaces*, *10*(23), 19615-19625. https://doi.org/10.1021/acsami.8b02471

Li, P., Gui, Y., & Blackwood, D. J. (2018). Development of a nanostructured α-MnO2/carbon paper composite for removal of Ni2+/Mn2+ ions by electrosorption. *ACS applied materials & interfaces*, *10*(23), 19615-19625.

Li, Y., Stewart, T. C., & Tang, H. L. (2018). A comparative study on electrosorptive rates of metal ions in capacitive deionization. *Journal of Water Process Engineering*, *26*, 257-263.

Li, Y., Xu, L., Gao, J., & Jin, X. (2017). Hydrothermal fabrication of reduced graphene oxide/activated carbon/MnO2 hybrids with excellent electrochemical performance for supercapacitors. *RSC Advances*, *7*(62), 39024-39033. https://doi.org/10.1039/c7ra07056j

Li, Y., Xu, R., Qiao, L., Li, Y., Wang, D., Li, D., Liang, X., Xu, G., Gao, M., Gong, H., Zhang, X., Qiu, H., Liang, K., Chen, P., & Li, Y. (2022). Controlled synthesis of ZnO modified N-doped porous carbon nanofiber membrane for highly efficient removal of heavy metal ions by capacitive deionization. *Microporous and Mesoporous Materials*, *338*, 111889. https://doi.org/10.1016/j.micromeso.2022.111889

Liang, P., Yuan, L., Yang, X., Zhou, S., & Huang, X. (2013). Coupling ion-exchangers with inexpensive activated carbon fiber electrodes to enhance the performance of capacitive deionization cells for domestic wastewater desalination. *Water Res*, *47*(7), 2523-2530. https://doi.org/10.1016/j.watres.2013.02.037

Licht, F., Davis, M. A., & Andreas, H. A. (2020). Charge redistribution and electrode history impact galvanostatic charging/discharging and associated figures of merit. *Journal of Power Sources*, *446*, 227354. https://doi.org/10.1016/j.jpowsour.2019.227354

Liu, H., Zhang, J., Ngo, H. H., Guo, W., Wu, H., Cheng, C., Guo, Z., & Zhang, C. (2015). Carbohydrate-based activated carbon with high surface acidity and basicity for nickel removal from synthetic wastewater. *RSC Advances*, *5*(64), 52048-52056.

Liu, L., Guo, X., Tallon, R., Huang, X., & Chen, J. (2017). Highly porous N-doped graphene nanosheets for rapid removal of heavy metals from water by capacitive deionization. *Chem Commun (Camb)*, *53*(5), 881-884. https://doi.org/10.1039/c6cc08515f

Liu, L., Qiu, G., Suib, S. L., Liu, F., Zheng, L., Tan, W., & Qin, L. (2017). Enhancement of Zn2+ and Ni2+ removal performance using a deionization pseudocapacitor with nanostructured birnessite and its carbon nanotube composite electrodes. *Chemical Engineering Journal*, *328*, 464-473. https://doi.org/10.1016/j.cej.2017.07.066

Liu, Q., Bi, S., Xu, X., Xiao, X., & Lei, Y. (2024). N, O-codoped carbon aerogel electrode improves capacitive deionization performance. *Journal of Colloid and Interface Science*.

Liu, X., Liu, L., Zhang, J., & Meng, Q. (2021). Capacitive deionization and methyl orange removal of holey graphene hydrogels. *Colloids and Surfaces A: Physicochemical and Engineering Aspects*, *618*, 126463. https://doi.org/10.1016/j.colsurfa.2021.126463

Liu, X., & Wang, J. (2020). Electro-assisted adsorption of Cs(I) and Co(II) from aqueous solution by capacitive deionization with activated carbon cloth/graphene oxide composite electrode. *Sci Total Environ*, *749*, 141524. https://doi.org/10.1016/j.scitotenv.2020.141524

Liu, X., Wu, J., & Wang, J. (2019). Electro-enhanced removal of cobalt ions from aqueous solution by capacitive deionization. *Sci Total Environ*, *697*, 134144. https://doi.org/10.1016/j.scitotenv.2019.134144

Liu, Y.-H., Hsi, H.-C., Li, K.-C., & Hou, C.-H. (2016). Electrodeposited Manganese Dioxide/Activated Carbon Composite As a High-Performance Electrode Material for Capacitive Deionization. *ACS Sustainable Chemistry & Engineering*, *4*(9), 4762-4770. https://doi.org/10.1021/acssuschemeng.6b00974

Liu, Y., Yang, Z., Yu, Z., Liu, Z., Liu, D., Lin, H., Li, M., Ma, S., Avdeev, M., & Shi, S. (2023). Generative artificial intelligence and its applications in materials

science: Current situation and future perspectives. *Journal of Materiomics*, *9*(4), 798-816.

Lota, G., Krawczyk, P., Lota, K., Sierczyńska, A., Kolanowski, Ł., Baraniak, M., & Buchwald, T. (2016). The application of activated carbon modified by ozone treatment for energy storage. *Journal of Solid State Electrochemistry*, *20*, 2857-2864.

Lu, H., Wang, Y., & Wang, J. (2015). Recovery of Ni2+ and pure water from electroplating rinse wastewater by an integrated two-stage electrodeionization process. *Journal of Cleaner Production*, *92*, 257-266. https://doi.org/10.1016/j.jclepro.2014.12.056

Lu, J., Kumar Mishra, P., Hunter, T. N., Yang, F., Lu, Z., Harbottle, D., & Xu, Z. (2022). Functionalization of mesoporous carbons derived from pomelo peel as capacitive electrodes for preferential removal/recovery of copper and lead from contaminated water. *Chemical Engineering Journal*, *433*, 134508. https://doi.org/https://doi.org/10.1016/j.cej.2022.134508

Lu, Z., Wang, H., Li, J., Yuan, L., & Zhu, L. (2015). Adsorption characteristics of bio-adsorbent on chromium(III) in industrial wastewater. *Water Sci Technol*, *72*(7), 1051-1061. https://doi.org/10.2166/wst.2015.237

Luo, H., Agata, W.-A. S., & Geise, G. M. (2020). Connecting the Ion Separation Factor to the Sorption and Diffusion Selectivity of Ion Exchange Membranes. *Industrial & Engineering Chemistry Research*, *59*(32), 14189-14206. https://doi.org/10.1021/acs.iecr.0c02457

Ma, C. Y., Huang, S. C., Chou, P. H., Den, W., & Hou, C. H. (2016). Application of a multiwalled carbon nanotube-chitosan composite as an electrode in the electrosorption process for water purification. *Chemosphere*, *146*, 113-120. https://doi.org/10.1016/j.chemosphere.2015.12.012

Ma, D., Yan, S., Xue, X., Niu, M., Li, H., Bao, D., Zhao, C., Li, X., Wang, P., Li, R., Huang, L., Yu, M., Jia, S., Wang, Y., Li, X., Zhang, Z., & Wang, T. (2024). Carbon nanotube wrapped hydrogen-bonded organic frameworks towards superior Na+ storage in the capacitive deionization process. *Separation and*

Purification Technology, *339*, 126728. https://doi.org/https://doi.org/10.1016/j.seppur.2024.126728

Ma, J., Liang, P., Sun, X., Zhang, H., Bian, Y., Yang, F., Bai, J., Gong, Q., & Huang, X. (2019). Energy recovery from the flow-electrode capacitive deionization. *Journal of Power Sources*, *421*, 50-55. https://doi.org/10.1016/j.jpowsour.2019.02.082

Maheshwari, K., Gupta, A. B., Gupta, R., & Agarwal, M. (2023). Desalinating RO retentate employing NF coupled with CDI: A path towards cleaner production. *Journal of Cleaner Production*, *395*, 136405. https://doi.org/https://doi.org/10.1016/j.jclepro.2023.136405

Manikandan, S., Subbaiya, R., Saravanan, M., Ponraj, M., Selvam, M., & Pugazhendhi, A. (2022). A critical review of advanced nanotechnology and hybrid membrane based water recycling, reuse, and wastewater treatment processes. *Chemosphere*, *289*, 132867. https://doi.org/10.1016/j.chemosphere.2021.132867

Mansoor, N. E., Diaz, L. A., Shuck, C. E., Gogotsi, Y., Lister, T. E., & Estrada, D. (2022). Removal and recovery of ammonia from simulated wastewater using Ti3C2T x MXene in flow electrode capacitive deionization. *npj Clean Water*, *5*(1), 26.

Martín-Lara, M. A., Blázquez, G., Trujillo, M. C., Pérez, A., & Calero, M. (2014). New treatment of real electroplating wastewater containing heavy metal ions by adsorption onto olive stone. *Journal of Cleaner Production*, *81*, 120-129. https://doi.org/10.1016/j.jclepro.2014.06.036

McNair, R., Cseri, L., Szekely, G., & Dryfe, R. (2020). Asymmetric Membrane Capacitive Deionization Using Anion-Exchange Membranes Based on Quaternized Polymer Blends. *ACS Appl Polym Mater*, *2*(7), 2946-2956. https://doi.org/10.1021/acsapm.0c00432

McNair, R., Szekely, G., & Dryfe, R. A. W. (2020). Ion-Exchange Materials for Membrane Capacitive Deionization. *ACS ES&T Water*, *1*(2), 217-239. https://doi.org/10.1021/acsestwater.0c00123

Mei, B.-A., Munteshari, O., Lau, J., Dunn, B., & Pilon, L. (2017). Physical Interpretations of Nyquist Plots for EDLC Electrodes and Devices. *The Journal of Physical Chemistry C*, *122*(1), 194-206. https://doi.org/10.1021/acs.jpcc.7b10582

Mei, B.-A., Munteshari, O., Lau, J., Dunn, B., & Pilon, L. (2018). Physical interpretations of Nyquist plots for EDLC electrodes and devices. *The Journal of Physical Chemistry C*, *122*(1), 194-206.

Millet, P. (2011). Membrane electrolysers for hydrogen (H 2) production. In A. Basile & S. P. Nunes (Eds.), *Advanced Membrane Science and Technology for Sustainable Energy and Environmental Applications* (pp. 568-609). Woodhead Publishing. https://doi.org/10.1533/9780857093790.4.568

Mohamed, M. A., Jaafar, J., Ismail, A. F., Othman, M. H. D., & Rahman, M. A. (2017). Fourier Transform Infrared (FTIR) Spectroscopy. In N. Hilal, A. F. Ismail, T. Matsuura, & D. Oatley-Radcliffe (Eds.), *Membrane Characterization* (pp. 3-29). Elsevier. https://doi.org/10.1016/b978-0-444-63776-5.00001-2

Mossad, M., & Zou, L. (2012). A study of the capacitive deionisation performance under various operational conditions. *J Hazard Mater*, *213-214*, 491-497. https://doi.org/10.1016/j.jhazmat.2012.02.036

Mossad, M., & Zou, L. (2013). Study of fouling and scaling in capacitive deionisation by using dissolved organic and inorganic salts. *J Hazard Mater*, *244-245*, 387-393. https://doi.org/10.1016/j.jhazmat.2012.11.062

Mubita, T., Porada, S., Aerts, P., & van der Wal, A. (2020). Heterogeneous anion exchange membranes with nitrate selectivity and low electrical resistance. *Journal of Membrane Science*, *607*, 118000. https://doi.org/10.1016/j.memsci.2020.118000

Mubita, T. M., Dykstra, J. E., Biesheuvel, P. M., van der Wal, A., & Porada, S. (2019). Selective adsorption of nitrate over chloride in microporous carbons. *Water Res*, *164*, 114885. https://doi.org/10.1016/j.watres.2019.114885

Mudau, F., Motsa, M., Hassard, F., & de Kock, L. A. (2022). Resin-Loaded Heterogeneous Polyether Sulfone Ion Exchange Membranes for Saline

Groundwater Treatment. *Membranes (Basel)*, *12*(8), 736. https://doi.org/10.3390/membranes12080736

Muraoka, Y., Chiba, H., Atou, T., Kikuchi, M., Hiraga, K., Syono, Y., Sugiyama, S., Yamamoto, S., & Grenier, J.-C. (1999). Preparation ofα-MnO2with an Open Tunnel. *Journal of Solid State Chemistry*, *144*(1), 136-142. https://doi.org/10.1006/jssc.1999.8133

Muratov, A., Belova, L., Vialkova, E., Glushchenko, E., Burdeev, V., Parfenov, Y., & Ignatieva, S. (2020). Treatment of electroplating wastewaters. *E3S Web of Conferences*, *203*. https://doi.org/10.1051/e3sconf/202020303009

Myint, M. T. Z., Al-Harthi, S. H., & Dutta, J. (2014). Brackish water desalination by capacitive deionization using zinc oxide micro/nanostructures grafted on activated carbon cloth electrodes. *Desalination*, *344*, 236-242. https://doi.org/10.1016/j.desal.2014.03.037

Nai, J., & Lou, X. W. D. (2019). Hollow Structures Based on Prussian Blue and Its Analogs for Electrochemical Energy Storage and Conversion. *Adv Mater*, *31*(38), e1706825. https://doi.org/10.1002/adma.201706825

NguyenTan, T., Babel, S., Bora, T., Sreearunothai, P., & Laohhasurayotin, K. (2024a). Preparation of heterogeneous cation exchange membrane and its contributions in enhancing the removal of Ni2+ by capacitive deionization system. *Chemosphere*, 141115.

NguyenTan, T., Babel, S., Bora, T., Sreearunothai, P., & Laohhasurayotin, K. (2024b). Preparation of heterogeneous cation exchange membrane and its contributions in enhancing the removal of Ni(2+) by capacitive deionization system. *Chemosphere*, *350*, 141115. https://doi.org/10.1016/j.chemosphere.2024.141115

Nightingale, E. R. (2002). Phenomenological Theory of Ion Solvation. Effective Radii of Hydrated Ions. *The Journal of Physical Chemistry*, *63*(9), 1381-1387. https://doi.org/10.1021/j150579a011

Nightingale Jr, E. (1959). Phenomenological theory of ion solvation. Effective radii of hydrated ions. *The Journal of Physical Chemistry*, *63*(9), 1381-1387.

Ntakirutimana, S., & Tan, W. (2021). Electrochemical capacitive behaviors of carbon/titania composite prepared by Tween 80-assisted sol-gel process for capacitive deionization. *Desalination*, *512*, 115131.

Obotey Ezugbe, E., & Rathilal, S. (2020). Membrane Technologies in Wastewater Treatment: A Review. *Membranes (Basel)*, *10*(5), 89. https://doi.org/10.3390/membranes10050089

Omosebi, A., Gao, X., Holubowitch, N., Li, Z., Landon, J., & Liu, K. (2017). Anion exchange membrane capacitive deionization cells. *Journal of The Electrochemical Society*, *164*(9), E242.

Osińska, M. (2016). Removal of lead(II), copper(II), cobalt(II) and nickel(II) ions from aqueous solutions using carbon gels. *Journal of Sol-Gel Science and Technology*, *81*(3), 678-692. https://doi.org/10.1007/s10971-016-4256-0

Pargoletti, E., Pifferi, V., Falciola, L., Facchinetti, G., Depaolini, A. R., Davoli, E., Marelli, M., & Cappelletti, G. (2019). A detailed investigation of MnO2 nanorods to be grown onto activated carbon. High efficiency towards aqueous methyl orange adsorption/degradation. *Applied Surface Science*, *472*, 118-126.

Pastushok, O., Zhao, F., Ramasamy, D. L., & Sillanpää, M. (2019). Nitrate removal and recovery by capacitive deionization (CDI). *Chemical Engineering Journal*, *375*, 121943. https://doi.org/10.1016/j.cej.2019.121943

Pei, L., Zhao, W., & Zhang, L. (2010). Preparation and characterization of porous poly(vinylidene fluoride) membranes for dehumidification with poly(ethylene glycol) as an additive. *Journal of Applied Polymer Science*, *118*(5), 2696-2703. https://doi.org/10.1002/app.32628

Peng, Z., Zhang, D., Shi, L., Yan, T., Yuan, S., Li, H., Gao, R., & Fang, J. (2011). Comparative Electroadsorption Study of Mesoporous Carbon Electrodes with Various Pore Structures. *The Journal of Physical Chemistry C*, *115*(34), 17068-17076. https://doi.org/10.1021/jp2047618

Pradhan, B. K., & Sandle, N. (1999). Effect of different oxidizing agent treatments on the surface properties of activated carbons. *Carbon*, *37*(8), 1323-1332.

Qasem, N. A. A., Mohammed, R. H., & Lawal, D. U. (2021). Removal of heavy metal ions from wastewater: a comprehensive and critical review. *npj Clean Water*, *4*(1). https://doi.org/10.1038/s41545-021-00127-0

Qin, X. Y., Chai, M. R., Ju, D. Y., & Hamamoto, O. (2018). Investigation of plating wastewater treatment technology for chromium, nickel and copper. *IOP Conference Series: Earth and Environmental Science*, *191*. https://doi.org/10.1088/1755-1315/191/1/012006

Raja, P. B., Munusamy, K. R., Perumal, V., & Ibrahim, M. N. M. (2022). Characterization of nanomaterial used in nanobioremediation. In H. M. N. Iqbal, M. Bilal, & T. A. Nguyen (Eds.), *Nano-Bioremediation : Fundamentals and Applications* (pp. 57-83). Elsevier. https://doi.org/10.1016/b978-0-12-823962-9.00037-4

Rajasulochana, P., & Preethy, V. (2016). Comparison on efficiency of various techniques in treatment of waste and sewage water – A comprehensive review. *Resource-Efficient Technologies*, *2*(4), 175-184. https://doi.org/10.1016/j.reffit.2016.09.004

Rathi, B. S., & Kumar, P. S. (2020). Electrodeionization theory, mechanism and environmental applications. A review. *Environmental Chemistry Letters*, *18*(4), 1209-1227. https://doi.org/10.1007/s10311-020-01006-9

Ravanchi, M. T., Kaghazchi, T., & Kargari, A. (2009). Application of membrane separation processes in petrochemical industry: a review. *Desalination*, *235*(1-3), 199-244.

Ryoo, M. W., Kim, J. H., & Seo, G. (2003). Role of titania incorporated on activated carbon cloth for capacitive deionization of NaCl solution. *J Colloid Interface Sci*, *264*(2), 414-419. https://doi.org/10.1016/S0021-9797(03)00375-8

Sahoo, T. R., & Prelot, B. (2020). Adsorption processes for the removal of contaminants from wastewater. In *Nanomaterials for the Detection and Removal of Wastewater Pollutants* (pp. 161-222). Elsevier. https://doi.org/10.1016/b978-0-12-818489-9.00007-4

Samaraweera, A., Priyantha, N., Gunathilake, W., Kotabewatta, P., & Kulasooriya, T. (2020). Biosorption of Cr (III) and Cr (VI) species on NaOH-modified peel of Artocarpus nobilis fruit. 1. Investigation of kinetics. *Applied Water Science*, *10*(5), 1-11.

Sayed, E. T., Obaid, M., Olabi, A. G., Abdelkareem, M. A., Al Radi, M., Al-Dawoud, A., Al-Asheh, S., & Ghaffour, N. (2023). Recent progress on the application of capacitive deionization for wastewater treatment. *Journal of Water Process Engineering*, *56*, 104379. https://doi.org/https://doi.org/10.1016/j.jwpe.2023.104379

Shang, X., Cusick, R. D., & Smith, K. C. (2017). A combined modeling and experimental study assessing the impact of fluid pulsation on charge and energy efficiency in capacitive deionization. *Journal of The Electrochemical Society*, *164*(14), E536.

Sharma, S. K., Petrusevski, B., & Amy, G. (2008). Chromium removal from water: a review. *Journal of Water Supply: Research and Technology—AQUA*, *57*(8), 541-553.

Shen, Y.-Y., Sun, S.-H., Tsai, S.-W., Chen, T.-H., & Hou, C.-H. (2021). Development of a membrane capacitive deionization stack for domestic wastewater reclamation: A pilot-scale feasibility study. *Desalination*, *500*, 114851. https://doi.org/https://doi.org/10.1016/j.desal.2020.114851

Shi, W., Ye, C., Xu, X., Liu, X., Ding, M., Liu, W., Cao, X., Shen, J., Yang, H. Y., & Gao, C. (2018). High-Performance Membrane Capacitive Deionization Based on Metal-Organic Framework-Derived Hierarchical Carbon Structures. *ACS omega*, *3*(8), 8506-8513. https://doi.org/10.1021/acsomega.8b01356

Shi, Y., Eze, C., Xiong, B., He, W., Zhang, H., Lim, T. M., Ukil, A., & Zhao, J. (2019). Recent development of membrane for vanadium redox flow battery applications: A review. *Applied Energy*, *238*, 202-224. https://doi.org/10.1016/j.apenergy.2018.12.087

Shim, J., Yoon, N., Park, S., Park, J., Son, M., Jeong, K., & Cho, K. H. (2021). Influence of natural organic matter on membrane capacitive deionization performance.

Chemosphere, *264*(Pt 2), 128519. https://doi.org/10.1016/j.chemosphere.2020.128519

Shim, J., Yoon, N., Park, S., Park, J., Son, M., Jeong, K., & Cho, K. H. (2021). Influence of natural organic matter on membrane capacitive deionization performance. *Chemosphere*, *264*, 128519.

Singh, A., Dhapola, P. S., Singh, S., Singh, P. K., Samsudin, A., Sahoo, N. G., & Rhee, H.-W. (2021). Highly conducting polymer electrolyte-ionic liquid and porous carbon material for sandwich electric double layer capacitor. *High Performance Polymers*, *33*(4), 469-475.

Singh, K., Agarwal, M., & Renu. (2017). Heavy metal removal from wastewater using various adsorbents: a review. *Journal of Water Reuse and Desalination*, *7*(4), 387-419. https://doi.org/10.2166/wrd.2016.104

Singh, V., & Ram, C. (2016). Physico-Chemical Characterization of Electroplating Industrial Effluents of Chandigarh and Haryana Region. *Journal of Civil & Environmental Engineering*, *6*(4). https://doi.org/10.4172/2165-784x.1000237

Srivastava, N. K., & Majumder, C. B. (2008). Novel biofiltration methods for the treatment of heavy metals from industrial wastewater. *J Hazard Mater*, *151*(1), 1-8. https://doi.org/10.1016/j.jhazmat.2007.09.101

Strasheim, A., & Buijs, K. (1961). Infra-red spectra of ion-exchangers on polystyrene base. *Spectrochimica Acta*, *17*(4), 388-392. https://doi.org/10.1016/0371-1951(61)80090-8

Su, Y., Muller, K. R., Yoshihara-Saint, H., Najm, I., & Jassby, D. (2021). Nitrate Removal in an Electrically Charged Granular-Activated Carbon Column. *Environ Sci Technol*, *55*(24), 16597-16606. https://doi.org/10.1021/acs.est.1c02152

Tan, T. N., & Babel, S. (2023). Unravelling the key contribution of a modified zinc oxide nanostructures on activated carbon cloth material for removal of Cu2+ in different configurations of capacitive deionization system. *Journal of Water Process Engineering*, *56*, 104268.

Tang, C. J., & (2017). More works on waste treatment and process improvement. 273-290. https://doi.org/10.1016/B978-0-12-803410-1.00010-4

Tang, W., He, D., Zhang, C., Kovalsky, P., & Waite, T. D. (2017). Comparison of Faradaic reactions in capacitive deionization (CDI) and membrane capacitive deionization (MCDI) water treatment processes. *Water Res*, *120*, 229-237. https://doi.org/10.1016/j.watres.2017.05.009

Tang, W., Liang, J., He, D., Gong, J., Tang, L., Liu, Z., Wang, D., & Zeng, G. (2019a). Various cell architectures of capacitive deionization: Recent advances and future trends. *Water Res*, *150*, 225-251. https://doi.org/10.1016/j.watres.2018.11.064

Tang, W., Liang, J., He, D., Gong, J., Tang, L., Liu, Z., Wang, D., & Zeng, G. (2019b). Various cell architectures of capacitive deionization: Recent advances and future trends. *Water Research*, *150*, 225-251. https://doi.org/10.1016/j.watres.2018.11.064

Tchounwou, P. B., Yedjou, C. G., Patlolla, A. K., & Sutton, D. J. (2012). Heavy metal toxicity and the environment. *Exp Suppl*, *101*, 133-164. https://doi.org/10.1007/978-3-7643-8340-4_6

TEPNET. (2024). *Development of Thailand electroplating professional network (TEPNET)*. Retrieved April 2024 from http://www.tepnet.or.th/about-tepnet

Thommes, M., Kaneko, K., Neimark, A. V., Olivier, J. P., Rodriguez-Reinoso, F., Rouquerol, J., & Sing, K. S. (2015a). Physisorption of gases, with special reference to the evaluation of surface area and pore size distribution (IUPAC Technical Report). *Pure and Applied Chemistry*, *87*(9-10), 1051-1069.

Thommes, M., Kaneko, K., Neimark, A. V., Olivier, J. P., Rodriguez-Reinoso, F., Rouquerol, J., & Sing, K. S. W. (2015b). Physisorption of gases, with special reference to the evaluation of surface area and pore size distribution (IUPAC Technical Report). *Pure and Applied Chemistry*, *87*(9-10), 1051-1069. https://doi.org/10.1515/pac-2014-1117

Tong, B., Hossain, M. M., Yang, Z., Cheng, C., Wang, Y., Jiang, C., & Xu, T. (2016). Development of heterogeneous cation exchange membranes using functional

polymer powders for desalination applications. *Journal of the Taiwan Institute of Chemical Engineers*, *67*, 435-442. https://doi.org/10.1016/j.jtice.2016.07.032

Tsehaye, M. T., Mourouga, G., Schmidt, T. J., Schumacher, J. O., Velizarov, S., Van der Bruggen, B., Alloin, F., & Iojoiu, C. (2023). Towards optimized membranes for aqueous organic redox flow batteries: Correlation between membrane properties and cell performance. *Renewable and Sustainable Energy Reviews*, *173*, 113059. https://doi.org/10.1016/j.rser.2022.113059

UN. (2023). *The United Nations World Water Development Report 2023: Partnerships and cooperation for water*. UNESCO Publishing. https://www.unwater.org/publications/un-world-water-development-report-2023

Van der Bruggen, B. (2015). Advances in electrodialysis for water treatment. In *Advances in membrane technologies for water treatment* (pp. 185-203). Elsevier.

Vardhan, K. H., Kumar, P. S., & Panda, R. C. (2019). A review on heavy metal pollution, toxicity and remedial measures: Current trends and future perspectives. *Journal of Molecular Liquids*, *290*, 111197.

Villar, I., Suarez-De la Calle, D. J., González, Z., Granda, M., Blanco, C., Menéndez, R., & Santamaría, R. (2011). Carbon materials as electrodes for electrosorption of NaCl in aqueous solutions. *Adsorption*, *17*, 467-471.

Vir Singh, M., Kumar Tiwari, A., & Gupta, R. (2023). Catalytic chemical vapor deposition methodology for carbon nanotubes synthesis. *ChemistrySelect*, *8*(32), e202204715.

Volodina, E., Pismenskaya, N., Nikonenko, V., Larchet, C., & Pourcelly, G. (2005). Ion transfer across ion-exchange membranes with homogeneous and heterogeneous surfaces. *J Colloid Interface Sci*, *285*(1), 247-258. https://doi.org/10.1016/j.jcis.2004.11.017

Vrandečić, N. S., Erceg, M., Jakić, M., & Klarić, I. (2010). Kinetic analysis of thermal degradation of poly(ethylene glycol) and poly(ethylene oxide)s of different

molecular weight. *Thermochimica Acta*, *498*(1-2), 71-80. https://doi.org/10.1016/j.tca.2009.10.005

Wang, C., Chen, L., & Liu, S. (2019). Activated carbon fiber for adsorption/electrodeposition of Cu (II) and the recovery of Cu (0) by controlling the applied voltage during membrane capacitive deionization. *J Colloid Interface Sci*, *548*, 160-169. https://doi.org/10.1016/j.jcis.2019.04.030

Wang, C., Li, T., Yu, G., & Deng, S. (2021). Removal of low concentrations of nickel ions in electroplating wastewater using capacitive deionization technology. *Chemosphere*, *284*, 131341. https://doi.org/10.1016/j.chemosphere.2021.131341

Wang, C., Song, H., Zhang, Q., Wang, B., & Li, A. (2015). Parameter optimization based on capacitive deionization for highly efficient desalination of domestic wastewater biotreated effluent and the fouled electrode regeneration. *Desalination*, *365*, 407-415.

Wang, H., Li, Y., Liu, Y., Xu, X., Lu, T., & Pan, L. (2025). Advancement of capacitive deionization propelled by machine learning approach. *Separation and Purification Technology*, *354*, 129423. https://doi.org/https://doi.org/10.1016/j.seppur.2024.129423

Wang, H., Zhu, Y., Hu, B., Yang, J., & Liu, J. (2024). Carbon-modified bentonite ion-exchange electrode in rocking-chair capacitive deionization with superior desalination capacity and high stability. *Desalination*, *586*, 117879.

Wang, J., Wang, G., Wu, T., Wang, D., Yuan, Y., Wang, J., Liu, T., Wang, L., & Qiu, J. (2018). Quaternary Ammonium Compound Functionalized Activated Carbon Electrode for Capacitive Deionization Disinfection. *ACS Sustainable Chemistry & Engineering*, *6*(12), 17204-17210. https://doi.org/10.1021/acssuschemeng.8b04573

Wang, S., Li, X., Zhao, H., Quan, X., Chen, S., & Yu, H. (2018). Enhanced adsorption of ionizable antibiotics on activated carbon fiber under electrochemical assistance in continuous-flow modes. *Water Res*, *134*, 162-169. https://doi.org/10.1016/j.watres.2018.01.068

Wang, T., Liu, W., Xiong, L., Xu, N., & Ni, J. (2013). Influence of pH, ionic strength and humic acid on competitive adsorption of Pb(II), Cd(II) and Cr(III) onto titanate nanotubes. *Chemical Engineering Journal*, *215-216*, 366-374. https://doi.org/10.1016/j.cej.2012.11.029

WHO. (2022). *Guidelines for drinking-water quality: incorporating the first and second addenda*. World Health Organization.

Witkowska, D., Słowik, J., & Chilicka, K. (2021). Heavy metals and human health: Possible exposure pathways and the competition for protein binding sites. *Molecules*, *26*(19), 6060.

Wu, F.-C., Tseng, R.-L., Huang, S.-C., & Juang, R.-S. (2009). Characteristics of pseudo-second-order kinetic model for liquid-phase adsorption: A mini-review. *Chemical Engineering Journal*, *151*(1-3), 1-9. https://doi.org/10.1016/j.cej.2009.02.024

Wu, S., Yan, P., Yang, W., Zhou, J., Wang, H., Che, L., & Zhu, P. (2021). ZnCl(2) enabled synthesis of activated carbons from ion-exchange resin for efficient removal of Cu(2+) ions from water via capacitive deionization. *Chemosphere*, *264*(Pt 2), 128557. https://doi.org/10.1016/j.chemosphere.2020.128557

Wu, T., Chen, X., Zhang, H., Zhao, M., Huang, L., Yan, J., Su, M., & Liu, X. (2023). MoS2-encapsulated nitrogen-doped carbon bowls for highly efficient and selective removal of copper ions from wastewater. *Separation and Purification Technology*, *304*, 122284. https://doi.org/10.1016/j.seppur.2022.122284

Xiao, W., Wang, D., & Lou, X. W. (2010). Shape-controlled synthesis of MnO2 nanostructures with enhanced electrocatalytic activity for oxygen reduction. *The Journal of Physical Chemistry C*, *114*(3), 1694-1700.

Xing, W., Liang, J., Tang, W., He, D., Yan, M., Wang, X., Luo, Y., Tang, N., & Huang, M. (2020). Versatile applications of capacitive deionization (CDI)-based technologies. *Desalination*, *482*. https://doi.org/10.1016/j.desal.2020.114390

Xu, Y., Zhou, H., Wang, G., Zhang, Y., Zhang, H., & Zhao, H. (2020). Selective Pseudocapacitive Deionization of Calcium Ions in Copper Hexacyanoferrate.

ACS Appl Mater Interfaces, *12*(37), 41437-41445. https://doi.org/10.1021/acsami.0c11233

Xue, Y., Cheng, W., Cao, M., Gao, J., Chen, J., Gui, Y., Zhu, W., & Ma, F. (2022). Development of nitric acid-modified activated carbon electrode for removal of Co2+/Mn2+/Ni2+ by electrosorption. *Environmental Science and Pollution Research*, *29*(51), 77536-77552.

Yang, I., Kim, S.-G., Kwon, S. H., Kim, M.-S., & Jung, J. C. (2017). Relationships between pore size and charge transfer resistance of carbon aerogels for organic electric double-layer capacitor electrodes. *Electrochimica Acta*, *223*, 21-30.

Yang, J., Bu, Y., Liu, F., Zhang, W., Cai, D., Sun, A., Wu, Y., Zhou, R., & Zhang, C. (2020). Potential Application of Membrane Capacitive Deionization for Heavy Metal Removal from Water: A Mini-Review. *International Journal of Electrochemical Science*, *15*(8), 7848-7859. https://doi.org/10.20964/2020.08.98

Yang, Y. L., Wu, Y., Lu, Y. X., Cai, Y., He, Z., Yang, X. L., & Song, H. L. (2021). A comprehensive review of nutrient-energy-water-solute recovery by hybrid osmotic membrane bioreactors. *Bioresour Technol*, *320*(Pt A), 124300. https://doi.org/10.1016/j.biortech.2020.124300

Yasin, A. S., Yousef Mohamed, A., Kim, D. H., Luu Luyen Doan, T., Chougule, S. S., Jung, N., Nam, S., & Lee, K. (2021). Design of zinc oxide nanoparticles and graphene hydrogel co-incorporated activated carbon for efficient capacitive deionization. *Separation and Purification Technology*, *277*, 119428. https://doi.org/10.1016/j.seppur.2021.119428

Yoon, H., Lee, J., Kim, S.-R., Kang, J., Kim, S., Kim, C., & Yoon, J. (2016). Capacitive deionization with Ca-alginate coated-carbon electrode for hardness control. *Desalination*, *392*, 46-53.

Yoon, J., Amy, G., Chung, J., Sohn, J., & Yoon, Y. (2009). Removal of toxic ions (chromate, arsenate, and perchlorate) using reverse osmosis, nanofiltration, and ultrafiltration membranes. *Chemosphere*, *77*(2), 228-235. https://doi.org/10.1016/j.chemosphere.2009.07.028

You, S.-M., Tasi, C.-K., Millet, P., & Doong, R.-A. (2020). Electrochemically capacitive deionization of copper (II) using 3D hierarchically reduced graphene oxide architectures. *Separation and Purification Technology*, *251*, 117368. https://doi.org/10.1016/j.seppur.2020.117368

Yu, F., Yang, Z., Cheng, Y., Xing, S., Wang, Y., & Ma, J. (2022). A comprehensive review on flow-electrode capacitive deionization: Design, active material and environmental application. *Separation and Purification Technology*, *281*, 119870. https://doi.org/10.1016/j.seppur.2021.119870

Zaghloul, M. S., & Achari, G. (2022). Application of machine learning techniques to model a full-scale wastewater treatment plant with biological nutrient removal. *Journal of Environmental Chemical Engineering*, *10*(3), 107430. https://doi.org/10.1016/j.jece.2022.107430

Zare, S., & Kargari, A. (2018). Membrane properties in membrane distillation. In *Emerging Technologies for Sustainable Desalination Handbook* (pp. 107-156). Elsevier. https://doi.org/10.1016/b978-0-12-815818-0.00004-7

Zhang, C., Dong, P., Wang, C., Liu, Y., Li, K., & Feng, G. (2024). Cr3+-doped α-MnO2 electrode with high specific capacitance and ultra-long cycle life. *Electrochimica Acta*, *481*, 143946. https://doi.org/10.1016/j.electacta.2024.143946

Zhang, C., He, D., Ma, J., Tang, W., & Waite, T. D. (2018). Faradaic reactions in capacitive deionization (CDI) - problems and possibilities: A review. *Water Res*, *128*, 314-330. https://doi.org/10.1016/j.watres.2017.10.024

Zhang, G., Li, W., Chen, Z., Long, J., & Xu, C. (2022). Freestanding N-doped graphene membrane electrode with interconnected porous architecture for efficient capacitive deionization. *Carbon*, *187*, 86-96.

Zhang, H., Wang, Q., Li, L., Huang, R., Gu, H., Chen, H., Wu, Z., & Wang, Z. (2024). Electric double layer capacitive adsorption and faradaic pseudo-capacitance behavior of ZnFe-PANI/CNT electrode for phosphate removal in capacitive deionization. *Separation and Purification Technology*, *333*, 125913. https://doi.org/10.1016/j.seppur.2023.125913

Zhang, M., & Kong, W. (2020). Recent progress in graphene-based and ion-intercalation electrode materials for capacitive deionization. *Journal of Electroanalytical Chemistry*, *878*. https://doi.org/10.1016/j.jelechem.2020.114703

Zhang, X., Zuo, K., Zhang, X., Zhang, C., & Liang, P. (2020). Selective ion separation by capacitive deionization (CDI) based technologies: a state-of-the-art review. *Environmental Science: Water Research & Technology*, *6*(2), 243-257. https://doi.org/10.1039/c9ew00835g

Zhao, C., Zhang, L., Ge, R., Zhang, A., Zhang, C., & Chen, X. (2019). Treatment of low-level Cu(II) wastewater and regeneration through a novel capacitive deionization-electrodeionization (CDI-EDI) technology. *Chemosphere*, *217*, 763-772. https://doi.org/10.1016/j.chemosphere.2018.11.071

Zhao, W.-Y., Zhou, M., Yan, B., Sun, X., Liu, Y., Wang, Y., Xu, T., & Zhang, Y. (2018). Waste Conversion and Resource Recovery from Wastewater by Ion Exchange Membranes: State-of-the-Art and Perspective. *Industrial & Engineering Chemistry Research*, *57*(18), 6025-6039. https://doi.org/10.1021/acs.iecr.8b00519

Zhao, Y., Wang, Y., Wang, R., Wu, Y., Xu, S., & Wang, J. (2013). Performance comparison and energy consumption analysis of capacitive deionization and membrane capacitive deionization processes. *Desalination*, *324*, 127-133.

Zhong, L., Yang, J., Liu, L., & Xing, B. (2015). Oxidation of Cr(III) on birnessite surfaces: The effect of goethite and kaolinite. *J Environ Sci (China)*, *37*, 8-14. https://doi.org/10.1016/j.jes.2015.03.026

Zhou, F., Gao, T., Luo, M., & Li, H. (2018). Preferential electrosorption of anions by C/Na0.7MnO2 asymmetrical electrodes. *Separation and Purification Technology*, *191*, 322-327. https://doi.org/10.1016/j.seppur.2017.09.058

APPENDICES

APPENDIX A

EXPERIMENT 1

Table A.1 Characteristics of the prepared materials.

Parameters	Unit	Value		
		ACC	ACC/MnO_2	MnO_2
Specific surface area - using BET	m2/g	1316.2	1017.4	35.83
Total pore volume - using BET	cm3/g	0.5638	0.4537	0.2427
Total pore volume - using NLDFT & GCMC	cm3/g	0.515	0.4132	0.2772
Total pore volume microporous (pore size < 2 nm) - using NLDFT & GCMC	cm3/g	0.4751	0.3642	0.005274
Total pore volume non- microporous (pore size > 2 nm) - using NLDFT & GCMC	cm3/g	0.0399	0.0490	0.271843

Table A.2 Parameters of kinetic models in CDI test of ACC and ACC/MnO_2 at 1.2 V.

Element	Sample	Concentration (mg/L)	Pseudo first order			Pseudo second order		
			$q_{e,cal}$ (mg/g)	k_1 (1/min)	R^2	$q_{e,cal}$ (mg/g)	k_2 (g/mg/min)	R^2
Cr(III)	ACC	200	6.37	0.026	0.9919	8.47	0.003	0.9941
		500	8.24	0.003	0.9822	10.77	0.002	0.9903
		1000	8.85	0.024	0.9692	11.63	0.002	0.9819
	ACC/MnO_2	200	9.05	0.021	0.9880	12.41	0.0014	0.9920
		500	10.29	0.036	0.9933	12.96	0.003	0.9968
		1000	12.58	0.003	0.9762	16.02	0.002	0.9909

Cr(VI)	ACC	200	20.97	0.022	0.9891	28.42	$6.70*10^{-4}$	0.9955
		500	27.16	0.018	0.9857	38.10	$3.81*10^{-4}$	0.9909
		1000	36.28	0.022	0.9901	49.74	0.020	0.9952
	ACC/MnO_2	200	25.94	0.023	0.9892	35.12	$5.57*10^{-4}$	0.9946
		500	35.23	0.021	0.9848	48.43	$3.58*10^{-4}$	0.9912
		1000	48.4	0.018	0.9899	68.37	$2.11*10^{-4}$	0.9932

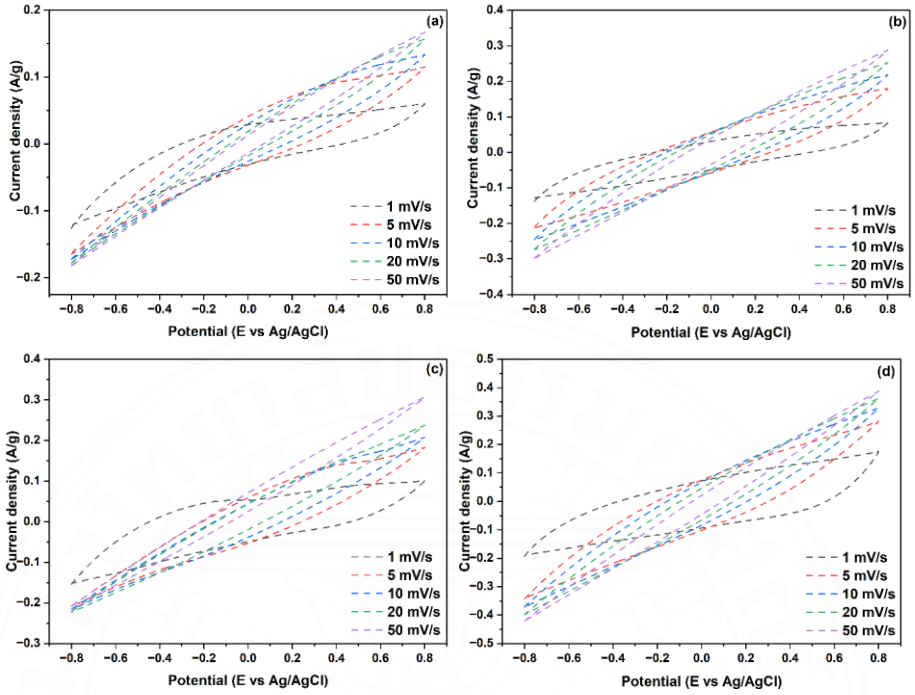

Figure A.1 CV curves at various scan rates of (a) ACC and Cr(III), (b) ACC and Cr(VI), (c) ACC/MnO_2 and Cr(III), (d) ACC/MnO_2 and Cr (VI).

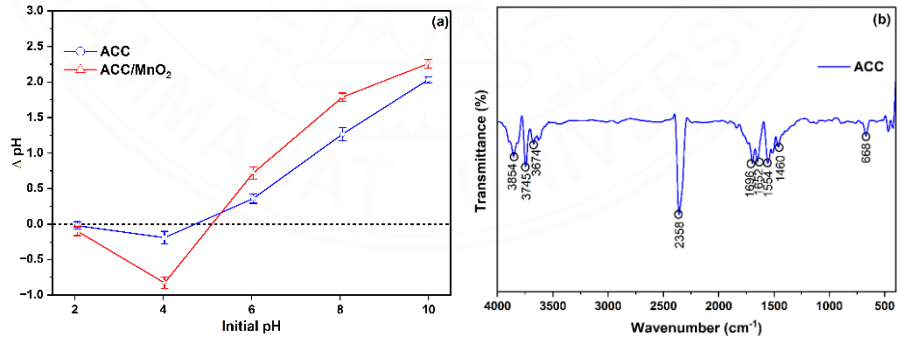

Figure A.2 (a) Point of zero charge of (PZC) of ACC material and ACC/MnO_2 material and (b) FTIR spectra of ACC material.

APPENDIX B
EXPERIMENT 2

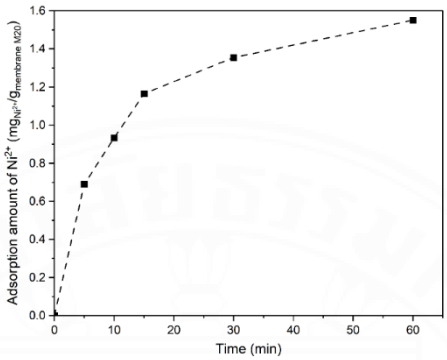

Figure B.1 Adsorption amount of Ni^{2+} on membrane M20 at a concentration of 200 mg/L Ni^{2+} in 100 mL.

Table B.1 Estimated parameters in the PFO model of CDI experiments.

Flow rate (mL/min)	Unit	Ni^{2+} concentration (mg/L)	Estimated value		
			$q_{e,cal}$ (mg Ni^{2+}/g_{ACC})	k_1 (1/min)	R^2
5	CDI	50	4.22	0.042	0.995
	CDI	100	8.26	0.032	0.993
	CDI	200	9.24	0.030	0.992
	MCDI	50	8.57	0.019	0.998
	MCDI	100	10.55	0.026	0.993
	MCDI	200	12.56	0.031	0.998
10	CDI	50	6.63	0.027	0.993
	CDI	100	9.65	0.024	0.998
	CDI	200	10.27	0.022	0.998
	MCDI	50	11.40	0.014	0.996
	MCDI	100	17.87	0.022	0.996
	MCDI	200	19.80	0.030	0.988
15	CDI	50	7.84	0.023	0.992
	CDI	100	11.83	0.020	0.998
	CDI	200	13.19	0.019	0.999
	MCDI	50	9.12	0.026	0.997
	MCDI	100	16.75	0.028	0.998
	MCDI	200	18.49	0.034	0.998

APPENDIX C

EXPERIMENT 3

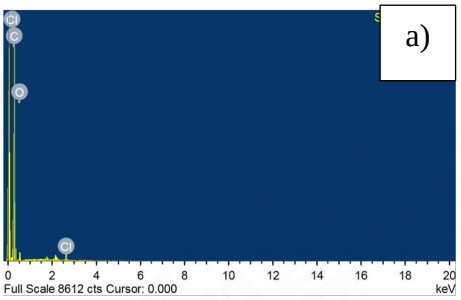

Element	Weight (%)	Atomic (%)
C	88.67	91.47
O	10.76	8.33
Cl	0.57	0.20

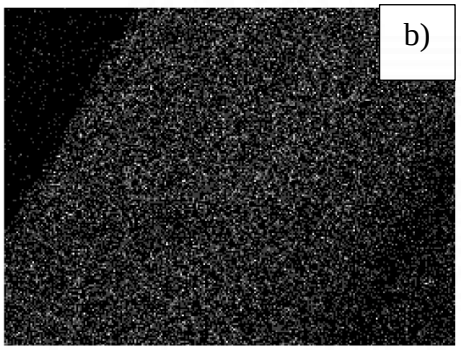

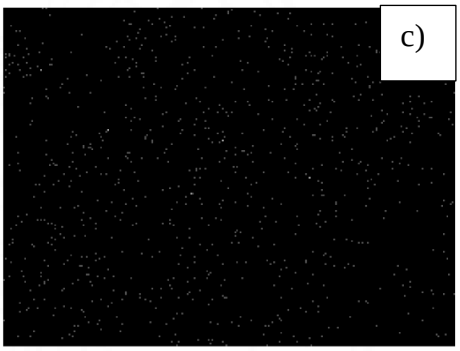

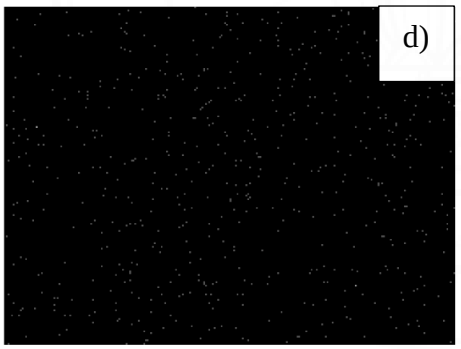

Figure C.1 EDS elemental mapping of ACC where a) Area EDS spectrum and the atomic and weight percentage of various elements b) C c) O d) Cl.

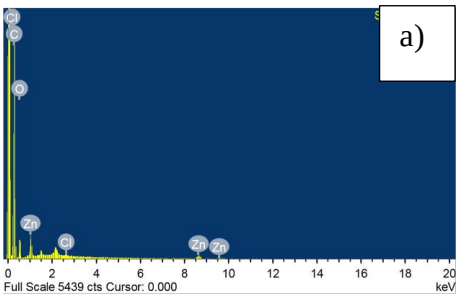

Element	Weight (%)	Atomic (%)
C	79.80	87.06
O	14.25	11.67
Cl	0.41	0.15
Zn	5.55	1.11

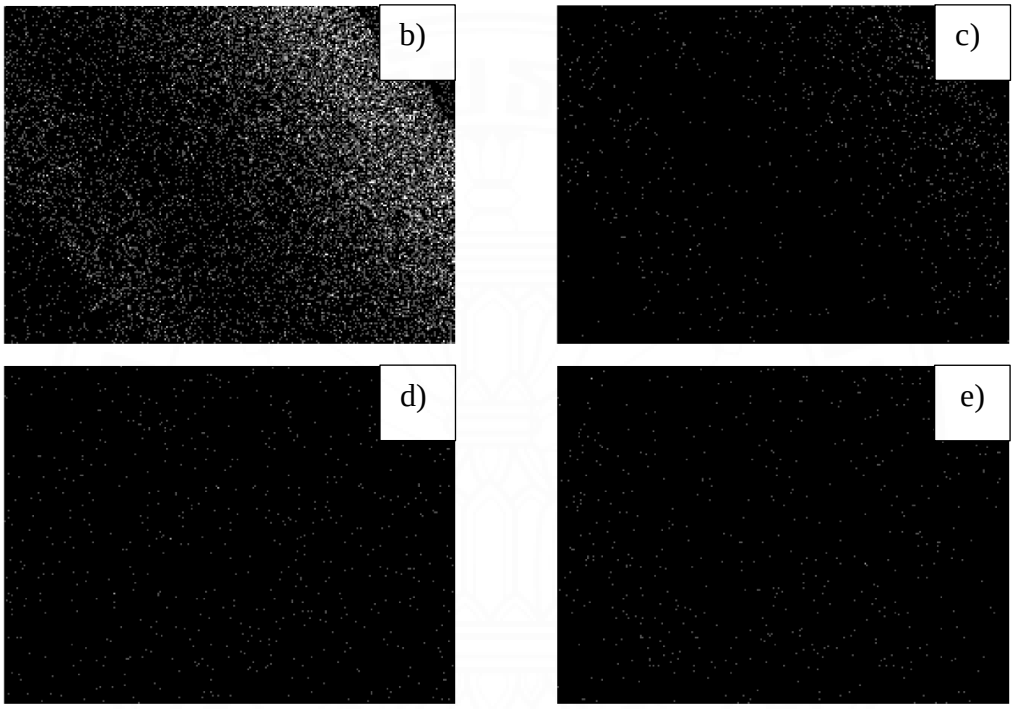

Figure C.2 EDS elemental mapping of ACC/ZnO-nPs where a) Area EDS spectrum and the atomic and weight percentage of various elements b) C c) O d) Cl e) Zn.

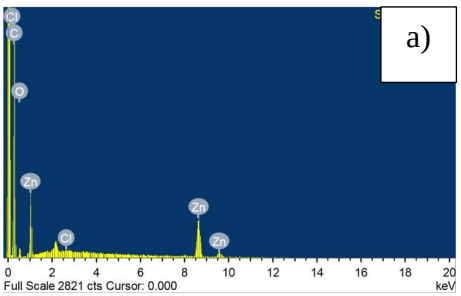

Element	Weight (%)	Atomic (%)
C	81.08	92.14
O	6.0	5.11
Cl	0.28	0.11
Zn	12.65	2.64

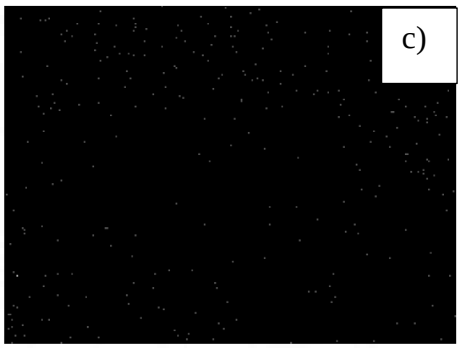

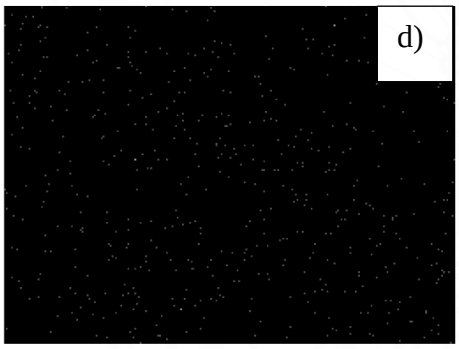

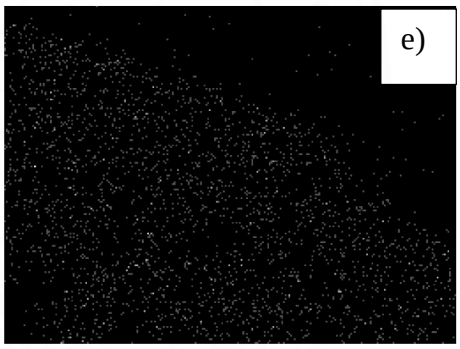

Figure C.3 EDS elemental mapping of ACC/ZnO-nRs where a) Area EDS spectrum and the atomic and weight percentage of various elements b) C c) O d) Cl e) Zn.

Table C.1 Parameters of kinetic models in CDI cell of ACC, ACC/ZnO-nPs, and ACC/ZnO-nRs at 1.2 V.

Sample	Concentration (mg/L)	Pseudo first order			Pseudo second order		
		$q_{e,cal}$ (mg/g)	k_1 (1/min)	R^2	$q_{e,cal}$ (mg/g)	k_2 (g/mg/min)	R^2
ACC	50	18.41	0.043	0.9887	22.82	$19.2*10^{-4}$	0.9928
	100	21.67	0.0325	0.9964	28.03	$10.8*10^{-4}$	0.9967
	200	27.81	0.0354	0.9808	33.02	$12.8*10^{-4}$	0.9963
	500	49.95	0.0211	0.9849	65.54	$3.1*10^{-4}$	0.9920
	1000	51.61	0.0468	0.8857	75.74	$3.0*10^{-4}$	0.9638
ACC/ZnO-nPs	50	22.75	0.0408	0.9635	25.88	$23.9**10^{-4}$	0.9962
	100	25.14	0.0867	0.8792	29.17	$24.8*10^{-4}$	0.9865

	200	33.95	0.0363	0.9952	42.29	$9.0*10^{-4}$	0.9965
	500	54.42	0.0286	0.9548	60.69	$6.5*10^{-4}$	0.9933
	1000	65.02	0.0294	0.9888	85.51	$3.1*10^{-4}$	0.9928
ACC/ZnO-nRs	50	25.27	0.0399	0.9902	31.41	$13*10^{-4}$	0.9965
	100	27.39	0.058	0.9586	32.13	$21.7*10^{-4}$	0.9890
	200	41.26	0.0304	0.9542	47.69	$9.1*10^{-4}$	0.9940
	500	59.16	0.0267	0.9140	63.09	$6.6*10^{-4}$	0.9770
	1000	71.71	0.0264	0.9897	96.37	$2.3*10^{-4}$	0.9930

Table C.2 Parameters of the kinetic model in MCDI cell of ACC, ACC/ZnO-nPs, and ACC/ZnO-nRs at 1.2 V.

Sample	Concentration (mg/L)	Pseudo first order			Pseudo second order		
		$q_{e,cal}$ (mg/g)	k_1 (1/min)	R^2	$q_{e,cal}$ (mg/g)	k_2 (g/mg/min)	R^2
ACC	50	22.68	0.0407	0.9738	26.54	$20.3*10^{-4}$	0.9917
	100	34.88	0.0284	0.9898	45.98	$5.5*10^{-4}$	0.9923
	200	40.46	0.0319	0.9879	55.65	$4.3*10^{-4}$	0.9902
	500	80.27	0.0316	0.993	104.3	$2.8*10^{-4}$	0.9965
	1000	89.5	0.0286	0.9907	118.84	$2.1*10^{-4}$	0.9931
ACC/ZnO-nPs	50	27.1	0.0537	0.8238	27.98	$47.7*10^{-4}$	0.9586

	100	39.53	0.0244	0.9299	46.43	$5.8*10^{-4}$	0.9601
	200	50.74	0.0193	0.9759	71.04	$2.0*10^{-4}$	0.9877
	500	96.17	0.0289	0.9923	127.09	$2.0*10^{-4}$	0.9969
	1000	107.16	0.0261	0.9875	144.66	$1.54*10^{-4}$	0.992
ACC/ZnO-nRs	50	27.4	0.0726	0.8743	30.80	$34.0*10^{-4}$	0.9424
	100	40.42	0.0655	0.9694	46.83	$17.5*10^{-4}$	0.9952
	200	60.36	0.0202	0.9741	80.75	$2.1*10^{-4}$	0.9829
	500	105.2	0.0271	0.9692	137.9	$1.8*10^{-4}$	0.9785
	1000	120.81	0.0202	0.9909	170.72	$9.36*10^{-5}$	0.9925

Table C.3 Adsorption amount of Cu^{2+} from the prepared material at various voltages at the 5th cycle and the 10th cycle.

Configuration	Potential (V)	5th cycle			10th cycle		
		ACC	ACC/ZnO-nPs	ACC/ZnO-nRs	ACC	ACC/ZnO-nPs	ACC/ZnO-nRs
CDI	0.4	3.9 mg/g	5.7 mg/g	6.4 mg/g	3.9 mg/g	5.3 mg/g	6.4 mg/g
	0.8	5.1 mg/g	7.9 mg/g	8.0 mg/g	5.4 mg/g	7.6 mg/g	8.5 mg/g
	1.2	6.1 mg/g	8.1 mg/g	9.0 mg/g	6.2 mg/g	7.9 mg/g	8.9 mg/g
MCDI	0.4	6.1 mg/g	6.2 mg/g	7.1 mg/g	6.4 mg/g	6.6 mg/g	7.4 mg/g
	0.8	8.7 mg/g	9.2 mg/g	9.8 mg/g	8.6 mg/g	8.9 mg/g	10.4 mg/g
	1.2	9.4 mg/g	9.9 mg/g	11.1 mg/g	9.5 mg/g	9.6 mg/g	10.9 mg/g

Table C.4 Recovery rate of Cu^{2+} from the prepared material at various voltages at the 5th cycle and the 10th cycle.

Configuration	Potential (V)	5th cycle			10th cycle		
		ACC	ACC/ZnO-nPs	ACC/ZnO-nRs	ACC	ACC/ZnO-nPs	ACC/ZnO-nRs
CDI	0.4	40.8 %	47.2 %	51.8 %	39.2 %	47.3 %	50.9 %
	0.8	44.9 %	52.5 %	55.9 %	43.5 %	54.3 %	55.0 %
	1.2	60.9 %	64.1 %	67.2 %	59.8 %	63.8 %	67.5 %
MCDI	0.4	21.7 %	28.0 %	31.6 %	29.2 %	31.4 %	31.6 %
	0.8	33.7 %	34.2 %	34.5 %	34.5 %	36.0 %	36.3 %
	1.2	33.2 %	34.4 %	35.6 %	33.9 %	36.7 %	37.1 %

APPENDIX D

EXPERIMENT 4

Table D.1 Kinetic model parameters in CDI tests for ACC, ACC/MnO_2, and ACC/ZnO at potential of 1.2 V with single ion of Ni^{2+}, Cu^{2+} and Cr^{3+}.

Element	Sample	Initial concentration (mg/L)	Pseudo-first order			Pseudo-second order		
			$q_{e,cal}$ (mg/g)	k_1 (1/min)	R^2	$q_{e,cal}$ (mg/g)	k_2 (g/mg/min)	R^2
Ni^{2+}	ACC	500	19.51	28.3E-3	0.9935	25.35	10.4E-4	0.9980
	ACC/MnO_2	500	21.84	44.4E-3	0.9879	26.11	19.7E-4	0.9958
	ACC/ZnO	500	26.36	45.4E-3	0.9721	31.72	16.1E-4	0.9977
Cu^{2+}	ACC	500	43.42	26.3E-3	0.9934	57.58	4.1E-4	0.9939
	ACC/MnO_2	500	48.87	37.9E-3	0.9744	59.74	6.9E-4	0.9922
	ACC/ZnO	500	53.69	33.3E-3	0.9671	66.80	5.2E-4	0.9871
Cr^{3+}	ACC	500	8.31	26.4E-3	0.9816	10.82	22.8E-4	0.9896
	ACC/MnO_2	500	10.33	35.6E-3	0.9928	12.94	27.8E-4	0.9960
	ACC/ZnO	500	12.16	48.8E-3	0.9782	14.38	40.5E-4	0.9966

Table D.2 Kinetic model parameters in CDI cell and MCDI cell for ACC, ACC/MnO_2, and ACC/ZnO at potential of 1.2 V with mixed of Ni^{2+}, Cu^{2+} and Cr^{3+} as scenario A.

Configuration	Sample	Elements	Initial concentration (mg/L)	Pseudo-first order			Pseudo-second order		
				$q_{e,cal}$ (mg/g)	k_1 (1/min)	R^2	$q_{e,cal}$ (mg/g)	k_1 (1/min)	R^2
CDI cell	ACC	Ni^{2+}	500	13.43	31.9E-3	0.9796	16.89	19.1E-4	0.9938
		Cu^{2+}	500	19.79	32.7E-3	0.9922	24.97	13.1E-4	0.9994
		Cr^{3+}	500	7.96	18.2E-3	0.9945	11.33	12.5E-4	0.9963
	ACC/MnO_2	Ni^{2+}	500	17.94	47.6E-3	0.9857	21.37	25.9E-4	0.9988
		Cu^{2+}	500	26.63	40.1E-3	0.9891	32.40	13.7E-4	0.9992
		Cr^{3+}	500	9.78	22.9E-3	0.9931	13.37	14.3E-4	0.9934
	ACC/ZnO	Ni^{2+}	500	23.22	46.0E-3	0.9964	27.89	18.6E-4	0.9986
		Cu^{2+}	500	33.32	38.3E-3	0.9934	41.00	9.9E-4	0.9999
		Cr^{3+}	500	10.39	23.7E-3	0.9953	14.04	14.4E-4	0.9970

MCDI cell	ACC	Ni^{2+}	500	19.66	28E-3	0.9905	25.51	11E-4	0.9960
		Cu^{2+}	500	30.53	28E-3	0.9930	39.43	7E-4	0.9992
		Cr^{3+}	500	12.88	18E-3	0.9987	18.29	8E-4	0.9998
	ACC/MnO_2	Ni^{2+}	500	25.81	34E-3	0.9851	32.23	11E-4	0.9970
		Cu^{2+}	500	36.23	33E-3	0.9924	45.70	7E-4	0.9995
		Cr^{3+}	500	18.71	31E-3	0.9861	23.79	13E-4	0.9965
	ACC/ZnO	Ni^{2+}	500	30.66	39E-3	0.9971	37.74	11E-4	0.9991
		Cu^{2+}	500	42.22	34E-3	0.9953	53.00	7E-4	0.9996
		Cr^{3+}	500	22.16	36E-3	0.9955	27.70	13E-4	0.9978

Table D.3 Kinetic model parameters in CDI cell and MCDI cell for ACC, ACC/MnO_2, and ACC/ZnO at potential of 1.2 V with mixed of Ni^{2+}, Cu^{2+} and Cr^{3+} as scenario B.

Configuration	Sample	Elements	Initial concentration (mg/L)	Pseudo-first order			Pseudo-second order		
				$q_{e,cal}$ (mg/g)	k_1 (1/min)	R^2	$q_{e,cal}$ (mg/g)	k_1 (1/min)	R^2
CDI cell	ACC	Ni^{2+}	200	7.49	38E-3	0.9886	9.24	43E-4	0.9976
		Cu^{2+}	500	28.72	22E-3	0.9935	39.11	4.7E-4	0.9978
		Cr^{3+}	100	4.22	46E-3	0.9857	5.08	10.1E-4	0.9953
	ACC/MnO_2	Ni^{2+}	200	10.95	35E-3	0.9963	13.68	26.3E-4	0.9989
		Cu^{2+}	500	31.56	46E-3	0.9927	38.02	13.5E-4	0.9962
		Cr^{3+}	100	7.27	23E-3	0.9927	9.82	19.9E-4	0.9977
	ACC/ZnO	Ni^{2+}	200	12.47	43E-3	0.9908	15.07	32.1E-4	0.9994
		Cu^{2+}	500	38.72	37E-3	0.9922	48.01	8.0E-4	0.9987
		Cr^{3+}	100	9.57	42E-3	0.9959	11.66	38.8E-4	0.9985

MCDI cell	ACC	Ni^{2+}	200	10.30	34E-3	0.9701	12.81	27.6E-4	0.9890
		Cu^{2+}	500	42.19	28E-3	0.9970	55.16	4.6E-4	0.9991
		Cr^{3+}	100	7.44	19E-3	0.9772	10.24	15.7E-4	0.9859
	ACC/MnO_2	Ni^{2+}	200	15.12	33E-3	0.9702	18.84	18.5E-4	0.9886
		Cu^{2+}	500	46.84	31E-3	0.9965	60.40	4.8E-4	0.9975
		Cr^{3+}	100	10.28	21E-3	0.9915	14.10	12.3E-4	0.9969
	ACC/ZnO	Ni^{2+}	200	20.03	23E-3	0.9930	26.97	7.4E-4	0.9975
		Cu^{2+}	500	51.64	30E-3	0.9970	66.54	4.3E-4	0.9953
		Cr^{3+}	100	11.99	38E-3	0.9717	14.65	28E-4	0.9909

Table D.4 Kinetic model parameters in CDI cell and MCDI cell for ACC, ACC/MnO_2, and ACC/ZnO at potential of 1.2 V with mixed of Ni^{2+}, Cu^{2+} and Cr^{3+} as scenario C.

Configuration	Sample	Elements	Initial concentration (mg/L)	Pseudo-first order			Pseudo-second order		
				$q_{e,cal}$ (mg/g)	k_1 (1/min)	R^2	$q_{e,cal}$ (mg/g)	k_1 (1/min)	R^2
CDI cell	ACC	Ni^{2+}	100	6.21	24.0E-3	0.9937	8.32	25.3E-4	0.9984
		Cu^{2+}	500	31.82	26.6E-3	0.9935	41.72	5.8E-4	0.9991
		Cr^{3+}	200	6.30	30.0E-3	0.9624	7.94	37.8E-4	0.9819
	ACC/MnO_2	Ni^{2+}	100	6.58	34.6E-3	0.9776	8.24	42.8E-4	0.9901
		Cu^{2+}	500	37.60	31.4E-3	0.9957	47.91	6.37E-4	0.9997
		Cr^{3+}	200	11.18	20.5E-3	0.9970	15.50	10.8E-4	0.9993
	ACC/ZnO	Ni^{2+}	100	9.57	24.3E-3	0.9935	12.84	16.5E-4	0.9970
		Cu^{2+}	500	44.02	32.8E-3	0.9853	55.40	6.0E-4	0.9967
		Cr^{3+}	200	11.74	27.3E-3	0.9979	15.41	16.1E-4	0.9995

MCDI cell	ACC	Ni^{2+}	100	9.98	24.9E-3	0.9977	13.36	16.3E-4	0.9991
		Cu^{2+}	500	48.15	22.2E-3	0.9951	65.45	2.9E-4	0.9991
		Cr^{3+}	200	9.67	29.4E-3	0.9894	12.47	22.4E-4	0.9970
	ACC/MnO_2	Ni^{2+}	100	9.50	34.3E-3	0.9904	11.91	29.2E-4	0.9984
		Cu^{2+}	500	58.19	22.7E-3	0.9974	79.03	2.4E-4	0.9996
		Cr^{3+}	200	12.27	33.8E-3	0.9873	15.44	22.0E-4	0.9965
	ACC/ZnO	Ni^{2+}	100	14.02	36.6E-3	0.9971	17.44	21.6E-4	0.9988
		Cu^{2+}	500	66.59	22.2E-3	0.9934	90.24	2.1E-4	0.9982
		Cr^{3+}	200	15.52	32.6E-3	0.9925	19.59	16.6E-4	0.9977

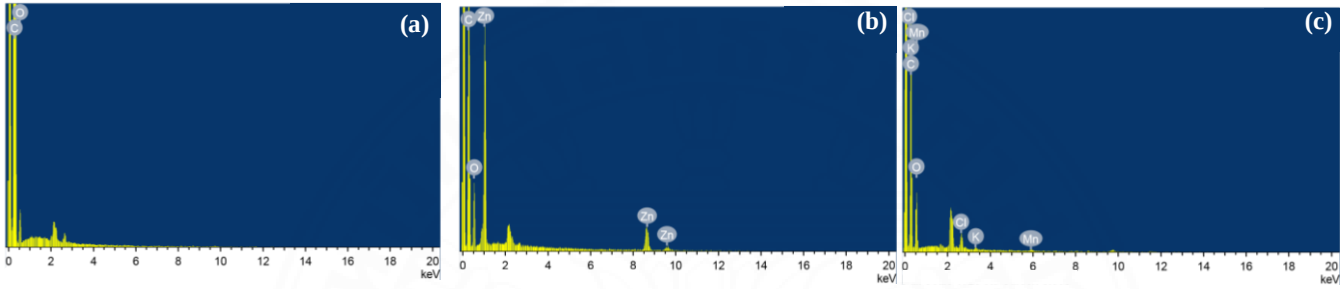

Element	Weight (%)	Atomic (%)
C	90.31	92.55
O	9.69	7.45

Element	Weight (%)	Atomic (%)
C	61.24	79.03
O	16.09	15.59
Zn	22.68	5.38

Element	Weight (%)	Atomic (%)
C	71.31	78.46
O	24.08	19.89
Cl	3.74	1.39
K	0.43	0.14
Mn	0.45	0.11

Figure D.1 EDS spectra analysis for (a) ACC, (b) ACC/ZnO, and (c) ACC/MnO_2 corresponding to Figure 4.20 (a), (b), and (c), respectively.

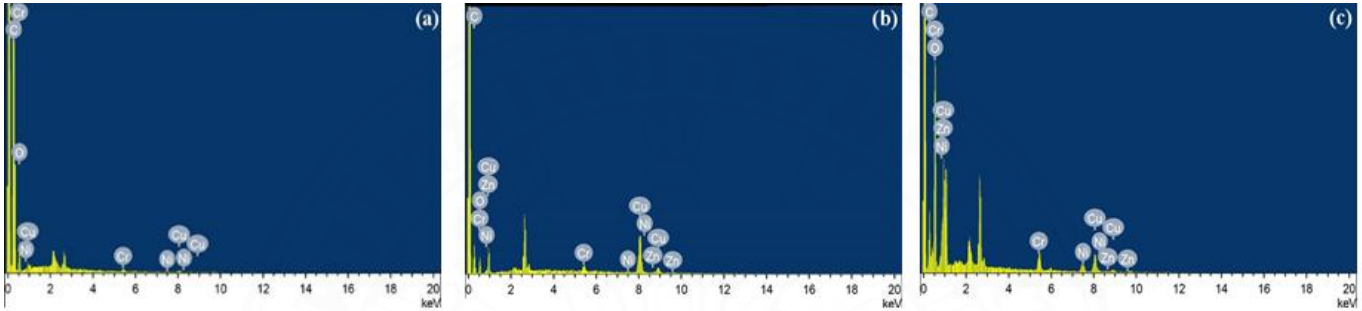

Element	Weight (%)	Atomic (%)
C	79.49	85.00
O	17.98	14.43
Cu	1.12	0.23
Ni	0.21	0.05
Cr	1.20	0.30

Element	Weight (%)	Atomic (%)
C	44.79	68.07
O	18.17	20.73
Zn	1.30	0.36
Cu	25.89	7.44
Ni	1.61	0.50
Cr	8.23	2.89

Element	Weight (%)	Atomic (%)
C	20.68	36.87
O	35.98	48.17
Zn	14.04	4.6
Cu	19.66	6.63
Ni	5.08	1.85
Cr	4.56	1.88

Figure D.2 EDS spectra analysis for the surface cathode of a) ACC in CDI cell with SA mixture, (b) ACC/ZnO in CDI cell with SA mixture, and (c) ACC/ZnO in CDI cell with SA-COD mixture after 50 cycles corresponding to Figure 4.26 (b), (c), and (d), respectively.

APPENDIX E

EXPERIMENT 5

Table E.1 The value of parameters in electroplating wastewater plant.

Parameter	Unit	Value of wastewater	National industrial effluent limit
pH	-	4.54	5.5 – 9.0
COD (Chemical Oxygen Demand)	mg/L	105.60	<120
Total Chromium (Cr)	mg/L	2.51	1.0
Zinc (Zn)	mg/L	273.41	5.0
Cadmium (Cd)	mg/L	0.09	0.03
Lead (Pb)	mg/L	0.20	0.2
Nickle (Ni)	mg/L	4.31	1.0
Copper (Cu)	mg/L	4.46	2.0
Selenium (Se)	mg/L	0.10	0.02
Arsenic (As)	mg/L	2.16	0.25
Manganese (Mn)	mg/L	15.96	5.0

Table E.2 Adsorption amount and recovery rate of ACC and ACC/ZnO in CDI cell and MCDI cell at flow rate of 10 mL/min.

Ion	ACC in CDI cell				ACC in MCDI cell				ACC/ZnO in CDI cell				ACC/ZnO in MCDI cell			
	5th cycle		50th cycle		5th cycle		50th cycle		5th cycle		50th cycle		5th cycle		50th cycle	
	A	R	A	R	A	R	A	R	A	R	A	R	A	R	A	R
Zn	2.55	35.7	2.1	24.3	2.94	41.2	2.69	31.2	2.67	38.1	1.82	29.0	3.13	43.7	2.81	36.4
Mn	< 0.1	-	< 0.1	-	0.1	37.5	< 0.1	-	< 0.1	-	< 0.1	-	0.13	40.0	< 0.1	-
Ni	< 0.1	-	< 0.1	-	< 0.1	-	< 0.1	-	< 0.1	-	< 0.1	-	< 0.1	-	< 0.1	-
Cu	< 0.1	-	< 0.1	-	< 0.1	-	< 0.1	-	< 0.1	-	< 0.1	-	< 0.1	-	< 0.1	-
Cr	< 0.1	-	< 0.1	-	< 0.1	-	< 0.1	-	< 0.1	-	< 0.1	-	< 0.1	-	< 0.1	-
As	< 0.1	-	< 0.1	-	< 0.1	-	< 0.1	-	< 0.1	-	< 0.1	-	< 0.1	-	< 0.1	-
Se	< 0.1	-	< 0.1	-	< 0.1	-	< 0.1	-	< 0.1	-	< 0.1	-	< 0.1	-	< 0.1	-

Cd	< 0.1	-	< 0.1	-	< 0.1	-	< 0.1	-	< 0.1	-	< 0.1	-	< 0.1	-	< 0.1	-
Pb	< 0.1	-	< 0.1	-	< 0.1	-	< 0.1	-	< 0.1	-	< 0.1	-	< 0.1	-	< 0.1	-

Note: A is Adsorption amount (mg/g) and R is recovery rate (%)

Table E.3 Adsorption amount and recovery rate of ACC and ACC/ZnO in CDI cell and MCDI cell at flow rate of 15 mL/min.

Ion	ACC in CDI cell				ACC in MCDI cell				ACC/ZnO in CDI cell				ACC/ZnO in MCDI cell			
	5th cycle		50th cycle		5th cycle		50th cycle		5th cycle		50th cycle		5th cycle		50th cycle	
	A	R	A	R	A	R	A	R	A	R	A	R	A	R	A	R
Zn	3.60	38.5	3.0	27.9	4.54	45.4	3.22	34.6	4.04	42.2	3.56	30.4	5.19	50.5	3.51	37.4
Mn	< 0.1	-	< 0.1	-	0.12	45.5	< 0.1	-	0.1	50.0	< 0.1	-	0.17	43.8	< 0.1	-
Ni	< 0.1	-	< 0.1	-	< 0.1	-	< 0.1	-	< 0.1	-	< 0.1	-	< 0.1	-	< 0.1	-
Cu	< 0.1	-	< 0.1	-	< 0.1	-	< 0.1	-	< 0.1	-	< 0.1	-	< 0.1	-	< 0.1	-
Cr	< 0.1	-	< 0.1	-	< 0.1	-	< 0.1	-	< 0.1	-	< 0.1	-	< 0.1	-	< 0.1	-
As	< 0.1	-	< 0.1	-	< 0.1	-	< 0.1	-	< 0.1	-	< 0.1	-	< 0.1	-	< 0.1	-
Se	< 0.1	-	< 0.1	-	< 0.1	-	< 0.1	-	< 0.1	-	< 0.1	-	< 0.1	-	< 0.1	-

Cd	< 0.1	-	< 0.1	-	< 0.1	-	< 0.1	-	< 0.1	-	< 0.1	-	< 0.1	-	< 0.1	-
Pb	< 0.1	-	< 0.1	-	< 0.1	-	< 0.1	-	< 0.1	-	< 0.1	-	< 0.1	-	< 0.1	-

Note: A is Adsorption amount (mg/g) and R is recovery rate (%)

Table E.4 Adsorption amount and recovery rate of ACC and ACC/ZnO in CDI cell and MCDI cell at flow rate of 25 mL/min.

Ion	ACC in CDI cell				ACC in MCDI cell				ACC/ZnO in CDI cell				ACC/ZnO in MCDI cell			
	5th cycle		50th cycle		5th cycle		50th cycle		5th cycle		50th cycle		5th cycle		50th cycle	
	A	R	A	R	A	R	A	R	A	R	A	R	A	R	A	R
Zn	2.04	30.1	1.39	19.8	3.44	35.0	2.85	26.3	2.42	33.9	1.97	23.5	4.45	36.9	3.23	29.8
Mn	< 0.1	-	< 0.1	-	0.13	33.3	< 0.1	-	0.12	33.3	< 0.1	-	0.18	35.3	< 0.1	-
Ni	< 0.1	-	< 0.1	-	< 0.1	-	< 0.1	-	< 0.1	-	< 0.1	-	< 0.1	-	< 0.1	-
Cu	< 0.1	-	< 0.1	-	< 0.1	-	< 0.1	-	< 0.1	-	< 0.1	-	< 0.1	-	< 0.1	-
Cr	< 0.1	-	< 0.1	-	< 0.1	-	< 0.1	-	< 0.1	-	< 0.1	-	< 0.1	-	< 0.1	-
As	< 0.1	-	< 0.1	-	< 0.1	-	< 0.1	-	< 0.1	-	< 0.1	-	< 0.1	-	< 0.1	-
Se	< 0.1	-	< 0.1	-	< 0.1	-	< 0.1	-	< 0.1	-	< 0.1	-	< 0.1	-	< 0.1	-

Cd	< 0.1	-	< 0.1	-	< 0.1	-	< 0.1	-	< 0.1	-	< 0.1	-	< 0.1	-	< 0.1	-
Pb	< 0.1	-	< 0.1	-	< 0.1	-	< 0.1	-	< 0.1	-	< 0.1	-	< 0.1	-	< 0.1	-

Note: A is Adsorption amount (mg/g) and R is recovery rate (%)

BIOGRAPHY

Name	Nguyen Tan Thong
Education	2014: Bachelor of Engineering (Environmental Engineering), Ho Chi Minh City University of Technology (HCMUT), Vietnam National University Ho Chi Minh City, Vietnam 2018: Master of Engineering (Environmental Engineering), Ho Chi Minh City University of Technology (HCMUT), Vietnam National University Ho Chi Minh City, Vietnam

Publications

Tan, T. N., Patcharanuruksakorn, A., Kerdchouay, A., Bunraksa, P., & Babel, S. (2024). Enhancing copper removal through integrated capacitive deionization with heterogeneous cation exchange membrane. *Suranaree Journal of Science and Technology*, *31*(2), p.030185.

Tan, T. N., Babel, S., Bora, T., Sreearunothai, P., & Laohhasurayotin, K. (2024). Preparation of heterogeneous cation exchange membrane and its contributions in enhancing the removal of Ni2+ by capacitive deionization system. *Chemosphere*, *350*, 141115.

Tan, T. N., & Babel, S. (2023). Unravelling the key contribution of a modified zinc oxide nanostructures on activated carbon cloth material for removal of Cu2+ in different configurations of capacitive deionization system. *Journal of Water Process Engineering*, *56*, 104268.